5-15-2009

Fog Cooling, Wet Compression and Droplet Dynamics In Gas Turbine Compressors

Jobaidur Rahman Khan
University of New Orleans

Fog Cooling, Wet Compression and Droplet Dynamics In Gas Turbine Compressors

A Dissertation

Submitted to the Graduate Faculty of the
University of New Orleans
in partial fulfillment of the
requirements for the degree of

Doctor of Philosophy
in
Engineering and Applied Science

by

Jobaidur Rahman Khan

B.S., Bangladesh University of Engineering and Technology, 1996
M.S., University of New Orleans, 2001

May, 2009

ACKNOWLEDGMENTS

Author thanks first Allah who gave the patience to complete this work. The author likes to pay his respect and gratitude to his thesis advisor Dr. Ting Wang, Professor, Mechanical Engineering Department, for his active guidance, constant inspiration and encouragement, invaluable suggestions and constructive criticism throughout the research that helped it to come up to the present state. Respects and gratitude are also paid to Dr. Kazim Akyuzlu, Professor of Mechanical Engineering Department, Dr. Martin Guillot, Associate Professor and Graduate Coordinator of Mechanical Engineering Department, Dr. Carsie Hall, Assistant Professor of Mechanical Engineering Department, Dr. Paul Herrington, Professor and Chairman of Mechanical Engineering Department and Dr. Juliette Ioup, Professor of Physics Department for serving as the thesis committee members.

The author also acknowledges the gratitude for the active support and inspiration of his family members, specially his wife, son, parents and siblings.

TABLE OF CONTENTS

LIST OF FIGURES

LIST OF TABLES

ABSTRACT

During hot days, gas turbine power output deteriorates significantly. Among various means to augment gas turbine output, inlet air fog cooling is considered as the simplest and most cost-effective method. During fog cooling, water is atomized to micro-scaled droplets and introduced into the inlet airflow. In addition to cooling the inlet air, overspray can further enhance output power by intercooling the compressor. However, there are concerns that the water droplets might damage the compressor blades and increased mass might cause potential compressor operation instability due to reduced safety margin. Furthermore, the two-phase flow thermodynamics during wet compression in a rotating system has not been fully established, so continued research and development in wet compression theory and prediction model are required.

The objective of this research is to improve existing wet compression theory and associated models to accurately predict the compressor and the entire gas turbine system performance for the application of gas turbine inlet fog cooling. The following achievements have been accomplished:

(a) At the system level, a global gas turbine inlet fog cooling theory and algorithm have been developed and a system performance code, FogGT, has been written according to the developed theory.

(b) At the component level, a stage-stacking wet compression theory in the compressor has been developed with known airfoil configurations.

(c) Both equilibrium and non-equilibrium water droplet thermal-fluid dynamic models have been developed including droplet drag forces, evaporation rate, breakup and coalescence. A liquid erosion model has also been developed and incorporated.

(d) Model for using computational fluid dynamics (CFD) code has been developed to simulate multiphase wet compression in the rotating compressor stage.

In addition, with the continued increase in volatility of natural gas prices as well as concerns regarding national energy security, this research has also investigated employing inlet fogging to gas turbine system fired with alternative fuels such as low calorific value synthetic gases. The key results include discovering that the saturated fogging can reduce compressor power consumption, but overspray, against conventional intuition, actually increases compressor power. Nevertheless, inlet fogging does increase overall net power output.

Keywords: Wet compression, Overspray, Axial Compressor.

CHAPTER ONE

INTRODUCTION

Gas turbines (GT) suffer from both decreasing output power and efficiency as the ambient temperature increases because the air becomes less dense (which results in less mass flow rate), and the compressor works harder as ambient temperature increases. It has been found that every 1°F raise of ambient temperature reduces gas turbine output power by approximately 0.3-0.5%, reported by Meher-Homji et. al. (1999). Gas turbine inlet air fog cooling is considered a simple and cost-effective method ($40-60/kW, 2008 money) to increase power output and often also increase thermal efficiency. **Fog cooling** is done by spraying micro-scaled water droplets into gas turbine inlet. The air through evaporation absorbs heat until the air is saturated before entering the compressor; this is called **"saturated fogging"**. If there are water droplets remaining after the air flow reaching saturation at the wet bulb temperature, the remaining droplets will enter the compressor as **overspray (or high fogging)**, which can further cool the compressor. When the water is sprayed after the air enters the compressor is called the **interstage fogging**. An example of fog cooling set up is shown in Fig 1.1.

Fog cooling is gaining popularity due to its low initial and maintenance costs. However, there are several concerns associated with the overspray and interstage fog cooling: (a) potential erosion of compressor blades caused by tiny water droplets, (b) drilling holes through the compressor casings to install fogging devices may cause problem of maintaining the compressor integrity, and (c) manufacturer's warranty could be voided. Among these concerns, the erosion problem is most controversial and requires both theoretical and experimental investigations.

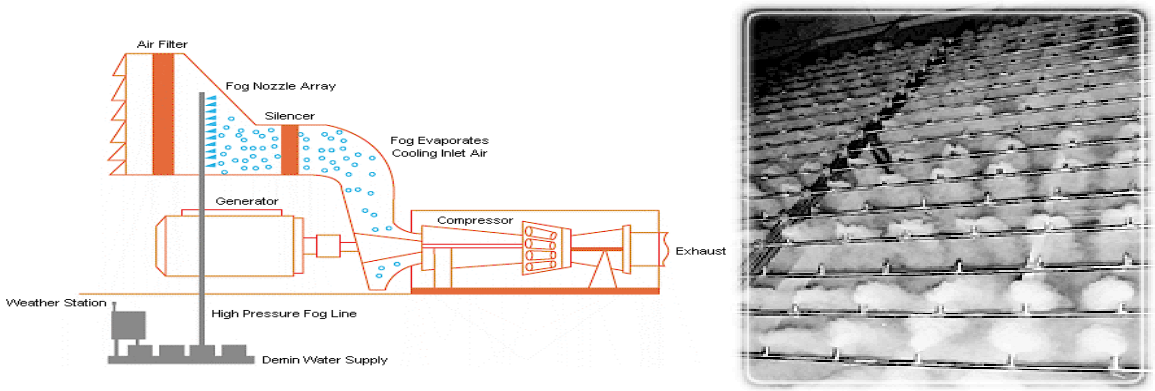

Figure 1.1 Fog cooling setup (Courtesy of MEE Industries)

1.1 Literature Review

The literature review will include thermodynamic formulation for wet compression, analysis of experimental and theoretical studies of gas turbine inlet fog cooling, design and off-design performances of compressor, parametric analysis of inlet fogging, and water droplet dynamics and heat transfer.

1.1.1 Fog/Overspray and Wet Compression

Spraying water before the compressor is very old practice, which started since 1940's. Gas turbines used to suffer from high back work ratio and thermal stress due to high temperature difference between inlet and exit. Kleinschmidt (1947) started development of theory for spraying water before a rotary positive-replacement type compressor. His theoretical analysis (no experiment) showed that a reduction of compressor work by 15% can reduce the back work ratio from 2/3 to 1/2 for a given pressure ratio and thermal efficiency improved 3% point using 3% weight of air. Wetzel and Jennings (1949) conducted a theoretical analysis of wet compression with pressure ratios of 4.8 and 7. They found that specific compressor work reduced. They experimented a 11-stage war-time supercharger with two different RPM (25,000 and 28,000), for both the cases they found the reduction of compressor specific work with complete evaporation of mist without any blade erosion. Hill (1963) developed comprehensive thermodynamic, aerodynamic and heat transfer theory of wet compression. He also conducted experiments on wet compression. (water or alcohol were considered as coolant).

Poletavkin (1970) presented formulation of wet compression thermodynamics. He showed theoretically that wet compression is very much effective for high pressure ratio (30 and up) and efficiency can be increased up to 50% by reducing the adiabatic index to 1.08-1.15. Slobodyanyuk (1973) showed that spraying 0.08 kg of distilled water (30-40 μm droplet dia.) per kg of dry air into the air intake of a compressor can augment the power by roughly 35%. Gasparovic and Hellemans (1973) showed that water injection in different places, like (a) before compressor, (b) after the compressor in a heat exchanger, (c) into or after combustor, increases net output with given pressure ratio. They showed that gas turbine works most efficiently when air is saturated with water vapor, which is proved by many researchers even now a days.

Brandon and Fortin (1982, 1983) modified Brayton Cycle utilizing alcohol fuels by spraying it during compression and after that using alcohol as fuel. They found that due to the evaporative cooling during compression, compressor work was reduced and as alcohol fuel was already preheated for combustion after compression, so the evaporation energy was not penalized by increased fuel. But Combustion chamber needed to be redesigned to burn the lean mixture delivered by the compressor. Murthy, Ehresman and Haykin (1986) conducted a comprehensive theoretical and experimental study on wet compression as they found that aircraft turbines were prone to water ingestion through the engine inlet during take-off from rough runways with puddles of water and flight through rainstorms. They studied the wet compression effect on engine (specially thrust, fuel consumption, surge margin and rotational speed). They took 4 basic processes in consideration for performance analysis e.g. aerodynamic interactions, radial displacement of discrete phase, heat and mass transfer and droplet size adjustment. Among the four processes, aerodynamic interactions and redistribution of discrete phases are significant, both individually and jointly. The heat and mass transfer processes also become important when the pressure and temperature were large across a compressor. A consequence of interphase heat and mass transfer is the increase in water vapor content. This led to changes in both density and specific heats. It was clear that changes in compressor performance due to water ingestion affect engine performance appreciably, but depended upon compressor losses, compressor outlet temperature and pressure, reduction in gas phase mass flow available in the turbine and the nozzles, engine control parameters etc. When some of the water entered the burner and evaporated therein, the extent of evaporation along the burner had a significant effect on engine behavior. If the amount of water evaporating in the burner would be small, then the engine might

operate satisfactorily even at high water ingestion rate provided the compression subsystem was affected within tolerable limit.

Nolan and Twombly (1990) discussed the design, installation, operation and performance of a direct mixing evaporative cooling system for gas turbine power augmentation. Saturation to the air was provided. The design flow capacity was doubled to allow for drift, pressure fluctuations, leaks and other losses, and the possibility of "overspray", which resulted 9.6% gain of power over the baseline output of 13.5 MW (80MW ISO), of which 7.4 % were attributed to the evaporative cooling and 2.2 % attributed to the reported 1.3 % increase in mass flow through the compressor. They also found that gas turbine exit temperature dropped of approximately 15°F and the firing temperature was increased so as to achieve the 1,000°F exhaust temperature limit. Young (1995) described the formulation of fundamental equations of gas-droplet multiphase flow. He showed how to calculate thermodynamic parameters for gas-droplet mixture, which are useful for wet compression simulation, which is used in this study where stage-stacking method is used and will be discussed elaborately later. Mee and Meher-Homji (1999) produced wet compression theory (which included psychrometry, steam table, air property table etc.), different performance curves for off-design conditions and industrial set-up for the fog cooling, which are already shown before.

Thermodynamic model of wet compression was developed by Zheng et. al. (2003 a) (Swapping a and b in the reference.) to analyze the effect of fog inlet cooling on gas turbine performance. Their analysis showed that the compressor work decreases and net output power increases with increased fog mass flow rate, whereas the efficiency curve is flat for a wider range of compression pressure ratio and turbine inlet temperature. They also showed that effective cooling reduces compression work. The wet compression work can even be lower than that of dry air isentropic compression work. Because of the compressor work reduction, index of compression is lowered. They also modeled the water droplet evaporation time, droplet break-up time and the droplet sizes after breakup. Later, Zheng et al. (2003 b) expanded their analysis to a regenerative gas turbine cycle, in which they discussed the concept of continuous evaporation and internal cooling of compressor through wet compression.

Bhargava et. al. (2002) presented the results of a comprehensive parametric analysis on the effect of inlet fogging on a wide range of existing gas turbines. Both evaporative and overspray fogging conditions were analyzed. They correlated the performance parameters (e.g.

power boost, heat rate, fuel flow rate, fog water flow rate per unit power boost and compressor temperature rise per unit power boost and compressor temperature rise per unit specific power boost etc.) with main gas turbine design parameters as a result of fogging. They indicated that aero-derivative gas turbines, in comparison to the industrial machines, have achieved higher performance improvements from inlet fogging. The study consistently showed that gas turbines with low values of specific work and turbine inlet temperature have a higher power boost and heat rate improvement compared to machines with lower corresponding values. They also showed that higher performance improvements were achieved using high pressure fogging at higher ambient temperature and lower relative humidity.

Chaker et. al. (2004) presented the results of extensive experimental and theoretical studies conducted over several years and coupled with practical aspects learned in the implementation of nearly 500 inlet fogging systems on gas turbines ranging from 5 to 250 MW. Their studies covered the underlying theory of droplet thermodynamics and heat transfer and provided practical points relating to implementing inlet fogging to gas turbine engines. They modeled the heat and mass transfer coefficients of droplet for natural and forced convection and described the effect of airflow velocity on fog droplet behavior. They also discussed the different measurement techniques and criteria for measuring the droplets composition from different nozzle designs. Compressor erosion, corrosion and fouling from experiments were introduced in these papers. These papers collectively provided experimental data on different nozzles and recommended a standardized nozzle testing method for gas turbine inlet air fogging. The complex behavior of fog droplets in the inlet duct was addressed and experimental results from several wind tunnel studies were documented. They introduced the pressure drop consideration in wet compression. They also showed the importance of proper and efficient drainage.

A one-dimensional analysis of compressor off-design performance was developed by Horlock (2001) to illustrate the compressor performance due to decrease in temperature for water injection. For the calculation of a 6-stage compressor he assumed the evaporation rate as evaporation throughout the stages. He cautioned that overspray could cause compressor operation to approach stalling point. Although he did not get any evidence of compressor stall from fog cooling from Utamura et. al. (1999), he suggested for more tests on land-based gas turbines.

To investigate the mist transport in the entrance duct, Wang et. al. (2008) conducted a computational fluid dynamic (CFD) study of different fundamental geometries including a straight tunnel, a diffuser, a contraction, and a 90^{o} bend. These geometries were used to investigate the separate effect of acceleration, deceleration, and centrifugal force on mist transport and cooling effectiveness, respectively. Lastly, a duct representing a real application was used for simulation. The effects of droplet size, droplet distribution, and humidity on cooled air temperature distribution were examined. Analysis on droplet history (trajectory and size) was employed to interpret the mechanism of droplet dynamics under influence of acceleration, diffusion, and body forces. They showed that in the contraction, the acceleration significantly lowers the cooling effectiveness when large droplets of 50-μm were used. In the diffuser, the average temperature increases near the exit because the flow separates and the reverse flow entrains warmer airflow from downstream. Near exit of the diffuser, high evaporation ratio occurs due to the high average temperature as well as lower flow velocity (for longer residence time). In the 90-degree bend, centrifugal force and secondary flow move the droplets toward the outer wall and result in a non-uniform temperature distribution at the exit with cooler area near the outer wall. High cooling effectiveness is achieved due to the secondary flow mixing. Simulation with a complex duct similar to those used in real applications shows regions of large recirculation. The recirculation regions should be removed or minimized because they produce flow pulsation, induce aerodynamic losses, trap water droplets, and could allow water droplets to coalesce into larger ones that may be detrimental to the compressor blades.

Quantitative analysis of inlet fogging system was provided by Willems et. al. (2003) on the basis of turbine operating conditions. Their data considered the actual combustion turbine operating conditions, psychrometric considerations and field measurements. They also considered the application of specialized temperature measurement equipment suitable for accurate dry bulb temperature detection in an environment that may contain free water in the air stream. Their test results showed that water evaporation does not take place homogeneously and it is obvious that the air stream at or near saturation does not absorb any water. As the fogging system does not homogeneously cool the incoming air, stratified regions of warmer and cooler airstreams co-exist in the bulk air stream. The result showed that the temperature in the duct profile had 3-7°C of temperature difference among different areas of the duct. Although power

output was certainly improved in all the test cases, the amount of power increase was largely determined by the ambient temperature, pressure and relative humidity.

Bhargava et. al. (2003) conducted a comprehensive analysis of different configurations of combined cycle power plants (CCPP) gas turbine inlet fog cooling. They reported that high pressure fogging is effective for recovering lost output power for hot ambient conditions. The power increases with increase of amount of overspray fogging. They showed that CCPP with advanced technology gas turbine systems showed smaller power boost compared to traditional CCPP due to fogging, but increase in fuel efficiency was found higher.

Bagnoli et. al. (2004) investigated effects of interstage water injection on the performance of a 17-stage gas turbine using aero-thermodynamic modeling. They discussed the impact of interstage injection on the stage-by-stage compressor performance characteristics of the selected gas turbine to estimate the overall gas turbine performance. They found that the maximum power could be obtained if the water is injected at the upstream of the compressor (i.e. saturation or overspraying) compared to the other interstage injection locations. Moreover, the maximum amount of water injection is limited by ambient conditions, maximum allowable gas turbine power output (which should not be more than 25-30% of design power) and the compressor surge limit. They cautioned that increased amount of water injection causes the last compressor stage to operate with closer to the surge line. Their result showed that in case of 40°C with 40% relative humidity, the loss of power output when compared with design ISO condition, could be recovered by injecting about 1.2% of water to air ratio upstream from the first stage, and loss of thermal efficiency could be recovered by 1.4% of water spray.

Sexton et. al. (2003) conducted a computational simulation to examine the concept of water injection, fogging and overspray. They studied the compressor performances under different conditions of ambient temperature, pressure and humidity, flow rate, overspray and water temperature. They designed the inlet duct to have realistic evaporative properties, e.g. flow rates, evaporation time and droplet diameter reduction. As a result of nonuniform droplet distribution, he found that there was a carryover of water droplets into the compressor blades even though the water is sprayed in the amount only meant for air to achieve saturation before enter the compressor. The droplets were so small that they followed the air path and evaporated in the first few stages of the compressor.

Hartel et. al. (2003) studied the effects of high fogging (overspray) on the work of compression. They used a droplet model where they took finite time of evaporation into account by introducing heat and mass transfer between discrete liquid droplets and gaseous phase. Their results showed that the beneficial effects of wet compression diminished when evaporation was slowed down. For compression ratios typical of modern heavy-duty gas turbines, droplets need to be as small as about 1-μm in order to achieve evaporation under approximate thermodynamic equilibrium during compression.

White and Meacock (2004) evaluated the effect of water injection on compressor performance. They investigated the thermodynamic and aerodynamic aspects of wet compression by a numerical method applicable to very fine droplet sprays. They showed that the entropy production due to irreversible phase change is strongly dependent on droplet size. Their results showed that individual compressor stages would, however, operate considerably off design, with front stages moving toward choke and rear stages toward stall, which had the effect of lowering the aerodynamic efficiency and narrowing the efficiency peak. The combination of thermodynamic losses and impaired aerodynamic efficiency resulted in the fractional work reduction due to evaporative intercooling being substantially less than that suggested by ideal wet compression calculations. On that basis, they suggested some redesign of the compressor to achieve the full benefits that were possible with water-injected cycles.

Li et. al. (2004) investigated wet compression on compressor operation instabilities. Their results indicated that water injection was not only a technique to improve the thermodynamic performance of a gas turbine, but also an effective method to stabilize the compression system. Compressor's steady and transient characteristics changed after the water injection. The compression system could come out of instability after water injection. They stated spraying water into the compressor was one of the most effective and active ways for controlling instability by avoiding surge and rotating stall, extending operating region, and increasing surge margin under certain conditions (Fig.1.2). Li et. al.'s conclusions somehow were opposite to White and Meacoke's conclusions.

1.1.2 Interstage Wet Compression

There are several reasons for implementing the interstage fogging. Ingistov (2001) pointed out that water injection system was installed in a 7EA gas turbine to wash the compressor blades in order to preserve the gas turbine output power rather than augment the power output. Shepherd et. al. (2006) presented field data from a Siemens gas turbine to compare the performance between applying inlet and interstage fogging. The data showed that the output power augmentation obtained by applying the interstage fogging was almost insensitive to the ambient temperature variation. They treated this feature as a merit of interstage fogging. The data further showed the NO_x reduction was more pronounced by applying interstage fogging than inlet cooling. They also mentioned about the risks associated with spraying water into a compressor; for examples, the issues related to water distribution, degradation of compressor inlet duct materials, fouling of the compressor, compressor casing distortion, disturbance to the combustion dynamic pressure, and the need to tune the control system integration.

Bagnoli et. al. (2008 a) developed a calculation code by modeling the exchange of latent heat at the inlet and outlet stage and the exchange of sensible heat at constant temperature and pressure in the middle of the stage. Using the model developed above, Bagnoli et. al. (2008 b) investigated the effects of interstage water injection on the performance of a GE Frame 7EA gas turbine using for aerodynamic modeling. Their analysis showed that the compressor performance depended on the location of water spray. A careful examination of the 1st and 17th stage performance characteristics showed an unloading of the first stage and an increase in loading of the 17th stage for every case of injection point and ambient condition investigated. Increasing the amount of water injected caused 17th stage operating point to move closer to the surge line suggesting that one had to be cautious in selecting the water amount to inject inside the compressor. They found that gas turbine lost approximately 15% power output due to high ambient temperature compared to the ISO case. 1.6% of water injection at stator of the compressor stage #2 allowed recovering the lost power for high ambient temperature. They also found that the power boost per unit of water injection decreased as the injection point moves from first to fifth stage. The droplet residence time decreased as the injection point moved closer to the compressor inlet. The maximum reduction in compressor specific work (that reach values of about 97% of the specific work in ISO dry case) was achieved in case of water injection

taking place in the inlet duct and the highest water injection mass flow rate at high ambient temperature conditions.

A simple numerical method based on both droplet evaporation and compressor mean-line calculation was presented by Abdelwahab (2006) for the computation of wet compression processes applied to a centrifugal compressor. His compressor model was coupled to a water droplet model, which assumed small droplets with no internal temperature gradients and negligible slip with the gas velocities. The small droplet diameter was presented due to the high injection rates. Sufficiently small water droplets needed to be used in order to avoid mechanical problems such as exerting a braking torque as well as producing excessive erosion on the impeller blades. The combined droplet-compressor model was used to predict the compressor stage performance at various inlet conditions, water injection rates, water droplet radii, and design pressure ratios. The analysis showed that the small droplet radii lead to much faster evaporation time compared to the fluid particle travel time and hence more wet compression effects were available in both the impeller and collector. For droplet radii less than 10μm, the evaporation time in the collector was much shorter than the fluid particle residence time. As the pressure ratio of the stage increased the fluid particles traveled through the impeller at faster speeds and hence the available time for water droplets to evaporate was reduced.

Sanaye et. al. (2006) studied the effects of inlet fogging and wet compression on gas turbine performance. They modeled the evaporation of water droplets in the compressor inlet duct and estimated the diameter of water droplets at end of the inlet duct. They compared the results with the results from FLUENT software. They also predicted the compressor discharge air temperature due to the presence of unevaporated water at the inlet duct. They showed that with overspraying, the compressor power input decreased due to wet compression (intercooling) effect relative to the inlet fogging case. This phenomenon was observed from both computed and reported results for 1% and 2% overspraying. It should be mentioned that the compressor specific work input decreased for all inlet fogging, 1% and 2% overspray cases. They found that flow coefficient increased in first few stages due to the water spray, which led to the increase in axial velocity at the first few stages, also the corrected speed increased due to the cooling of compressor inlet air. This effect resulted to an increase in density and pressure and decrease in the axial velocity at the next compressor stages. The amount of water injection increased with increasing pressure ratio. Following the work of Spina (2002), Sanaye et. al. employed the

approach of using the generalized compressor performance curve to calculate the rotor work coefficient of each stage by using empirical value Shape Factor and compared the results with the results obtained from FLUENT.

During the development of the wet compression model, one roadblock is associated with the unavailability of the compressor performance map, which has been highly guarded by the gas turbine manufacturers as proprietary information. To overcome this problem, Cerri (et. al. (1993) introduced the concept of Shape Factor (SF) by using a single value of shape factor to represent the overall performance of a compressor on a "generalized compressor performance chart" which shows the performance change corresponding to the designed point.

The Shape Factor used in Spina's work was first introduced by Muir et. al. (1989). Spina (2002) summarized the method of using generalized performance curves of compressors and compare the computed data with the experimental work performed by Muir et al. (1989), see Fig. 1.2. Spina (2002) introduced the stage-stacking procedure in a program for gas turbine thermodynamic cycle calculation and used the SF parameter as a “tuning” unknown parameter which was determined in order to minimize the mean square error between measured (or available) data on a gas turbine and the corresponding data computed by a computer program. Typically the SF values can be determined by the values of overall gas turbine efficiency (or fuel mass flow rate), pressure and temperature at the compressor outlet and turbine outlet temperature at some loads and ambient temperature.

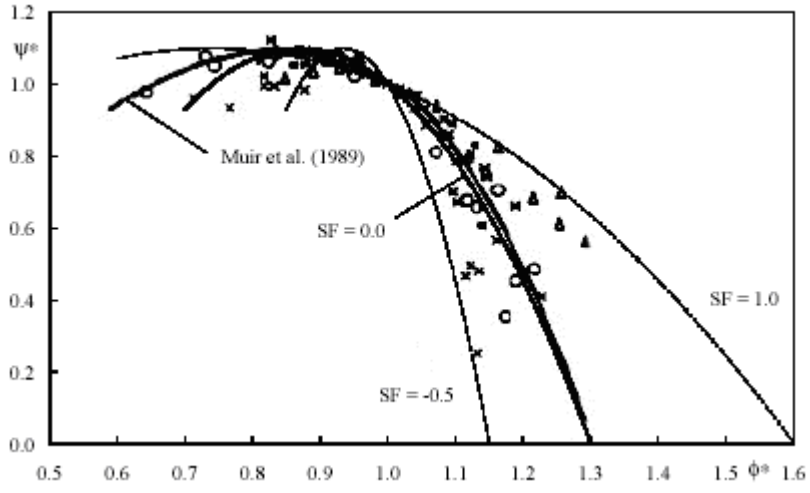

Figure 1.2 Generalized stage characteristics $\psi^* = F_\psi(\phi^*, SF)$ and experimental data points [Muir, (1989)]

In using the generalized performance curves, a Shape Factor (SF) needs to be determined. Unfortunately, the selection of the SF is also an uncertain process. The characteristics of the method proposed by Spina was that unknown parameters defining the generalized stage performance curves were determined by combining a cycle program with compressor and turbine performance maps obtained using the "stage-stacking" procedure. The results showed that the capability of the method in the program accurately reproduced the available data. The high nonlinearity of the program encountered some convergence error, so robust algorithm was suggested for better results.

The expression of shape factor has a lot of limitations and will be one of the subjects for this research.

Kim et. al. (2006) explained the theoretical limits of machines via a heat and mass transfer model and modeled continuous compression cooling via evaporation based on droplet evaporation analysis. Parametric studies showed that the effect of variables such as droplet size, water injection ratio or compression ratio on transient behavior of droplet evaporation process. Wet compression parameters such as evaporation time, compressor outlet temperature and compression work were estimated. Transient behavior of variables such as droplet mass and temperature, gas temperature and enthalpy were investigated. Evaporation time was explored thoroughly as a crucial design variable. They found that initially, the increase of the droplet temperature overrode the decrease in droplet mass and resulted in an internal energy increase in the droplet. The internal energy peaked and then decreased with time as the liquid evaporated. The evaporation time decreased as the water injection ratio or initial droplet radius decreased, or compression ratio increased. They found that the evaporation time exhibited a complex dependence on many compression and injection variables. They found the water injection ratio, compression ratio and droplet initial radius as the most significant variables. Those parameters largely defined the compressor power, which could be reduced to 70% of its value for a compression ratio of 25 and an injection ratio of 10%.

Water injection modifies the component operation. An adaptive performance model was developed by Roumeliotis et. al. (2003), who described the procedure for setting an accurate model of a twin-spool gas turbine equipped with the possibility for inlet evaporative cooling, intercooling by water injection, and water or steam injection in the combustion chamber. The

model covered water injection at engine inlet, between the compressors, and at the compressor exit. They showed how operation with water injection modified component operation. Since the operation for power generation was at constant speed of rotation, they showed that for obtaining the same power output with steam injection, the low pressure compressor operated at higher pressure ratio and when the steam was injected in high pressure compressor then operating point moved closes to surge limit. They discussed the impact of accurate modeling on performance diagnostics and they showed a model incorporating the possibilities for modeling the different types of wet operation was necessary for continuous reliable engine monitoring.

1.1.3 Droplet Dynamics

Droplet dynamics involves droplet evaporation, droplet breakup, droplet coalescence, droplet heat transfer, and droplets interactions etc, which have direct effects on wet compression performance. Models for droplet evaporation were developled by Zheng et. al. (2003 b) and White and Meacock (2004). Their models were based on pressure and temperature of main fluid and droplet, the diffusion coefficient, the droplet diameter and humidities. Zheng et. al. (2003 b) emphasized the evaporation rate of water droplet, which played a major role on the wet compression polytropic index. They assumed the evaporation rate remained constant throughout the wet compression.

Droplet evaporation depends on heat transfer between the droplet and main fluid (air). The forced convection takes place as long as there is a slip velocity between air and droplet, whereas, only natural convection prevails when slip velocity is zero as modeled by Chaker et. al. (2004).

1.1.3.1 Droplet Breakup

Droplet breakup models include two categories: liquid jet breakup to droplets and big droplets breakup to smaller droplets.

Liquid jet breakup depends on the liquid injection condition and the interaction between the liquid jet and the surrounding airflow conditions such as counter flow (air flow in opposite direction), parallel flow (air flow in the same direction), and crossflow (air flow in perpendicular direction). Madabhushi et. al. (2004) numerically simulated the break-up of a liquid jet in a crossflow air-stream at atmospheric pressure and temperature conditions using Reynolds

Average Navier-Stokes Equation. Their results showed that droplets encountered a breakup at a certain time due to crossflow (which was named as column break-up) and then break-up took place according to Weber number (the ratio of viscous force to surface tension). They mentioned that the breakup was a function of cross-flow velocity and droplet initial diameter, which depended on the injection orifice diameter of the nozzle. Their results indicated that breakup time was longer for smaller crossflow velocity and bigger diameter.

Duan et al. (2003) presented the numerical simulation of droplet breakup under an impulsive acceleration in another immiscible fluid by the Moving Particle with Semi-implicit (MPS) method, and the effect of the density ratio between droplet and ambient fluid on a critical Weber number. Their density ratios were very small (e.g. 1, 3, 5, 7 and 9), but the results showed that the Weber number was inversely proportional to density ratio and when the density ratio exceeded 3, the Weber number became less sensitive to the density ratio. The critical Weber number for their experimental density ratio was about 0.4.

O'Rourke and Amsden (1987) developed the Taylor Analogy Breakup (TAB) model. The TAB model is a classic method for calculating the droplet diameters after breakup, which is applicable to many engineering sprays. This method was based upon Taylor's analogy between an oscillating and distorting droplet and a spring mass system, where the spring surface tension forces, droplet drag force and droplet viscosity forces were made analogous to restoring, external, and damping forces as shown in Eqs (1.1) and (1.2). The equation governing a damped, forced oscillator is,

$$F_{sp} - k_{sp} x - d_{sp} \frac{dx}{dt} = m \frac{d^2 x}{dt^2} \qquad (1.1)$$

$$\frac{F_{sp}}{m} \sim \frac{\rho_a u^2}{\rho_w d}$$
$$\frac{k_{sp}}{m} \sim \frac{\sigma}{\rho_w d^3} \qquad (1.2)$$
$$\frac{d_{sp}}{m} \sim \frac{\mu_w}{\rho_w d^2}$$

where x is the displacement of the droplet equator from its spherical undisturbed position. The coefficients of this equation are taken from Taylor's analogy:

When the droplet oscillations grow to a critical value of Weber number, droplets break up into a number of child droplets. In the work of O'Rourke and Amsden (1987), the critical value for Weber number was 6.

1.1.3.2 Droplet Coalescence

Martula et. Al. (2000) introduced coalescence induced coalescence (CIC) model of inviscid droplets in a viscous fluid. They stated that two droplets coalesced when they came into contact at a sufficiently high capillary number (ratio between the viscous force and surface tension). A neck forms at the junction, creating gradients in curvature that caused the newly formed composite droplet to relax to a sphere. This shape relaxation disturbed the surrounding fluid, thereby induced a flow field. In CIC model, the flow field transported nearby droplets and caused other coalescence events. As each subsequent event created another flow field that could affect other droplets into contacts and coalescence, thereby a cascade of coalescence events resulted. The resultant velocity of each droplet in the suspension was calculated by superimposing all of the coalescence-induced flow fields. The Faxen's law was applied to calculate the resultant velocity of each droplet in the suspension

Pan and Suga (2005) developed a numerical model of two-phase droplet collision for high density ratio (e.g. air-water mixture). They showed the importance of Weber number on coalescence. They located two coalescence regimes, one accompanied with a significant deformation of the drops and another with a minimum deformation during the coalescence process. They linked the appearance of such a feature to the physical properties (density and viscosity) of both fluids as well as the ambient gas pressure. They also speculated that the intermolecular forces, the molecular structures of the liquid and the ambient gas controled the tendency for the final merging of the droplet surface and found that the presence of fuel vapor in a fuel spray promoted coalescence.

An analytical model was presented by Stegman et. al. (1999), who predicted the deformation of Newtonian droplets in an axisymmetric, time-dependent, elongational viscous flow. An analytical expression for the droplet-stretching rate was derived for a Newtonian droplet subjected to a (time-varying) Newtonian elongational flow. The shape of the droplet was assumed to be an ellipsoid of revolution, which, in first order approximation, was confirmed by

experimental results. Their experiments showed the critical length for breakup of visco-elastic droplet exceeded those for Newtonian droplets.

Van den Hengel et. al. (2005) employed a discrete bubble model (DBM) to investigate the hydrodynamics, coalescence and breakup occurring in a bubble column. They accounted for the encounters between two bubbles and between a bubble and a wall. They modeled the coalescence rate as a product of collision frequency and coalescence efficiency (a random function). They formulated contact time and energy dissipation on the basis of turbulence. They modeled the breakup in the similar manner as the result of interaction between turbulent eddies and droplets.

Qiang et. al. (2006) implemented a mesh-independent and less time consuming collision and coalescence model, although it was not clear about the extent of mesh independency. They set some numbers (18 for 2-D, 54 for 3-D) of neighboring droplets as a probable collision partner. Their results showed that they had same collision outcome for coarser and finer meshes, which were not the same in the O'Rourke's model (1981). Although the coarser mesh gave the same result of coalescence, but might not be good for overall simulation (e.g. mass, momentum and energy conservation equations). O'Rourke considered coalescence as an outcome of collision. O'Rourke's algorithm assumed that two droplets might collide only if they were in the same continuous-phase cell. This assumption could prevent droplets that were quite close to each other, but not in the same cell, from colliding, although the effect of the error due to this assumption was lessened by allowing some droplets that were farther apart to collide. The overall accuracy of the scheme was second-order in space. Once it was determined that two parcels could collide, the outcome of the collision was "coalescence" if the droplets collided head on, and "bouncing" if the collision was more oblique. Droplet coalescence model improves discrete phase calculation when strong local acceleration or deceleration presents in the flow field such as over the airfoil surface.

O'Rourke's model is further described below. The probability of two droplets colliding is derived from the point of view of the larger droplet, called the collector droplet and identified below as the number 1. The smaller droplet is identified in the following derivation as the number 2. The calculation is in the frame of reference of the larger droplet, so the velocity of the collector droplet is zero. Only the relative distance between the collector and the smaller droplet is important in this derivation. If the smaller droplet is on a collision course with the collector,

the centers will pass within a distance of ½(d_1+d_2). More precisely, if the smaller droplet center passes within a circle centered around the collector of area ¼π(r_1+r_2)² perpendicular to the trajectory of the smaller droplet, a collision will take place. This disk can be used to define the collision volume, which is the area of the aforementioned disk multiplied by the distance traveled by the smaller droplet in one time step, namely ¼π(r_1+r_2)²V_{rel} Δt, where V_{rel} is the relative velocity between the two droplets. The algorithm of O'Rourke uses the concept of a collision volume to calculate the probability of collision. Rather than calculate whether or not the position of the smaller droplet center is within the collision volume, the algorithm calculates the probability of the smaller droplet being within the collision volume. It is known that the smaller droplet is somewhere within the continuous-phase cell of volume ~~V~~. If there is a uniform probability of the droplet being anywhere within the cell, then the chance of the droplet being within the collision volume is the ratio of the two volumes. Thus, the probability of the collector colliding with the smaller droplet is,

$$P_1 = \frac{\pi(d_1 + d_2)^2 V_{rel} \Delta t}{4\text{~~V~~}} \qquad (1.3)$$

Eq. (1.3) can be generalized for parcels, where there are n_1 and n_2 droplets in the collector and smaller droplet parcels, respectively. The collector undergoes a mean expected number of collisions given by

$$\bar{n} = \frac{n_2 \pi(d_1 + d_2)^2 V_{rel} \Delta t}{4\text{~~V~~}} \qquad (1.4)$$

The actual number of collisions that the collector experiences is not generally the mean expected number of collisions. The probability distribution of the number of collisions follows a Poisson distribution, according to O'Rourke, which is given by,

$$P(n) = e^{-\bar{n}} \frac{\bar{n}^n}{n!} \qquad (1.5)$$

where n is the number of collisions between a collector and other droplets. This modeled developed by O'Rourke (1981) is employed in this present study.

1.1.3.3 Droplet-Induced Blade Erosion

When droplet flows in the air stream and hits the compressor blades (stator and rotor), the blades may encounter erosion or accretion. Water droplet erosion poses a serious potential threat to the critical path of maintenance outages in steam turbine. Lam et. al. (2003) estimated erosion rate in steam turbines from empirical formula. They presented two applications for the demonstration of erosion rates. Their results showed that the large droplets impact on the leading edge suction side due to insufficient axial clearance for the droplets to break up. Their another case handled with extremely wet steam which was developed by a film of water accumulated on the stationary blades. Although the film got enough space for breaking up, higher liquid droplet density had caused the premature erosion nonetheless.

Erosion is significantly dependent on the attack angle. Haugen et. al. (1995) tested a total of 28 materials at impact angles of 22.5° and 90°, and some at 7.5°, with test air velocities at 22, 55 and 320 m/s. C-Steel was selected as a reference material and was, as such, subject to more extensive examination than the other materials, with additional tests also performed at impact angles of 15°, 30° and 45°. Impact angles 22.5° and 90° were selected since maximum erosion was achieved at those angles for ductile and brittle materials, respectively. The basic premise was that the cutting action of the particles is more important for ductile materials and deformation (or displacement) is more significant for brittle materials. Of the 28 materials, the most erosion resistant were found to be the three solid tungsten carbide materials and two of the ceramics, Si_3N and B_4C. Only one coating, a Degun tungsten carbide layer, was found to give significantly improved erosion characteristics as compared with the reference material, C-Steel. Nokleberg et. al. (1998) studied the erosion of the choke valve used in oil and gas industry. A Langrangian trajectory calculation with stochastic tracking had been used by them to account for the effect of local turbulence quantities predicted in the continuous phase (k-ε model) for their erosion model. The forces on the particles included drag force, gravity and pressure. Three different choke openings were simulated with flow, particle tracking and erosion: 10%, 12.5% and 25% open. In addition the flow field was simulated for 50% choke opening. A velocity restitution factor after wall impact (normal velocity ratio) of 90% was used. The erosion tests in both the modified Needle & Seat choke and the External Sleeve choke gave peak erosion rates only 2-3 times larger than calculated. This was near the uncertainty of the erosion model alone. Other uncertainties were particle sharpness and reflection velocities after several impacts in the

chokes. The predicted behavior was thus satisfactory for such complex flow geometries, especially since there was such a large difference in the maximum erosion rate for the two types of chokes for the same test condition.

Tabakoff et. al. (1990) presented the results of investigation of blade erosion due to ash particles. They considered typical ash particle size distribution. The results indicated a significant influence of size distribution on blade erosion. They showed that not only the magnitude of erosion was influenced by location of blade but also the location of maximum blade erosion. They also showed that in the first stage, the maximum erosion took place at the blade trailing edge of the stator blade and leading edge of the rotor blade. For the multi-stage turbines the maximum erosion took place at the outmost radial location. The blade trailing edge erosion could present a serious problem because of the smaller blade thickness. They concluded that the blade erosion was generally lower for non-uniform distribution of particles. The result of ash particle erosion could be similar to liquid droplet erosion in terms of erosion locations on blades, but with different erosion magnitude.

Liquid particle erosions shown by Chattopadhayay (2001), Budinki (1996), Fayall (1966), Finnie et. al. (1967, 1968) and Bowden et. al. (1964), are different from solid particle erosion. The erosion pits were formed at the initial steady state of liquid erosion shown by Chattopadhayay (2001). Beyond the steady state, the cracks were formed at the walls and bases of the pits, propagation of which led to detachment of fragments of materials. For the liquid particle erosion, a critical impact velocity was considered below which erosion did not take place.

Fayall et. al. (1996) reviewed the erosion problem in aircraft due to rain. They showed that the factors affecting the rain erosion characteristics included type of material, surface finish, shape of component, speed and rainfall intensity. They collected the experimental data and derived an empirical database with those affecting factors. Bowden et. al. (1964) showed the difference between the solid particle impact and liquid particle impact. In case of solid particle impact the stress to produce fracture occurred at a much lower impact velocity than with a liquid, and the rise time of the stress was correspondingly greater. They documented that the impact duration of a solid particle was in the order of 100 micro-seconds compared to the 1-2 micro-seconds of high speed liquid impact. The fracture pattern of a solid impact of moderate velocity was found resembling more closely to that produced by static loading and the fracture energy

was seen being dissipated in forming a ring crack and in developing a relatively small number of radial cracks. The circumferential fractures found with high-speed liquid impact and explosive loading were suggested as the result of the interaction of the Rayleigh Stress wave with flaws. Since the circumferential fractures were short and discrete, the fracture pattern on one specimen gave essentially the result of many tensile experiments.

1.1.4 Computational Model and Simulation

Incorporating the droplet dynamics into computational model and simulation is one of the goals of this study. The methodology employed in some of recent CFD work on mist film cooling of turbine blade can be used as a guidance for developing CFD wet compression model in this study. For example, Li et. al. (2006) explored film-cooling enhancement by injecting mist into the cooling air with various modeling schemes. The effect of turbulence models, dispersed-phase modeling, inclusion of different forces (Saffman lift, thermophoresis, and Brownian), trajectory tracking, and mist injection scheme were studied. They used the RNG k-ε model, RSM and the standard k-ε turbulence model with the enhanced wall treatment, which produced consistent and reasonable results. The thermophoretic force slightly increased the cooling effectiveness, but the effect of Brownian force and Saffman lift was imperceptible. By injecting a small amount of droplets (mist) into the cooling air, the performance of film cooling could be improved significantly. They concluded that injecting 2% mist into the coolant could increase the cooling effectiveness downstream about 45%. The turbulence dispersion showed a significant effect on mist film cooling by using the stochastic tracking scheme. Approximately 10 percentage points cooling effectiveness enhancement were resulted in addition to the enhancement from the mist film cooling without considering turbulence dispersion. Cooling effectiveness decreases by 5% by increasing turbulence intensity from 1 to 10%.

Wang and Dhanasekaran (2008) calibrated a CFD model for mist/steam impinging jet to cool turbine blade, by employing different turbulence models, computational cells, wall y^+ values, and selection of near-wall functions using the laboratory results. They also studied the effect of different forces (e.g. drag, thermophoretic, Brownian, and Saffman's lift force). None of the models were found good for all the flow regions from near the stagnation region to far-field downstream of the jets, however they found that the standard k-ε and RSM turbulence models

performed better than other models. The RSM model had produced the closest results to the experimental data.

1.2 Effect of Low Calorific Value (LCV) Fuels

All the studies of fog/overspray cooling are applied to gas turbines fired with nature gas (NG) or oils. With continued increase of volatility of natural gas prices and concerns regarding national energy security, alternative fuels such as synthesis gas (syngas) derived from gasification of coal (a more stable energy source), petcoke, or biomass (more environmentally friendly) are considered as important common fuels in the future. Depending on the feedstock types and gasification process, the heating value could range from 35% of the NG heating value from an oxygen-blown synthesis gas derived from coal to 10-15% of NG heating value from a producer gas derived from air-blown biomass gasification. When LCV fuels are used, more fuel mass flow rate (3 - 10 times) is needed to achieve the required heating value by adding an additional fuel compressor. This additional fuel mass flow rate will impose heavier load to the main compressor due to increased backpressure in comparison when natural gas is used. Implementation of fog/overspray cooling will further strain the already overloaded compressor if existing commercially available gas turbines are used. To achieve a better gas turbine performance, the existing gas turbines may need to be modified to accommodate the increased fuel flow rate in the combustor and turbine. In addition, the effect of fog/overspray on the performance of LCV fired gas turbine systems is not clear, which motivates the development of a wet compression thermodynamic model by including the fuel compressor work and the additional fuel mass flow rate in calculating the turbine inlet temperature and to specifically investigate the influence of fog/overspray on the output power and efficiency when LCV fuels are burned, and compare the results with those fired with natural gas.

In the subject of applying fog cooling to LCV-fired gas turbine, Yap et. al. (2007) has conducted related study by simulating power plants fired by producer gas with inlet fog cooling and steam injection using the Thermoflow commercial code. The producer gases were derived from biomass, which had the low heating value (4-10 MJ/kg about 10% of natural gas's heat value of 45MJ/kg). Due to the low heating value of the producer gases, the required fuel flow rate was 10-14 times higher than the same for natural gas. This high fuel flow rate caused the increased backpressure and affected operating conditions and gas turbine performance. They

showed that gas turbine inlet fogging further produced increased mass flow rate as an additional burden to the compressor due to increased backpressure. They analyzed two dozens of cases of different approaches to accommodate the increased flow rates and compressor backpressure such as by reducing turbine inlet temperature or opening the turbine nozzle openings. They found the best performance occurred when the designed pressure ratio was maintained by widening nozzle openings, even though the turbine inlet pressure was reduced under this adjustment.

1.3 Research Objectives

Since the two-phase flow thermodynamics during wet compression in a rotating system has not been fully established and the concerns that the water droplets might damage the compressor blades, and increased mass flow rate from fogging might cause potential compressor operation instability due to reduced safety margin. The **objective** of this research is to improve existing wet compression theory and associated models to accurately predict the compressor and the entire gas turbine system performance for the application of gas turbine inlet fog cooling.

The following specific **goals** are proposed to achieve the objectives:

(1) At the system level, develop a global gas turbine inlet fog cooling theory and write a system performance code, FogGT, based on the developed theory.

(2) At the component level, develop a stage-stacking equilibrium and non-equilibrium wet compression theory in the compressor and incorporate this stage-stacking theory into the FogGT system code.

(3) Modeling the important parameters for CFD simulation by incorporating the following mechanisms:
   (a) Heat transfer between droplets and air
   (b) Hydrodynamic and thermal response times between droplets and air
   (c) Erosion of blades by liquid droplets
   (d) Breakup of water droplets
   (e) Coalescence of water droplets

(4) Incorporate the above developed models into computational fluid dynamics (CFD) code to simulate multiphase wet compression in the rotating compressor stage.

(5) With the continued increase in volatility of natural gas prices as well as concerns regarding national energy security, alternative fuels such as low calorific value (LCV) synthesis gases (syngas) derived from gasification of coal, petroleum coke, or biomass are considered important common fuels of the future. This research will also study the effect of fogging/overspray on the performance of LCV fuel fired gas turbine systems.

CHAPTER TWO
DEVELOPMENTS OF MODELS FOR WET COMPRESSION AND DROPLET DYNAMICS

Development of analytical models include the following five categories:

1. Development of **thermodynamic models** for two-component and two-phase flow under wet compression. The major theme involves changing relationships of enthalpy-entropy, liquid droplet evaporation mechanisms, and variations of thermodynamic properties.
2. Development of stage-stacking model for **blade aerodynamics and load function** under the influence of wet compression.
3. Development of droplet dynamics models including fluid mechanics, heat transfer, breakup, coalescence.
4. Development a model for using low calorific value (LCV) fuels with fogging and wet compression.
5. Incorporating all the above models and developing the code FogGT to evaluate the complete gas turbine system performance (not just in the compressor) for wet compression.

2.1 Thermodynamic model of Gas Turbine System

A gas turbine system equipped with a fog sprayer device and a fuel compressor is shown in Fig. 2.1. The fuel compressor is used to compress low calorific value fuels (LCV) to match the backpressure increase due to either increased fuel flow rate or moist air flow rate.

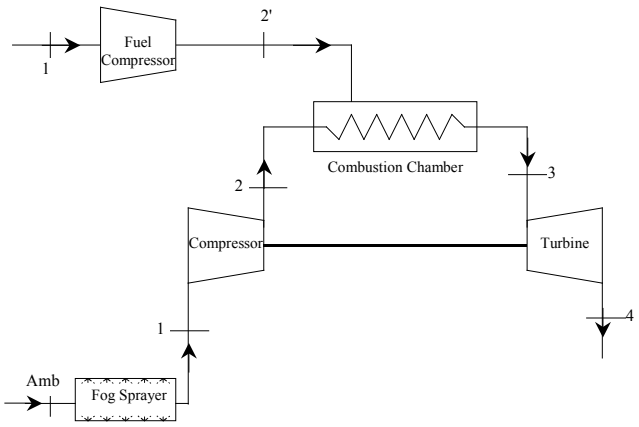

Figure 2.1 The gas turbine system with a fog spraying device and an additional fuel compressor

2.1.1 Effect of Elevated Ambient Temperature on GT Performance

The effect of elevated temperature on GT power output and efficiency can be explained by analyzing the P-v and T-s diagrams. Path 1-2-3-4 in Fig. 2.2 shows the ideal Brayton cycle at the reference ISO condition (59°F/288.2K and 60% relative humidity) and 1'-2'-3-4 shows the processes on a hot day.

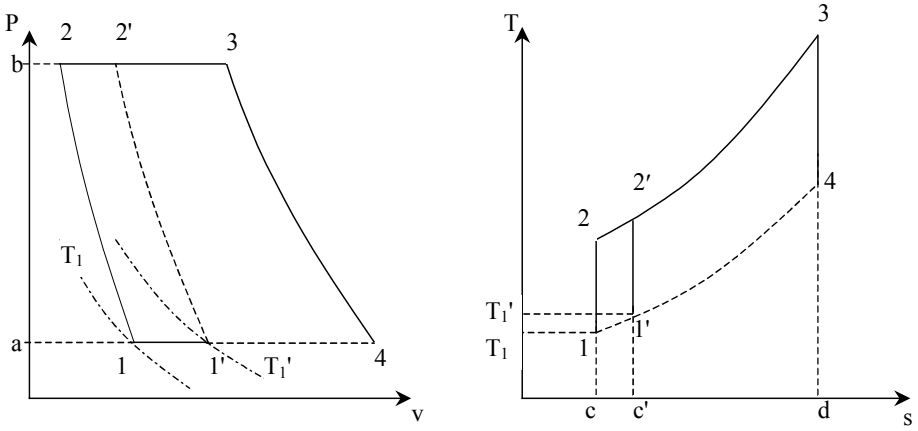

Figure 2.2 Effect of increased ambient temperature on P-v and T-S diagram of a gas turbine

At the ISO condition, the required compressor power is represented by the area 1-a-b-2, whereas, under elevated ambient temperature the required compressor power is represented by area 1'-a-b-2', which is larger than at the ISO condition. The turbine output power remains same in both conditions, so the net specific output power (per unit mass flow rate) decreases.

On the other hand, the rising isobaric curves (1-4 and 2-3) in T-s diagram shows heat addition in the combustion chamber at lower temperatures produces more fraction of useful energy. This can be explained by noticing that more heat will be rejected (area under curve 1-4) at higher T_1 if the same amount of useful energy (e.g. area 1-2-2'-1') is to be harnessed. Therefore, the GT efficiency will be reduced when the compressor inlet temperature T_1 increases.

Above analysis is based on per unit mass flow rate. Elevated ambient temperature further makes the air lighter and reduces air mass flow rate. Since the gas turbine is a constant volume flow rate machine at a fixed rotational speed, a reduced mass flow rate results to a reduction of the total output power. Because the output power is influenced by both compressor power and

mass flow rate, while efficiency is not affected by the mass flow rate, elevated ambient temperature will affect output power more than efficiency.

The effects of fog cooling and overspray are shown in Fig. 2.3. In Fig. 2.3, 1-2 shows the compression under the ISO condition; 1'-2' shows the compression in an elevated ambient temperature condition; 1'-1"-2" shows the moist compression with inlet cooling without overspray; and 1"-2'" shows the wet compression with overspray cooling. 1'-1" shows the effect of compressor inlet temperature drop due to inlet fog cooling to saturation without any overspray. Evaporation in 1'-1" saturates the air and reduces the air temperature to the wet bulb temperature (WBT) at state 1". (Note that the saturated air temperature could be slightly lower than the web bulb temperature due to the heat transfer between the saturated air and remaining water droplets when the water is supplied at a temperature below the wet bulb temperature.) Typically, fog inlet cooling does not reduce the inlet temperature lower than the ISO condition, so 1" is typically on the right of 1 on the P-v diagram. Notice that 1"-2'" is not parallel to 1'-2'. This is because wet compression reduces the polytropic index (k) of the compression work (Pv^k = Constant) from isentropic process (k = γ, specific heat ratio) to a k-value closer to the isothermal process (k = 1). 1"-2'" may or may not cross over the ISO path 1-2. The additional reduction of compressor work due to overspray is evident from the departure of curve 1"-2'" from the curve 1"-2" (moist compression without overspray). Therefore, fog and overspray cooling increases both the net output power and the cycle thermal efficiency. In the mean time, fog/overspray further increases the total mass flow rate, which does not affect the thermal efficiency but increases the power output. Hence, augmentation of the total power output is more pronounced than efficiency. It needs to be pointed out that Fig. 2.3 only represents the air component of the two-phase flow during wet compression. The liquid component is not included.

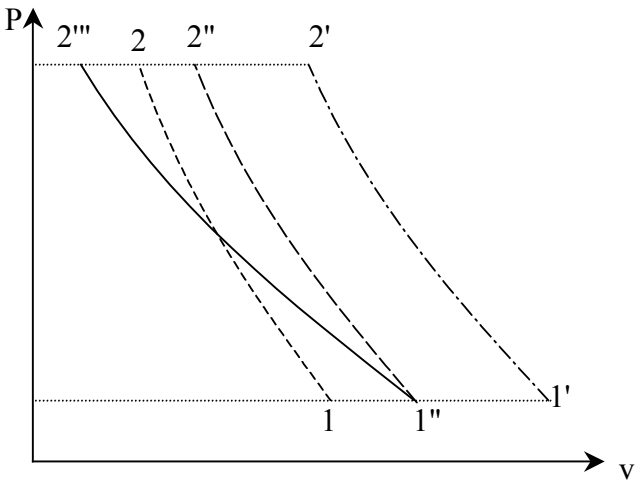

Figure 2.3 Different fog/overspray cooling processes in the compressor (Note: this figure only represents air excluding liquid droplets.)

2.1.2 Development of Wet Compression Formulation for Fog/Overspray Cooling GT System

Refer to Fig. 2.2 again, but with a different representation of curves 1-2 and 1'-2' from earlier description. During derivation of wet compression formulation, isobaric line 1'-1 represents the inlet fog cooling where evaporation of water takes place to saturate the air. Polytropic line 1-2 represents either dry compression (saturated air without overspray) or wet compression (liquid droplets in the air due to overspray). Isentropic line 1'-2' represents compression process of the main compressor without fog/overspray cooling. Assuming the fuel is supplied at the ambient temperature, line 1'-2' also represents the compression of the fuel compressor although at a different mass flow rate.

The development of the wet-compression formulation is similar to Zheng et. al. (2003 a, b), but they did not consider the fuel compressor work nor the fuel mass flow which is also essential especially in case of Low Calorific Value (LCV) fuel applications when the turbine inlet temperature (TIT) and excess air are calculated.

According to the Gibbs equation,

$$Tds = dh - \frac{dP}{\rho} \tag{2.1}$$

For an ideal wet compression, assume the evaporative heat equals to the reversible heat,

$$Tds = -L\,dW \tag{2.2}$$

From equations (2.1) and (2.2), we get,

$$-LdW = dh - \frac{dP}{\rho} \tag{2.3}$$

Here, $dh = c_P dT = \frac{\gamma R}{\gamma - 1} dT$ and γ is the specific ratio.

From the equation of state, $P = \rho RT \Rightarrow \frac{1}{\rho} = \frac{RT}{P}$

Substituting the value of dh and $\frac{1}{\rho}$, equation (2.3) becomes,

$$-LdW = \frac{\gamma R}{\gamma - 1} dT - \frac{RTdP}{P} \tag{2.4}$$

$$\Rightarrow \quad \frac{dP}{P} = \frac{\gamma}{\gamma - 1}\frac{dT}{T} + \frac{L}{R}\frac{dW}{dT}\frac{dT}{T}$$

$$\Rightarrow \quad \frac{dP}{P} = \left(\frac{\gamma}{\gamma - 1} + \frac{L}{R}\frac{dW}{dT}\right)\frac{dT}{T} \tag{2.5}$$

Assuming evaporative rate varies linearly with temperature, i.e. $\frac{dW}{dT}$ = Constant, the isentropic relation is obtained as, $Pv^k = C$ or

$$PT^{-\frac{k}{k-1}} = C \quad \text{[k = polytropic index of ideal wet compression]}$$

$$\Rightarrow \quad \frac{dP}{P} = \frac{k}{k-1}\frac{dT}{T} \tag{2.6}$$

Equations (2.5) and (2.6) give,

$$\frac{k}{k-1}\frac{dT}{T} = \left(\frac{\gamma}{\gamma - 1} + \frac{L}{R}\frac{dW}{dT}\right)\frac{dT}{T}$$

$$\Rightarrow \quad \frac{k}{k-1} = \frac{\gamma}{\gamma - 1} + \frac{L}{R}\frac{dW}{dT} \tag{2.7}$$

Equation (2.7) shows that the increase of evaporation rate decreases the polytropic index (k) of wet compression from isentropic process (k = γ) towards the isothermal process (k = 1), which results to a reduction of compression power. This can be seen in the P-v diagram in Fig. 2.3 as a less steeper curve (1"-2"' vs. 1"-2") requires a less compression power.

The effect of additional moisture on compressor performance due to overspray is analyzed below. At ambient temperature (T_{amb}) and relative humidity (ϕ), the following parameters can be obtained from the psychrometric chart: dew point (T_D), wet bulb temperature (WBT), the humidity ratio ω_0 (moisture content at DBT), and ω_1 (moisture content at WBT). The compressor inlet temperature T_1 is obtained by applying energy balance via enthalpy.

The moist air enthalpy at state 1 (Fig. 2.1), on the basis of mass fraction is,

$$h_1 = \frac{\sum m_{i_1} h_{i_1}}{\sum m_{i_1}} = \frac{m_{a_1} h_{a_1} + m_{f_1} h_{f_1} + m_{g_1} h_{g_1}}{m_{a_1} + m_{f_1} + m_{g_1}} \tag{2.8}$$

where m_a, m_f, and m_g represent the mass of dry air, liquid water, and water vapor, respectively. And, the moist air entropy at state 1, on the basis of mass fraction,

$$s_1 = \frac{\sum m_{i_1} s_{i_1}}{\sum m_{i_1}} = \frac{m_{a_1} s_{a_1} + m_{f_1} s_{f_1} + m_{g_1} s_{g_1}}{m_{a_1} + m_{f_1} + m_{g_1}} \tag{2.9}$$

Under fog/overspray cooling, the compressor inlet temperature is typically fully saturated at WBT. The inlet air will evaporate and absorb the moisture from the sprayed water as much as it needs to saturate itself; the rest of the water will be treated as overspray. In this study the overspray percentage is defined as the ratio of oversprayed water mass over the total air mass flow rate.

To determine state 2, the isentropic temperature of compressor discharge, T_{2S}, needs to be determined first. The moist air entropy at state 2, on the basis of mass fraction is,

$$s_2 = \frac{\sum m_{i_2} s_{i_2}}{\sum m_{i_2}} = \frac{m_{a_2}\left\{ s_{a_2} - R \ln\left(\frac{P_2}{P_1}\right)\right\} + m_{f_2} s_{f_2} + m_{g_2} s_{g_2}}{m_{a_2} + m_{f_2} + m_{g_2}} \tag{2.10}$$

In practice, all the water droplets shall be evaporated at the compressor discharge (i.e. $f_2 = 0$), so the above expression becomes,

$$s_2 = \frac{\sum m_{i_2} s_{i_2}}{\sum m_{i_2}} \Rightarrow s_2 = \frac{m_{a_2}\left[s_{a_2} - 0.287 \ln(r_P)\right] + m_{g_2} s_{g_2}}{m_{a_2} + m_{g_2}} \tag{2.11}$$

T_{2S} can be determined by letting $S_1 = S_2$. All the property values in these two expressions are the function of T_1 (which is already known) and T_{2S} (which is obtained by iteration). At state 2, the isentropic enthalpy of moist air is calculated as,

$$h_{2S} = \frac{\sum m_{i2} h_{i2S}}{\sum m_{i2}} = \frac{m_{a2} h_{a2S} + m_{g2} h_{g2S}}{m_{a2} + m_{g2}} \tag{2.12}$$

The Isentropic Compressor Efficiency is defined as,

$$\eta_c = \frac{h_{2S} - h_1}{h_2 - h_1} \tag{2.13}$$

Equation (2.13) gives the actual moist air enthalpy, which is,

$$h_2 = \frac{\sum m_{i2} h_{i2}}{\sum m_{i2}} = \frac{m_{a2} h_{a2} + m_{g2} h_{g2}}{m_{a2} + m_{g2}} \tag{2.14}$$

Iteration is needed to determine T_2 by satisfying all the property values as functions of T_2 in equation (2.14).

State 3 is known as the turbine inlet temperature (TIT), which is assigned as an operating parameter. The moist air enthalpy at state 3, on the basis of mass fraction is,

$$h_3 = \frac{\sum m_{i3} h_{i3}}{\sum m_{i3}} = \frac{m_{a3}(1+f')h_{a3} + m_{g3} h_{g3}}{m_{a3}(1+f') + m_{g3}} \tag{2.15}$$

The moist air entropy at state 3, on the basis of mass fraction is,

$$s_3 = \frac{\sum m_{i3} s_{i3}}{\sum m_{i3}} = \frac{m_{a3}(1+f')s_{a3} + m_{g3} s_{g3}}{m_{a3}(1+f') + m_{g3}} \tag{2.16}$$

The fuel mass flow rate is included in the gas flow in terms of (1+f '), where f ' is fuel/air ratio. To determine state 4, the isentropic state, T_{4S}, needs to be determined first. The moist air entropy at state 4 on the basis of mass fraction is:

$$s_4 = \frac{\sum m_{i_4} s_{i_4}}{\sum m_{i_4}} = \frac{m_{a_4}(1+f')\left[s_{a_4} - R\ln\left(\frac{P_4}{P_3}\right)\right] + m_{g4} s_{g4}}{m_{a_4}(1+f') + m_{g4}}$$

$$\Rightarrow \qquad s_4 = \frac{m_{a_4}(1+f')\left[s_{a_4} - 0.287\ln(r_P)\right] + m_{g4} s_{g4}}{m_{a_4}(1+f') + m_{g4}} \tag{2.17}$$

S_3 is set to equal S_4 to determine T_{4S}. All the property values in these two expressions are functions of T_3 (which is assigned as an operating parameter) and T_{4S} (which is determined by iterations). At state 4, the isentropic enthalpy of moist air is calculated as,

$$h_{4S} = \frac{\sum m_{i_4} h_{i_{4S}}}{\sum m_{i_4}} = \frac{m_{a_4}(1+f')h_{a_{4S}} + m_{g4} h_{g4S}}{m_{a_4}(1+f') + m_{g4}} \tag{2.18}$$

The Isentropic Turbine efficiency is defined as,

$$\eta_t = \frac{h_3 - h_4}{h_3 - h_{4S}} \tag{2.19}$$

Equation (2.19) gives h_4 at the actual state 4.

The specific compressor work is, $w_c = h_2 - h_1$ (2.20)

The specific turbine work is, $w_t = h_3 - h_4$ (2.21)

For LCV fuel applications, the fuel compressor needs a substantial amount of power to compress the fuel to the combustion chamber. Assuming the fuel behaves as an idea gas, the power required for fuel compressor is calculated as,

$$w_f = \frac{\gamma}{\gamma - 1}\left(\frac{P_2'}{\rho_{2f}'} - \frac{P_1}{\rho_{1f}}\right) \Big/ \eta_{fc} = \frac{\gamma R\left(T_2' - T_1\right)}{\eta_{fc}(\gamma - 1)} \tag{2.22}$$

To ensure the fuel can be injected into the combustion chamber, the fuel compressor is assigned to deliver 25% higher pressure than the compressor discharge pressure in equation (2.22) by letting $P_2' = 1.25P_2$. η_{fc} is the fuel compressor efficiency. The net work is:

$$W_{net} = W_t - W_c - W_f = (m_3 w_t - m_2 w_c - m_f w_f) \quad (2.23)$$

2.1.3 Development of the Computer Program, FogGT

An original computer program, FogGT, has been developed in-house and used for various purposes with an architecture especially designed for calculations related to wet compression. The properties are created digitally including steam tables, psychrometric relations, thermal-fluid properties of various gases (e.g. CO_2, N_2, O_2, water vapor, etc.), and the air property table. The SI units are used in all the property databases. Conversion to English units is automatically executed when the option of using English units is selected.

In the study of wet compression when the compressor is used as a single unit, the program is tailored to receive ambient temperature, relative humidity, ambient pressure, compression ratio, compressor isentropic efficiency, type of fuel, TIT, isentropic efficiency of turbine, mass flow rate of air, and percentage ratio of water flow rate with respect to the air flow rate as input.

For the ease of calculation, the program calculates and prompts the water flow rate required to saturate the air as well as the corresponding WBT once the ambient condition is provided. If the water mass specified is not enough to saturate the air, this is called **underspray**. If the supplied water mass is more than needed for saturating the air, it is called **overspray**. The percentage ratio of the water mass (that is left after saturating the air) to the dry air mass is defined as the overspray percentage, which is automatically calculated by the program. Up to 2% of overspray was considered in this study. Cataldi et. al. (2004) showed that overspray as high as 1-2% could be accepted without major changes to the engine design although specific engine adjustments and protections are needed.

The FogGT program provides a database of high and low heating values (HHV and LHV) for many general fuels. Combination of fuels can also be specified and the appropriate heating values be calculated. The program provides output including compressor power, turbine power, fuel compressor power, heat addition in combustion chamber, net output power, percentage of overspray, fuel flow rate, specific fuel consumption, etc. The iteration process is shown in the flow chart in Fig. 2.4. The detailed descriptions of FogGT program, the associated property database, and the source code are documented in Chapter 3.

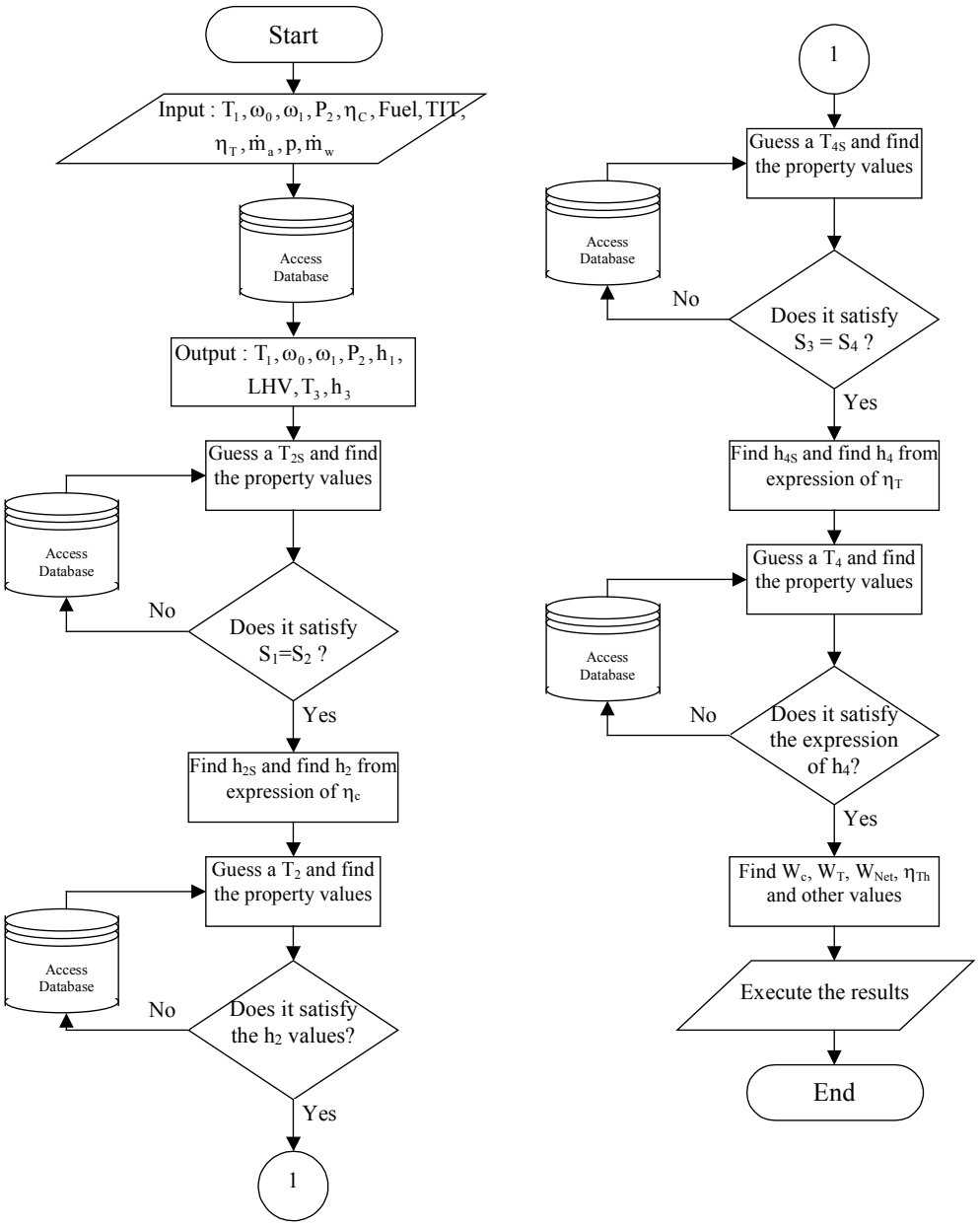

Figure 2.4 The flow chart of the main backbone architecture of the computer code FogGT

2.2 Thermodynamic Model of Compressor Interstage

Consider an axial flow compressor consisting of a number of successing stages. The difference between the single-stage efficiency, $\eta_{c,single}$, and the overall compressor efficiency, η_c increases as compression ratio increases. The increase in temperature due to irreversible friction in one-stage results in more work being required in the next stage. The effect is termed “preheat effect”. This phenomenon has led to the concept of “small-stage efficiency” (or polytropic

efficiency), which is defined as the isentropic efficiency of an elemental (or differential) stage in the process such that it is constant through the whole process.

The small-stage (or polytropic) efficiency for compressors is a well developed concept and has been widely explained in most of the turbomachinery or gas turbine textbooks or handbooks (Wilson and Korakianitis 1988, Cohen, et. al. , 1996, Dixon, 2005, and Boyce 2001). The small-stage efficiency concept can explained by the following example: If three exact stages are stacked up together with the same isentropic efficiency of 90% each, the total isentropic efficiency of this three-stage compressor will achieve less than 90%, say approximately 87%. This similar phenomenon also prevails if a single finite stage is shrunk into an infinitesimal elemental stage (i.e. there are infinite number of elemental stages in each finite stage) and take the limit of the isentropic efficiency with the pressure ratio approaching unity. This can be done mathematically by adding a perturbation term to the pressure ratio, expanding the isentropic efficiency around the pressure ratio with binomial theorem and take the limit of perturbation term towards zero as shown by Wilson and Korakianitis (1988). This will give the small-stage efficiency that will not change during the whole compressing process (Cohen, et. al., 1996). If the small-stage efficiency changes with the process, it is not the real small-stage efficiency. The term "small-stage efficiency" is used in steam turbine, and it is known as "polytropic efficiency" in gas turbines. The polytropic efficiency is the true aerodynamic efficiency exclusive of the pressure-ratio effect. Boyce (2001) stated that the polytropic efficiency of a multistage unit is equal to the stage efficiency if each stage has the same efficiency.

During interstage fogging, an opposite process occurs at each elemental stage due to evaporative cooling of tiny water droplets. Employing the same concept as the "preheat small-stage efficiency," a "precool small stage" approach is adopted in the analysis in this study. The merit of this approach is that the referenced isentropic efficiency of an elemental (or differential) stage can be treated constant throughout the entire process, irrespective of the local temperature and pressure when the blade row design is similar in successive stages. With this assumption, the effect of wet compression on compressor stage efficiency is included in terms of variations of thermal property values, mass flow rate, and blade aerodynamics. The only mechanism that is not included is the "change" of viscous effect. (Note that the original viscous effect has been already included in the dry compression efficiency, $\eta_{c,single}$.)

2.2.1 Preheat and Precool Effect of Small Stage with Modified T-s Diagram for Wet Compression

In Fig 2.5, the T-s diagram shows the elemental stages and their thermodynamic behavior. 1-2s, 2s-3s, 3s-4s show the ideal dry compression in the 1st, 2nd and 3rd stages. 1-2a, 2a-3a, 3a-4a show the actual dry compression in 1st, 2nd and 3rd stages. It is clear in the figure that T_{2a} is higher than T_{2s}, where this higher temperature preheats the second stage. Similarly T_{3a} preheats the third stage and so on. Since the isobaric lines diverge on the T-s diagram, the vertical distance between two isobaric lines increases at higher entropy values; hence, even if each differential stage compresses isentropically, the preheat effect will degrade the overall compressor efficiency.

During an interstage fogging application, for example, if water mist is sprayed in the second stage, evaporation takes place and the temperature at the end of the second stage (or the beginning of the third stage) will be reduced to T_{3w} from T_{3a}. T_{3w} could be lower or higher than $T_{3s'}$, which corresponds to the isentropic process starting at T_{2a}. If T_{3w} is higher than $T_{3s'}$, the preheat effect on stage 3 is reduced; if T_{3w} is lower than $T_{3s'}$, stage 3 is precooled. It should be noted that the evaporation process is irreversible and anisentropic; however, it can be represented as a cooling process of air with a anisentropic polytropic index k (not γ, which is the mixture's specific heat ratio.), which can put the state 3w on the right hand side of state 3a instead of left hand side. This fact will be discussed in the next paragraph in detail with brief explanation.

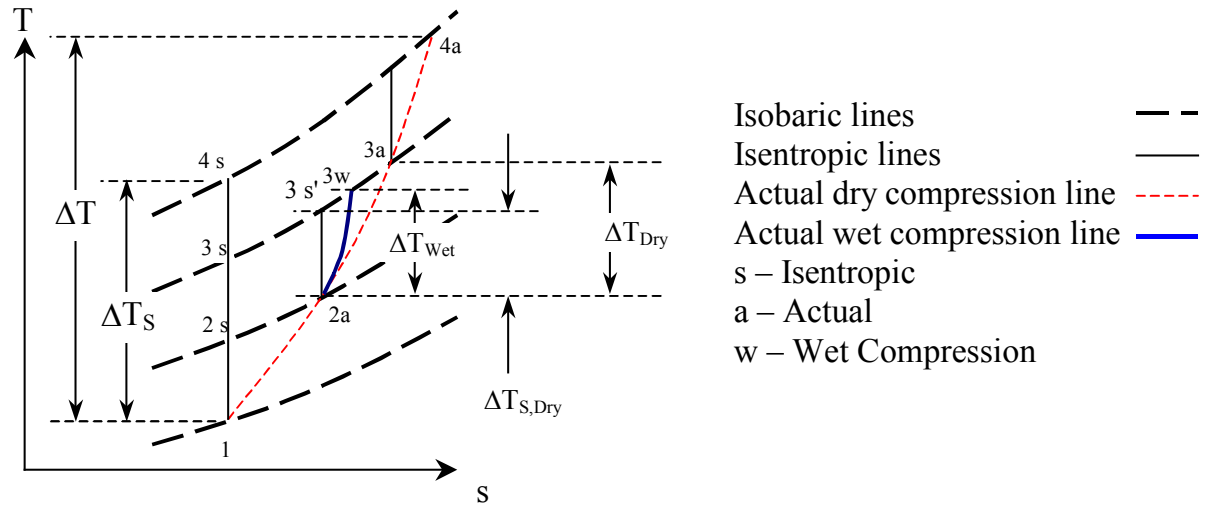

Figure 2.5 Pre-heat and pre-cool effect of air only (liquid water is not included)

It is obvious that evaporation enhances the compression efficiency, but due to irreversibility of evaporation, it produces entropy. It will be more complicated by showing the wet compression process on T-s diagram than on P-v diagram due to the continuous phase and mass fraction changes of air/water mixture. Figure 2.6 shows, the entropies of different species (air, saturated/superheated steam and liquid water) during wet compression. 1-2 shows the dry compression path (moist air only) without any water spray. The air state at 1 is the ambient condition with a relative humidity typically less than 100%. 3-4 shows the T-s curve for only the moist air component of a wet compression process. The air entropy production is less in wet compression than in dry compression, but this picture is different for the mixture of air, water vapor and liquid water. As wet compression progresses, the liquid water entropy increases, as it is shown in 5-6 in the saturated liquid side of the vapor dome (i.e., left curve) of the T-s diagram. When the liquid water evaporates, the entropy production is higher as the entropy in the water vapor side is higher than in the liquid side of the saturation dome (6-7). For example, at 20°C, the entropy of saturated water is 0.2966 kJ/kg.K while it is 8.6672 kJ/kg.K for saturated steam. This fact is revealed as the curve10-11 in Fig. 2.6 for the mixture in wet compression. Entropy increases significantly through 6-7 as long as evaporation takes place. Once all the liquid water evaporates to vapor, the saturated vapor keeps losing entropy as compression progresses as shown by 7-8 on the saturated vapor side (right curve) of the vapor dome. Although the saturated steam loses entropy, the mixture's entropy still increases through 10-11 as entropy production due to evaporation process dominates. When evaporation is completed (at point 11), the major source of entropy production is gone. The afterward minor entropy production due to air compression (1-2) is less than the entropy reduction by saturated vapor compression (7.5-8), so the total mixture entropy decreases before the water vapor begins to be superheated (at point 8). When the superheated water vapor (steam) is compressed, the entropy increases again, so does the air-steam mixture entropy (12-13-14). Figure 2.6 is qualitatively drawn for illustration purpose and is not to scale; the actual wet compression path in Fig. 2.7 & 2.8 is not as distinctive as shown in Fig. 2.6. Fig. 2.7 and 2.8 show the real data for a wet compression with the ambient temperature of 300K, 60% relative humidity, and 2% overspray of water.

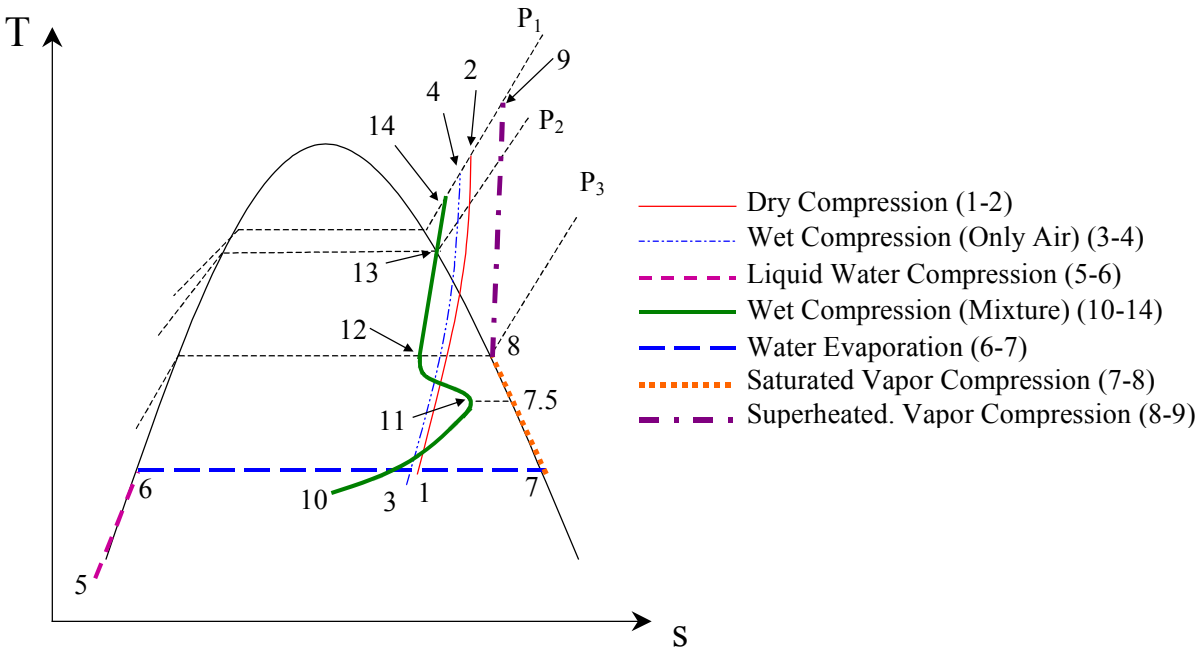

Figure 2.6 Qualitative T-s diagram to illustrate entropy changes of different components during a wet compression (Not to scale)

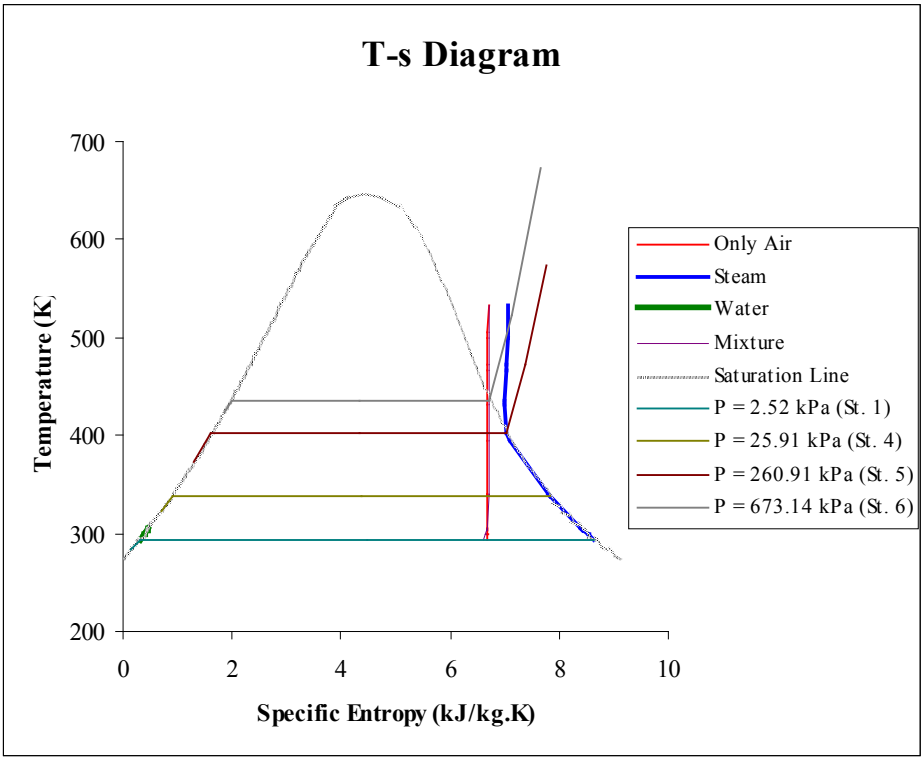

Figure 2.7 T-s Diagram illustrating the entropy changes during wet compression with the actual data

Fig. 2.7 shows the actual wet compression processes of the mixture and its elements drawn with real data on the T-s diagram in an 8-stage compressor used later in Chapter 4. The T-s graphs of air-only compression path and the mixture wet compression path are too close to differentiate from each other in Fig 2.7. An amplified view of these two paths are shown in Fig. 2.8.

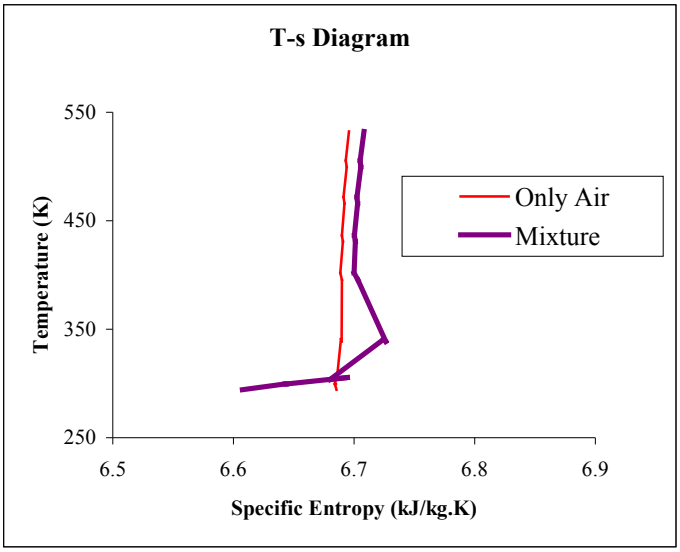

Figure 2.8 Amplified air and mixture T-s paths with actual data

2.2.2 Formulation of Interstage Wet Compression

For an ideal wet compression process from Young (1995),

$$\frac{dP}{P} = \left(\frac{\gamma}{\gamma - 1} + \frac{L}{R} \frac{dm}{dT} \right) \frac{dT_s}{T} \tag{2.24}$$

Integrating Eq. (2.24) between stage 1 and stage 2, we get,

$$\frac{T_{2s}}{T_1} = \left(\frac{P_2}{P_1} \right)^{1 \Big/ \left(\frac{\gamma}{\gamma - 1} + \frac{L}{R} \frac{dm}{dT} \right)} \tag{2.25}$$

Efficiency for the differential stage 1 and 2,

$$\eta_{St} = \frac{\left(m_{a_{1+ds}} h_a \big|_{T_1 + dT_s} - m_{a_1} h_a \big|_{T_1} \right) + \left(m_{f_{1+ds}} h_f \big|_{T_1 + dT_s} - m_{f_1} h_f \big|_{T_1} \right) + \left(m_{g_{1+ds}} h_g \big|_{T_1 + dT_s} - m_{g_1} h_g \big|_{T_1} \right)}{\left(m_{a_{1+d}} h_a \big|_{T_1 + dT} - m_{a_1} h_a \big|_{T_1} \right) + \left(m_{f_{1+d}} h_f \big|_{T_1 + dT} - m_{f_1} h_f \big|_{T_1} \right) + \left(m_{g_{1+d}} h_g \big|_{T_1 + dT} - m_{g_1} h_g \big|_{T_1} \right)} \tag{2.26}$$

where, $m_{f_{1+d}} = m_{f_1} - dm$ and $m_{g_{1+d}} = m_{g_1} + dm$

and, $m_{f_{1+ds}} = m_{f_1} - dm_s$ and $m_{g_{1+ds}} = m_{g_1} + dm_s$

Where, dm = Evaporated amount of water to water vapor

As the amount of dry air remains same, so $m_{a_{1+d}} = m_{a_{1+ds}} = m_{a_1} = m_a$

Putting these values into Eq. (2.26), the differential stage efficiency becomes,

$$\eta_p = \frac{m_a\left(h_a\big|_{T_1+dT_s} - h_a\big|_{T_1}\right) + m_{f_1}\left(h_f\big|_{T_1+dT_s} - h_f\big|_{T_1}\right) + m_{g_1}\left(h_g\big|_{T_1+dT_s} - h_g\big|_{T_1}\right) + L_{T_1+dT_s}dm_s}{m_a\left(h_a\big|_{T_1+dT} - h_a\big|_{T_1}\right) + m_{f_1}\left(h_f\big|_{T_1+dT} - h_f\big|_{T_1}\right) + m_{g_1}\left(h_g\big|_{T_1+dT} - h_g\big|_{T_1}\right) + L_{T_1+dT}dm}$$

$$\Rightarrow \quad \eta_p = \frac{m_a Cp_a + m_{f_1} Cp_f + m_{g_1} Cp_g + L_{T_1+dT_s}\dfrac{dm_s}{dT_s}}{m_a Cp_a + m_{f_1} Cp_f + m_{g_1} Cp_g + L_{T_1+dT}\dfrac{dm}{dT}}\frac{dT_s}{dT} \tag{2.27}$$

Here $\frac{dm}{dT}$ is the evaporation rate, which is assumed the same as the evaporation rate in the isentropic process. This assumption is based on the reasoning that even though the actual evaporated water mass and the temperature change during evaporation are different between the actual and isentropic process, their ratios (dm/dT and dm_s/dT_s). i.e. the evaporation rates, are approximately the same. So,

$$\frac{dm}{dT} = \frac{dm_s}{dT_s} = E$$

The latent heat, L, is a function of temperature. Taking the first-order approximation

$$L_{T_1+dT} = L(T_1 + dT) = L(T_1) + L'(T_1)dT$$
$$L_{T_1+dT_s} = L(T_1 + dT_s) = L(T_1) + L'_s(T_1)dT_s$$

In the numerator and denominator of Eq. (2.27), the first three terms and the zeroth order term of the Taylor's expansion are constant because the inlet condition is fixed, so

$$m_a Cp_a + m_{f_1} Cp_f + m_{g_1} Cp_g + L(T_1) = K$$

Eq. (2.27) becomes,

$$\eta_p = \frac{K + L_s'(T_1)EdT_s}{K + L'(T_1)EdT}\frac{dT_s}{dT}$$

$$\Rightarrow \quad \eta_p = \frac{KdT_s + L_s'(T_1)E(dT_s)^2}{KdT + L'(T_1)E(dT)^2}$$

$$\Rightarrow \quad \eta_p = \frac{KdT_s}{KdT} = \frac{dT_s}{dT} \qquad \text{[Neglecting higher order (e.g. } dT^2\text{) terms]}$$

$$\Rightarrow \quad \frac{T_2}{T_1} = \left(\frac{P_2}{P_1}\right)^{1\Big/\left[\eta_p\left(\frac{\gamma}{\gamma-1}+\frac{L}{R}\frac{dm}{dT}\right)\right]} \qquad (2.28)$$

The stage isentropic efficiency is,

$$\eta_s = \frac{\left(m_{a_{2s}}h_{a_{2s}} - m_{a_1}h_{a_1}\right) + \left(m_{f_{2s}}h_{f_{2s}} - m_{f_1}h_{f_1}\right) + \left(m_{g_{2s}}h_{g_{2s}} - m_{g_1}h_{g_1}\right)}{\left(m_{a_2}h_{a_2} - m_{a_1}h_{a_1}\right) + \left(m_{f_2}h_{f_2} - m_{f_1}h_{f_1}\right) + \left(m_{g_2}h_{g_2} - m_{g_1}h_{g_1}\right)} \qquad (2.29)$$

where, $m_{f_2} = m_{f_1} - m$ and $m_{g_2} = m_{g_1} + m$

and, $m_{f_{2s}} = m_{f_1} - m_s$ and $m_{g_{2s}} = m_{g_1} + m_s$

Where, m = Evaporated amount of water to water vapor

As the amount of dry air remains same, so, $m_{a_{2s}} = m_{a_2} = m_{a_1} = m_a$

$$\eta_s = \frac{\left(m_a Cp_a + m_{f_1} Cp_f + m_{g_1} Cp_g + EL_{2s}\right)(T_{2s} - T_1)}{\left(m_a Cp_a + m_{f_1} Cp_f + m_{g_1} Cp_g + EL_2\right)(T_2 - T_1)}$$

$$\Rightarrow \quad \eta_s = \frac{\left(m_a Cp_a + m_{f_1} Cp_f + m_{g_1} Cp_g + EL_{2s}\right)\left[r_p^{1\Big/\left(\frac{\gamma}{\gamma-1}+\frac{L}{R}\frac{dm}{dT}\right)} - 1\right]}{\left(m_a Cp_a + m_{f_1} Cp_f + m_{g_1} Cp_g + EL_2\right)\left[r_p^{1\Big/\left[\eta_p\left(\frac{\gamma}{\gamma-1}+\frac{L}{R}\frac{dm}{dT}\right)\right]} - 1\right]} \qquad (2.30)$$

Eq. (2.30) shows the overall compressor efficiency as a function of the overall pressure ratio including the stage pre-heat and pre-cooling effects. An equivalent polytropic index of an actual wet compression (k) can be calculated as Zheng et. al. (2003),

$$\frac{\gamma}{\gamma-1}+\frac{L}{R}\frac{dm}{dT}=\frac{k}{k-1} \tag{2.31}$$

This relationship makes Eq. (2.30) as,

$$\eta_s=\frac{\left(m_a Cp_a+m_{f_1} Cp_f+m_{g_1} Cp_g+EL_{2s}\right)\left[r_p^{(k-1)/k}-1\right]}{\left(m_a Cp_a+m_{f_1} Cp_f+m_{g_1} Cp_g+EL_2\right)\left[r_p^{(k-1)/k\eta_p}-1\right]} \tag{2.32}$$

Equation (2.32) is the relationship of the stage isentropic efficiency, η_s, and the small-stage efficiency, η_p, in terms of the equivalent polytropic index (k) for the moist air. A further approximation can be made by assuming $L_2 \approx L_{2s}$, and extend Eq. (2.32) to cover the entire compressor. Eq. (2.32) is approximated as Eq. (2.33), which is a theoretical result showing the relationship between the dry compression compressor efficiency and the wet compressor efficiency, η_c.

$$\eta_c \approx \frac{\left[r_p^{(k-1)/k}-1\right]}{\left[r_p^{(k-1)/k\eta_p}-1\right]} \tag{2.33}$$

It needs to be remembered that derivation of Eq. (2.33) involved several assumptions and could introduce approximately 5% error in compressor efficiency by assuming $L_2 \approx L_{2S}$, Eq. (2.32) is used in the current study, but not Eq. (2.33). It needs to be reminded that the above equation employs the assumption that the polytropic efficiency does not change due to wet compression as shown by White and Meacock (2004). In this study, it will be compared later with the stage-stacking result.

As mentioned earlier that many of the previous papers did not include the blades geometry and aerodynamics calculations; rather they used the generalized compressor

performance curve and guessed shape factors to estimate the airfoil's workload and aerodynamics performance. In contrast, this study employs the stage-stacking approach by developing a stage-by-stage wet-compression analysis using an actual 2D compressor airfoil geometry and stage settings at the mean radii of the airfoils. Similar approaches using meanline airfoil geometry were performed by White and Meacock (2004), Sexton et. al. (1998) and Klepper et. al. (2004).

2.3 Droplet Dynamics

In the thermal equilibrium analysis, the thermodynamic process is not able to determine the following mechanisms:

- whether the droplets get enough time to evaporate or not
- the amount of heat transfer between the droplet and main fluid (air),
- the drag force due to the slip velocity between the droplet and air,
- the outcome of droplet-droplet collision (whether they break up or coalesce with one another), and
- consequence of blade after being hitted by water droplets (whether thethere will be any erosion or not).

In the non-equilibrium analysis, the detailed droplet aerothermal mechanisms and droplet dynamics will need to be modeled and are detailed below.

2.3.1 Droplet Heat Transfer

A number of models for the heat transfer between a droplet and fluid have been developed. The Nusselt number for natural convection is formulated as,

$$Nu = 2 + 0.6 \times Gr^{0.25} \times Pr^{0.33} \tag{2.34}$$

Nusselt number for forced convection is,

$$Nu = 2 + 0.6 \times Re^{0.5} \times Pr^{0.33} \tag{2.35}$$

Where, Grashof number is defined as,

$$Gr = \frac{\rho_a^2 g \beta (T_a - T_d) D^3}{\mu_a^2} \tag{2.36}$$

Where, Air density, $\rho_a = 1.223$ Kg/m^3,

Gravitational acceleration, $g = 9.81$m/s^2,

Thermal Expansion Coefficient (for perfect gas), $\beta = 1/T_a$,

Temperature of Droplet = T_d,

Temperature of air = T_a,

Diameter of Droplet = D = 10μm = 10^{-5} m,

Air Viscosity, $\mu_a = 1.85\times10^{-6}$ Pa-sec

Droplet Reynolds number is defined as,

$$Re_d = \frac{\rho_a D|\text{Slip Velocity}|}{\mu_a} \tag{2.37}$$

Prandtl number for the air is, Pr = 0.7

An exemplary calculation for the droplet heat transfer is performed for a droplet with a slip velocity of 100 m/s.

T_a = 300K, T_d = 294.17K

Air velocity, u = 150m/s, Droplet velocity, v = 50m/s

So, the slip velocity = |u-v| = 100m/s

The droplet Reynolds number is,

$$Re_d = \frac{1.223\times10^{-5}\times100}{1.85\times10^{-5}} = 66$$

The Nusselt number is

$$Nu = 2 + 0.6\times66^{0.5}\times0.7^{0.33} = 6.33$$

For natural convection when slip velocity is zero, i.e. u = v, the Grashof number is

$$Gr = \frac{1.223^2\times9.81\times\frac{1}{300}\times(300-294.17)\left(10^{-5}\right)^3}{\left(1.85\times10^{-5}\right)^2} = 8.33\times10^{-7}$$

The Nusselt number becomes,

$$Nu = 2 + 0.6\times\left(8.33\times10^{-7}\right)^{0.25}\times0.7^{0.33} = 2.02 \approx 2$$

Table 2.1 shows the droplet heat transfer for slip velocity ranging from 100 m/s to zero. The third column in Table 2.1 shows the value of Re/Gr, which provides a reference value to evaluate the relative strength of forced convection versus natural convection. As can be seen, when the value of Re/Gr decreases, the relative strength of forced convection declines.

Table 2.1 Natural and forced convection

Natural and Forced Convection			
Velocity (m/s)	Rel. Vel. (m/s)	Re / Gr	Nu
50	100	66.11	6.337
75	75	49.58	5.756
100	50	33.05	5.067
125	25	16.53	4.168
150	0	8.33×10^{-7}	2.016

The values of density and viscosity are variable and are calculated according to the local temperature and pressure. The property of viscosity is calculated by using the empirical equations in the Chemistry Handbook in Eq. (2.38).

$$\mu_a = (0.00483T_a + 0.3976)\times10^{-5} \tag{2.38}$$

2.3.2 Droplet Evaporation

Several models have been proposed for calculating droplet evaporation time in the open literature. Zheng et. al. (2003 b) modeled the droplet evaporation time as

$$t = \frac{R\rho_d D^2}{8D_v\left(\frac{P_d}{T_d} - \frac{P_a}{T_a}\right)M} \tag{2.39}$$

White and Meacock (2004) proposed the following droplet evaporation time as,

$$t = \frac{D^2}{8\rho_a D_v \ln\left(\frac{1+\omega_1}{1+\omega_0}\right)} \tag{2.40}$$

where, Droplet density, $\rho_d = 1000 kg/m^3$

Diffusion Coefficient, $D_v = 2.48\times10^{-5} m^2/s$

Droplet Pressure (Saturation Pressure), $P_d = P_{sat}$ (kPa)

Air Pressure, $P_a = 101.35$ kPa,

Molecular Weight of droplet, M = 18 kg/kmole

Specific humidity or air at dry bulb temperature, ω_0 (kg/kg dry air)

Specific humidity or air at wet bulb temperature, ω_1 (kg/kg dry air)

Thermal Conductivity, K_a = 0.024 W/mK

The distance a droplet can travel before it completely evaporates can be calculated by multiplying the droplet evaporation time by the air velocity. Comparison of the above two models on the droplet evaporation time and travel distance is shown in Table 2.2. Zheng's model results in more than 3-4 times longer droplet evaporation time and travel distance and this model is used in this study for Non-equilibrium Stage-Stacking method, because prediction from this model is closer to the result obtained in CFD. (Which one is used in your study?) With a chord length of 5 cm, the 10 μm droplets completely evaporate under White and Mecock's model, but move into the next stage under Zheng et. al's model.

Table 2.2 Droplet evaporation

Droplet Evaporation												
Stage	P_a	T_a	P_{sat}	T_d	ρ	ω_0	ω_1	h_{fg}	Zheng Model		White Model	
	(kPa)	(K)	(kPa)	(K)	(kg/m³)			(kJ/kg)	t (ms)	d (cm)	t (ms)	d (cm)
1.5	108.9	300.4	3.68	294.2	1.262	0.016	0.022	2451.4	0.665	9.98	0.16	2.34
2	109.0	300.5	3.68	300.4	1.264	0.022	0.029	2451.4	0.664	9.96	0.13	2.02
2.5	115.9	306.5	5.16	300.5	1.318	0.029	0.029	2451.4	0.645	9.67	0.00	0.00

2.3.3 Droplet Response Time

The response times of a droplet to changes in flow velocity or temperature are important in establishing nondimensional parameters to characterize the flow. The momentum response time relates to the time required for a droplet to respond to a change in velocity. The equation of motion for a spherical droplet in a gas given by Tsuji and Crowe (1997) is

$$m\frac{dv}{dt} = \frac{1}{2}C_D\frac{\pi D^2}{4}\rho_g(u-v)|u-v| \tag{2.41}$$

[g→gas, d→droplet]

where, u = gas velocity and v = droplet velocity.

From equation (2.41), we get,

$$\frac{\pi}{6}D^3\rho_d\frac{dv}{dt}=\frac{1}{2}C_D\frac{\pi D^2}{4}\rho_g(u-v)|u-v|$$

$$\Rightarrow \quad \frac{dv}{dt}=\frac{18}{24}\frac{\mu_g C_D}{\rho_d D^2}(u-v)\left[\frac{\rho_g D|u-v|}{\mu_g}\right]$$

$$\Rightarrow \quad \frac{dv}{dt}=\frac{C_D\,Re_d}{24}\frac{18\mu_g}{\rho_d D^2}(u-v) \qquad (2.42)$$

The term, $\frac{C_D\,Re_d}{24}$, is related to the drag. The following three correlations are considered and compared:

(a) According to Stokes law, (i.e. for low Reynolds number with Re < 1) $\frac{C_D\,Re_r}{24}=1$

(b) Schiller and Naumann (1933) correlated the expression up to Re = 800, which is,

$$\frac{C_D\,Re_d}{24}=1+0.15\,Re_d^{0.687}$$

(c) Clift and Cauvin (1970) extended the Schiller and Naumann equation to cover the entire subcritical Reynols number range as,

$$\frac{C_D\,Re_d}{24}=1+0.15\,Re_d^{0.687}+0.0175\,Re_d\left(1+4.25\times10^4\,Re_d^{-1.16}\right)^{-1}$$

All the models are compared in Fig. 2.9 with the actual C_d curve.

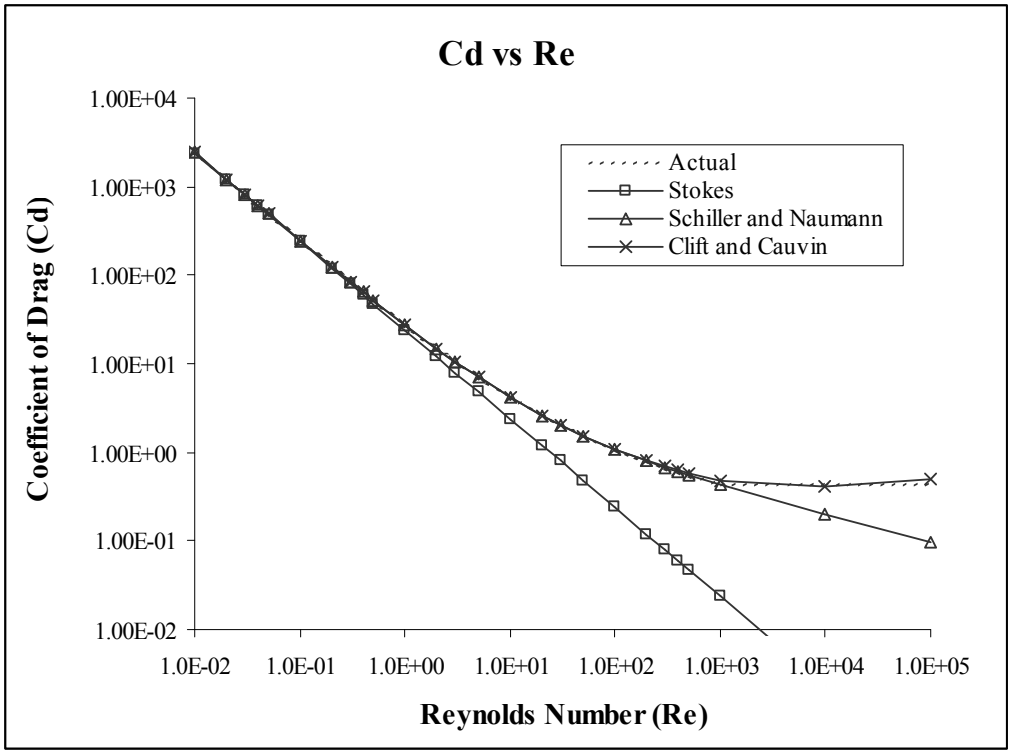

Figure 2.9 Comparison of three drag coefficient correlations

Clift and Cauvin's correlation provides the most accurate result. However, Schiller Naumann's (1933) correlation is adopted in this study because $Re_d < 1000$ in all studied cases.

By incorporating the Schiller Naumann's drag correlation, Eq. (2.42) becomes

$$\frac{dv}{dt} = \frac{18\mu_g}{\rho_d D^2}(u - v)\left[1 + 0.15\,Re_d^{0.687}\right]$$

$$\Rightarrow \qquad (u - v)\frac{dt}{dv} = \frac{\rho_d D^2}{18\mu_g\left[1 + 0.15\,Re_d^{0.687}\right]} \tag{2.43}$$

LHS of the equation (2.42) has the dimension of time, which is the **aerodynamic response time**,

$$\tau_v = \frac{\rho_d D^2}{18\mu_g\left[1 + 0.15\,Re_d^{0.687}\right]} \tag{2.44}$$

By assuming the temperature is uniform throughout the droplet, the equation for calculating the droplet temperature due to heat transfer between the droplet and the surrounding air without including the radiative effect is

$$mC_P \frac{dT_d}{dt} = Nu\pi K_g D\left(T_g - T_d\right) \tag{2.45}$$

$$\Rightarrow \quad \frac{\pi}{6} D^3 \rho_d C_P \frac{dT_d}{dt} = Nu\pi K_g D\left(T_g - T_d\right)$$

$$\Rightarrow \quad \frac{dT_d}{dt} = \frac{6NuK_g}{\rho_d C_P D^2}\left(T_g - T_d\right)$$

$$\Rightarrow \quad \left(T_g - T_d\right)\frac{dt}{dT_d} = \frac{\rho_d C_P D^2}{6NuK_g} \tag{2.46}$$

LHS of the equation (2.46) has the dimension of time, which is the **thermal response time**,

$$\tau_t = \frac{\rho_d C_P D^2}{6NuK_g} \tag{2.47}$$

A sample calculation for a 10μm water droplet is shown below.

$\rho_d = 1000 Kg/m^3$, $C_P = 4200$ J/kg.K

For Air,

$\rho_g = 1.2$ Kg/m³, $\mu_g = 1.85 \times 10^{-5}$ Pa.s, $K_g = 0.024$ W/m.K, $Re_d = 64$

The aerodynamic response time with Schiller & Naumann model is calculated as,

$$\tau_v = \frac{1000 \times \left(10 \times 10^{-6}\right)^2}{18 \times 1.85 \times 10^{-5}\left[1 + 0.15 \times 64^{0.687}\right]} = 8.31 \times 10^{-5} s = 0.0831 ms$$

The travel distance before the droplet catch up the air (or vice versa) is approximately 1.25 cm (= 150 × 0.0000831 = 0.0125 m), which in about one fourth of the rotor chord length.

The thermal response time for natural convection (with Nu = 2) is,

$$\tau_t = \frac{1000 \times 4200 \times \left(10 \times 10^{-6}\right)^2}{12 \times 0.024} = 0.00145 s = 1.45 ms$$

For forced convection, (e.g. Nu = 9), the thermal response time is

$$\tau_t = \frac{1000 \times 4200 \times \left(10 \times 10^{-6}\right)^2}{6 \times 9 \times 0.024} = 0.00032 s = 0.32 ms$$

Both the thermal response times are longer than the aerodynamic time. This means the droplet slip velocity quickly reaches zero and the natural convection dominates. This also implies that the droplet will take a bit longer to reach the local air temperature. In this example, the droplet will fly a distance of 21 cm (150 × 0.00145 = 0.21 m) which in more than two complete stages to achieve the air temperature. Quite often, the local air temperature is higher than the saturation temperature; so the droplet seems already evaporate before it even reaches the local air temperature. Therefore, it seems sufficient by instituting the evaporation model in the wet compression without including the calculating the thermal and aerodynamic response times.

2.4 Numerical Algorithm for Stage-Stacking Wet Compression Calculation

The numerical algorithm for stage-stacking method is developed with both equilibrium and non-equilibrium thermodynamic models. The numerical process begins with the input of the blade geometry, ambient condition, and fogging conditions.

2.4.1 Numerical Algorithm for Stage Performance

First, the geometries of the airfoils (stator and rotor) and the stagger angle are selected. The compressor passage geometry is designed on the basis of ISO Condition (288K and 60% relative humidity).

In the design condition, the rotor absolute inlet flow at each stage is assigned with zero tangential velocity. The blade inlet angle is set equal to the air inlet angle. The detailed procedure and formulation for stage-to-stage wet compression is documented in the next chapter. Figure 2.10 shows the rotor-stator orientation. A brief summary of the procedure is provided here:

In summary, the inlet condition at the first stage rotor is given as the static condition. The total (or stagnation) status is obtained by guessing a total temperature and iterating until the total enthalpy obtained by two different methods converge. The air-water mixture mass flow rate at the first rotor inlet is calculated by assuming the compressor functions with the constant-volume-flow characteristics at the inlet with a fixed rotation speed (i.e. constant RPM). At the rotor exit, the flow is assumed to be turned at the exact angle as the blade camber angle. The status at the rotor exit is determined by matching the exit mass flow rate with the mass flow at the inlet plus the interstage mist injection if any. Two unknowns, density and absolute axial flow velocity, need to be determined during this mass flow rate matching process; therefore, two iterating loops

are required. The first iteration starts by guessing the absolute axial exit velocity and drawing the velocity diagram. Iterations are conducted to ensure specific stage work obtained from the velocity diagram matches the total enthalpy increase obtained from the polytropic relationship. Using the stagnation status obtained by the first iteration loop, the second iteration calculates the air-water mixture density and goes back to the first loop until the mass conservation is satisfied.

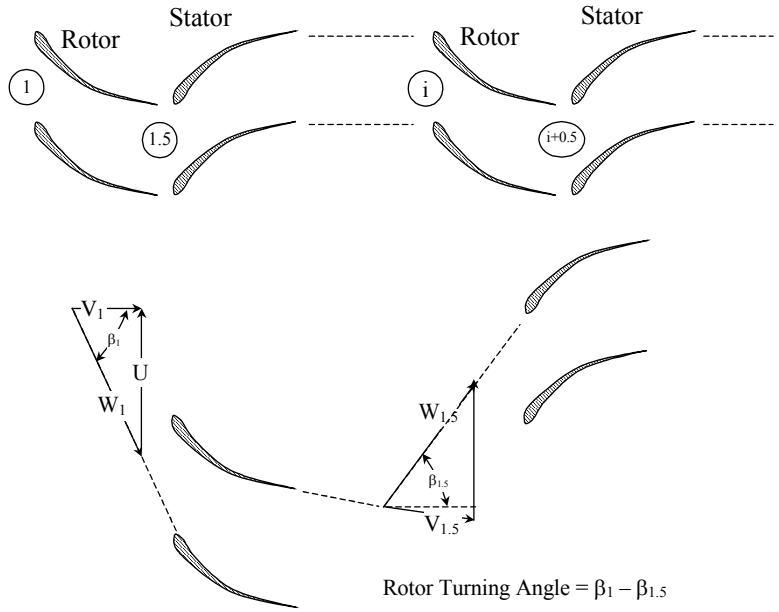

Figure 2.10 Rotor-Stator Staging

The procedure for determining the second or later rotor inlet condition is different from determining the first rotor inlet status. Instead, the total status at the later stage rotor inlet is known, and the static status needs to be determined. The procedure for determining the rotor exit condition is the same for all stages.

The effect of inlet or interstage fogging will change the flow coefficient and the flow inlet angle, which in turn will affect the pressure ratio and specific work of each stage. The detail numerical procedure is shown in Chapter 3.

CHAPTER THREE

DEVELOPMENT OF WET COMPRESSION PROGRAM

The computer program FogGT has been used in this study for many purposes and has been developed in MSACCESS using VBA (Visual Basic Access) for backend code. This program is able to find properties of different gases (e.g. air, oxygen, nitrogen, carbon-dioxide etc.), to perform psychrometric calculation, to find steam property, to analyze gas turbine system with or without mist spray thermodynamically, to simulate compressor with or without mist spray using both equilibrium and non-equilibrium evaporation models with stage-stacking method. This chapter shows the theory behind all the calculations along with the Graphical User Interface (GUI). The program starts with a main switchboard (Fig. 3.1), which navigates to all available windows for calculation. All the buttons in the switchboard are self-explanatory from their names.

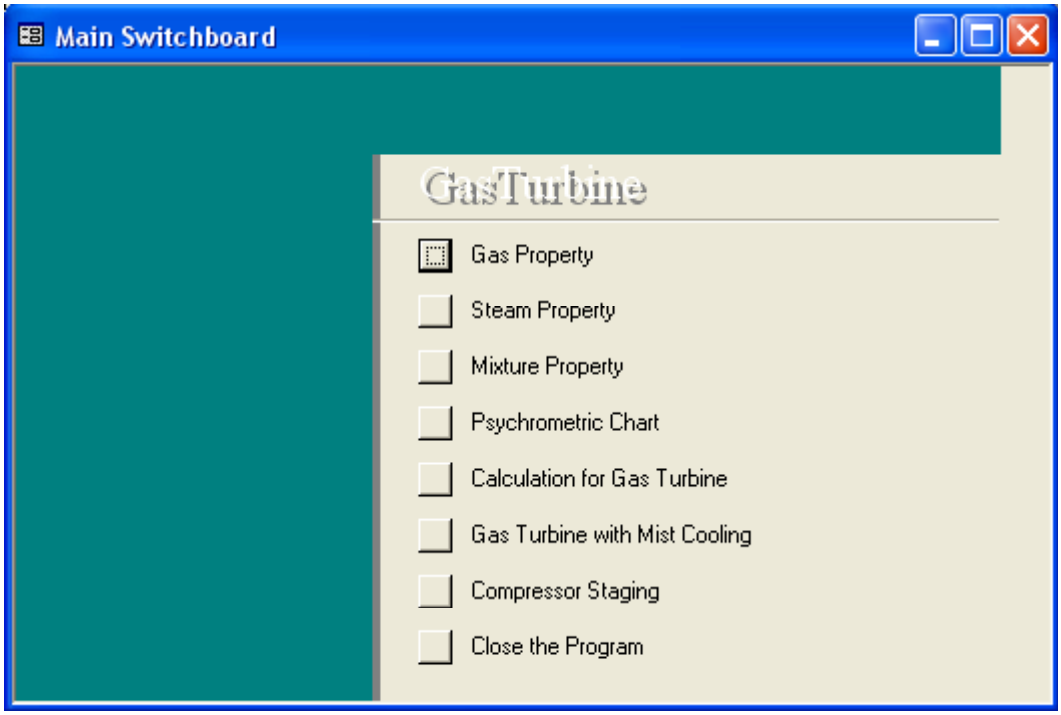

Figure 3.1 Main Switchboard

3.1 Property Calculations

Different properties are calculated from this program as mentioned earlier.

3.1.1 Gas Property Calculation

This program provides databases for general gas properties including specific heat, enthalpy, entropy, and reduced pressure in different temperatures for Air, CO, CO_2, H_2, H_2O, N_2, and O_2. Both ideal gases and real gases are considered.

When a temperature is given to calculate the properties of a gas, the program searches that temperature in the table. If that temperature is found, the program takes the corresponding property values and displays in the interface (Fig. 3.3). If that temperature is not found, it may have two possibilities: either that temperature is out of range or that temperature lies between two temperatures in the table, which will need interpolation to find the properties for a given temperature. If the data is out of range, the program shows an error message as "Data is out of range." When the data needs interpolation, first the program finds the two closest temperatures for the given temperature. The solid rectangle shows the two temperatures for interpolation in Fig. 3.2. Then it interpolates the property values between these two temperatures and generates the property values as output shown in Fig. 3.3.

Temperature	Specific Heat	Enthalpy	Entropy	Reduced Press
300	37.121	-393427.1	213.898	0.1489
350	39.37	-391511.6	219.799	0.3027
400	41.309	-389493.7	225.185	0.5786
450	43.053	-387384	230.153	1.0517
500	44.624	-385191.3	234.772	1.833
550	46.044	-382924	239.093	3.082
600	47.329	-380589.2	243.155	5.024
650	48.497	-378193.1	246.99	7.969
700	49.561	-375741.2	250.624	12.336
750	50.534	-373238.5	254.077	18.688
800	51.425	-370689.2	257.367	27.76

Figure 3.2 A set of temperatures

The interface for the "Gas property calculation" is found by clicking the first tab in main switchboard (Fig. 3.1).

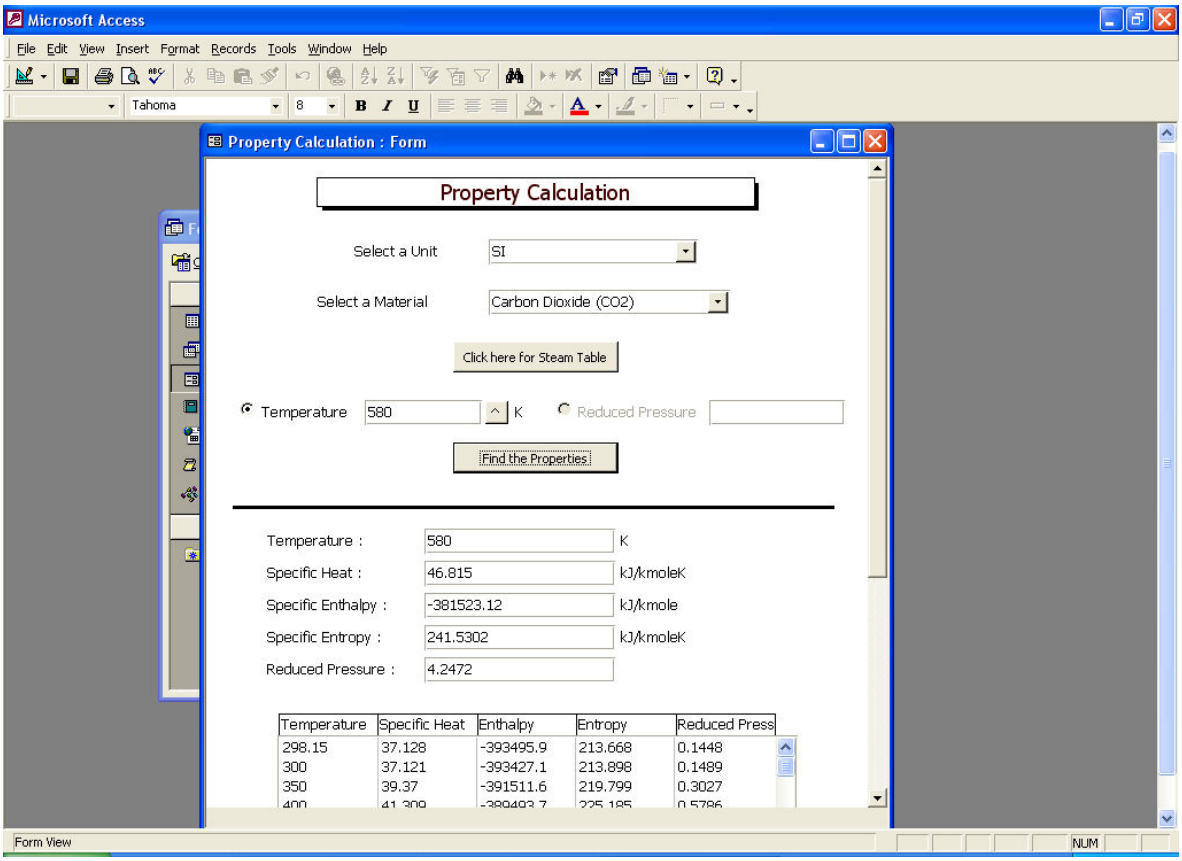

Figure 3.3 Gas property calculation interface

The first drop-down list provides an option to choose the unit (SI or English). The second list gives the option to choose the gas. Then the program requires the input of an absolute temperature or a reduced pressure to find the gas properties. It should be noticed from Fig. 3.3 that the temperature must be given in the absolute scale (K or ^{o}R).

3.1.2 Steam Property Calculation

For steam property calculation, three water phases are considered: compressed water, wet steam, and superheated steam. Fig. 3.4 is a T-s phase diagram showing five water states: compressed water (A), saturated water (B), wet steam (C), saturated steam (D), and superheated steam (E).

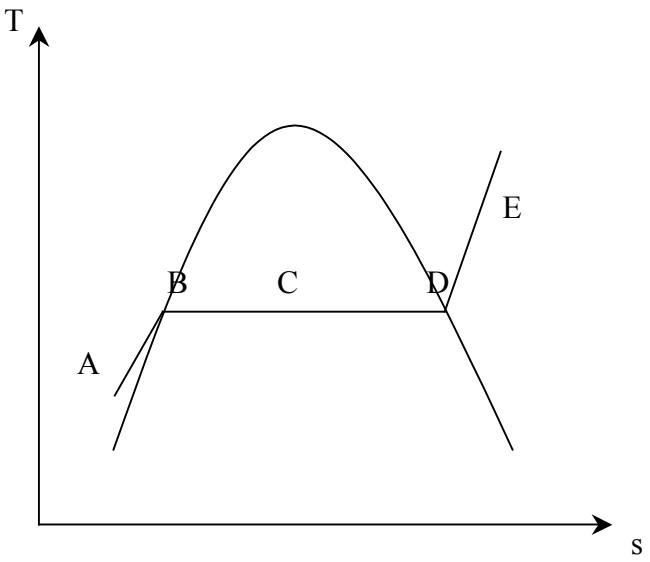

Figure 3.4 T-s diagram of steam

First, the program finds the state of the water. When a temperature and pressure are given, the program finds the saturation pressure for that temperature. If the given pressure is higher than the saturation pressure then the water is compressed water. If the given pressure is exactly equal to the saturation pressure then it is a wet steam, a mixture of liquid and water vapor with a quality less than 1. If the given pressure is lower than the saturation pressure, it is a superheated steam. Once the state is defined, the program finds the corresponding table out of the compressed water table, the saturated steam table or the superheated steam table. From the appropriate table, the program obtains the properties including specific volume, specific internal energy, specific enthalpy, and specific entropy with the given temperature and pressure. If that temperature is found in the table it extracts the values directly, otherwise linear interpolation is performed to obtain the property value. In case of wet steam the program will need to know the quality of steam to calculate the property values. If any one of the property values is known, the program will be able to calculate the quality and other property values.

Steam table interface (Fig. 3.5) has the options for SI or English unit. The temperatures are input as °C or °F. The first drop-down box is for the unit option. The second box is for temperature, and the third one is for pressure. If the pressure is the saturation pressure for that

temperature or vice versa, then the next box (quality of steam) is enabled automatically requesting input of steam quality (in percentage). For users' convenience, the saturation pressure or temperature corresponding to the input temperature or pressure can be found by simply clicking the radio button adjacent to the temperature and pressure box, respectively. When either the Saturation Pressure or the Saturation Temperature button is selected, the steam quality box is enabled. In the same way, saturation temperature is also obtained from a given pressure by clicking the “Saturation Temperature” radio button. By default, the steam quality is 0% (i.e. saturated water). For users' convenience, an "^" (upper arrow key) is placed adjacent to the temperature input box to increase the temperature by 1°C or 1°F.

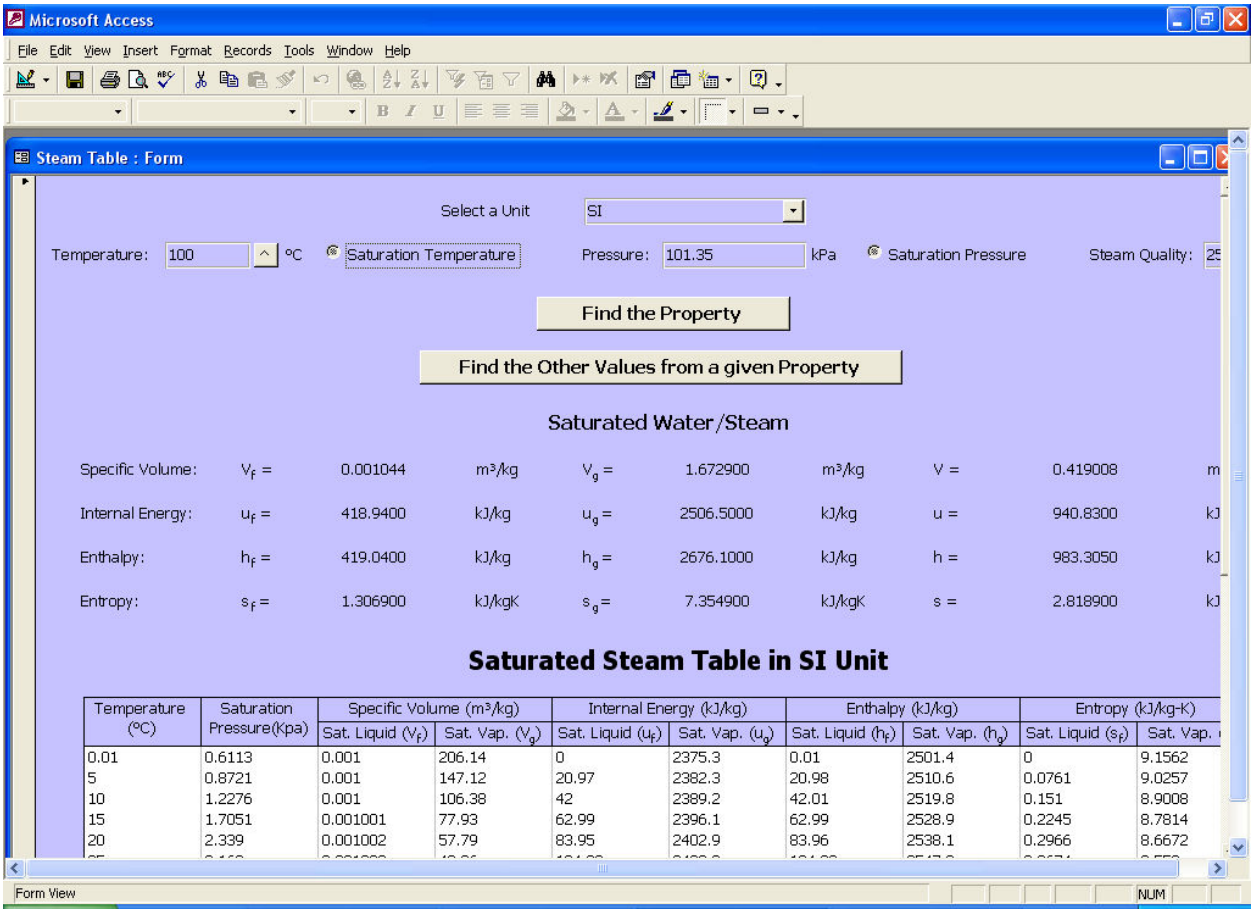

Figure 3.5 Steam table interface

Once the temperature, pressure and/or steam quality are provided and "Find the Property" button clicked, the program immediately determines the appropriate type of the state (compressed water, saturated water, wet steam, saturated steam, or superheated steam.)

If it is compressed water, the program searches that temperature and pressure in compressed water table. If the exact temperature and pressure are not found, the program finds the closest larger and smaller temperatures and pressures and then performs double interpolations (extrapolation is needed if the temperature or pressure is either larger than the largest value or smaller than the smallest value in the table) to find the properties (e.g. specific volume, specific internal energy, specific enthalpy and specific entropy). The program does the same calculation for superheated steam from superheated steam table. If the steam is saturated, the program uses saturation table to find properties for saturated water and saturated steam. If the quality is given, the program finds the properties of the wet steam of that quality by interpolation. The type of the steam will be displaced on screen.

This program is also designed to receive input other than temperature and pressure as long as at least two parameters are provided. In this situation, another interface (Fig 3.6a) needs to be selected by clicking the button "Find the Values from two given Parameters." For example, if specific volume and pressure are known and user needs to find the other property values, the program will use the value of the first parameter (specific volume) value to find all the possible states for that parameter including all three possible types (compressed, saturated or superheated). Then with the given second parameter the state can be obtained.

The output is shown as Fig. 3.6a. If it is wet steam, the steam quality is also shown. The program also presents all the possible states when the first parameter is provided. At the bottom of this interface (Fig. 3.6b) there are three buttons for three types of steam. If the given first parameter corresponds to any value in the compressed water table, then “Compressed Table” button is enabled and so on. By clicking these buttons, it is possible to see all the possible states of steam with the given value of the first parameters in a report form.

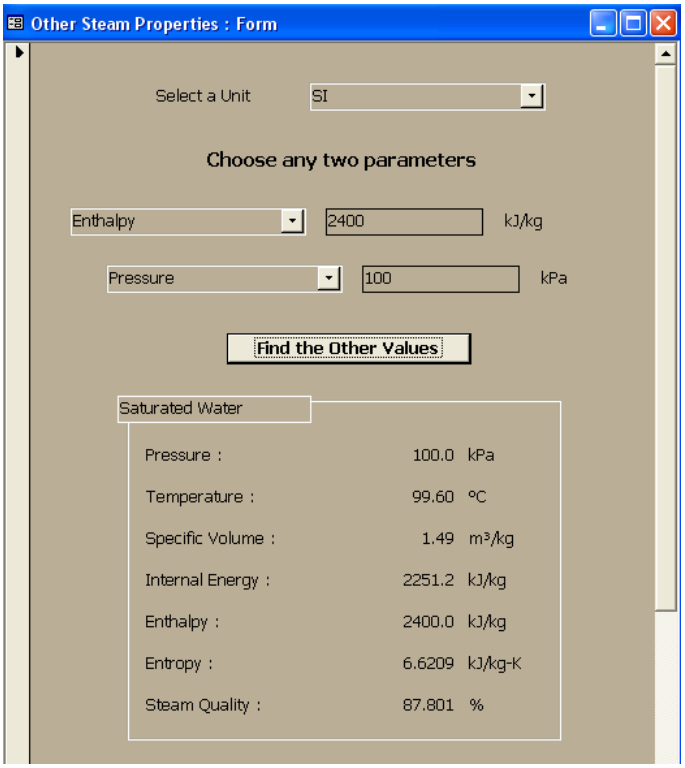

Figure 3.6(a) Properties from two parameters

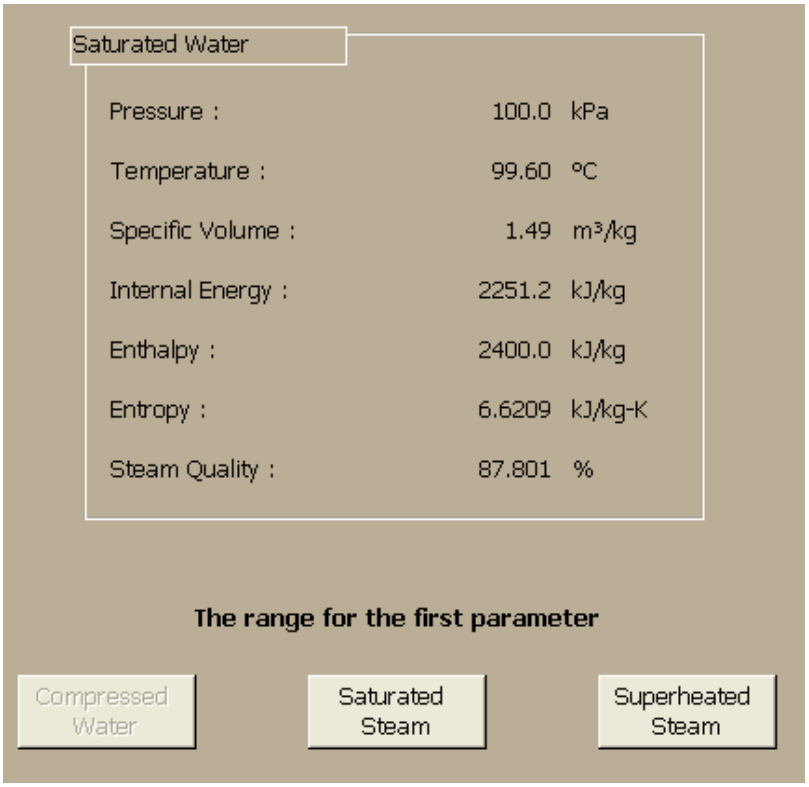

Figure 3.6(b) Output from two different properties

3.1.3 Mixture Property Calculation

Properties of multi-phase flow are often necessary in wet compression simulation. This is calculated by weight-average method. This program is able to do it in wet compression itself, but hand calculations are advised to spot-validate some selected results. Properties of mixture are found from "Mixture Property" form, which is activated from the third button on the switchboard. It also has an option for both the units.

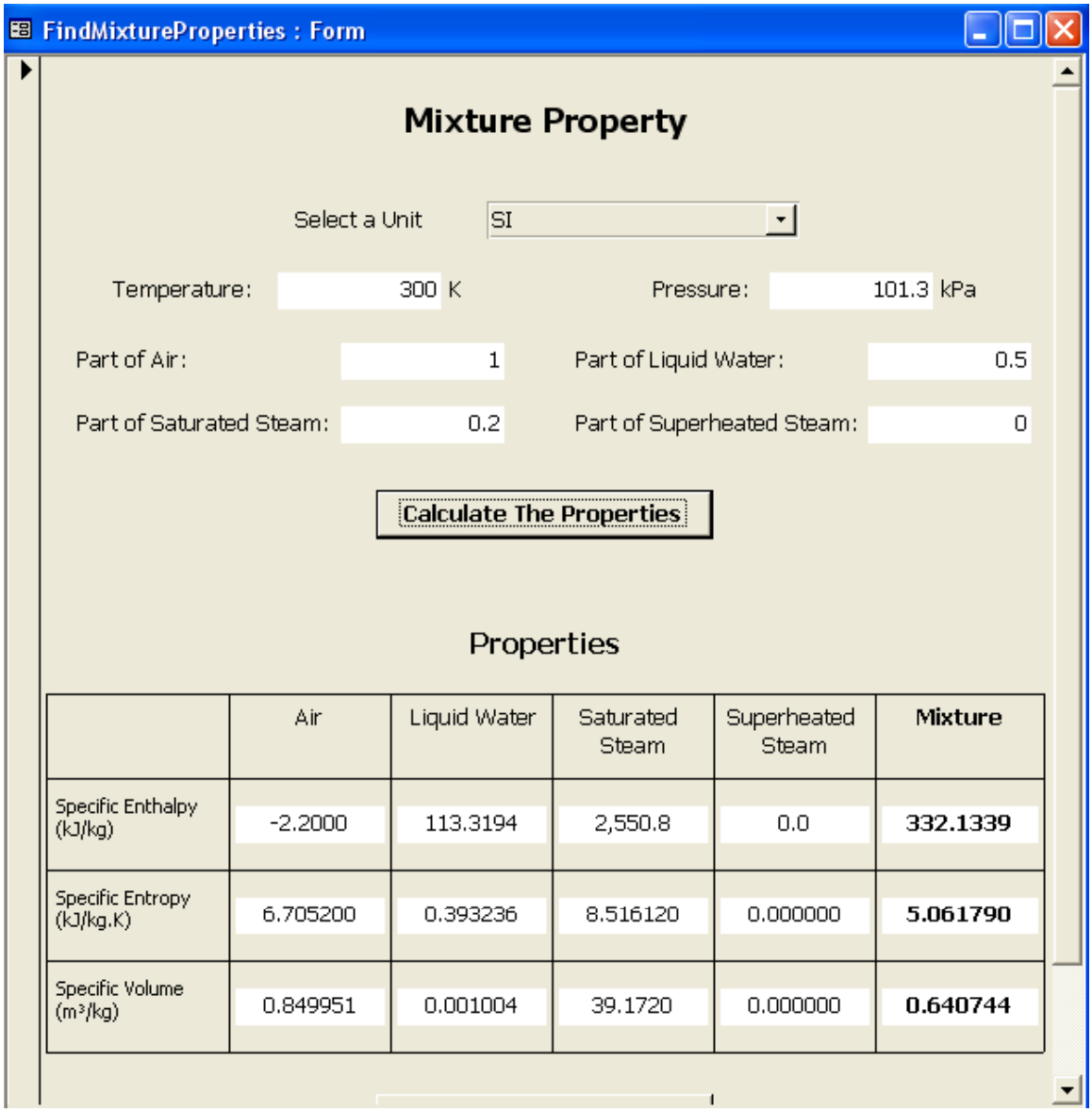

Figure 3.7 Mixture property interface

The interface needs the pressure and temperature first, then it needs the fraction of all the phases on the basis of mass. Figure 3.7 shows one example and all the masses are normalized by air mass (including moisture) and this is the way that is used in wet compression. Specific enthalpy, specific entropy and specific volume of different mixtures are calculated from this interface by Eqs. 3.1, 3.2 and 3.3.

$$h = h(T,P) = \frac{h_a + fh_f + gh_g + Sh_s}{1 + f + g + S} \tag{3.1}$$

$$s = s(T,P) = \frac{s_a + fs_f + gs_g + Ss_s}{1 + f + g + S} \tag{3.2}$$

$$\rho = \rho(T,P) = \frac{1 + f + g + S}{\frac{1+g}{\rho_m} + fv_l + Sv_s} \tag{3.3}$$

Subscripts:

a	Dry air
g	Water vapor
f	Liquid water
s	Superheated
m	mixture of air and moisture

Where, f = mass fraction of liquid water for P and T.

g = mass fraction of water vapor for P and T.

S = mass fraction of superheated steam for P and T.

h_a = air specific enthalpy at P and T. (From Property Table)

h_f = liquid water specific enthalpy at P and T. (From Steam Table)

h_g = water vapor specific enthalpy at P and T. (From Steam Table)

h_s = superheated steam specific enthalpy at P and T. (From Superheated Steam Table)

s_a = air specific entropy at P and T. (From Property Table)

s_f = liquid water specific entropy at P and T. (From Steam Table)

s_g = water vapor specific entropy at P and T. (From Steam Table)

s_s = superheated steam specific entropy at P and T. (From Superheated Steam Table)

v_l = liquid water specific volume at P and T. (From Steam Table)

v_s = superheated steam specific volume at P & T. (From Steam Table)

ρ_m = Mixture density of Air and Water Vapor = $P_1/(R_m T_1)$

R_m = Gas constant for air and water vapor mixture = R_0/M_m.

R_0 = Universal gas constant = 8.314 kJ/kmole.K

M_m = Molecular weight of air and water vapor mixture = (28.965+18g)/(1+g)

Dry bulb temperature ≡ T_{DBT}

Wet Bulb Temperature ≡ T_{WBT},

Specific humidity at DBT ≡ ω_0

Specific humidity at WBT ≡ ω_1

Dew point ≡ T_{DP}

Relative humidity ≡ $\phi = P_g/P_{DBT}$

Enthalpy ≡ h

Specific volume ≡ v

Ambient pressure ≡ P_{amb}

Specific heat of dry air ≡ Cp

Water vapor saturation pressure at DBT ≡ P_{DBT}

Water vapor saturation pressure at WBT ≡ P_{WBT}

Partial pressure of air at DBT ≡ P_a

Partial pressure of water vapor at DBT ≡ P_g

Enthalpy of saturated steam at DBT ≡ $h_{g,DBT}$

Enthalpy of saturated steam at WBT ≡ $h_{g,WBT}$

Enthalpy of saturated water at DBT ≡ $h_{f,DBT}$

Enthalpy of saturated water at WBT ≡ $h_{f,WBT}$

Gas constant ≡ R

3.1.4 Psychrometric Calculation

Psychrometry is the study of atmospheric air and its associated moisture content. Air comprises a mixture of gases of which nitrogen makes up 78%, oxygen 21% (on a molar basis) and carbon dioxide and the inert gases (such as argon, neon, krypton, helium etc.) the remainder. These are known as the dry gases of the atmosphere. In the air mixture, the dry gases and associated water vapor behave according to the "Dalton's law of Partial Pressures." So, they behave independently of one another and each item exerts pressure individually to produce an overall "atmospheric pressure." For any given temperature there is a maximum amount of vapor that can be absorbed or associated with a given volume of air. Under certain conditions the mass of water vapor changes due to condensation or evaporation, but the mass of dry air remains constant. It is therefore convenient to relate all properties of the mixture to the mass of dry air rather than to the combined mass of air and water vapor. The following terminologies are commonly used in psychrometric calculations.

Dry Bulb Temperature (DBT, T_{DBT}): The dry bulb temperature is the true temperature of the moist air at rest as measured with a normal thermometer.

Saturated Vapor Pressure (P_{sat}): The pressure produced by the water vapor in this fully saturated condition is known as the saturated vapor pressure and since at a given temperature the air cannot absorb more water than its saturated condition, the saturated vapor pressure is the maximum pressure of water vapor that can occur at any given temperature.

Dew Point (T_{DP}): When an air-water vapor mixture is cooled at a constant pressure, the temperature at which the water vapor becomes saturated and moisture begins to condense is called the "dew point" temperature of the air. Since the temperature of saturated water vapor depends only on the absolute pressure, the dew point temperature is simply the saturation temperature corresponding to the partial pressure of the water vapor in the air-water vapor mixture.

Specific Humidity (ω): Specific humidity is the ratio of the mass of water vapor in a mixture to the mass of dry air in the mixture. Specific humidity is also referred to as the **humidity ratio** or the **absolute humidit**y.

Relative Humidity (ϕ): Relative humidity is the ratio of the mole fraction of water vapor in the moist air to the mole fraction of water vapor in saturated moist air at the same temperature and pressure.

Wet Bulb Temperature (WBT, T_{WBT}): This is the temperature which can be obtained if the air becomes 100% saturated due to water evaporation at a given dry bulb temperature and relative humidity. Wet bulb temperature is a close approximation of adiabatic saturation temperature.

Specific Volume of Moist Air (v): The volume of moist air per unit mass of dry air in the mixture is called the specific volume of moist air or **psychrometric volume**.

Specific Enthalpy of Moist Air (h): The specific enthalpy of moist air is the sum of the enthalpy of a unit mass of dry air and the enthalpy of water vapor associated with it.

According to Dalton's law of partial pressures, the ambient pressure, $P_{amb} = P_a + P_g$ (3.4)

So, the relations are,

$$\omega_0 = \frac{0.622 \times \phi \times P_{DBT}}{P_{amb} - (\phi \times P_{DBT})} = f(\phi, t_{DBT}) \tag{3.5}$$

$$\omega_0 = \frac{C_P \times (t_{WBT} - t_{DBT}) + \omega_1 \times (h_{g,WBT} - h_{f,WBT})}{h_{g,DBT} - h_{f,WBT}} = f(t_{DBT}, t_{WBT}, \omega_1) \tag{3.6}$$

$$\omega_1 = \frac{0.622 \times P_{WBT}}{P_{amb} - P_{WBT}} = f(t_{WBT}) \tag{3.7}$$

$$h = Cp \times t_{DBT} + \omega_0 \times h_{g,DBT} = f(t_{DBT}, \omega_0) \tag{3.8}$$

$$v = \frac{R \times T_{DBT}}{P_{amb} - (\omega_0 \times P_{DBT})} = f(t_{DBT}, \omega_0) \tag{3.9}$$

As the program performs the psychrometric calculation from any two given values out of 7 parameters (e.g. DBT, WBT, dew point, relative humidity, specific humidity, enthalpy and specific volume), the possible cases could be tabulated as below. Dew Point does not couple with any of them because the dew point itself is a state with equal DBT and WBT. Sixteen different possible cases are categorized in Table 3.1. Case number can be found from Table 3.1 by cross-matching the one parameter from column and another from row, for example Relative Humidity from column and WBT from row cross each other at 6, so their case number is 6.

Table 3.1 Different cases for psychrometry

Cases	DBT	WBT	Dew Pt	Rel Hum	Sp Hum	Enthalpy	Sp. Vol.
DBT		1		2	3	4	5
WBT				6	7	8	9
Dew Pt			10				
Rel Hum					11	12	13
Sp Hum						14	15
Enthalpy							16
Sp Vol							

The detailed calculation procedures are explained for each case below. (Italic letters are used for the given parameters and the bold letters are used for calculated parameters.)

Case 1 (DBT, t_{DBT}, and WBT, t_{WBT}, are known):

i. From t_{DBT} and t_{WBT}, $\mathbf{P_{DBT}}$ and $\mathbf{P_{WBT}}$ are obtained from the steam table.

ii. $\boldsymbol{\omega_1}$ is obtained by using $\mathbf{P_{WBT}}$ in Eq. (3.7).

iii. $\mathbf{h_{g,WBT}}$, $\mathbf{h_{f,WBT}}$, $\mathbf{h_{g,DBT}}$ are obtained from the steam table.

iv. $\boldsymbol{\omega_0}$ is obtained by using $\mathbf{h_{g,WBT}}$, $\mathbf{h_{f,WBT}}$, $\mathbf{h_{g,DBT}}$ and $\boldsymbol{\omega_1}$ in Eq. (3.6).

v. $\boldsymbol{\phi}$ is obtained by using $\mathbf{P_{DBT}}$ and $\boldsymbol{\omega_0}$ in Eq. (3.5).

vi. **h** is calculated by using t_{DBT}, $\boldsymbol{\omega_0}$ and $\mathbf{h_{g,DBT}}$ in Eq. (3.8).

vii. **v** is calculated by using t_{DBT} and $\boldsymbol{\omega_0}$ in Eq. (3.9).

viii. $\mathbf{t_{DP}}$ is calculated from the definition of Dew point.

Case 2 (DBT, $t_{DBT,,}$, and relative humidity, ϕ, are known):

i. From t_{DBT}, $\mathbf{P_{DBT}}$ and $\mathbf{h_{g,DBT}}$ are obtained from the steam table.

ii. $\boldsymbol{\omega_0}$ is obtained by using $\mathbf{P_{DBT}}$ and ϕ in Eq. (3.5).

iii. A $\mathbf{t_{WBT}}$ is guessed and $\mathbf{h_{g,WBT}}$, $\mathbf{h_{f,WBT}}$ and $\mathbf{P_{WBT}}$ are calculated from it. $\boldsymbol{\omega_1}$ is calculated from Eq. (3.6) {using $\mathbf{h_{g,WBT}}$, $\mathbf{h_{f,WBT}}$, $\mathbf{h_{g,DBT}}$ and $\boldsymbol{\omega_0}$} and Eq. (3.7) {using $\mathbf{P_{WBT}}$} and iterate until convergence. At the end of the iteration, both $\boldsymbol{\omega_1}$ and $\mathbf{t_{WBT}}$ are obtained.

iv. **h** is calculated by using t_{DBT}, $\boldsymbol{\omega_0}$, and $\mathbf{h_{g,DBT}}$ in Eq. (3.8).

v. **v** is calculated by using t_{DBT} and $\boldsymbol{\omega_0}$ in Eq. (3.9).

vi. $\mathbf{t_{DP}}$ is calculated from the definition of dew point.

Case 3 (DBT, t_{DBT}, and specific humidity, ω_0, are known):

i. From t_{DBT}, $\mathbf{P_{DBT}}$ and $\mathbf{h_{g,DBT}}$ are obtained from the steam table.

ii. $\boldsymbol{\phi}$ is obtained by using $\mathbf{P_{DBT}}$ and ω_0 in Eq. (3.5).

iii. A $\mathbf{t_{WBT}}$ is guessed and $\mathbf{h_{g,WBT}}$, $\mathbf{h_{f,WBT}}$ and $\mathbf{P_{WBT}}$ are calculated from it. $\boldsymbol{\omega_1}$ is calculated from Eq. (3.6) {using $\mathbf{h_{g,WBT}}$, $\mathbf{h_{f,WBT}}$, $\mathbf{h_{g,DBT}}$ and ω_0} and Eq. (3.7) {using $\mathbf{P_{WBT}}$} and iterate until convergence. At the end of the iteration, both $\boldsymbol{\omega_1}$ and $\mathbf{t_{WBT}}$ are obtained.

iv. **h** is calculated by using t_{DBT}, ω_0 and $\mathbf{h_{g,DBT}}$ in Eq. (3.8).

v. **v** is calculated by using t_{DBT} and ω_0 in Eq. (3.9).

vi. $\mathbf{t_{DP}}$ is calculated from the definition of dew point.

Case 4 (DBT, t_{DBT}, and moist air enthalpy, h, are known):

i. From t_{DBT}, $\mathbf{P_{DBT}}$ and $\mathbf{h_{g,DBT}}$ are obtained from the steam table.

ii. $\boldsymbol{\omega_0}$ is obtained by using $\mathbf{h_{g,DBT}}$ and h in Eq. (3.8).

iii. $\boldsymbol{\phi}$ is obtained by using $\mathbf{P_{DBT}}$ and $\boldsymbol{\omega_0}$ in Eq. (3.5).

iv. A $\mathbf{t_{WBT}}$ is guessed and $\mathbf{h_{g,WBT}}$, $\mathbf{h_{f,WBT}}$ and $\mathbf{P_{WBT}}$ are calculated from it. $\boldsymbol{\omega_1}$ is calculated from Eq. (3.6) {using $\mathbf{h_{g,WBT}}$, $\mathbf{h_{f,WBT}}$, $\mathbf{h_{g,DBT}}$ and $\boldsymbol{\omega_0}$} and Eq. (3.7) {using $\mathbf{P_{WBT}}$} and iterate until convergence. At the end of the iteration, both $\boldsymbol{\omega_1}$ and $\mathbf{t_{WBT}}$ are obtained.

v. **v** is calculated by using t_{DBT} and $\boldsymbol{\omega_0}$ in Eq. (3.9).

vi. $\mathbf{t_{DP}}$ is calculated from the definition of dew point.

Case 5 (DBT, t_{DBT}, and specific volume, v, are known):

i. From t_{DBT}, $\mathbf{P_{DBT}}$ and $\mathbf{h_{g,DBT}}$ are obtained from the steam table.

ii. $\boldsymbol{\omega_0}$ is obtained by using $\mathbf{h_{g,DBT}}$ and v in Eq. (3.9).

iii. $\boldsymbol{\phi}$ is obtained by using $\mathbf{P_{DBT}}$ and $\boldsymbol{\omega_0}$ in Eq. (3.5).

iv. A $\mathbf{t_{WBT}}$ is guessed and $\mathbf{h_{g,WBT}}$, $\mathbf{h_{f,WBT}}$ and $\mathbf{P_{WBT}}$ are calculated from it. $\boldsymbol{\omega_1}$ is calculated from Eq. (3.6) {using $\mathbf{h_{g,WBT}}$, $\mathbf{h_{f,WBT}}$, $\mathbf{h_{g,DBT}}$ and $\boldsymbol{\omega_0}$} and Eq. (3.7) {using $\mathbf{P_{WBT}}$} and iterate until convergence. At the end of the iteration, both $\boldsymbol{\omega_1}$ and $\mathbf{t_{WBT}}$ are obtained.

v. **h** is calculated by using t_{DBT}, $\boldsymbol{\omega_0}$ and $\mathbf{h_{g,DBT}}$ in Eq. (3.8).

vi. $\mathbf{t_{DP}}$ is calculated from the definition of dew point.

Case 6 (WBT, t_{WBT}, and relative humidity, ϕ, are known):

i. From t_{WBT}, $\mathbf{P_{WBT}}$, $\mathbf{h_{g,WBT}}$ and $\mathbf{h_{f,WBT}}$ are obtained from the steam table.

ii. $\boldsymbol{\omega_1}$ is obtained by using $\mathbf{P_{WBT}}$ in Eq. (3.7).

iii. A $\mathbf{t_{DBT}}$ is guessed and $\mathbf{h_{g,DBT}}$ and $\mathbf{P_{DBT}}$ are calculated from it. ω_0 is calculated from Eqs. (3.5) {using $\mathbf{P_{DBT}}$ and ϕ} and Eq. (3.6) {using $\mathbf{h_{g,WBT}}$, $\mathbf{h_{f,WBT}}$, $\mathbf{h_{g,DBT}}$ and $\boldsymbol{\omega_1}$} and iterate until convergence. At the end of the iteration, both $\boldsymbol{\omega_0}$ and $\mathbf{t_{DBT}}$ are obtained.

iv. **h** is calculated by using $\mathbf{t_{DBT}}$, $\boldsymbol{\omega_0}$ and $\mathbf{h_{g,DBT}}$ in Eq. (3.8).

v. **v** is calculated by using $\mathbf{t_{DBT}}$ and $\boldsymbol{\omega_0}$ in Eq. (3.9).

vi. $\mathbf{t_{DP}}$ is calculated from the definition of dew point.

Case 7 (WBT, t_{WBT}, and specific humidity, ω_0, are):

i. From t_{WBT}, $\mathbf{P_{WBT}}$, $\mathbf{h_{g,WBT}}$ and $\mathbf{h_{f,WBT}}$ are obtained from the steam table.

ii. $\boldsymbol{\omega_1}$ is obtained by using $\mathbf{P_{WBT}}$ in Eq. (3.7).

iii. A $\mathbf{t_{DBT}}$ is guessed and $\mathbf{h_{g,DBT}}$ is calculated from it. $\boldsymbol{\omega_0}$ is calculated from Eqs. (3.6) {using $\mathbf{h_{g,WBT}}$, $\mathbf{h_{f,WBT}}$, $\mathbf{h_{g,DBT}}$ and $\boldsymbol{\omega_1}$} and iterate until it gets closer to the given specific humidity, ω_0. At the end of the iteration, $\mathbf{t_{DBT}}$ is obtained, from which $\mathbf{P_{DBT}}$ is obtained.

iv. $\boldsymbol{\phi}$ is obtained by using $\mathbf{P_{DBT}}$ and ω_0 in Eq. (3.5).

v. $\mathbf{h}$ is calculated by using $\mathbf{t_{DBT}}$, ω_0 and $\mathbf{h_{g,DBT}}$ in Eq. (3.8).

vi. $\mathbf{v}$ is calculated by using $\mathbf{t_{DBT}}$ and ω_0 in Eq. (3.9).

vii. $\mathbf{t_{DP}}$ is calculated from the definition of dew point.

Case 8 (WBT, t_{WBT}, and moist air enthalpy, h, are known):

i. From t_{WBT}, $\mathbf{P_{WBT}}$, $\mathbf{h_{g,WBT}}$ and $\mathbf{h_{f,WBT}}$ are obtained from the steam table.

ii. $\boldsymbol{\omega_1}$ is obtained by using $\mathbf{P_{WBT}}$ in Eq. (3.7).

iii. A $\mathbf{t_{DBT}}$ is guessed and $\mathbf{h_{g,DBT}}$ is calculated from it. $\boldsymbol{\omega_0}$ is calculated from Eqs. (3.6) {using $\mathbf{h_{g,WBT}}$, $\mathbf{h_{f,WBT}}$, $\mathbf{h_{g,DBT}}$ and $\boldsymbol{\omega_1}$} and (3.8) {using h, $\mathbf{t_{DBT}}$ and $\mathbf{h_{g,DBT}}$} and iterate until convergence. At the end of the iteration, $\boldsymbol{\omega_0}$ and $\mathbf{t_{DBT}}$ are obtained.

iv. From $\mathbf{t_{DBT}}$, $\mathbf{P_{DBT}}$ is obtained from the steam table.

v. $\boldsymbol{\phi}$ is obtained by using $\mathbf{P_{DBT}}$ and $\boldsymbol{\omega_0}$ in Eq. (3.5).

vi. $\mathbf{v}$ is calculated by using $\mathbf{t_{DBT}}$ and $\boldsymbol{\omega_0}$ in Eq. (3.9).

vii. $\mathbf{t_{DP}}$ is calculated from the definition of Dew point.

Case 9 (WBT, t_{WBT}, and specific volume, v, are known):

i. From t_{WBT}, $\mathbf{P_{WBT}}$, $\mathbf{h_{g,WBT}}$ and $\mathbf{h_{f,WBT}}$ are obtained from the steam table.

ii. $\boldsymbol{\omega_1}$ is obtained by using $\mathbf{P_{WBT}}$ in Eq. (3.7).

iii. A $\mathbf{t_{DBT}}$ is guessed and $\mathbf{h_{g,DBT}}$ and $\mathbf{P_{DBT}}$ are calculated from it. $\boldsymbol{\omega_0}$ is calculated from Eqs. (3.6) {using $\mathbf{h_{g,WBT}}$, $\mathbf{h_{f,WBT}}$, $\mathbf{h_{g,DBT}}$ and $\boldsymbol{\omega_1}$} and (3.9) {using v, $\mathbf{t_{DBT}}$ and

$\mathbf{P_{DBT}}$} and iterate until convergence. At the end of the iteration, $\boldsymbol{\omega_0}$ and $\mathbf{t_{DBT}}$ are obtained.

iv. $\boldsymbol{\phi}$ is obtained by using $\mathbf{P_{DBT}}$ and $\boldsymbol{\omega_0}$ in Eq. (3.5).

v. **h** is calculated by using $\mathbf{t_{DBT}}$, $\boldsymbol{\omega_0}$ and $\mathbf{h_{g,DBT}}$ in Eq. (3.8).

vi. $\mathbf{t_{DP}}$ is calculated from the definition of dew point.

Case 10 (Dew point, $\mathbf{t_{DP}}$ is known):

i. At the dew point, DBT, WBT and dew points are same with 100% relative humidity. So, other values can be found by using Eqs. (3.4), (3.8) and (3.9).

Case 11 (Relative humidity, ϕ, and specific humidity, ω_0, are known):

i. $\mathbf{P_{DBT}}$ is calculated from Eq. (3.5) using ω_0, from which $\mathbf{t_{DBT}}$ is calculated.

ii. A $\mathbf{t_{WBT}}$ is guessed and $\mathbf{h_{g,WBT}}$, $\mathbf{h_{f,WBT}}$ and $\mathbf{P_{WBT}}$ are calculated from it. $\boldsymbol{\omega_1}$ is calculated from Eq. (3.6) {using $\mathbf{h_{g,WBT}}$, $\mathbf{h_{f,WBT}}$, $\mathbf{h_{g,DBT}}$ and ω_0} and Eq. (3.7) {using $\mathbf{P_{WBT}}$} and iterate until convergence. At the end of the iteration, both $\boldsymbol{\omega_1}$ and $\mathbf{t_{WBT}}$ are obtained.

iii. **h** is calculated by using $\mathbf{t_{DBT}}$, ω_0 and $\mathbf{h_{g,DBT}}$ in Eq. (3.8).

iv. **v** is calculated by using $\mathbf{t_{DBT}}$ and ω_0 in Eq. (3.9).

v. $\mathbf{t_{DP}}$ is calculated from the definition of dew point.

Case 12 (Relative humidity, ϕ, and moisture enthalpy, h, are known):

i. A $\mathbf{t_{DBT}}$ is guessed and $\mathbf{P_{DBT}}$ is calculated from it. $\boldsymbol{\omega_0}$ is calculated from Eqs. (3.5) {using $\mathbf{P_{DBT}}$ and ϕ} and (3.8) {using $\mathbf{t_{DBT}}$, $\boldsymbol{\omega_0}$ and $\mathbf{h_{g,DBT}}$} and iterate until convergence. At the end of the iteration, both $\boldsymbol{\omega_0}$ and $\mathbf{t_{DBT}}$ are obtained.

ii. A $\mathbf{t_{WBT}}$ is guessed and $\mathbf{h_{g,WBT}}$, $\mathbf{h_{f,WBT}}$ and $\mathbf{P_{WBT}}$ are calculated from it. $\boldsymbol{\omega_1}$ is calculated from Eq. (3.6) {using $\mathbf{h_{g,WBT}}$, $\mathbf{h_{f,WBT}}$, $\mathbf{h_{g,DBT}}$ and $\boldsymbol{\omega_0}$} and Eq. (3.7) {using $\mathbf{P_{WBT}}$} and iterate until convergence. At the end of the iteration, both $\boldsymbol{\omega_1}$ and $\mathbf{t_{WBT}}$ are obtained.

iii. **v** is calculated by using $\mathbf{t_{DBT}}$ and ω_0 in Eq. (3.9).

iv. $\mathbf{t_{DP}}$ is calculated from the definition of dew point.

Case 13 (Relative humidity, ϕ, and specific volume, v, are known):

i. A $\mathbf{t_{DBT}}$ is guessed and $\mathbf{P_{DBT}}$ is calculated from it. $\boldsymbol{\omega_0}$ is calculated from Eqs. (3.5) {using $\mathbf{P_{DBT}}$ and ϕ} and (3.9) {using $\mathbf{t_{DBT}}$, $\boldsymbol{\omega_0}$ and $\mathbf{P_{DBT}}$} and iterate until convergence. At the end of the iteration, both $\boldsymbol{\omega_0}$ and $\mathbf{t_{DBT}}$ are obtained.

ii. A $\mathbf{t_{WBT}}$ is guessed and $\mathbf{h_{g,WBT}}$, $\mathbf{h_{f,WBT}}$ and $\mathbf{P_{WBT}}$ are calculated from it. $\boldsymbol{\omega_1}$ is calculated from Eq. (3.6) {using $\mathbf{h_{g,WBT}}$, $\mathbf{h_{f,WBT}}$, $\mathbf{h_{g,DBT}}$ and $\boldsymbol{\omega_0}$} and Eq. (3.7) {using $\mathbf{P_{WBT}}$} and iterate until convergence. At the end of the iteration, both $\boldsymbol{\omega_1}$ and $\mathbf{t_{WBT}}$ are obtained.

iii. **h** is calculated by using $\mathbf{t_{DBT}}$, $\boldsymbol{\omega_0}$ and $\mathbf{h_{g,DBT}}$ in Eq. (3.8).

iv. $\mathbf{t_{DP}}$ is calculated from the definition of dew point.

Case 14 (Specific humidity, ω_0, and moist air enthalpy, h, are known):

i. $\mathbf{t_{DBT}}$ is guessed, from which $\mathbf{h_{g,DBT}}$ is obtained from the steam table and placed in Eq. (3.8) to find enthalpy until the calculated enthalpy gets closer to the given enthalpy, h. $\mathbf{t_{DBT}}$ is obtained at the end of iteration.

ii From $\mathbf{t_{DBT}}$, $\mathbf{P_{DBT}}$ is obtained from the steam table.

iii. $\boldsymbol{\phi}$ is calculated from Eq. (3.5) using $\mathbf{P_{DBT}}$ and ω_0.

iv. A $\mathbf{t_{WBT}}$ is guessed and $\mathbf{h_{g,WBT}}$, $\mathbf{h_{f,WBT}}$ and $\mathbf{P_{WBT}}$ are calculated from it. $\boldsymbol{\omega_1}$ is calculated from Eq. (3.6) {using $\mathbf{h_{g,WBT}}$, $\mathbf{h_{f,WBT}}$, $\mathbf{h_{g,DBT}}$ and ω_0} and Eq. (3.7) {using $\mathbf{P_{WBT}}$} and iterate until convergence. At the end of the iteration, both $\boldsymbol{\omega_1}$ and $\mathbf{t_{WBT}}$ are obtained.

v. **v** is calculated by using $\mathbf{t_{DBT}}$ and ω_0 in Eq. (3.9).

vi. $\mathbf{t_{DP}}$ is calculated from the definition of dew point.

Case 15 (Specific humidity, ω_0, and specific volume, v, are known):

i. $\mathbf{t_{DBT}}$ is guessed, from which $\mathbf{P_{DBT}}$ is obtained from the steam table and placed in Eq. (3.9) to find specific volume until the calculated specific volume gets closer to the given specific volume, v. $\mathbf{t_{DBT}}$ is obtained at the end of iteration.

ii From $\mathbf{t_{DBT}}$, $\mathbf{P_{DBT}}$ is obtained from the steam table

iii. $\boldsymbol{\phi}$ is calculated from Eq. (3.5) using $\mathbf{P_{DBT}}$ and ω_0.

iv. A $\mathbf{t_{WBT}}$ is guessed and $\mathbf{h_{g,WBT}}$, $\mathbf{h_{f,WBT}}$ and $\mathbf{P_{WBT}}$ are calculated from it. $\boldsymbol{\omega_1}$ is calculated from Eq. (3.6) {using $\mathbf{h_{g,WBT}}$, $\mathbf{h_{f,WBT}}$, $\mathbf{h_{g,DBT}}$ and ω_0} and Eq. (3.7) {using $\mathbf{P_{WBT}}$} and iterate until convergence. At the end of the iteration, both $\boldsymbol{\omega_1}$ and $\mathbf{t_{WBT}}$ are obtained.

v. $\mathbf{h}$ is calculated by using $\mathbf{t_{DBT}}$, $\boldsymbol{\omega_0}$ and $\mathbf{h_{g,DBT}}$ in Eq. (3.8).

vi. $\mathbf{t_{DP}}$ is calculated from the definition of dew point.

Case 16 (Moist air enthalpy, *h*, and specific volume, v, are known):

i. A $\mathbf{t_{DBT}}$ is guessed and $\mathbf{h_{g,DBT}}$ is calculated from it. $\boldsymbol{\omega_0}$ is calculated from Eqs. (3.8) {using *h*, $\mathbf{t_{DBT}}$ and $\mathbf{h_{g,DBT}}$} and (3.9) {using $\mathbf{t_{DBT}}$, $\mathbf{P_{DBT}}$ and v} and iterate until convergence. At the end of the iteration, both $\boldsymbol{\omega_0}$ and $\mathbf{t_{DBT}}$ are obtained.

ii From $\mathbf{t_{DBT}}$, $\mathbf{P_{DBT}}$ is obtained from the steam table.

iii. $\boldsymbol{\phi}$ is calculated from Eq. (3.5) using $\mathbf{P_{DBT}}$ and $\boldsymbol{\omega_0}$.

iv. A $\mathbf{t_{WBT}}$ is guessed and $\mathbf{h_{g,WBT}}$, $\mathbf{h_{f,WBT}}$ and $\mathbf{P_{WBT}}$ are calculated from it. $\boldsymbol{\omega_1}$ is calculated from Eq. (3.6) {using $\mathbf{h_{g,WBT}}$, $\mathbf{h_{f,WBT}}$, $\mathbf{h_{g,DBT}}$ and ω_0} and Eq. (3.7) {using $\mathbf{P_{WBT}}$} and iterate until convergence. At the end of the iteration, both $\boldsymbol{\omega_1}$ and $\mathbf{t_{WBT}}$ are obtained.

v. T_{DP} are calculated from the definition of dew point.

In general, when DBT is known, WBT needs to be obtained by iteration. The initial guess of the WBT value starts with the DBT value and then the iteration proceeds with negative increments of 0.01^{o}C until the convergence is achieved. The interface for the "Psychrometry" is obtained by clicking the fourth tab in the main switchboard (Fig. 3.1)

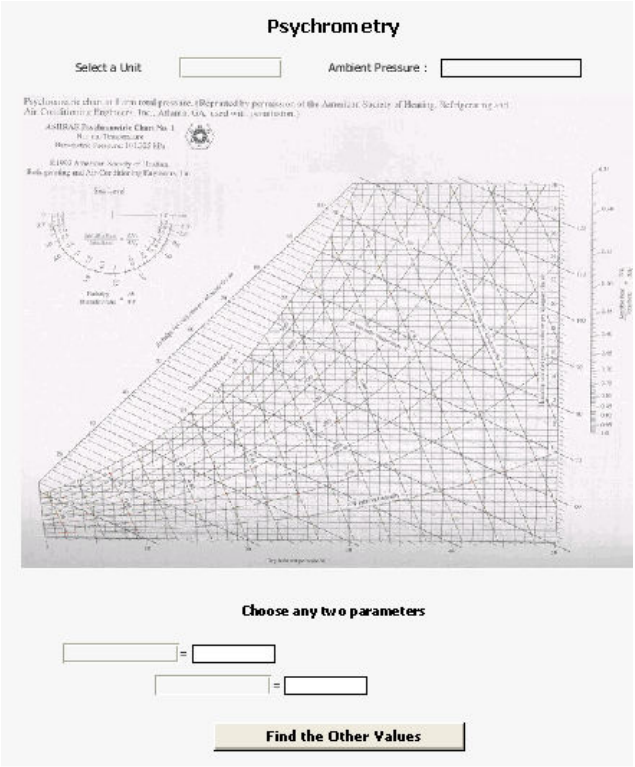

Figure 3.8 Psychrometry interface

The first drop-down list gives the option to choose the unit (SI or English). The ambient pressure is 1.0135 bar by default. The second drop-down list gives the option to choose the first parameter and the third one gives the option to choose the second parameter. It should be noticed that the temperature must be given in °C and °F in SI or English unit. Then the program calculates all the other values (Fig. 3.9) and shows the state in the chart.

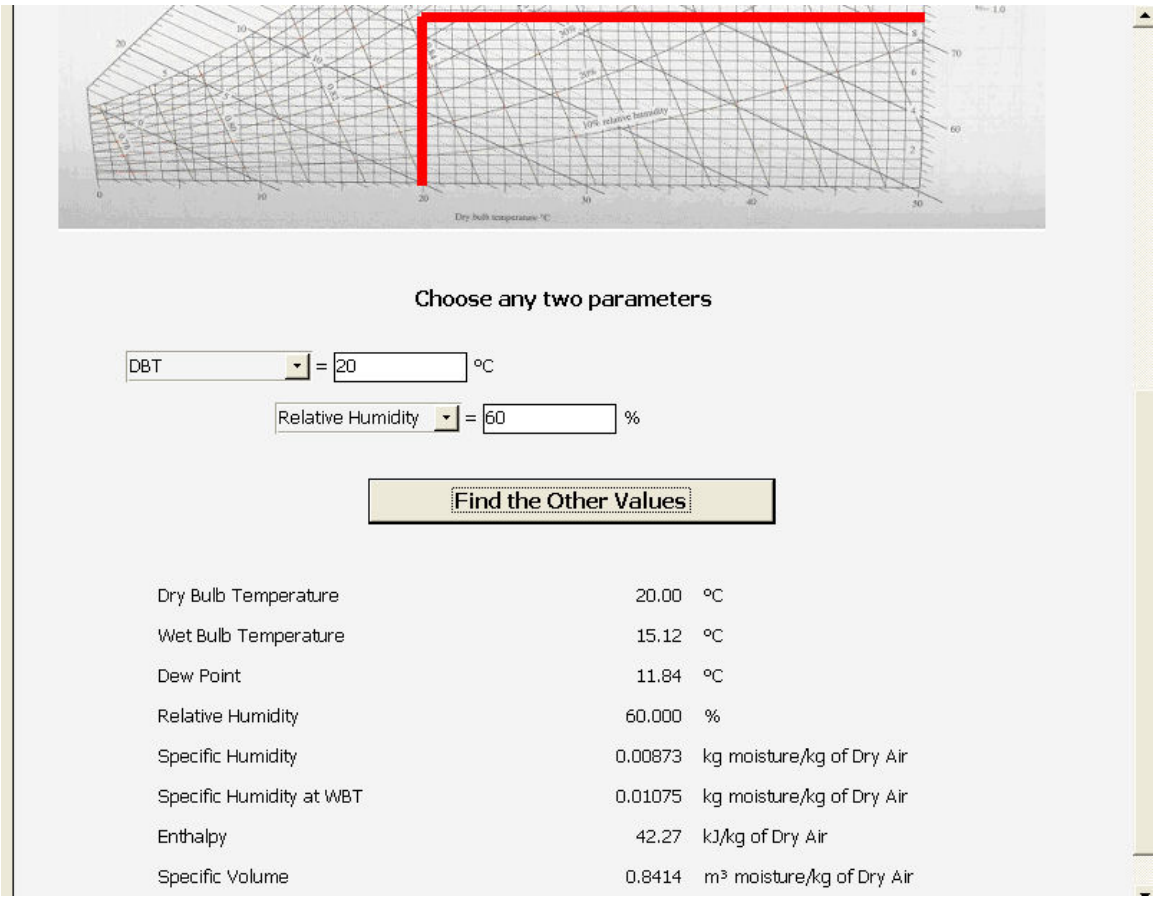

Figure 3.9 Calculated property values

3.2 Gas Turbine Calculation (Non-Stacking Method)

This part of the chapter discusses about the thermodynamic (non-stacking) calculation of gas turbine system. The three major components of the GT system: compressor, combustor, and turbine are treated as black boxes, each with a given efficiency. Interfaces of gas turbine calculation without and with mist cooling are obtained by clicking fifth and sixth button on the main switchboard (Fig. 3.1).

3.2.1 Gas Turbine Calculation (Without Mist Cooling)

A simple gas turbine system follows the Brayton cycle, which consists of two isentropic lines (encircled s in Fig. 3.10) and two isobaric lines (encircled P in Fig. 3.10)

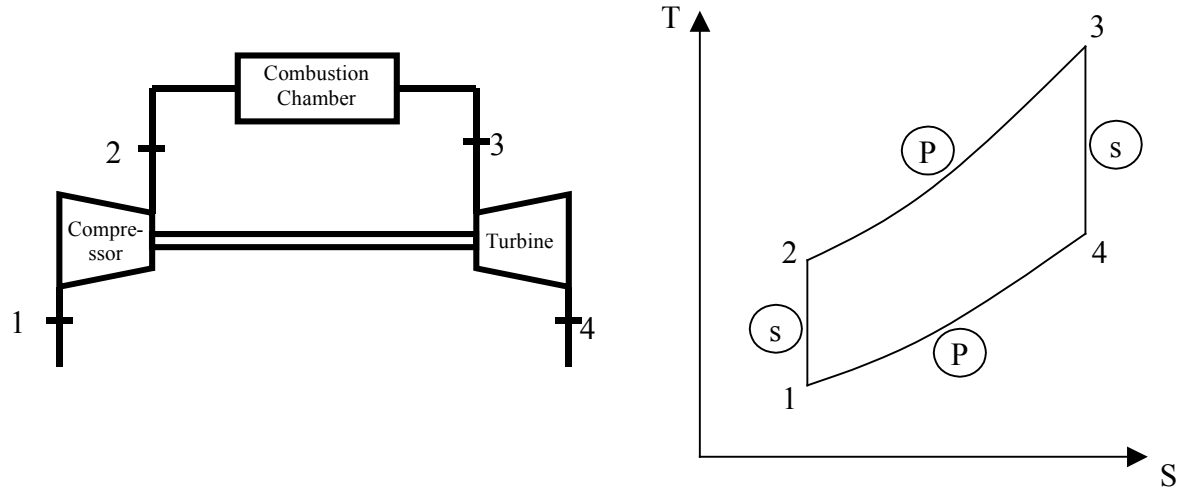

Figure 3.10 Brayton cycle

The program requests input of the ambient temperature = T_1, the Turbine Inlet Temperature (TIT) = T_3, the Pressure ratio = r_p, and the isentropic efficiencies of compressor (η_c) and turbine (η_t). The program will determine the four states and calculate the local enthalpies and temperatures, compressor power, turbine power, net output power, thermal efficiency, and other important information. The calculation procedure is described in detail below.

1. With T_1, the enthalpy at compressor inlet (State 1) $\equiv h_1$ and the Reduced Pressure ($\equiv Pr_1$) are obtained from the air property table.
2. The reduced pressure at compressor exit (isentropic state 2s) is calculated as $Pr_2 = r_p \times Pr_1$.
3. From Pr_2, the enthalpy at the isentropic state 2s, h_{2s}, is obtained from the air property table.

4. Using the given compressor efficiency, the actual enthalpy at state 2 is calculated from the equation:

$$\eta_c = \frac{h_{2S} - h_1}{h_2 - h_1} \Rightarrow h_{2S} - h_1 = \eta_c (h_2 - h_1) \Rightarrow h_{2S} = h_1 + \eta_c (h_2 - h_1)$$

5. From h_2, the temperature at state 2 (T_2) is obtained from the air property table.
6. The turbine inlet temperature, T_3, is given, so the enthalpy at Turbine inlet (State 3), h_3, and the reduced pressure, Pr_3, are obtained from the air property table.
7. The reduced pressure at the turbine exit (isentropic state 4s) is calculated as, $Pr_4 = Pr_3 / r_p$.
8. From Pr_4, the enthalpy at the isentropic state 4s, h_{4s}, is obtained from the air property table.
9. To find out the actual enthalpy at state 4, using the turbine efficiency to calculate h_4 as:

$$\eta_t = \frac{h_3 - h_4}{h_3 - h_{4S}} \Rightarrow h_3 - h_{4S} = \frac{h_3 - h_4}{\eta_t} \Rightarrow h_{4S} = h_3 - \frac{h_3 - h_4}{\eta_t}$$

10. From h_4, the actual temperature at state 4, T_4, is calculated from the air property table.
11. Calculate the compressor work per unit mass flow rate, $w_c = h_2 - h_1$.
12. Calculate the turbine work per unit mass flow rate, $w_t = h_3 - h_4$.
13. Calculate the net output work per unit mass flow rate, $w_{net} = w_t - w_c$.
14. Calculate the heat input per unit air mass flow rate, $q_{in} = h_3 - h_2$ (If fuel mass is neglected.). If the mass of fuel is considered (e.g. n-Octane is used), the heat input is calculated by balancing the enthalpy of combustion reaction. The example of using Octane, C_8H_{18}, is shown below:

$$\underbrace{C_8H_{18} + XD.A.}_{T_2} \rightarrow \underbrace{8CO_2 + 9H_2O + XD.A. - 12.5O_2}_{T_3}$$

Where X is the total number of moles of dry air (D.A.) supplied per mole of fuel.

Energy balance: $H_{Pr} = H_{Re}$ [Pr→Product, Re→Reactant]

$$\Rightarrow \sum \left(n_i \bar{h}_{T_3}\right)_{Pr} = \Delta H_{f,C_8H_{18}} + X\bar{h}_{air,T_2}$$ [n→number of moles, $\Delta H_f \rightarrow$ Heat of Formation]

$$\Rightarrow n_{CO_2}\left(\bar{h}_{T_3}\right)_{CO_2} + n_{H_2O}\left(\bar{h}_{T_3}\right)_{H_2O} + XM_{air}h_3 - n_{O_2}\left(\bar{h}_{T_3}\right)_{O_2} = \Delta H_{f,C_8H_{18}} + XM_{air}h_2$$

[M→Molecular Weight]

$\bar{h}_{T_3}$ values are obtained from the gas property table of each corresponding gas. These tables can be called out from the "Gas Property Calculation" interface. In the above equation, all

the values are known except X. This equation is solved to obtain the total mole number of the dry air (X) per mole of the fuel.

15. The percentage of the excess air is calculated as $\left(\frac{X - r}{r}\right) \times 100\ \%$

    Where, r ≡ the stoichiometric value of dry air.

16. Calculate the fuel air mass ratio, $f' = \frac{M_{C_8H_{18}}}{XM_{air}}$

18. Calculate the heat input per unit air mass flow rate when the excess air is considered,

    $q_{in} = f' \times LHV$ [LHV→Lower Heating Value of the fuel]

19. Thermal Efficiency, $\eta_{th} = \frac{w_{net}}{q_{in}}$

3.2.2 Gas Turbine Calculation (With Mist Cooling)

Figure 3.11 shows a gas turbine system equipped with a fog sprayer device and a fuel compressor.

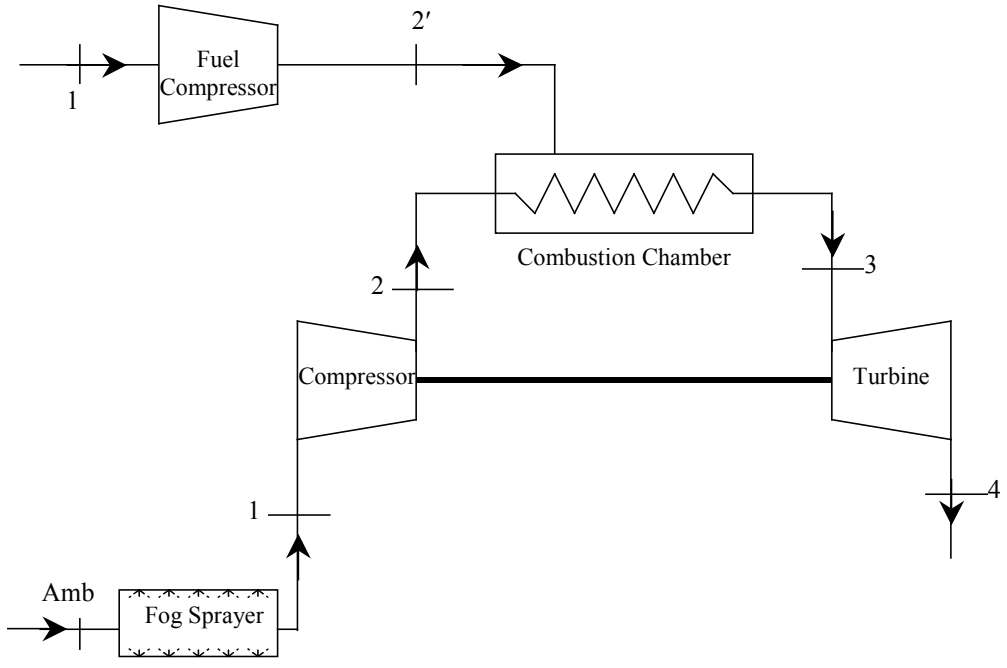

Figure 3.11 Gas turbine system with fog cooling device and a fuel compressor

This program requests input for the ambient temperature (T_{amb}), the relative humidity (ϕ), and turbine inlet temperature (TIT = T_3), pressure ratio (r_P), the isentropic efficiencies of

compressor (η_C) and turbine (η_T), and the ratio of sprayed water mass flow rate over the inlet dry air mass flow rate This program determines four different states, local enthalpies, and local temperatures, and calculates the compressor power, the turbine power, the net output power, the thermal efficiency, and the other important information e.g. F/A ratio, excess air percentage, fuel compressor power, SFC etc. The calculation procedure is described with a flow chart, which is followed by the solution procedure. Input and output windows are shown in Figs. 3.13, 3.14 and 3.15.

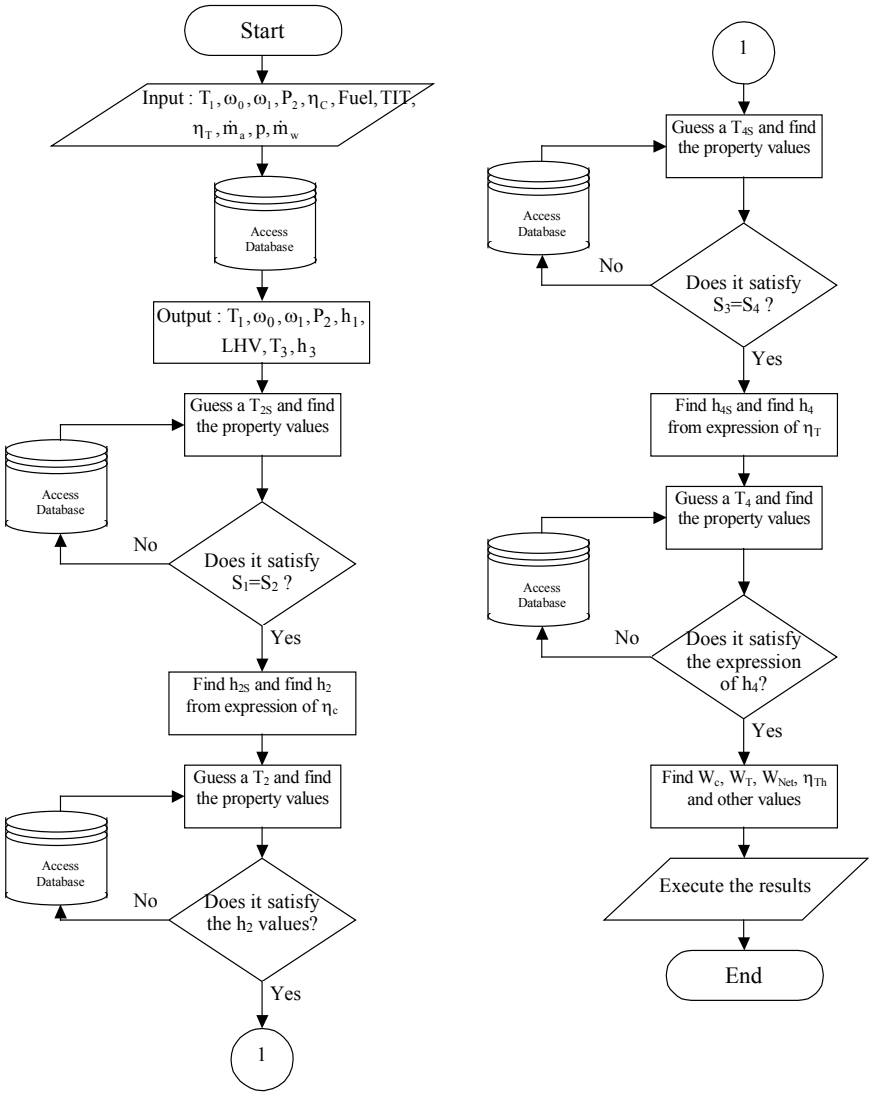

Figure 3.12 Flow chart showing power and efficiency calculation process for a gas turbine system with fog cooling device and a fuel compressor

Ambient condition: P_1, T_{amb} and ϕ (Relative humidity)

Compressor information: Pressure ratio = r_P, Efficiency = η_c

Fuel compressor information: Discharge pressure = P_2', Efficiency = η_{fc}

Turbine information: TIT = T_3, Efficiency = η_t

Air information: Flow = m_a, Temperature = T_{amb}, Relative humidity = ϕ

Solution:

At the ambient condition,

Specific humidity = ω_0

Relative humidity at WBT (or saturation) = ω_1

Compressor inlet temperature, T_1 = WBT (assuming fully saturated)

Water spray fraction is, $p = \omega_1 - \omega_0$ (to saturate the air)

$= \omega_1 - \omega_0 + OS$ (for overspray)

Water flow, $m_w = p \times m_a$

State 1: The temperature is, T_1 = WBT

$$\text{So, } h_1 = \frac{m_{a_1} h_{a_1} + m_{f_1} h_{f_1} + m_{g_1} h_{g_1}}{m_{a_1} + m_{f_1} + m_{g_1}} = \frac{h_{a_1} + \frac{m_{f_1}}{m_{a_1}} h_{f_1} + \frac{m_{g_1}}{m_{a_1}} h_{g_1}}{1 + \frac{m_{f_1}}{m_{a_1}} + \frac{m_{g_1}}{m_{a_1}}}$$

Here, h_{a_1} = Enthalpy of dry air at T_1

h_{f_1} = Enthalpy of compressed water at T_1 and P_1

h_{g_1} = Enthalpy of saturated steam at T_1

$\frac{m_{f_1}}{m_{a_1}}$ = Ratio of overspray with dry air

$\frac{m_{g_1}}{m_{a_1}}$ = Ratio of vapor with dry air = ω_1

$$h_1 = \frac{h_{a_1} + (p - \omega_1 + \omega_0) h_{f_1} + \omega_1 h_{g_1}}{1 + p + \omega_0} \tag{3.10}$$

$$\text{Entropy, } s_1 = \frac{m_{a_1} s_{a_1} + m_{f_1} s_{f_1} + m_{g_1} s_{g_1}}{m_{a_1} + m_{f_1} + m_{g_1}} = \frac{s_{a_1} + (p - \omega_1 + \omega_0) s_{f_1} + \omega_1 s_{g_1}}{1 + p + \omega_0} \tag{3.11}$$

s_{a_1} = Entropy of dry air at T_1

s_{f_1} = Entropy of compressed water at T_1 and P_1

s_{g_1} = Entropy of saturated steam at T_1

State 2: To find out state 2, first the T_{2s} needs to be calculated by satisfying $s_1 = s_2$. So, a temperature for T_{2s} needs to be guessed and iterated until convergence. Based on the current applications with not more than 2% overspray being employed, typically, there is no more water in liquid form left at T_2 or T_{2s}. So, the total amount water will be used as water vapor in the following calculations. This assumption is appropriate when the compressor is treated as a black box and the detailed local evaporation condition inside the compressor is not known. More complicated models have been developed for stage-stacking method to be presented later. In eq. (3.12), s_{a2}, s_{g2} are the functions of T_{2s} and P_2 ($P_2 = r_p \times P_1$)

$$s_2 = \frac{m_{a_2}\left(s_{a_2} - R\ln r_P\right) + m_{g_2}s_{g_2}}{m_{a_2} + m_{g_2}} = \frac{s_{a_2} - R\ln r_P + \frac{m_{g_2}}{m_{a_2}}s_{g_2}}{1 + \frac{m_{g_2}}{m_{a_2}}} = \frac{s_{a_2} - R\ln r_P + (p + \omega_0)s_{g_2}}{1 + p + \omega_0} \quad (3.12)$$

h_{2s} can be calculated from Eq. (3.13), where h_{a2}, h_{g2} are the functions of T_{2s} and P_2.

$$h_{2s} = \frac{m_{a_2}h_{a_2} + m_{g_2}h_{g_2}}{m_{a_2} + m_{g_2}} = \frac{h_{a_2} + \frac{m_{g_2}}{m_{a_2}}h_{g_2}}{1 + \frac{m_{g_2}}{m_{a_2}}} = \frac{h_{a_2} + (p + \omega_0)h_{g_2}}{1 + p + \omega_0} \quad (3.13)$$

Then, h_2 can be determined by using Eq. (3.14).

$$\eta_c = \frac{h_{2s} - h_1}{h_2 - h_1} \quad (3.14)$$

Now, T_2 can be by another iteration using Eq. (3.15), where h_2 has been calculated from Eq. (3.14) and h_{a2}, h_{g2} are the functions of T_2 and P_2.

$$h_2 = \frac{h_{a_2} + (p + \omega_0) h_{g_2}}{1 + p + \omega_0} \tag{3.15}$$

Combustion:

The mole of water in the air = $\frac{28.965X \times (p + \omega_0)}{18} = 1.6092X \times (p + \omega_0)$

Where, X = mole of D.A.

The reaction is

$CH_4 + X$ D.A. $+ 1.6092X\ (p+\omega_0)\ H_2O$ (At T_2)

$\Rightarrow CO_2 + [2 + 1.6092X\ (p+\omega_0)]\ H_2O + X$ D.A. $- 2\ O_2$ (At T_3)

Here, Enthalpy in the reactant side and product side are same.

$$\Sigma Re = \Sigma Pr$$

$$\Rightarrow \quad Hf0 + 28.965X\ h_{air@T2} + 1.6092X\ (p+\omega_0)\ h_{H2O@T2} = h_{CO2@T3} + 2\ h_{H2O@T3}$$
$$+ 1.6092X\ (p+\omega_0)\ h_{H2O@T3} + 28.965X\ h_{air@T3} - 2\ h_{O2@T3} \tag{3.16}$$

[Hf0 ≡ Enthalpy of formation of fuel]

X can be calculated from this equation by substituting all the enthalpy values

Percentage of excess air = $\frac{X - 2 \times (\text{Mole of Stoichometric air})}{2 \times (\text{Mole of Stoichometric air})} \times 100\%$ (3.17)

F/A ratio = $\frac{16.043}{X \times 28.965} = f'$ (3.18)

Fuel Compressor: The fuel compressor work,

$$W_{fc} = \frac{\gamma f'}{\gamma - 1}\left(P_2{}' v_2{}' - P_{Amb} v_{Amb}\right) = \frac{\gamma R f'}{\eta_{fc}(\gamma - 1)}\left(T_2{}' - T_{Amb}\right) \tag{3.19}$$

Here, γ = Specific Heat ratio = 1.4, R = Gas Constant = $\frac{8.314}{16.043}\text{kJ/kg}\cdot\text{K} = 0.51823\text{kJ/kg}\cdot\text{K}$

$P_2{}' = 1.25P_2 = 1.25 \times r_P \times P_1 = 1.25 \times 12 \times P_1 = 15P_1$

(The fuel compressor is assumed to have 25% more pressure than the pressure in the combustion chamber)

From isentropic relation, we get, $\frac{T_2{}'}{T_1} = \left(\frac{P_2{}'}{P_1}\right)^{\frac{\gamma-1}{\gamma}} = (15)^{\frac{0.4}{1.4}} = 2.1678$

Power of fuel compressor, $P_{fc} = m_a W_{fc}$

State 3: The temperature is, T_3 = TIT, so enthalpy

$$h_3 = \frac{m_{a3}(1+f')h_{a3} + m_{g3}h_{g3}}{m_{a3} + m_{g3}} = \frac{(1+f')h_{a3} + \frac{m_{g3}}{m_{a3}}h_{g3}}{(1+f') + \frac{m_{g3}}{m_{a3}}} = \frac{(1+f')h_{a3} + (p+\omega_0)h_{g3}}{(1+f') + p + \omega_0} \tag{3.20}$$

$$\text{Entropy, } s_3 = \frac{(1+f')s_{a3} + (p+\omega_0)s_{g3}}{(1+f') + p + \omega_0} \tag{3.21}$$

State 4: To determine state 4, first the T_{4s} needs to be calculated by satisfying $s_3 = s_4$. So, a temperature for T_{4s} needs to be guessed and iterated until convergence, where s_{a4} and s_{g4} are the functions of T_{4s} and P_4 ($P_4 = P_1$).

$$s_4 = \frac{(1+f')(s_{a4} + R\ln r_P) + (p+\omega_0)s_{g4}}{1 + f' + p + \omega_0} \tag{3.22}$$

h_{4s} can be calculated from Eq. (3.23), where h_{a4} and h_{g4} are the functions of T_{4s} and P_4.

So, at T_{4s}, $h_{4s} = \dfrac{(1+f')h_{a_4} + (p+\omega_0)h_{g_4}}{1+f'+p+\omega_0}$ (3.23)

h_4 can be found out by using Eq. (3.24).

$$\eta_t = \frac{h_3 - h_4}{h_3 - h_{4s}} \tag{3.24}$$

Now, T_4 can be determined by another iteration using Eq. (3.23), where h_4 has been calculated from Eq. (3.25) and h_{a4}, h_{g4} values are functions of T_4 and P_4..

$$h_4 = \frac{h_{a_4} + (p+\omega_0)h_{g_4}}{1+p+\omega_0} \tag{3.25}$$

Compressor: Compressor work,

$$w_c = (1 + p + \omega_0)\,(h_2 - h_1) \tag{3.26}$$

The compressor power is, $P_c = m_a\, w_c$ (3.27)

Turbine: Turbine work,

$$w_t = (1 + f' + p + \omega_0)\,(h_4 - h_3) \tag{3.28}$$

The turbine power is, $P_t = m_a\, w_t$ (3.29)

Combustion Chamber: Heat input,

$$q_{in} = f' \times LHV \tag{3.30}$$

Combustion Chamber power, $P_Q = m_a\, q_{in}$ (3.31)

So, the net output power is, $P_{net} = P_t - P_c - P_{fc}$ (3.32)

The thermal efficiency is, $\eta_{th} = \frac{P_{net}}{P_Q}$ (3.33)

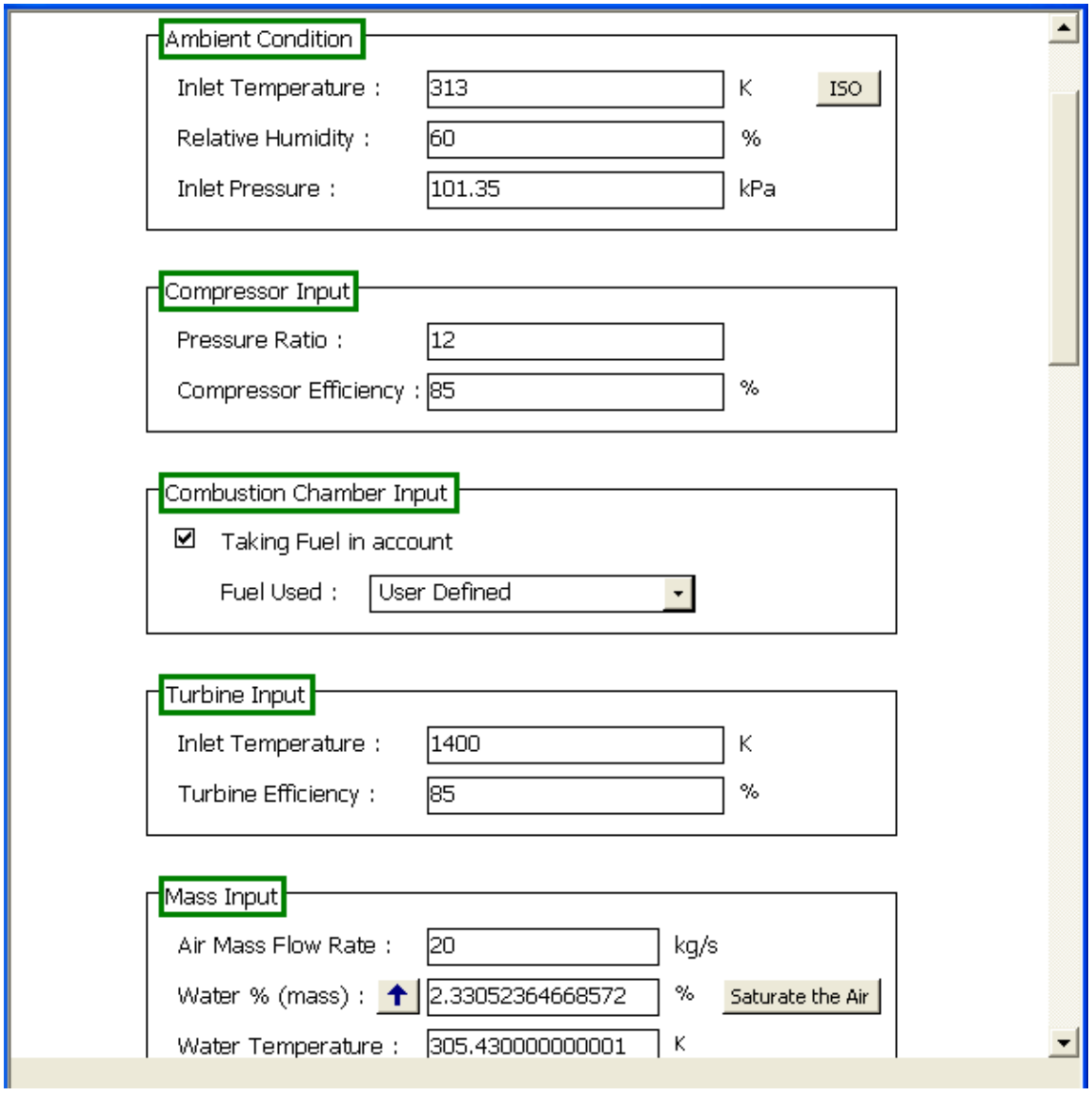

Figure 3.13 Wet compression input

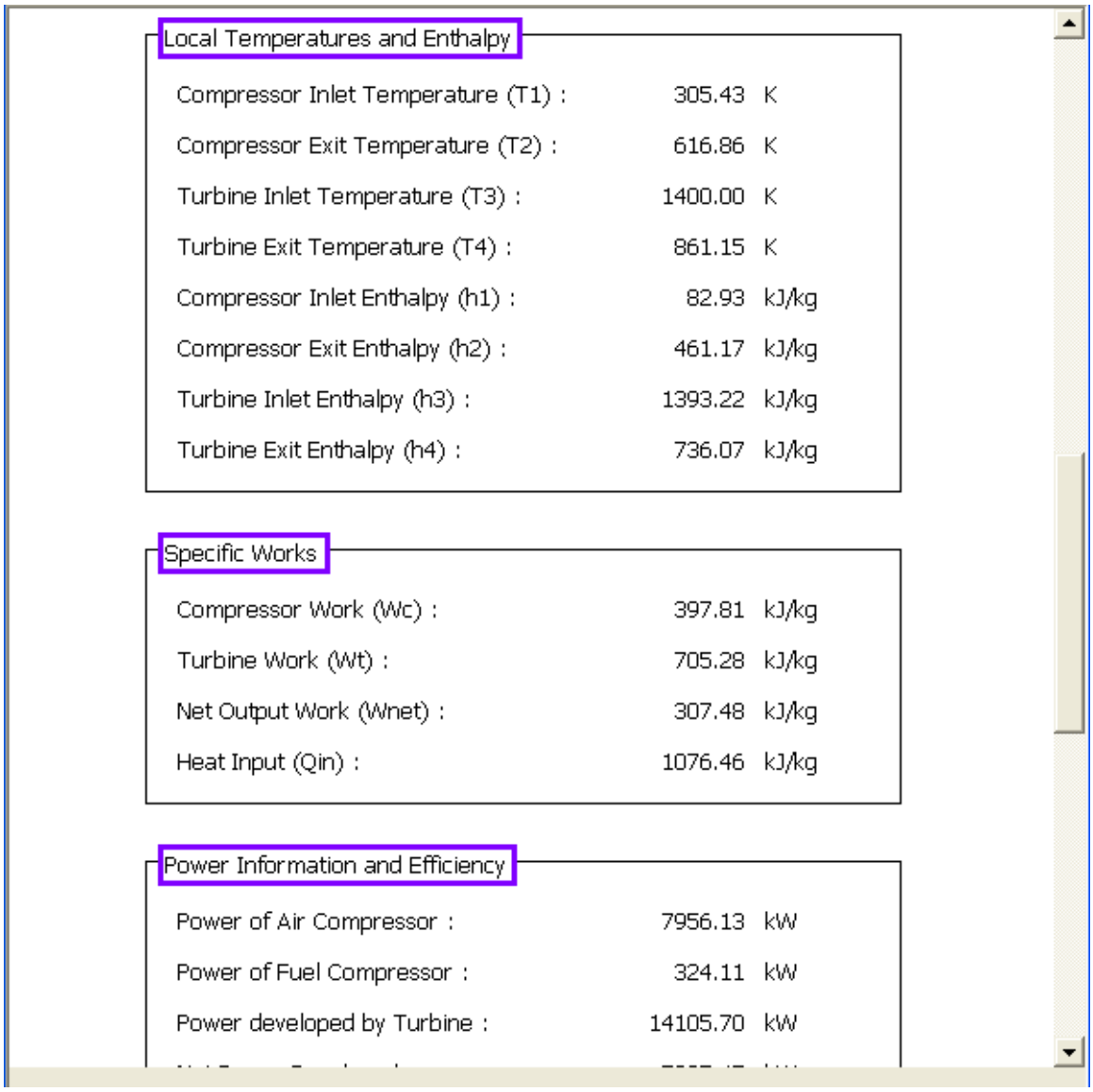

Figure 3.14 Wet compression output (first part)

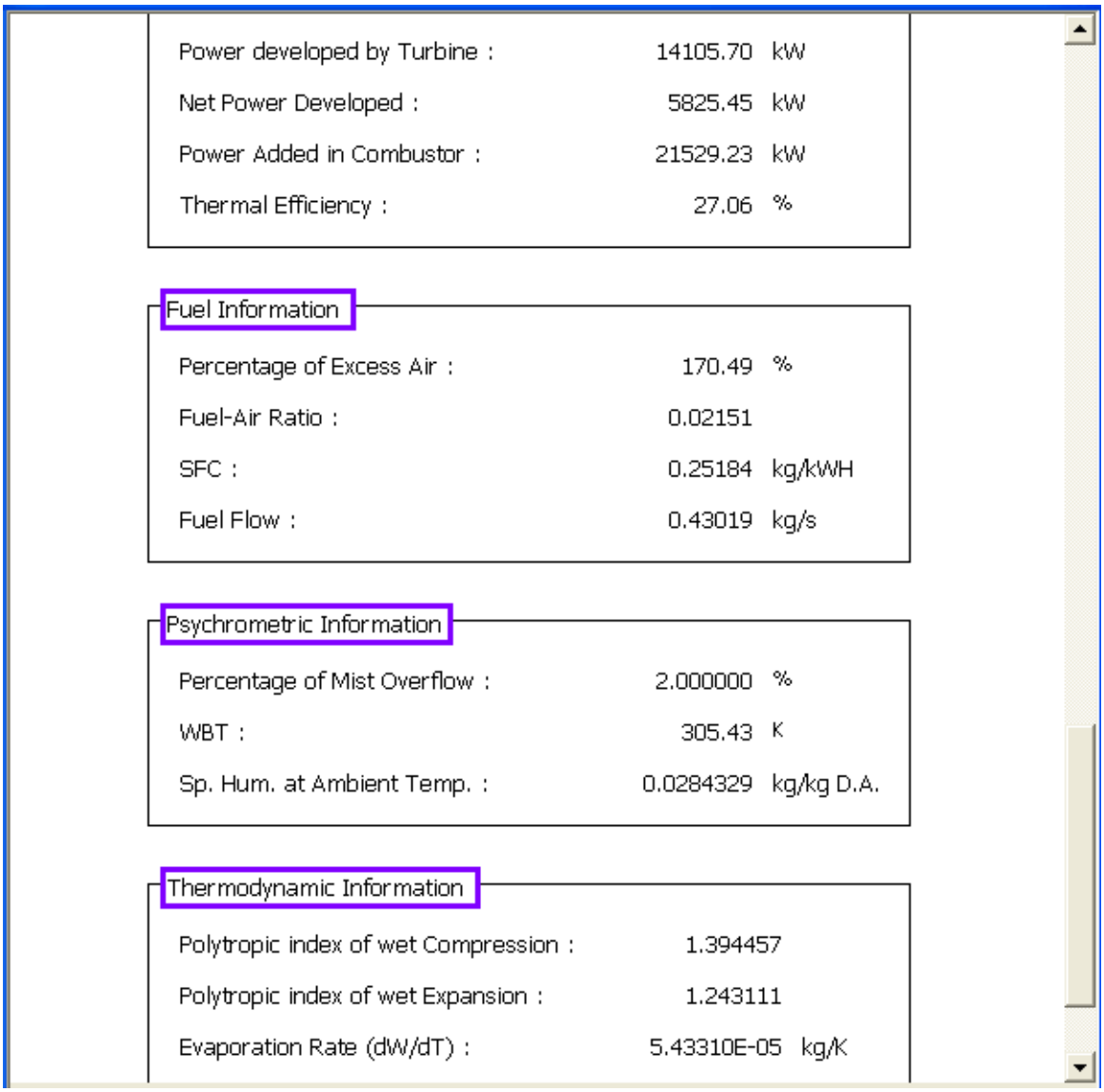

Figure 3.15 Wet compression output (second part)

3.3 Compressor Staging Calculation

The previous section handles the whole compressor as a single unit. This section simulates the compressor stage by stage with the stage-stacking method. Stage-stacking method can be performed by either thermal equilibrium or non-equilibrium method to model the droplet evaporation. Both methods use same window, which can be opened by the seventh button on the switchboard (Fig. 3.1). The **thermally equilibrium method** assumes the air is saturated at the end of each stage as long as sufficient water exists. Different form the equilibrium method, the **non-equilibrium method** calculates the heat and mass transfer between the surrounding air and the droplets to evaluate the transient state of the droplets. If the aerodynamic residence time is shorter than the evaporation residence time, the droplets only evaporate partially and the remaining liquid mass and droplet diameter at the end of the stage are calculated.

3.3.1 Stage-Stacking Scheme

The calculation requires the following inputs for the stage-stacking method; Fig. 3.16 shows the interface of input for the equilibrium method.

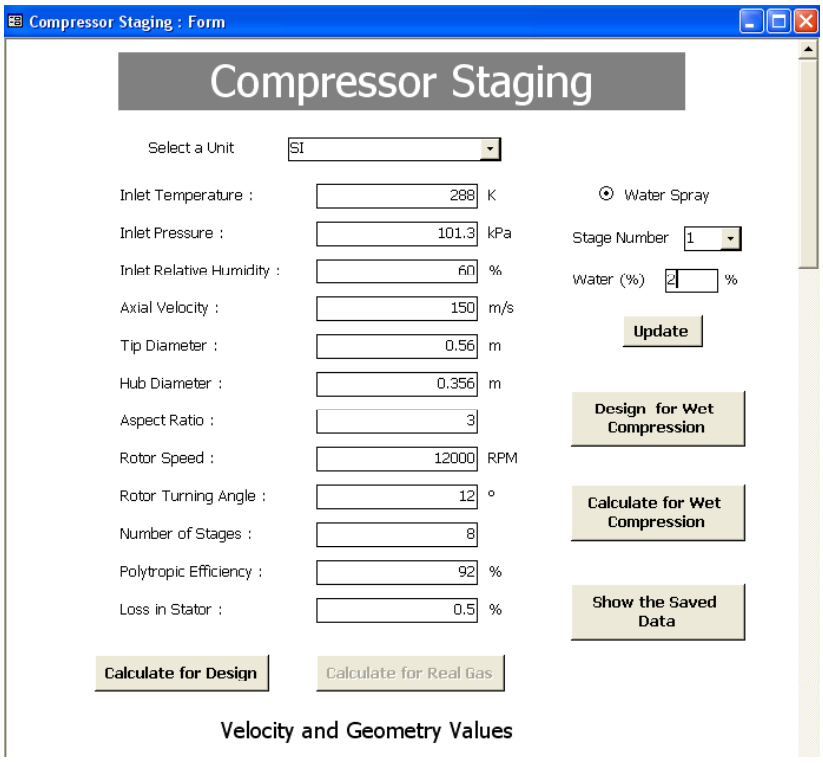

Figure 3.16 Interface for equilibrium stage-stacking input

1. Provide the blade geometry (Tip Diameter – D_t, Hub Diameter – D_h, Hub-tip ratio and Cross-sectional area of flow passage – A).
2. Provide Ambient Temperature (T_{amb}), Pressure ($P_{amb} = P_1$), Relative Humidity (RH), Inlet Axial Velocity (V_{a1}), RPM (N), Water mass flow rate sprayed in each stage (if any) and **in case of non-equilibrium method, Droplet Diameter (d) and Droplet Temperature (T_f).** Fig. 3.17 shows the interface of input for non-equilibrium method with the small input box for the diameter of droplet. The program only accepts one-size of uniform diameter droplets for each input. Non-uniform droplet distributions are not modeled by this program.

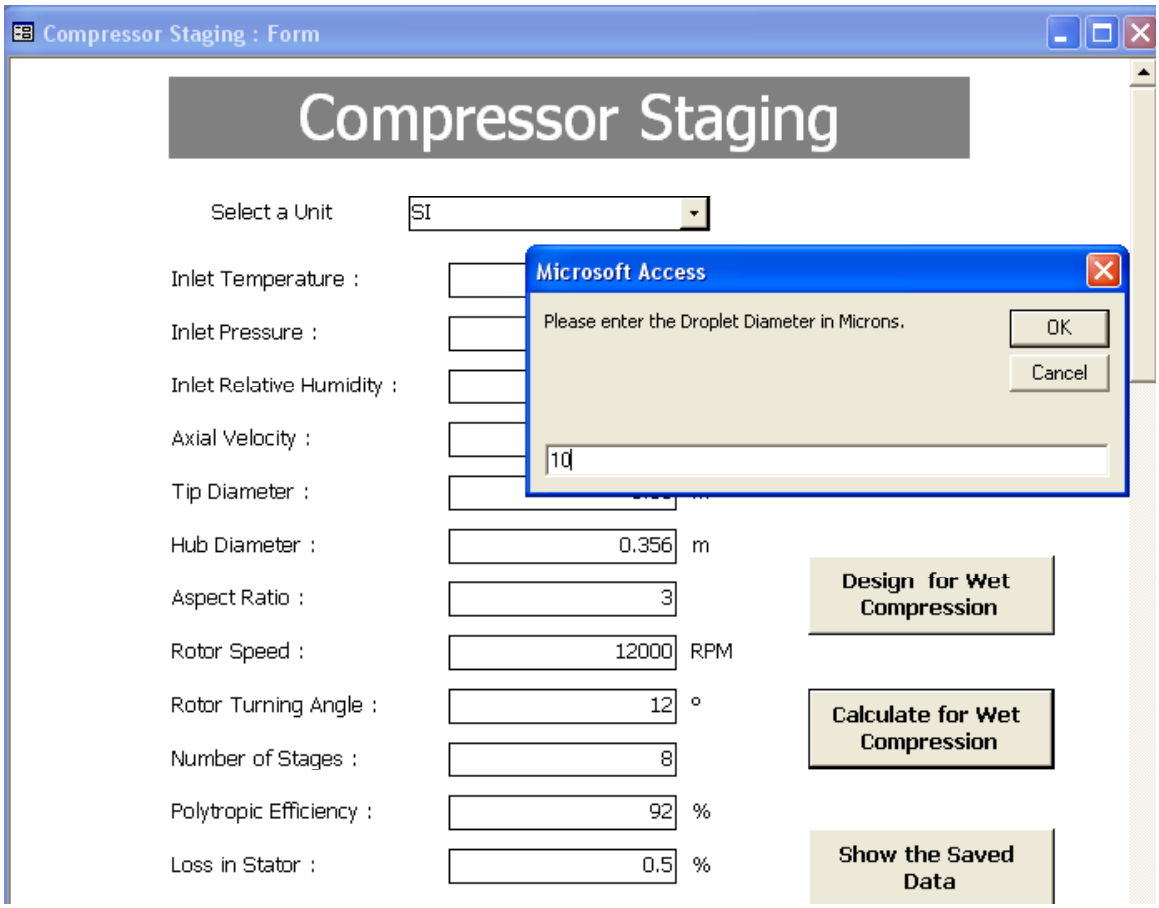

Figure 3.17 Interface for non-equilibrium stage-stacking input

3. Calculate the ambient inlet air psychrometric condition (ω_0, ω_1). In this study ω_0 is defined as the absolute humidity at the ambient inlet condition and ω_1 is defined as the absolute humidity (water vapor content per unit dry air) at the saturation state. If water is sprayed, calculate if saturation is reached before entering the compressor. If saturation is reached, calculate how much water has vaporized and how much water will enter the compressor in the liquid form. On the basis of calculated psychrometric condition, the static temperature at the inlet of the first stage is determined. If air is saturated and/or oversprayed, the temperature is set at the Wet Bulb Temperature (WBT); if air is not saturated, the temperature is calculated using the energy balance of a mixture.
4. Calculate the total amount of water entering into each stage on the basis of upstream condition and the inter-stage spray on each stage.
5. Density (ρ_1) is calculated on the basis of static temperature (T_1) and static pressure (P_1) from Eq. (3.34).

$$\rho_1 = \rho_1(T_1, P_1) = \frac{1 + f_1 + g_1 + s_1}{\frac{1 + g_1}{\rho_m} + f_1 v_1 + s_1 v_s} \tag{3.34}$$

Where,

f_1 = mass fraction of liquid water for P_1 and T_1.

g_1 = mass fraction of water vapor for P_1 and T_1.

v_1 = liquid water specific volume at P_1 and T_1. (From Steam Table)

v_s = Superheated steam specific volume at P_1 & T_1. (From Steam Table)

ρ_m = Mixture density of air and water vapor = $P_1/(R_m T_1)$

R_m = Gas constant for air and water vapor mixture = R_0/M_m.

R_0 = Universal gas constant = 8.314 kJ/kmole.K

M_m = Molecular weight of air and water vapor mixture = $(28.965+18g_1)/(1+g_1)$

f_1 and g_1 are calculated from Psychrometry. For T_1, saturation pressure (P_{sat}) is determined from the steam table. ω_1 is calculated from Eq. (3.35).

$$\omega_1 = \frac{0.622 P_{sat}}{P_1 - P_{sat}} \tag{3.35}$$

If ω_1 is larger than or equal to total amount of water per unit dry air in the current stage, the air will not reach saturation; then,

g_1 = Total amount of water in stage 1, and $f_1 = 0$

otherwise, $g_1 = \omega_1 / (1 +$ Total amount of water in stage 1),

and f_1 = Total amount of water in stage 1 – g_1.

Here, the total amount of water is normalized by dry air mass

If P_{sat} is larger than P_1, the steam is superheated and the entire amount of water is superheated, which means there is no liquid water or saturated steam (i.e. $f_1 = g_1 = 0$).

(Note: f, g and s are denoted for the liquid water mass fraction, water vapor mass fraction and superheated steam mass fraction respectively. f, g and s are used in subscripts to denote the property values for liquid water component, water vapor component and superheated steam component, respectively).

6. Mass flow rate (m_1) is calculated from mass conservation (Eq. 3.36).

$$m_1 = \rho_1 A_1 V_1 \tag{3.36}$$

If the process is equilibrium, steps 7 and 8 are skipped.

7. The inlet condition at the first stage rotor is given as the static condition and the air is assumed to be saturated due to inlet fogging (Fig. 3.18) for both equilibrium and non-equilibrium cases. The droplet diameter is assigned uniformly at the fog sprayer first, and the droplet diameter at the compressor inlet is recalculated based on the amount of water evaporated for achieving saturation by the Eq. (3.37).

$$\frac{f_{inlet}}{f_{fogger}} = \frac{\rho_{inlet} d_{inlet}^3}{\rho_{fogger} d_{fogger}^3} \tag{3.37}$$

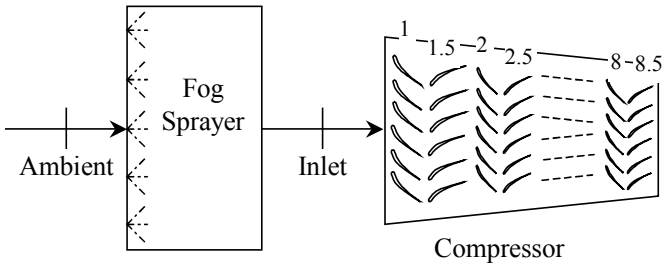

Figure 3.18 Calculation domain including the fog sprayer and 8-stage compressor

due to incompressible nature of water, $\rho_{inlet} \approx \rho_{inlet}$ and droplet at the inlet is assumed to be unchanged until stage 1. Eq. (3.37) can be reduced to eq. (3.38).

$$\frac{f_1}{f_{fogger}} \approx \frac{d_1^3}{d_{fogger}^3} \tag{3.38}$$

Where, f_1 = mass fraction of liquid water at first stage rotor inlet after saturation

f_{fogger} = mass fraction of liquid water at the fogger

d_1 = droplet diameter at first stage rotor inlet after saturation

d_{fogger} = mass of liquid water at the fogger

ρ_1 = water density at first stage rotor inlet

ρ_{fogger} = water density at the fogger $\approx \rho_1$

8. The aerodynamic residence time is calculated from Eq. (3.39).

$$\Delta t_1 = \frac{L_1}{Vel_1} \tag{3.39}$$

Where, L_1 = Chord length at Stage 1 Rotor

Vel_1 = Relative Velocity at Rotor exit (Absolute Velocity is taken for stator)

Evaporation/Boiling time is calculated from Eq. (3.40).

$$\tau_1 = \begin{cases} \dfrac{R\rho_f d_1^2}{8D_1\left(P_1/T_1 - P_{sat}/T_f\right)} & \left[\text{for } P_1 > P_{Sat}, \text{ i.e. evaporation}\right] \\ \dfrac{\rho_f d_1^2 h_{fg}}{\lambda_1\left(1+0.23\sqrt{Re}\right)\left(T_1 - T_f\right)} & \left[\text{for } P_1 < P_{Sat}, \text{ i.e. boiling}\right] \end{cases} \tag{3.40}$$

Where, R = Gas Constant for air = 0.287 kJ/kg.K

ρ_f = water density (kg/m³) at T_1

D_1 = Diffusion Coefficient (m²/s) = 2.26×10^{-5} $(101.325/P_1)$ $(T_1/273.15)$

[Handbook of Chemistry, (1979)]

P_{Sat} = Saturation vapor pressure at T_1 (kPa)

T_f = water temperature (K)

h_{fg} = Latent heat of vaporization at T_1 (kJ/kg)

λ_1 = Thermal Conductivity of air (W/m.K) = $(46.766 + 0.7143T_1)\times10^{-4}$

[Handbook of Chemistry, (1979)]

If the aerodynamic residence time is longer than the evaporation/boiling time, all the water droplets are assumed to be evaporated or boiled; otherwise, the diameter of the droplet in the next stage is calculated by Eq. (3.41).

$$\frac{d_{1.5}}{d_1} = \sqrt{\frac{\Delta t_1}{\tau_1}} \tag{3.41}$$

Once the droplet diameter is calculated in the next stage, the amount of survived liquid water mass can be determined from equation (3.42)

$$\frac{f_{1.5}}{f_1} = \frac{\rho_{1.5} d_{1.5}^3}{\rho_1 d_1^3} \approx \frac{d_{1.5}^3}{d_1^3} \tag{3.42}$$

(assuming $\rho_1 \approx \rho_{1.5}$)

The amount of newly evaporated water vapor is calculated by deducting this remaining amount of water from the amount of water at the stage inlet. If the amount of newly calculated water vapor becomes more than the amount of water needed to saturate the air according to the local temperature and pressure, then the actually evaporated

amount of water vapor is set to be the amount needed for saturation, and the actually remaining liquid water and the droplet diameter are recalculated.

9. The mass flow rate from Eq. (3.36) remains constant throughout the process unless there is any further interstage spray in downstream stage(s). If there is spray in other stage(s), on the basis of amount of water in each stage, flow rate in each stage is updated. (Note, for non-equilibrium method interstage spray is not allowed for calculation, because the model assumes all the droplet with same diameter, whereas insterstage spray introduces different diameter droplets, which cannot be tracked by this program)

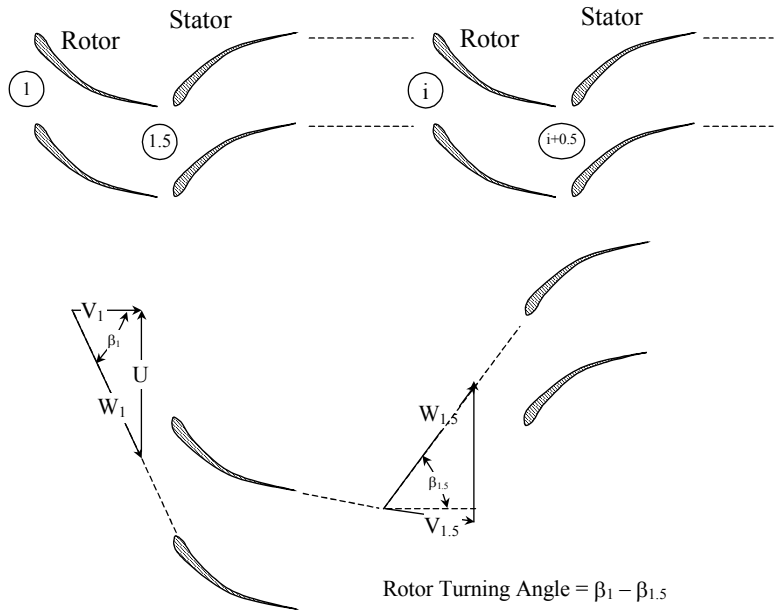

Figure 3.19 Rotor-stator staging

First Stage Rotor Inlet (Stage 1 in Fig. 3.19):

10. Rotor inlet velocity is assumed coming in as a pure axial velocity (i.e. $V_1 = V_{a1}$) without the tangential component. The relative velocity (W_1) is calculated from the velocity diagram (Fig. 3.20) with the known tangential velocity $U = \pi DN/60$. Axial velocity remains the same for the stator (i.e. $V_{a1} = V_{a1.5}$) for the design case, but the axial velocity

changes for off-design cases (such as fogging and wet compression) to satisfy mass conservation and other thermodynamic properties.

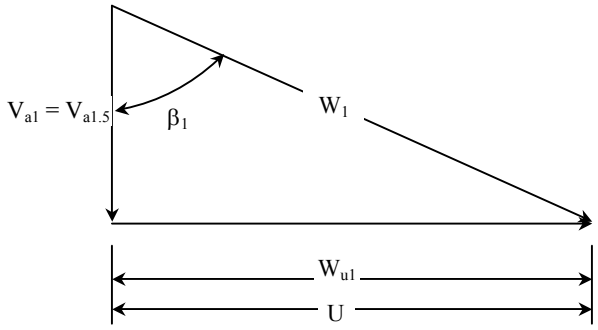

Figure 3.20 Velocity diagram

11. Moist air static enthalpy (h_1) is calculated from Eq. (3.43).

$$h_1 = h_1(T_1, P_1) = \frac{h_{a1} + f_1 h_{f1} + g_1 h_{g1} + s_1 h_{s1}}{1 + f_1 + g_1 + s_1} \tag{3.43}$$

Where,

h_{a1} = dry air enthalpy at T_1. (From air property table)

h_{f1} = liquid water enthalpy at P_1 and T_1. (From the steam table)

h_{g1} = saturated vapor water enthalpy at T_1. (From the steam table)

h_{s1} = superheated steam enthalpy at P_1 and T_1. (From the steam table)

s_1 = mass fraction of superheated steam for P_1 and T_1.

f_1, g_1 and s_1 are calculated from the procedure shown in step 5.

12. The stagnation enthalpy (ho_1) for rotor is calculated from Eq. (3.44).

$$ho_1 = h_1 + \tfrac{1}{2} V_1^2 \tag{3.44}$$

13. The stagnation temperature (To_1) and stagnation pressure (Po_1) for rotor are determined by iteration:

(a) Guess a stagnation temperature (To_1) and calculate the stagnation pressure (Po_1) from Eq. (3.45) using equivalent polytropic index for moist air.

$$\frac{Po_1}{P_1} = \left(\frac{To_1}{T_1}\right)^{\frac{\gamma}{\gamma-1}} \tag{3.45}$$

(b) Determine the stagnation enthalpies of all phases with guessed stagnation temperature (To_1) and stagnation pressure (Po_1). Moist air stagnation enthalpy (ho_1) is calculated from Eq. (3.46).

$$ho_1 = ho_1(To_1, Po_1) = \frac{h_{a1} + f_1 ho_{f1} + g_1 ho_{g1} + s_1 ho_{s1}}{1 + f_1 + g_1 + s_1} \tag{3.46}$$

f_1, g_1 & s_1 are calculated from the procedure shown in step 5.

(c) Determine the moist air stagnation enthalpy from Eq. (3.46) and compare it with the calculated stagnation enthalpy from Eq. (3.44). Repeat step (a) to (c) until convergence.

First Stage Rotor Exit or Stator Inlet (Stage 1.5 in Fig. 3.19):

14. Determine the relative velocity angle ($\beta_{1.5}$) from β_1 and rotor turning angle (θ) with Eq. (3.47) by assuming the velocity follows the rotor surface contour and exits the rotor without deviating from the tangent of the camber line (i.e. the flow angles are the same as camber angles). The rotor turning angle (i.e. camber angle), θ, is known from the design blade geometry.

$$\beta_{1.5} = \beta_1 + \theta \tag{3.47}$$

15. Axial velocity ($Va_{1.5}$) at rotor exit is determined by iteration:

(a) Guess a rotor exit velocity ($Va_{1.5}$).

(b) Determine the other velocity components at the rotor exit from the tentative velocity diagram (Fig. 3.21)

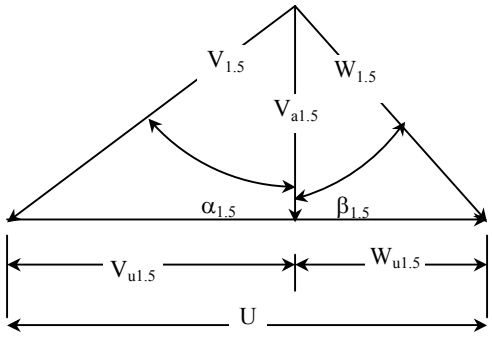

Figure 3.21 Velocity diagram at rotor exit

(c) The specific isentropic work imposed on the rotor is calculated from:

$$\text{Work}_s = U(Vu_1 - Vu_{1.5}) \tag{3.48}$$

Since the flow is assumed to turn exactly the same angle as the camber turning angle, the work produced is therefore the ideal (isentropic) work. Because in the real process, the friction in the boundary layer or secondary flow will affect the flow angle and requires more compressor work. The flow will leave the trailing edge with a deviation angle.

(d) Determine the stagnation enthalpy at rotor exit as:

$$ho_{1.5} = ho_1 - \text{Work}_s/\eta_s \tag{3.49}$$

where, η_s is the stage isentropic efficiency or polytropic efficiency.

(e) The stagnation temperature ($To_{1.5}$) and the stagnation pressure ($Po_{1.5}$) at rotor exit is determined by iteration:

(i) Guess a stagnation temperature ($To_{1.5}$) and calculate stagnation pressure ($Po_{1.5}$) from:

$$\frac{Po_{1.5}}{Po_1} = \left(\frac{To_{1.5}}{To_1}\right)^{\frac{k\eta_s}{(k-1)}} \tag{3.50}$$

Note that stage isentropic efficiency, η_s, is used here instead of small-stage efficiency, η_p, because the calculation is cross over the entire stage instead of an infinitesimal small element.

(ii) Determine the stagnation enthalpies of all phases with the guessed temperature ($To_{1.5}$) and the calculated stagnation pressure ($Po_{1.5}$) from Eq. (3.50). Moist air stagnation enthalpy ($ho_{1.5}$) is calculated from Eq. (3.46) by changing the subscript from 1 to 1.5.

(f) Calculate the static enthalpy ($h_{1.5}$) from Eq. (3.51).

$$h_{1.5} = ho_{1.5} - \tfrac{1}{2} V_{1.5}^2 \tag{3.51}$$

(g) Determine the rotor exit static temperature ($T_{1.5}$) and static pressure ($P_{1.5}$) by iteration:

(i) Guess a static temperature and calculate static pressure by Eq. (3.45) by changing the subscripts from 1 to 1.5.

(ii) Determine enthalpies of all phases with guessed temperature ($T_{1.5}$) and the calculated static pressure ($P_{1.5}$) from Eq. (3.45). Moist air static enthalpy ($h_{1.5}$) is calculated from Eq. (3.43) by changing subscripts from 1 to 1.5.

(iii) Calculate the moist air static enthalpy from Eq. (3.43) and compare it with calculated static enthalpy from Eq. (3.51). Repeat step (i) to (ii) until convergence.

(j) Density ($\rho_{1.5}$) is calculated from Eq. (3.34) on the basis of static temperature ($T_{1.5}$) and static pressure ($P_{1.5}$) shown in step 5.

(k) Calculate the mass flow rate from Eq. (3.52).

$$m_{1.5} = \rho_{1.5} A_{1.5} V_{1.5} \tag{3.52}$$

(l) Compare the mass flow rate from Eq. (3.52) with that from Eq. (3.36) of step 6 and repeat step (a) to (k) until convergence.

16. Determine the other velocity component at rotor exit from the velocity diagram (Fig. 3.21)

17. Torque, power and work are calculated from Eqs. (3.53), (3.54) & (3.48).

$$\text{Torque}_1 = \dot{m} \frac{D}{2} \left(Vu_1 - Vu_{1.5} \right) \tag{3.53}$$

$$\text{Power}_1 = \text{Torque} \times \frac{2\pi N}{60} \tag{3.54}$$

18. Determine the stagnation enthalpy at rotor exit from Eq. (3.49).

19. At this point, although the stagnation temperature ($To_{1.5}$) and stagnation pressure ($Po_{1.5}$) at the rotor exit has been calculated in step 15(e), they need to be updated with correct

axial velocity obtained by Eq. (3.52) in step 15(k). Therefore, the stagnation temperature ($To_{1.5}$) and stagnation pressure ($Po_{1.5}$) at rotor exit needs to be determined again by iteration:

(a) Guess a stagnation temperature ($To_{1.5}$) and calculate stagnation pressure ($Po_{1.5}$) from Eq. (3.45) by changing subscripts from 1 to 1.5.

(b) Determine the stagnation enthalpies of all phases with guessed temperature ($To_{1.5}$) and the calculated stagnation pressure ($Po_{1.5}$) from step (a). Moist air stagnation enthalpy ($ho_{1.5}$) is calculated from Eq. (3.46) by changing subscripts from 1 to 1.5.

(c) Compare the stagnation enthalpy from step 19(b) with calculated stagnation enthalpy from step 18 and repeat step (a) to (c) until convergence.

20. Calculate the static enthalpy ($h_{1.5}$) at rotor exit from Eq. (3.51).

21. Determine the static temperature ($T_{1.5}$) and static pressure ($P_{1.5}$) at rotor exit by iteration:

(a) Guess a static temperature and calculate static pressure by Eq. (3.45) by changing subscripts from 1 to 1.5.

(b) Determine static enthalpies of all phases with guessed temperature ($T_{1.5}$) and calculated static pressure ($P_{1.5}$). Moist air static enthalpy ($h_{1.5}$) is calculated from Eq. (3.43) by changing subscripts from 1 to 1.5.

(c) Compare the moist air static enthalpy from step 21(b) with the calculated enthalpy from step 20 and repeat step (a) to (b) until convergence.

22. Density ($\rho_{1.5}$) is calculated on the basis of static temperature ($T_{1.5}$) and static pressure ($P_{1.5}$) from equation shown in step 5.

If the process is equilibrium, skip steps 23 and 24 .

23. Calculate the droplet temperature from Eq. (3.55)

$$f_l Cp_f \frac{T_{f_{1.5}} - T_{f_1}}{\Delta t_1} = H_1 A\left(T_{1.5} - T_{f_1}\right) \tag{3.55}$$

Where,

Cp_f = Specific Heat of Water (4.2 kJ/kg.K)

T_{f1} = Droplet temperature (K) at stage 1

$T_{f1.5}$ = Droplet temperature (K) at stage 1.5

A = Surface area = $\pi d_1^2 = \frac{\frac{1}{6}\pi d_1^3 \rho_1}{\frac{1}{6}\rho_1 d_1} = \frac{6f_1}{\rho_1 d_1}$

H_1 = Heat transfer coefficient, which is formulated with Nusselt number as,

$Nu_1 = 2 + 0.6\,Re_1^{0.5}\,Pr_1^{0.33}$

Re_d = Droplet Reynolds Number = $\frac{\rho_1 V_{slip} d_1}{\mu_1}$

V_{slip} = Slip velocity [which is 10% of local velocity according to Khan and Wang (2008)]

[The local velocity is the inlet absolute velocity for stator stages and inlet relative velocity of rotor stages]

μ_1 = Dynamic Viscosity of air (Pa.s) = $(0.004823\ T_1 + 0.3976) \times 10^{-5}$

[Handbook of Chemistry]

Pr_1 = Prandtl Number = $\frac{\mu_1 \rho_1}{D_1}$

24. Repeat step 8 to find the diameter of droplet and maximum possible amount of liquid water in the second stage by changing the indices from 1 to 1.5 and 1.5 to 2.

<u>Other Stage Rotor Inlet (Stage i in Fig. 3.19) with inter-stage fogging:</u>

25. If water is sprayed at the previous stator stage (Stage i-0.5), calculate if saturation is reached before exiting the previous stator stage. If saturation is reached, calculate how much water vaporizes, and how much water will enter the compressor in the liquid form. Calculate air psychrometric condition (ω_0, ω_1) at the rotor inlet (Stage i). On the basis of calculated psychrometric condition, the static temperature at the stage i rotor inlet is determined. If air is saturated and/or evaporated, the temperature is set at WBT; if air is not saturated, the temperature is calculated using the energy balance of a mixture.

26. Update the mass fractions of all components f_i, g_i and s_i.

27. Since no heat or frictional loss are assumed over the stator stage, at the inlet or rotor stage i, the stagnation pressure ($Po_i = Po_{i-0.5}$), stagnation enthalpy ($ho_i = ho_{i-0.5}$) and inlet velocity angle ($\alpha_i = \alpha_{i-0.5}$ – stator turning angle) are calculated from the previous stator

inlet. When a loss in stator is assigned at the input, stagnation pressure is calculated on that basis.

28. Static temperature, static pressure and inlet velocity and axial velocity at rotor inlet are iterated:

    (a) Guess a static temperature (T_i) and calculate static pressure (P_i) by Eq. (3.45) by changing subscripts from 1 to i.

    (b) Determine the static enthalpies of all phases with guessed temperature (T_i) and the calculated static pressure (P_i) from Eq. (3.45). Moist air static enthalpy (h_i) is calculated from Eq. (3.43) by changing subscripts from 1 to i.

    (c) Density (ρ_i) is calculated on the basis of static temperature (T_i) and static pressure (P_i) from Eq. (3.34) shown in step 5.

    (d) Calculate the rotor inlet velocity (V_i) from Eq. (3.56).

$$h_i = ho_i - \tfrac{1}{2} V_i^2 \tag{3.56}$$

    (e) Calculate the axial velocity (Va_i) from Eq. (3.57).

$$Va_i = V_i \mathrm{Cos}(\alpha_i) \tag{3.57}$$

    (f) Find the flow rate (m_i) from Eq. (3.58).

$$\dot{m}_i = \rho_i A_i Va_i \tag{3.58}$$

    Compare this value with the flow rate calculated from Eq. (3.36) and repeat step (a) to (f) until convergence.

29. Determine the other velocity components at rotor inlet from the velocity diagram Fig. 3.22. Find the static enthalpy from Eq. (3.43) by changing subscripts from 1 to i.

30. Density (ρ_i) is calculated on the basis of static temperature (T_i) and static pressure (P_i) from Eq. (3.34) as shown in step 5.

31. Find the other velocities for the stator from the velocity diagram (Fig. 3.22)

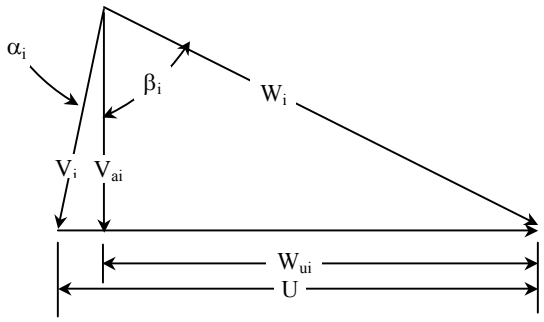

Figure 3.22 Velocity diagram

If the process is equilibrium, skip steps 32 and 33.

32. Repeat step 23 to find droplet temperature in i-th stage by changing indices 1 to i-0.5 and 1.5 to i.

33. Repeat step 8 to find the diameter of droplet and maximum possible amount of liquid water in the next stage by changing the indices from 1 to i and 1.5 to i+0.5.

Other Stage Rotor Exit or Stator Inlet (Stage i+0.5 in Fig. 3.19) including inter-stage fogging :

Repeat step 14-24.

Figure 3.23 shows a part of output for equilibrium stage-stacking method.

Velocity and Geometry Values

Stage #	U (m/s)	V (m/s)	Va (m/s)	Vu (m/s)	ß (°)	W (m/s)	Wu (m/s)	α (°)	Φ
1	152.68	90	90	0	-59.48	177.23	-152.68	0	0.589
1.5	0	130.11	95.03	88.86	-33.88	114.47	-63.82	43.08	0.622
2	152.68	99.6	97.72	-3.94	-58.04	184.61	-156.63	-2.31	0.64
2.5	0	135.14	103.49	86.91	-32.44	122.62	-65.78	40.02	0.678
3	0	0	0	0	0	0	0	0	0

Other Important Values

Stage #	Total Pressure (kPa)	Absolute Pressure (kPa)	Total Temp (K)	Absolute Temp (K)	Blade Height (m)	Absolute Mach #	Relative Mach #	Hub-Tip Ratio	Chord Leng. (m)
1	101.7	96.77	297.98	294.09	0.09	0.262	0.516	0.8	0.03
1.5	105.87	100.62	301.45	297.42	0.0832	0.376	0.331	0.8136	0.027743
2	105.85	101.94	301.43	298.44	0.0802	0.287	0.532	0.8196	0.026759
2.5	116.28	105.09	309.69	301.51	0.0746	0.387	0.351	0.8312	0.024878
3	116.23	0	0	0	0	0	0	0	0

Figure 3.23 Equilibrium stage-stacking output

Figure 3.24 shows a part of output for stage-stacking method with different non-equilibrium data (e.g. droplet temperature, droplet density, residence time, evaporation time etc.).

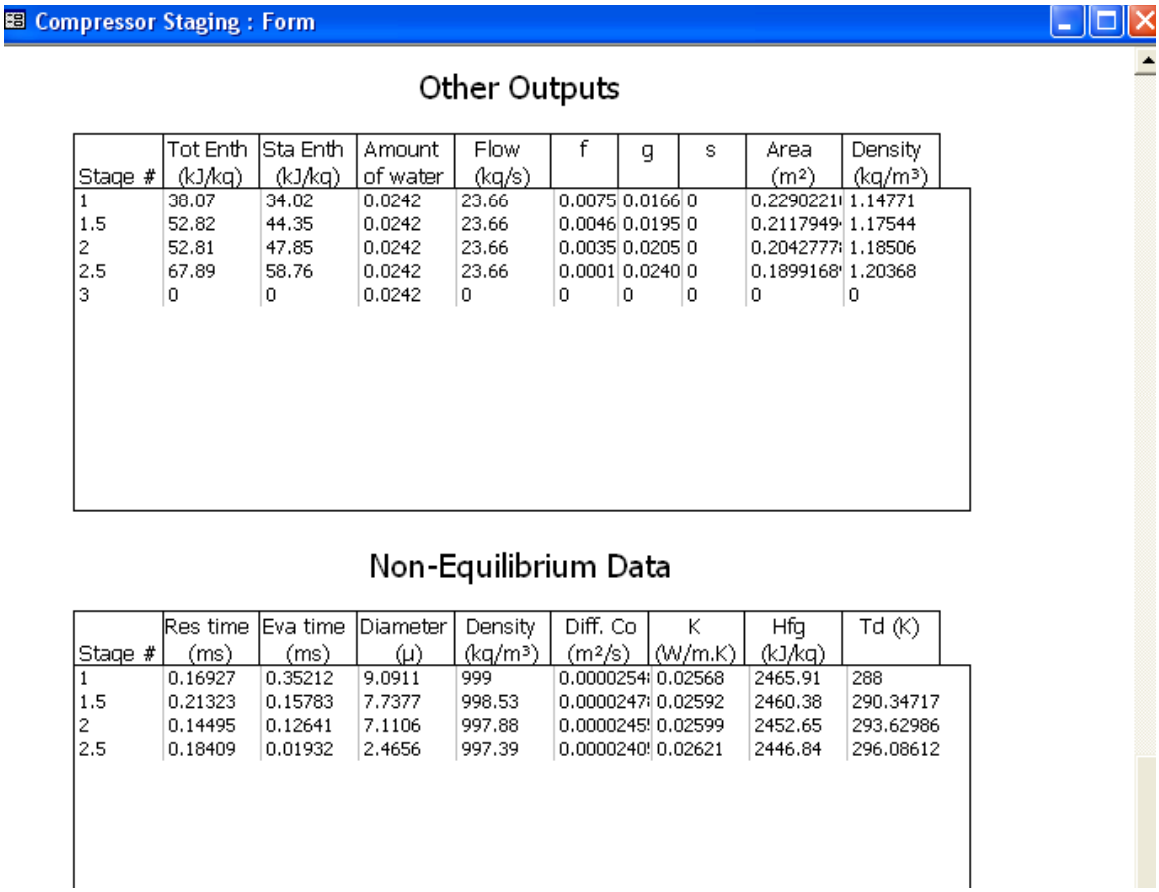

Figure 3.24 Interface for non-equilibrium stage-stacking output

Figure 3.25 shows the Flow diagram of the algorithm for the equilibrium method.

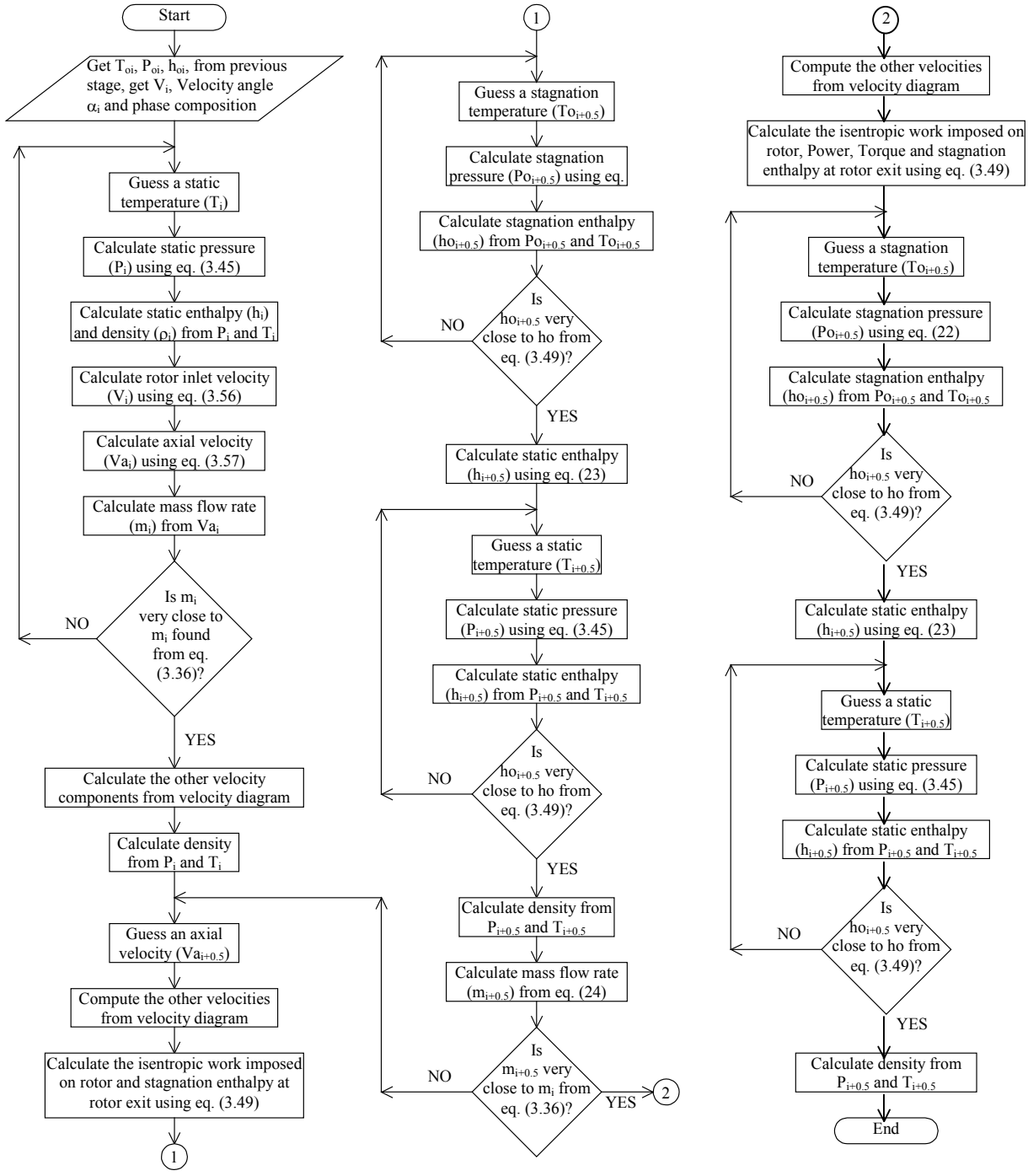

Figure 3.25 Flow diagram of the algorithm for the equilibrium method

CHAPTER FOUR
RESULTS AND DISCUSSIONS OF THERMODYNAMIC ANALYSIS

The computer program FogGT was ran for the Gas Turbine system first, where the compressor, combustion chamber, turbine and fuel compressor are considered as a single unit each.

4.1 Gas Turbine System with Fog Cooling for Burning Low Calorific Value Fuels

All the cases in the first batch are calculated by keeping the values of the following parameter fixed: compression ratio (12), TIT (1400K), air mass flow rate (20Kg/s), inlet pressure (1atm), compressor isentropic efficiency (88% for both the main and the fuel compressors), and turbine isentropic efficiency (88%). Methane is used as the fuel for the reference case. Two different LCV fuels are used, and the performances are compared with the reference case. Four different ambient conditions are considered: low temperature low humidity (ISO condition, 288.2K and 60% Rh), low temperature high humidity (288.2K and 90% Rh), high temperature low humidity (313K and 60% Rh), and high temperature high humidity (313K and 90% Rh). Although the condition of 313K (40°C) and 90% Rh is extremely rare to occur, it presents an upper limit of the hot-and-humid condition that shows the minimum augmentation fog/overspray can achieve at a hot environment. These ambient conditions are also applied as the inlet condition for the fuel compressor. Although the fuel is usually preheated in practice, the heating energy is also paid by some means. Therefore, using the ambient condition as the fuel compressor inlet condition implicitly include all the energy required to compress the fuel to 25% above the pressure in the combustor.

Four different fog cooling are analyzed including moist compression (unsaturated air), compression with saturated air, 1% overspray and 2% overspray. More than 2% overspray is not recommended (Yap and Wang, 2007). The results of the first batch are shown in Table 4.2.

The computations were performed by implicitly assuming that each case is matched with a gas turbine that is specifically designed to meet the specifications of air mass flow rate, fuel flow rate, pressure ratio, and TIT. This means that the sizes of the compressor, turbine, and combustor, will be different from case to case if the same operating considerations are imposed such as the surge margin of the compressor, the inlet guide vane angle, the component efficiency

of compressor, turbine, and combustion chamber, the stagnation pressure losses, and the blade cooling air, etc.

In the second batch (see Table 4.2), the TIT for the cases of burning LCV fuels is reduced to match the net power output of NG fueled GT. With reduced TIT, the fuel flow rate is reduced and the size of the gas turbine will become comparable to the NG fueled GT, so only modest modification of the NG-fired GT is needed to burn the LCV fuels.

4.1.1 Heat Input from Natural Gas and Low Calorific Value (LCV) Fuels

Natural gas and two LCV fuels derived from biomass gasification are used in this study. LCV1 is identical with LCV2 but is diluted with nitrogen. The compositions of the LCV fuels are given in Table 4.1.

Table 4.1 Studied LCV fuels

Compound	LCV1 Vol(%)	LCV2 Vol(%)	NG Vol(%)
Methane (CH_4)	7.00	11.15	100
Ethane (C_2H_6)	0.08	0.13	
Ethylene (C_2H_4)	0.11	0.18	
Benzene (C_6H_6)	0.14	0.22	
Carbon-Dioxide (CO_2)	14.60	23.2	
Carbon-Monoxide (CO)	10.60	16.8	
Hydrogen (H_2)	7.30	11.62	
Oxygen (O_2)	0.05	0.08	
Water Vapor (H_2O)	22.92	36.62	
Nitrogen (N_2)	37.20	0	
Total	100.00	100.00	100.00
Low Heating Value (KJ/Kg)	4,358	7,405	50,046

The heat input obtained from chemical reaction of the fuel with excess air can be obtained by the following equation from Bathie (1998) using LCV-1 fuel as an example:

$$n_{H_2}H_2 + n_{O_2}O_2 + n_{H_2O}H_2O + n_{CO}CO + n_{CO_2}CO_2 + n_{CH_4}CH_4 + n_{C_2H_6}C_2H_6 + n_{C_2H_4}C_2H_4$$
$$+ n_{C_6H_6}C_6H_6 + X\ \text{D.A.} + x\ H_2O$$
$$\rightarrow \left(n_{CO} + n_{CO_2} + n_{CH_4} + 2n_{C_2H_6} + 2n_{C_2H_4} + 6n_{C_6H_6}\right)CO_2 + \left(n_{H_2} + n_{H_2O} + 2n_{CH_4} + 3n_{C_2H_6}\right.$$

$$+2n_{C_2H_4}+3n_{C_6H_6}+x\Big)H_2O+X\ \text{D.A.}-\Big(\tfrac{1}{2}n_{H_2}-n_{O_2}+\tfrac{1}{2}n_{CO}+3n_{CH_4}+3\tfrac{1}{2}n_{C_2H_6}$$
$$+3n_{C_2H_4}+7\tfrac{1}{2}n_{C_6H_6}\Big)O_2 \qquad (4.1)$$

where D.A. is the Dry Air (O_2 +3.768 N_2).

By equating the enthalpy of reaction on both sides, the value of X (the mole of Dry Air) can be obtained. The mole of moisture (x) can be calculated from the psychrometric chart. The mole numbers of all the reactants are basically the volumetric percentage of the gases.
The enthalpy of the reactants is,

$$H_{Re}=\sum\left(n_i\,\bar{h}_{i,T_2}\right) \qquad (4.2)$$

The enthalpy of the products is,

$$H_{Pr}=\sum\left(n_i\,\bar{h}_{i,T_3}\right) \qquad (4.3)$$

From the value of X, the excess air percentage and fuel-air ratio (f') can be calculated. Hence, the heat addition into the combustion chamber can be obtained as:

$q_{in} = f'(LHV)$ (4.4)

and the thermal efficiency is obtained as,

$$\eta_{th}=\frac{w_{Net}}{q_{in}}\ \text{(independent of mass flow rate)} \qquad (4.5)$$

4.1.2 Fog/Overspray Effect on Compressor

Figures 4.1 and 4.2 show the compressor discharge temperature and compressor power under four different ambient conditions, respectively. In both figures, a vertical saturation line is drawn to clearly separate underspray from overspray regions. Figure 4.1 shows that the compressor discharge temperature decreases with an increase of water spray but with a decrease of ambient temperature or humidity. Increasing ambient relative humidity allows less water spray to achieve saturation, so the compressor discharge temperature increases. Figure 4.2 shows

the compressor power increases with an increase of ambient temperature or humidity, but decreases with the increase of water spray due to increased air density as previously explained in the theory.

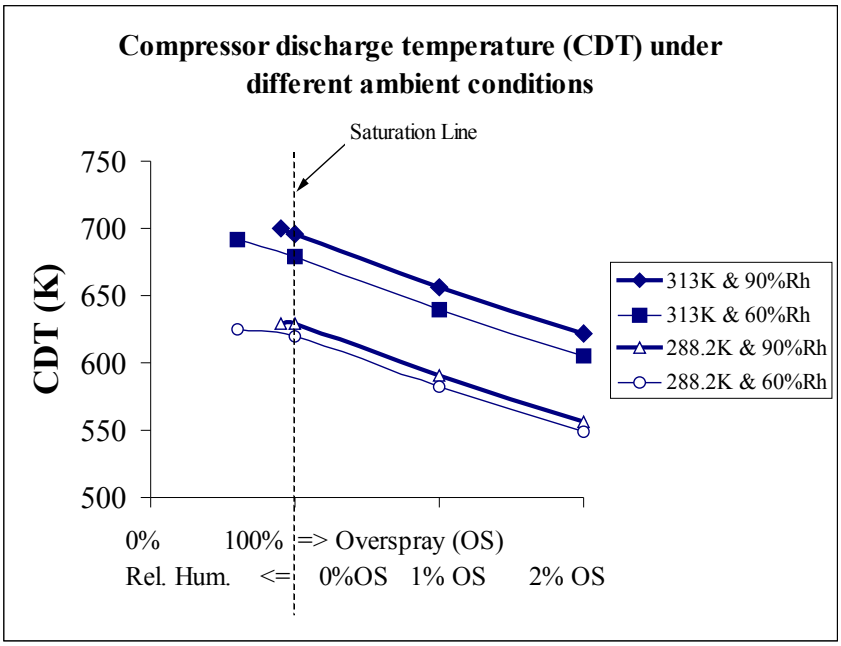

Figure 4.1 Compressor discharge temperatures under different ambient conditions

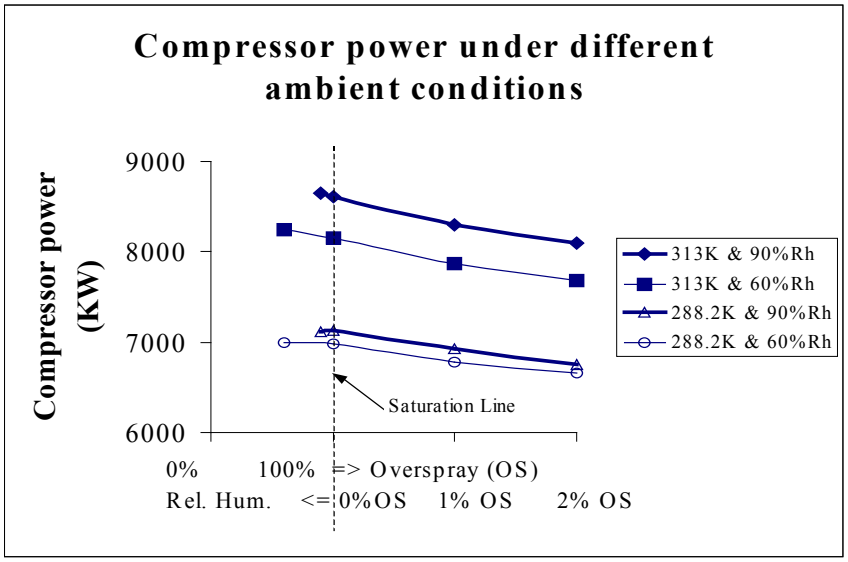

Figure 4.2 Compressor power under different ambient conditions

4.1.3 Fog/Overspray Effect on Fuel Compressor

Figure 4.3 shows the fuel compressor work using both NG and LCV fuels. Fuel compressor work is significant for LCV fuels. As these fuels have less heating values, more mass flow rates are needed to achieve the required heat input in the combustion chamber. When natural gas is used, fuel compressor consumes about 4% of the main air compressor power (about 2% of the gross power produced by the turbine). The effect of fog/overspray is negligible on fuel compressor power in NG fired GT, as shown by overlapped curves in Fig. 4.3. The fuel compressor power increases to 20-40% of the main air compressor power (or 10-16% of the gross turbine power) when LCV-2 and LCV-1 fuels are burned respectively.

Figure 4.3 also shows that the fuel compressor power increases with the increase of overspray percentage because more overspray requires more fuel (see Fig. 4.4) to achieve the TIT value at 1400K. This is contrary to the descending power consumption trend of the main air compressor when overspray is increased in Fig. 4.2. Effect of ambient temperature and relative humidity on the required fuel compressor power is not significant because the ambient pressure does not change. The only change takes place due to the ambient condition is air density, which is considered in Eq. (2.22). The effect of fuel heating value is predominant.

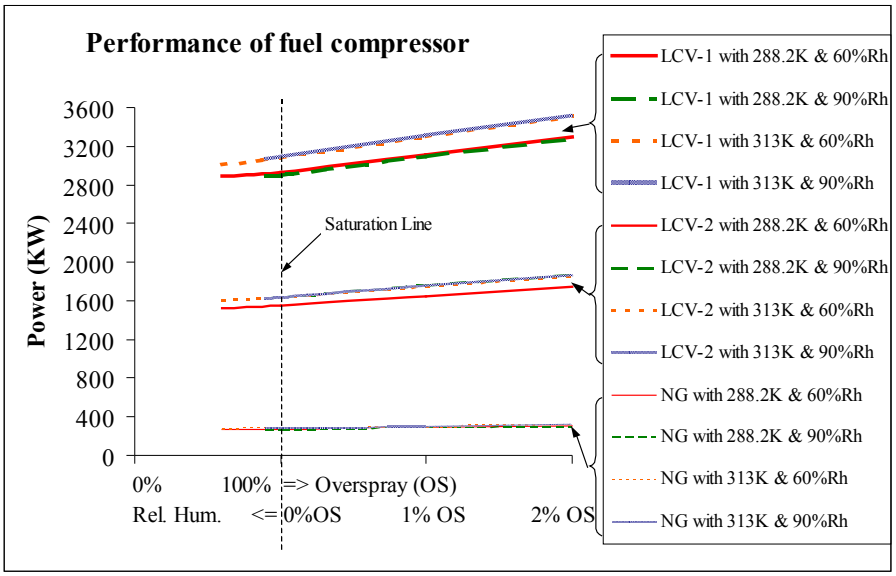

Figure 4.3 Fuel compressor power under different ambient conditions

As more mass flow rate of LCV fuels are needed to provide sufficient energy as in the NG cases, additional energy is needed to heat up the inert gases in the LCV fuels as shown in Figure 4.5. The heating value of LCV-1 fuel is less than one tenth of the natural gas, and the required fuel mass flow rate is about 17 times more than NG to achieve TIT = 1400K. The heating value of LCV-2 fuel is about one seventh of the NG and the required fuel mass flow rate is about 8 times more than NG to achieve required TIT.

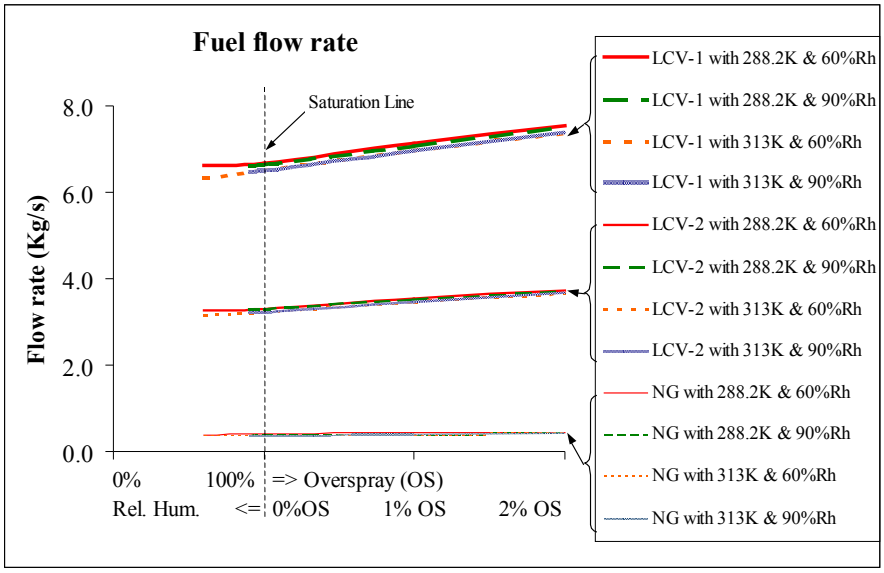

Figure 4.4 Fuel mass flow rate under different ambient conditions for various fuels

4.1.4 Fog/Overspray Effect on Combustor

Figure 4.5 shows that the heat added into the combustion chamber from LCV-1 and LCV-2 fuels is 46% and 23% more than NG, respectively. As heating value decreases for LCV fuels, there are more non-combustible gases in the fuel to absorb the energy and suppress the combustion temperature, so more heat addition is required to allow the combusted gas to reach the desired TIT. LCV-1 consists of 37% N_2, 23% water vapor and 11% CO_2, and LCV-2 consists of 37% water vapor and 17% CO_2, which are all non-combustible gases. When the overspray percentage is increased, more non-combustible water vapor is in the combustion gas to absorb heat, so the required heat addition is further increased as overspray ratio increases (see Fig. 4.5).

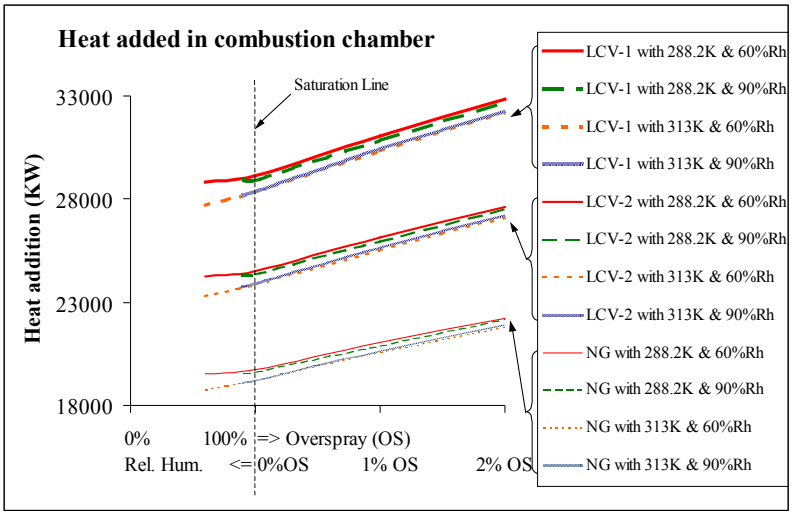

Figure 4.5 Heat added in the combustor under different ambient conditions

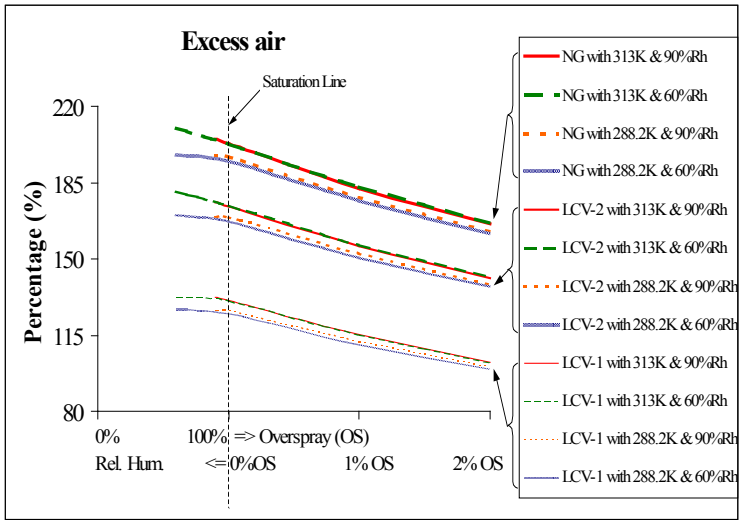

Figure 4.6 Percentage of excess air under different ambient conditions

Heat addition is not very much affected by the ambient condition; lower ambient temperature obviously requires more heat addition. Excess air reduces as overspray increases (Fig. 4.6) due to increased water vapor acting as a temperature-suppressing diluent.

4.1.5 Fog/Overspray Effect on Turbine

Figure 4.7 shows turbine gross power increases up to 30% for using LCV-1 fuel and up to 15% for using LCV-2 fuel from the NG fueled output because fuel mass flow rates are significantly increased for using LCV fuels. Notice again, as previously discussed, the LCV fired

GT size will be different from the NG-fired GT if the same operating condition (surge margin, stagnation pressure loss, etc.) and component efficiencies are imposed. The gross turbine power also increases as the overspray percentage increases. For example, an overspray of 2% increases turbine power up to 4% for natural gas and 6% for using LCV fuels.

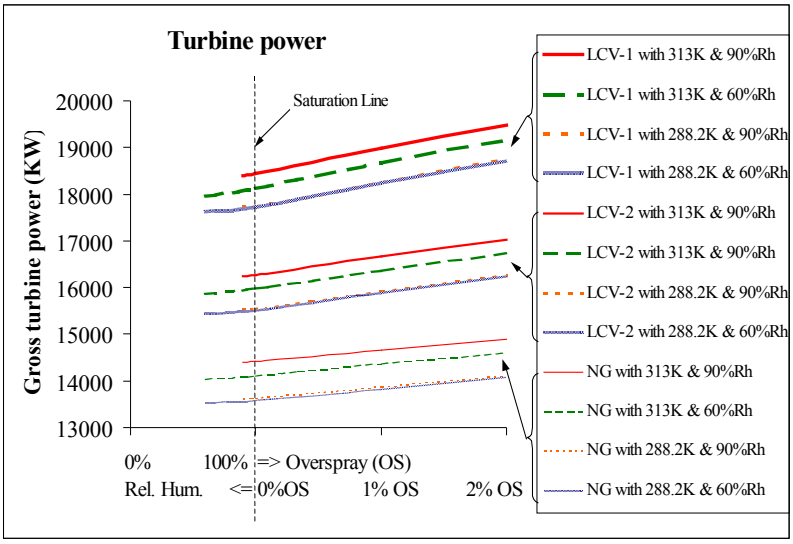

Figure 4.7 Gross turbine power under different ambient conditions

The net output power is calculated by deducting the air compressor power and fuel compressor power from the gross turbine power. Figure 4.8 shows that LCV fuels produce more net output power than natural gas even though LCV fuels significantly increases fuel compressor power 3.8 times for using LCV-1 and 6 times for using LCV-2 (see Fig. 7). When LCV fuels are burned, fog/overspray cooling seems as effective in achieving net power enhancement as when natural gas is burned. With saturated fogging, the net output power increases approximately 1-2%. With 2% of overspray, the net output power increases as high as 20%. As the ambient temperature increases, the net output power decreases; likewise increase of relative humidity lowers the net output power but with less impact than from the increased ambient temperature. Judging from the slopes of the curves in Fig. 4.8, rate of increase of net output power for overspray is higher for higher temperature and higher humidity when either NG or LCV fuels are burned.

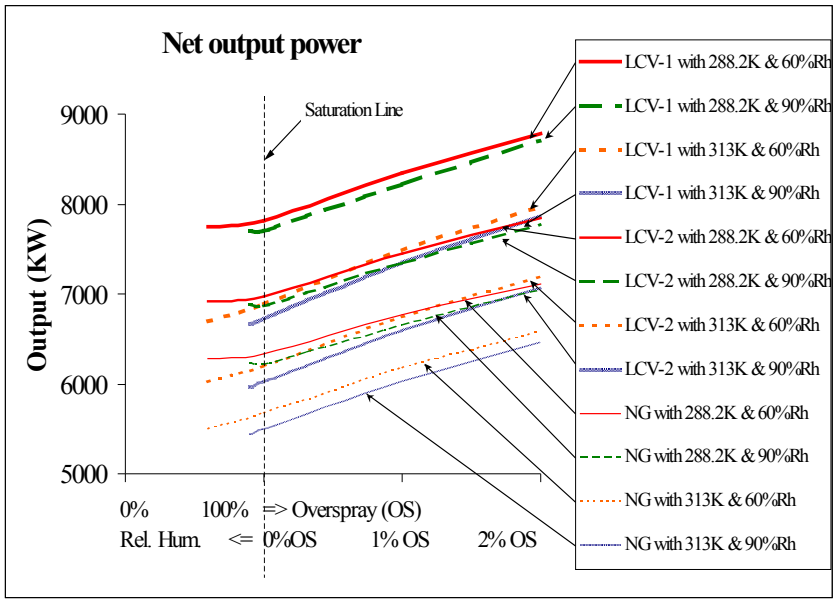

Figure 4.8 Net output power under different ambient conditions

Figure 4.7 shows that higher ambient temperature or humidity actually increases the gross turbine power; in these conditions, however, both the air and fuel compressor powers consumed are also increased (Fig. 2.2 & 2.3). As a result, the net effect favors larger net power output at low ambient and humidity conditions.

4.1.6 Fog/Overspray Effect on Thermal Efficiency

For cases using LCV fuels, the thermal efficiency is approximately 10~16% (or 3 ~ 5 percentage points) less than using NG because the fuel compressor consumes a significant auxiliary power. In the previous discussions, the influence of fog/overspray is either monotonously decreasing (such as compressor power and excess air) or monotonously increasing (such as fuel compressor power and net power output). The trend of efficiency variation is not so straightforward. Taking natural gas in Fig. 4.9 for example, the efficiency monotonously decreases slightly as overspray increases at T_{amb} = 288.2K, whereas when T_{amb} increases to 313K, the thermal efficiency increases slightly instead of decreasing as fog overspray increases. This reversing trend of thermal efficiency indicates that applying overspray is more efficient at hotter days. Since the thermal efficiency may slightly decrease or increase under fog/overspray

conditions, considering the uncertainty of the current ideal model, fog/overspray should be considered as a means to augment power output, but not necessarily efficiency.

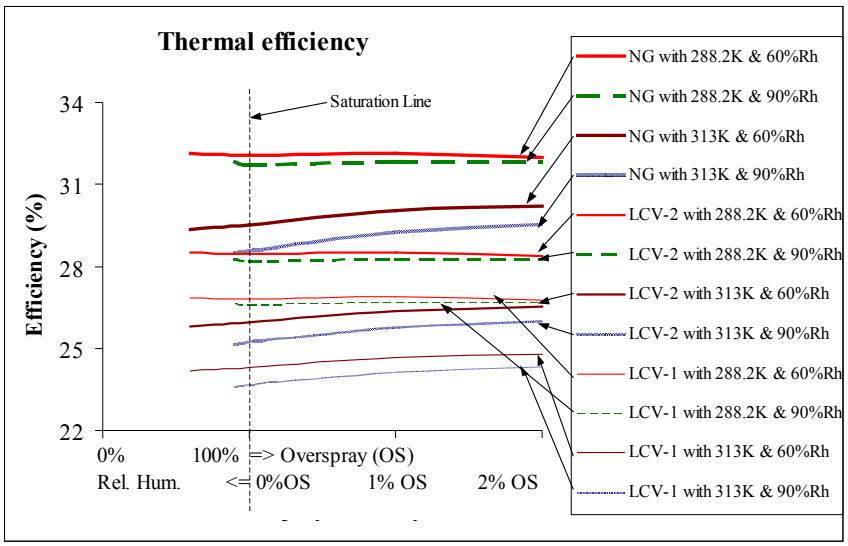

Figure 4.9 Thermal efficiency under different ambient conditions

4.1.7 Modifications of NG-fired GT for Burning LCV fuels

Although the above results show that using the LCV fuels produces more net output power, as previously discussed, the present simulation requires to use bigger GT to burn LCV fuels if the same operating condition (surge margin, stagnation pressure loss, etc.) and component efficiencies are imposed as the NG-fired GT.

This simulation treats the combustor as a black box and assumes that the combustor is functional when LCV fuels are burned. The actual combustion mechanisms are not modeled. In this study, the pressure ratio is maintained at a fixed value of 12 by using the same compressor but different turbines. The turbine could be modified by (a) increasing the tip/hub ratio, (b) reducing the solidity (i.e. reducing the turbine blade numbers) but increasing the loading factor of each blade, or (c) using the same airfoils but with different staggering angle and incidence angle. Method (a) will increase the radius of the turbine. Method (b) can maintain the same size of the turbine but needs to redesign the turbine airfoils in order to achieve the same turbine performance. Method (c) keeps the same turbine airfoils but with degraded turbine performance because the incidence angle and lift coefficient will be altered as the staggering angle is compromised.

In the real application when a commercial GT is used, the turbine nozzle area needs to be opened (method C above) to maintain this fixed pressure ratio when LCV fuels are burned. Otherwise, the flow may be choked at the first-stage turbine nozzle. Consequently, the pressure will increase due to this choking condition as well as the increased friction in combustor and in the non-modified turbine stages. When the compressor is working against a higher than designed back pressure, it will operate off the design point with a reduced stability margin. Brun, et. al. (2005) specifically discussed a simplified method to evaluate the principal factors that affect the aerodynamic stability of a single shaft gas turbine's axial compressor. Their analysis showed that when inlet and interstage water injection is combined with other factors such as LCV fuels and combustor steam injection, gas turbine compressor aerodynamic stability problems such as rotating stall and flutter will likely occur. These aerodynamic instabilities can be directly linked to blade high-cycle fatigue and possible catastrophic gas turbine failure. Furthermore, any water injection into a gas turbine may affect the hot-section turbine parts life. Therefore, care must be taken to employ inlet fog cooling when LCV fuels are burned. A companion paper by Roy and Wang (2006) assesses the option of changing pressure and TIT to optimize a commercial GT output power and efficiency when producer gases are burned.

If the NG-fired GT is to be used to burn LCV fuels and it is desired to minimize modifications, it would be interested in studying the effect of reducing TIT on the GT performance. Reducing TIT will decrease the work output and hence will reduce the load on each blade. This approach will allow method (c) to be used by changing the stagger angle without changing the airfoils. Figures 4.10 & 4.11 show the results of varying TIT (see data in Table 4.3). An upper limit of 125% output power is drawn in Figs. 4.10 & 4.11 to represent the two limiting factors: the maximum shaft power rating and the capacity of electric generators. Both are designed with accepting 20-25% additional power output. (Note, some OEMs do not recommend operating over 15% of the rated capacity.) The lower broken line is the designed power output of the NG-fired GT.

In each case, the performance curves for dry compression and saturation compression almost coincide. When LCV fuels are burned, all of the cases are within the maximum limit except three LCV1 case are above the 125% limit. Take the Case of 288K, 60%RH with 2% overspray for example, the net output power is unacceptable high (over 125%) to the NG-fired GT. However, if the TIT is reduced to 1250K, the output power is comparable to the NG-fired

GT. In this case, it is interesting to see that the net output power of LCV1-fired GT degrades profoundly 27% as TIT decreases 150K, but the thermal efficiency only reduces less than 0.5 percentage point (Table 4.3).

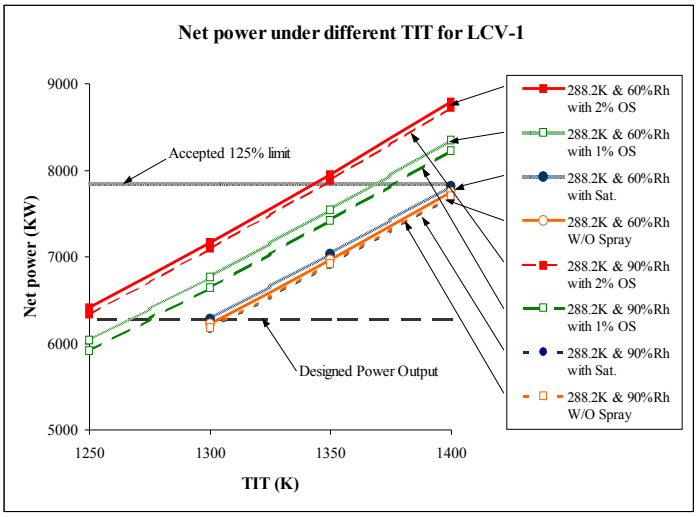

Figure 4.10 Net output power under different TIT conditions for LCV-1

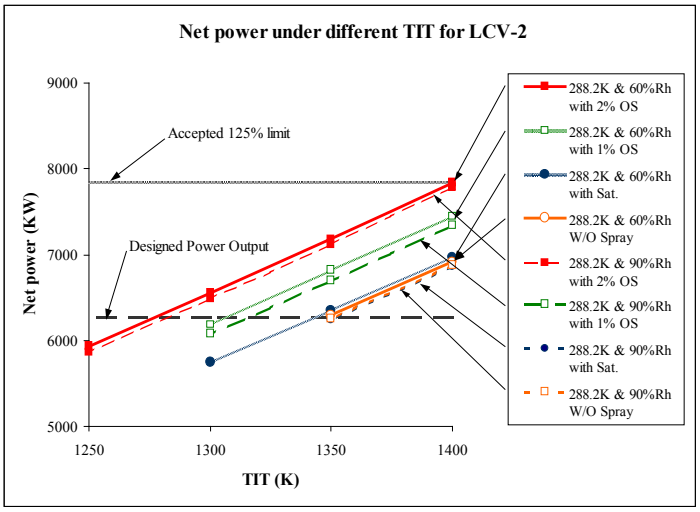

Figure 4.11 Net output power under different TIT conditions for LCV-2

Table 4.2 Data for different cases for gas turbine system. All cases are conducted with a pressure ratio 12, compressor and turbine adiabatic efficiencies of 88%, and 20Kg/s of air flow rate. The power and thermal efficiency increases are compared with the first case (no fogging) in each category separated with alternating gray shade. "Dry" means no fogging, but the airflow contains moisture from the ambient.

Case	Description	CIT (K)	CDT (K)	Comp. Power (KW)	Fuel Comp. Power (KW)	Fuel Flow (Kg/s)	Heat Add. (KW)	Excess Air (%)	Turb. Power (KW)	Net Output Power (KW)	Therm Eff (%)	Net Power Increase (%)	Eff. Increase (%)
01	NG-288.2K w. 60%Rh	288.2	625.5	6997	271	0.391	19544	198.0	13546	6278	32.12	----	----
02	NG-288.2K w. 60%Rh, Sat.	283.9	619.7	6982	274	0.395	19746	194.9	13588	6333	32.07	0.87%	-0.17%
03	NG-288.2K w. 60%Rh, 1% OS	283.9	581.8	6775	292	0.420	21042	176.8	13833	6766	32.16	7.77%	0.10%
04	NG-288.2K w. 60%Rh, 2% OS	283.9	549.0	6653	308	0.444	22242	161.8	14077	7115	31.99	13.33%	-0.42%
05	NG-288.2K w. 90%Rh	288.2	629.0	7113	272	0.391	19588	197.3	13621	6237	31.84	----	----
06	NG-288.2K w. 90%Rh, Sat.	287.2	628.7	7133	272	0.392	19613	196.9	13631	6227	31.75	-0.16%	-0.28%
07	NG-288.2K w. 90%Rh, 1% OS	287.2	590.9	6926	290	0.418	20905	178.6	13876	6660	31.86	6.78%	0.06%
08	NG-288.2K w. 90%Rh, 2% OS	287.2	556.2	6758	307	0.443	22153	162.9	14120	7055	31.85	13.12%	0.03%
09	NG-313K w. 60%Rh	313.0	691.6	8244	283	0.375	18775	210.2	14037	5510	29.35	----	----
10	NG-313K w. 60%Rh, Sat.	305.4	678.8	8155	289	0.384	19213	203.1	14118	5674	29.53	2.98%	0.64%
11	NG-313K w. 60%Rh, 1% OS	305.4	639.4	7872	310	0.411	20572	183.1	14363	6182	30.05	12.20%	2.40%
12	NG-313K w. 60%Rh, 2% OS	305.4	605.2	7685	329	0.436	21825	166.8	14607	6594	30.21	19.68%	2.96%
13	NG-313K w. 90%Rh	313.0	699.6	8648	288	0.382	19119	204.6	14388	5452	28.51	----	----
14	NG-313K w. 90%Rh, Sat.	311.2	696.2	8616	290	0.384	19237	202.7	14408	5503	28.60	0.94%	0.32%
15	NG-313K w. 90%Rh, 1% OS	311.2	656.5	8305	310	0.412	20621	182.4	14654	6039	29.28	10.77%	2.70%
16	NG-313K w. 90%Rh, 2% OS	311.2	622.2	8096	330	0.437	21892	166.0	14898	6472	29.57	18.73%	3.69%
17	LCV 1-288.2K w. 60%Rh	288.2	625.5	6997	2894	6.619	28847	127.1	17639	7748	26.86	----	----
18	LCV 1-288.2K w. 60%Rh, Sat.	283.9	619.7	6982	2924	6.687	29146	124.8	17724	7817	26.82	0.90%	-0.14%
19	LCV 1-288.2K w. 60%Rh, 1% OS	283.9	581.8	6775	3116	7.126	31058	111.0	18240	8348	26.88	7.75%	0.08%
20	LCV 1-288.2K w. 60%Rh, 2% OS	283.9	549.0	6653	3294	7.532	32829	99.6	18735	8787	26.77	13.42%	-0.34%
21	LCV 1-288.2K w. 90%Rh	288.2	629.0	7113	2901	6.634	28913	126.6	17723	7709	26.66	----	----
22	LCV 1-288.2K w. 90%Rh, Sat.	287.2	628.7	7133	2904	6.642	28949	126.3	17738	7701	26.60	-0.11%	-0.23%
23	LCV 1-288.2K w. 90%Rh, 1% OS	287.2	590.9	6926	3096	7.080	30856	112.3	18254	8231	26.68	6.77%	0.05%
24	LCV 1-288.2K w. 90%Rh, 2% OS	287.2	556.2	6758	3281	7.502	32698	100.4	18759	8721	26.67	13.12%	0.02%
25	LCV 1-313K w. 60%Rh	313.0	691.6	8244	3020	6.358	27713	136.4	17969	6705	24.19	----	----
26	LCV 1-313K w. 60%Rh, Sat.	305.4	678.8	8155	3090	6.507	28358	131.0	18141	6897	24.32	2.86%	0.52%
27	LCV 1-313K w. 60%Rh, 1% OS	305.4	639.4	7872	3309	6.967	30365	115.8	18672	7491	24.67	11.73%	1.97%
28	LCV 1-313K w. 60%Rh, 2% OS	305.4	605.2	7685	3510	7.391	32213	103.4	19178	7983	24.78	19.06%	2.43%
29	LCV 1-313K w. 90%Rh	313.0	699.6	8648	3075	6.475	28220	132.2	18391	6668	23.63	----	----
30	LCV 1-313K w. 90%Rh, Sat.	311.2	696.2	8616	3094	6.515	28394	130.7	18436	6727	23.69	0.88%	0.26%
31	LCV 1-313K w. 90%Rh, 1% OS	311.2	656.5	8305	3317	6.983	30437	115.3	18972	7351	24.15	10.24%	2.20%
32	LCV 1-313K w. 90%Rh, 2% OS	311.2	622.2	8096	3521	7.414	32313	102.8	19483	7866	24.34	17.96%	3.01%
33	LCV 2-288.2K w. 60%Rh	288.2	625.5	6997	1531	3.277	24266	169.9	15443	6915	28.50	----	----
34	LCV 2-288.2K w. 60%Rh, Sat.	283.9	619.7	6982	1547	3.311	24517	167.2	15505	6976	28.45	0.88%	-0.15%
35	LCV 2-288.2K w. 60%Rh, 1% OS	283.9	581.8	6775	1648	3.528	26126	150.7	15875	7452	28.52	7.76%	0.09%
36	LCV 2-288.2K w. 60%Rh, 2% OS	283.9	549.0	6653	1742	3.729	27616	137.2	16235	7840	28.39	13.37%	-0.38%
37	LCV 2-288.2K w. 90%Rh	288.2	629.0	7113	1534	3.284	24322	169.3	15522	6875	28.27	----	----
38	LCV 2-288.2K w. 90%Rh, Sat.	287.2	628.7	7133	1536	3.288	24352	169.0	15534	6866	28.19	-0.13%	-0.26%
39	LCV 2-288.2K w. 90%Rh, 1% OS	287.2	590.9	6926	1637	3.505	25956	152.3	15905	7341	28.28	6.78%	0.05%
40	LCV 2-288.2K w. 90%Rh, 2% OS	287.2	556.2	6758	1735	3.714	27506	138.1	16270	7777	28.27	13.12%	0.02%
41	LCV 2-313K w. 60%Rh	313.0	691.6	8244	1597	3.148	23312	181.0	15859	6018	25.81	----	----
42	LCV 2-313K w. 60%Rh, Sat.	305.4	678.8	8155	1634	3.221	23855	174.6	15982	6194	25.96	2.92%	0.58%
43	LCV 2-313K w. 60%Rh, 1% OS	305.4	639.4	7872	1750	3.449	25543	156.4	16360	6738	26.38	11.98%	2.20%
44	LCV 2-313K w. 60%Rh, 2% OS	305.4	605.2	7685	1856	3.659	27098	141.7	16725	7184	26.51	19.39%	2.71%
45	LCV 2-313K w. 90%Rh	313.0	699.6	8648	1626	3.206	23739	175.9	16243	5969	25.14	----	----
46	LCV 2-313K w. 90%Rh, Sat.	311.2	696.2	8616	1636	3.225	23885	174.2	16275	6023	25.22	0.91%	0.29%
47	LCV 2-313K w. 90%Rh, 1% OS	311.2	656.5	8305	1754	3.457	25604	155.8	16655	6596	25.76	10.51%	2.46%
48	LCV 2-313K w. 90%Rh, 2% OS	311.2	622.2	8096	1862	3.670	27182	141.0	17023	7065	25.99	18.36%	3.37%

Table 4.3 Design data for varying TIT. All cases are conducted with a pressure ratio 12, compressor and turbine adiabatic efficiencies of 88%, and 20Kg/s of air flow rate. The net power of each case is graphed in Figures 13a and 13b to show the results of changing TIT. The power and thermal efficiencies are compared with the first case in each category separated with alternating gray shade.

Amb. Temp.	Rel. Hum.	TIT	Fogging	Fuel	Net Power	Efficiency	Fuel	Net Power	Efficiency
(K)	(%)	(K)			(KW)	(%)		(KW)	(%)
288.2	60	1400	Dry	NG	6278	30.00	NG	6278	30.00
288.2	60	1400	Dry	LCV 1	7748	26.86	LCV 2	6915	28.50
288.2	60	1350	Dry	LCV 1	6966	26.74	LCV 2	6295	28.36
288.2	60	1300	Dry	LCV 1	6223	26.54	LCV 2	-------	-------
288.2	60	1400	Sat	LCV 1	7817	26.82	LCV 2	6976	28.45
288.2	60	1350	Sat	LCV 1	7032	26.70	LCV 2	6353	28.31
288.2	60	1300	Sat	LCV 1	6285	26.50	LCV 2	5744	28.10
288.2	60	1400	1% OS	LCV 1	8348	26.88	LCV 2	7452	28.52
288.2	60	1350	1% OS	LCV 1	7539	26.78	LCV 2	6813	28.41
288.2	60	1300	1% OS	LCV 1	6769	26.61	LCV 2	6190	28.23
288.2	60	1250	1% OS	LCV 1	6038	26.37	LCV 2	-------	-------
288.2	60	1400	2% OS	LCV 1	8787	26.77	LCV 2	7840	28.39
288.2	60	1350	2% OS	LCV 1	7955	26.67	LCV 2	7185	28.28
288.2	60	1300	2% OS	LCV 1	7164	26.51	LCV 2	6548	28.11
288.2	60	1250	2% OS	LCV 1	6412	26.27	LCV 2	5927	27.86
288.2	90	1400	Dry	LCV 1	7709	26.66	LCV 2	6875	28.27
288.2	90	1350	Dry	LCV 1	6924	26.52	LCV 2	6251	28.11
288.2	90	1300	Dry	LCV 1	6177	26.30	LCV 2	-------	-------
288.2	90	1400	Sat	LCV 1	7701	26.60	LCV 2	6866	28.19
288.2	90	1350	Sat	LCV 1	6915	26.45	LCV 2	6241	28.03
288.2	90	1300	Sat	LCV 1	6167	26.23	LCV 2	-------	-------
288.2	90	1400	1% OS	LCV 1	8231	26.68	LCV 2	7341	28.28
288.2	90	1350	1% OS	LCV 1	7421	26.55	LCV 2	6700	28.14
288.2	90	1300	1% OS	LCV 1	6651	26.36	LCV 2	6076	27.93
288.2	90	1250	1% OS	LCV 1	5919	26.08	LCV 2	-------	-------
288.2	90	1400	2% OS	LCV 1	8721	26.67	LCV 2	7777	28.27
288.2	90	1350	2% OS	LCV 1	7887	26.56	LCV 2	7121	28.15
288.2	90	1300	2% OS	LCV 1	7095	26.39	LCV 2	6482	27.96
288.2	90	1250	2% OS	LCV 1	6342	26.14	LCV 2	5859	27.70
313	60	1400	Dry	LCV 1	6705	24.19	LCV 2	6018	25.81
313	60	1350	Dry	LCV 1	5932	23.85	LCV 2	-------	-------
313	60	1400	Sat	LCV 1	6897	24.32	LCV 2	6194	25.96
313	60	1350	Sat	LCV 1	6116	24.00	LCV 2	-------	-------
313	60	1400	1% OS	LCV 1	7491	24.67	LCV 2	6738	26.38
313	60	1350	1% OS	LCV 1	6686	24.41	LCV 2	6090	26.10
313	60	1300	1% OS	LCV 1	5922	24.07	LCV 2	-------	-------
313	60	1400	2% OS	LCV 1	7983	24.78	LCV 2	7184	26.51
313	60	1350	2% OS	LCV 1	7155	24.55	LCV 2	6520	26.27
313	60	1300	2% OS	LCV 1	6369	24.25	LCV 2	5874	25.94
313	90	1400	Dry	LCV 1	6668	23.63	LCV 2	5969	25.14
313	90	1350	Dry	LCV 1	5876	23.22	LCV 2	-------	-------
313	90	1400	Sat	LCV 1	6727	23.69	LCV 2	6023	25.22
313	90	1350	Sat	LCV 1	5932	23.30	LCV 2	-------	-------
313	90	1400	1% OS	LCV 1	7351	24.15	LCV 2	6596	25.76
313	90	1350	1% OS	LCV 1	6532	23.83	LCV 3	5935	25.42
313	90	1300	1% OS	LCV 1	5755	23.42	LCV 4	-------	-------
313	90	1400	2% OS	LCV 1	7866	24.34	LCV 2	7065	25.99
313	90	1350	2% OS	LCV 1	7023	24.07	LCV 2	6387	25.69
313	90	1300	2% OS	LCV 1	6225	23.70	LCV 2	5729	25.31

4.2 Analysis of Compressor Performance by Stage-to-Stage by Equilibrium Stacking Method

The studied compressor has 8 stages. The ISO condition (59°F and 60% Relative Humidity) is used as the design case, and the diameters (hub and tip diameters) are determined at the design condition. The axial velocity (150 m/s) is designed as a constant value throughout the compressor with the following parameters: rotor speed (12,000 RPM), rotor turning angle (12°), inlet pressure (1atm), and isentropic stage efficiency (92%). Note that the axial velocity for non-baseline cases will change due to changed mass flow rate. The wet compression process is represented by a cooling polytropic process with a polytropic index (k) of 1.36. A 2D compressor airfoil geometry and stage setting at the mean radius are employed. The detailed stator and rotor information are given in Table 4.7. All the general assumptions are listed below:

1. Constant inlet axial velocity (or inlet flow coefficient) -- The compressor is assumed to behave as a constant-volume-flow-rate device at the inlet when the rotating speed is fixed, so the inlet axial velocity maintains constant. When fogging is applied, the volume flow rate at the inlet does not change although the mass flow rate increases due to increased air density. Therefore, it is important to realize that the inlet velocity maintaining a constant does not mean the mass flow rate maintains constant at the inlet. Once the mass is determined at the inlet, the mass flow rate (plus the overspary mass) maintains constant throughout the entire compressor, and the volume flow rate will change at different stages.
2. The mean diameter was designed the same for all the stages.
3. All the losses are assumed to occur in the rotor. There is no loss in stator, and the stator is assumed adiabatic (i.e. isentropic), so the stagnation property values are the same at the inlet and exit of stators.
4. Property values (e.g. density, enthalpy) of mixture are calculated by mass-weighted average method, similar to the process described by Young (1995).
5. Equation of state holds true for all conditions.
6. The system is assumed in thermodynamic equilibrium for droplet evaporation, i.e. water evaporation is governed by only thermodynamics per saturation requirement in each stage, although in reality, water evaporation is also governed by heat and mass transfer.

7. The water droplets are assumed incompressible, so the multi-phase flow can be represented by the polytropic process of moist air (dry air plus water vapor) with an equivalent polytropic index, k. Klepper et al. (2004) showed that k is approximately 1.36 for a wide range of air water mixture.

Six cases are studied with the ISO condition being the baseline; one was studied on a hot day, one was studied on the same hot day with saturated cooling, and the other three cases were studied employing water spray in different locations at the inlet and inside the compressor:

Case 1: Designed baseline case at ISO condition (288K and 60% RH).
Case 2: Under hot weather at 300K and 60% RH
Case 2S: Saturated (0.245%) spray at the 1st rotor inlet at 300K and 60% RH.
Case 3: 2% overspray at the 1st rotor inlet at 300K and 60% RH
Case 4: 2% over spray at stage 1 rotor inlet at 300K, 60% RH and 1% at stage 3 stator inlet
Case 5: 2% spray at stage 1 rotor inlet at 300K and 60% RH and 1% at stage 4 rotor inlet

In this study, the term "fogging" indicates the action of generating the fog. Depending on the amount of the injected water, "saturated fogging" (Case 2S) implies the process of saturating the air to 100% relative humidity and "overspray" implies the process of injecting more than the water amount required to achieve saturated air. Strictly speaking, a 1% overspray implies the amount water that weighs 1% of the dry air flow is injected in addition to the amount required to saturate the air. However, for simplicity, overspay fogging also includes saturated fogging in this study. For example, 2% water overspray with an ambient condition of 300K and 60% RH implies that 0.245% water is needed to saturate the air and (2 – 0.245) = 1.755% is actually used for overspray. In this study, “dry” air means no water vapor in the air (RH=0); ”moist” air means air contains water vapor but not water droplets (RH>0); and “wet” air means air contains water droplets. The term “dry compression” has been used by industry to indicate compression of dry or moist air with no water droplets. Although it is a misnomer because the air is not completely dry, this study adopts it nonetheless by following industry practice.

In the simulation of the Case 1 (designed case), the axial velocity is kept as a constant in each stage by adjusting the flow area (i.e. hub and tip diameter) The variation of hub and tip

diameters in different stages is shown in Fig. 4.12. For the cases of inlet fogging or interstage fogging, the designed geometry is unchanged; the local flow velocity vector, thermal properties, rotor loading condition of each stage are calculated by the stage-stacking scheme. An example showing the effect of fogging on velocity diagram is illustrated in Fig. 4.13 by juxtaposing the velocity diagrams of Stage 2 in Cases 1, 2 and 3 for comparison. The following changes are observed:

a. All the velocity directions and magnitude are changed. For example, the absolute rotor inlet velocity changes from purely axial direction to deviating 0.42° for Case 2, –0.26° for Case 2S, and 1.975° for Case 3 from the axis. Interstage spray of Cases 4 and 5 further increases the incidence angles until the water droplets evaporate.

b. The flow coefficient ($\phi = V_a/U$) increases 3% for Case 2, decreases 2.3% for Case 2S, and 24% for Case 3, while the rotor work coefficient Ψ increases 1.5% for Case 2, decreases 3.3% for Case 2S, and decreases 17% for Case 3.

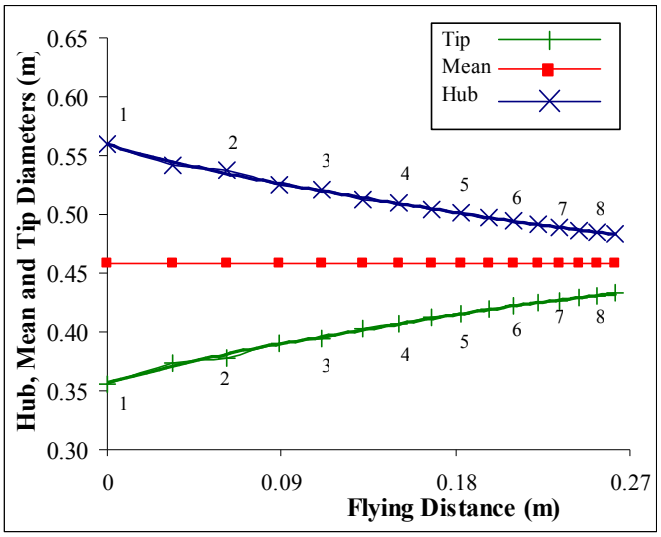

Figure 4.12 Designed compressor tip and hub diameters (the numbers on the top of the curves represent the stage numbers)

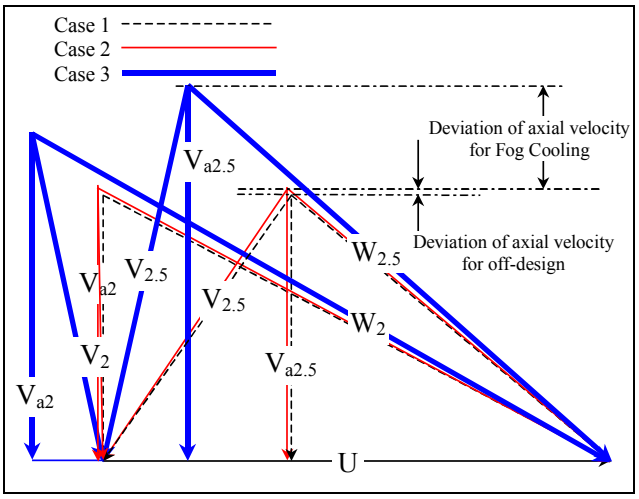

Figure 4.13 Velocity diagram for cases 1 and 2 in second stage

4.2.1 Effect on Static Temperature

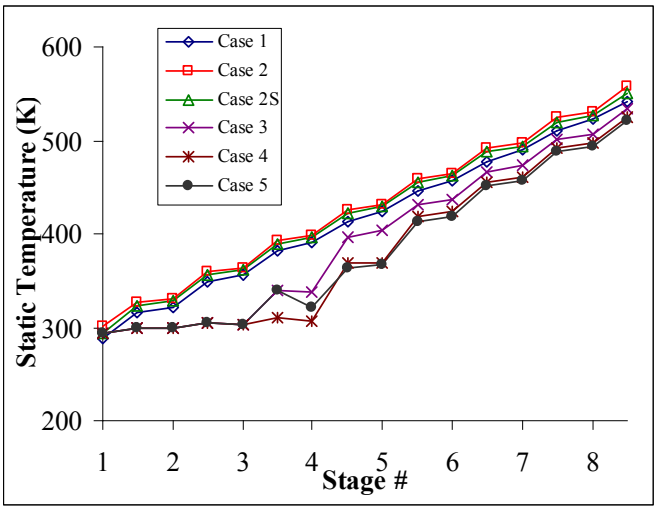

Figure 4.14 Static temperature variations: overspray induces an excessive reduction of static temperature

Figure 4.14 shows the static temperature variation in different stages. The temperature for Case 2 is higher than Case 1 in every stage. Saturated fogging (Case 2S) results in temperature reduction in every stage from Case 2 with a reduction of 6°C, 2°C, and 3°C for the first three stages and 2°C, 3°C, and 4°C for the final three stages, respectively. Overspray (Case 3) significantly reduces the static temperature due to absorption of latent heat during water evaporation. When 2% overspray is applied only at the entrance of the first stage, the

temperature drops 6°C, 32°C, and 60°C in the first three stages respectively and maintains an almost constant value for the first three stages before the completion of evaporating all the water droplets.

When an additional 1% overspray is applied at the 3rd stage stator (Case 4), the temperature drops further to 30°C below the same stage temperature in Case 3 and 91°C below Case 2. When an 1% overspray is applied at the 4th stage rotor, the temperature drops further to 26°C below the same stage temperature in Case 3 and 76°C below Case 2.

4.2.2 Effect on Pressure, Pressure Ratio

Local pressure ratio variations of each stage are shown in Fig. 4.15. When overspray is applied in the first stage (Case 3), the local pressure ratio experiences a significant drop from 1.4 to 1.1 due to excessive reduction of temperature. This is very different from the condition in saturated fogging case (Case 2S), which the pressure ratio actually increases from 1.4 to 1.44. Not until the third stage when most of the water droplets vaporize, does the local pressure ratio of Case 3 outperforms Cases 1, 2 and 2S. A further spray of water at stage 3 stator in Case 4 keep the local pressure ratio low at stage 3, but the pressure ratio quickly increases afterwards. Case 5 delays the additional spray to stage 4 rotor and shows a similar trend as in Case 4: the local pressure ratio reduces immediately after spray due to excessive cooling and rises quickly afterwards.

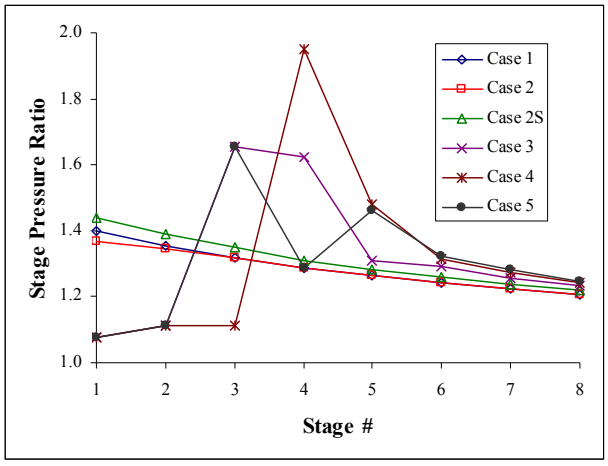

Figure 4.15 Stage stagnation pressure ratio variation: overspray results in a reduction of local pressure due to an excessive temperature drop, followed by a splurge of pressure rise

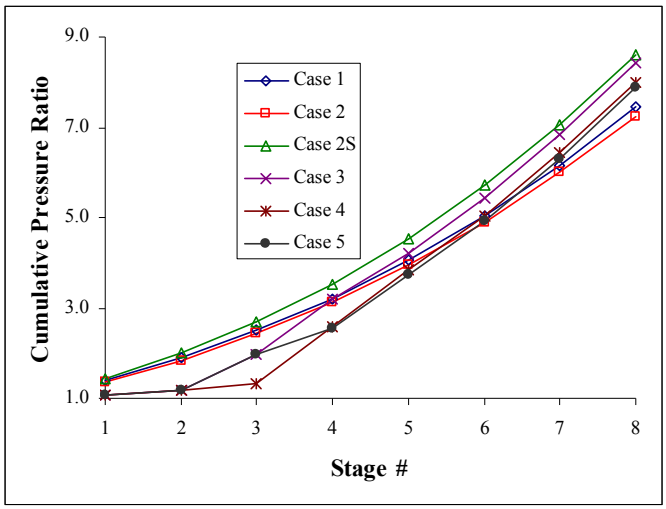

Figure 4.16 Cumulative compressor stagnation pressure ratio variation

Figure 4.15 shows interesting local pressure ratio changes in response to local water spray; whereas Fig. 4.16 shows the overall pressure ratio variations (the integration of the local stage pressure ratio in Fig. 4.15) for all cases. The pressure ratios of no-fogging Cases 1 and 2 are lowest at 7.45 and 7.23, respectively. Saturated fogging, Case 2S, is shown to achieve the highest overall pressure ratio (8.6), followed by Cases 3, 4, and 5 at 8.42, 8.0 and 7.9, respectively. Increasing pressure ratio due to fogging tends to push the compressor operation towards surge stalling line.

4.2.3 Effect on Density

Generally the density increases when fogging is applied due to reduced temperature and the presence of moisture in the air. We are surprised to discover that this general rule only applies to saturated fogging in dry compression; however, it does not apply to the wet compression process with overspray. For example, Fig. 4.17 shows that the density unexpectedly decreases with the overspray in Cases 3,4, and 5. A further investigation reveals the following reason: When overspray is applied, temperature drops significantly (70 - 90^{o}C) due to water evaporation. This excessive temperature reduction results in a significant reduction in pressure. Pressure usually reduces more than the temperature as it can be seen in the polytropic relation that $PT^{k/(k-1)}$ = Constant, i.e. $P \propto T^{(k-1)/k\gamma}$. Take k = 1.36 for moist air for example, so k/(k-1) = 3.78, which means if the temperature reduces 10%, the pressure will reduce for 33%. Based on

the ideal gas law $\rho \sim P/RT$, the density reduces instead of increasing. Although the air receives more water vapor when water droplets vaporize, the slightly increased density due to water evaporation is not large enough to compensate for the density reduction due to temperature-induced pressure reduction.

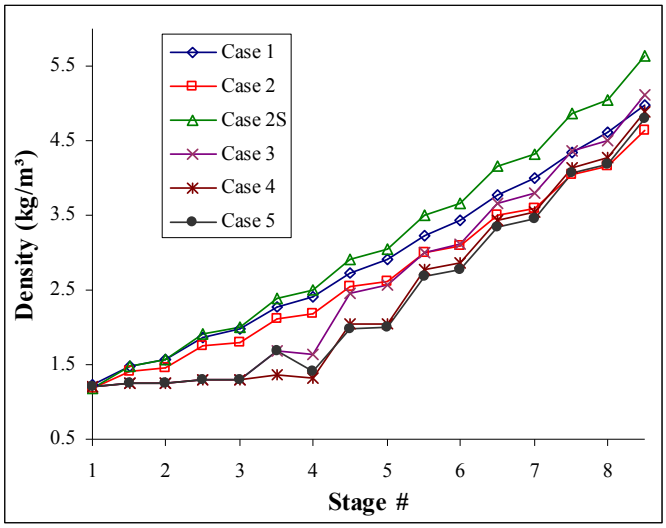

Figure 4.17 Density variation

4.2.4 Effect on Velocity and Flow Coefficient

In the baseline case (Case 1), the axial velocity at each rotor inlet is designed as the same value throughout the compressor. Recall that the algorithm assumes that the compressor performs as a constant-volume flow rate device at the compressor inlet. Once the mass flow rate is established at the inlet, the mass flow is conserved throughout the entire compressor, and the volume flow rate will be adjusted according to the local flow area and density variations. Therefore, all the cases have the same axial velocity at the inlet only. When the ambient temperature rises in Case 2, the density reduces, so the mass flow rate reduces at the inlet. The reduction of density (from Case 1 to Case 2) continues along the compressor results to an increase of axial velocity in Case 2 as shown in Fig. 4.18. When saturated fogging is applied, the above trend is reversed. The air density increases and mass flow rate increases at the inlet. The increase of density (from Case 1 to Case 2S) continues along the compressor, which results in a decrease of axial velocity as shown in Fig. 4.18. However, when overspray is applied, excessive

cooling produces an appreciable reduction of pressure (Fig. 4.15), which in turn, results in a reduction in density (see previous explanation in the section of density). Therefore, the air velocity increases. The variation of inlet velocity at each stage is shown in Fig. 4.18. Significant variations are found in Stages 2 to 5 in Cases 3, 4, and 5, due to the presence of interstage water spray at these stages. Once the water droplets vaporize, the variation trend approaches those of Cases 1 and 2. This velocity change is reflected on the flow coefficient (ϕ) variations in Fig. 4.19. When overspray is applied at the first stage, the flow coefficient continuously increases up to Stage 3 for Cases 3, 4, and 5 as evaporation has not completed before Stage 3. Once the water completely evaporates, the flow coefficient decreases and approaches Cases 2 and 2S in 6^{th}, 7^{th}, and 8^{th} stages. This trend is coherent with the results obtained by White and Meacock (2004). They showed that the flow coefficient (ϕ) increases till third stage and then decreases and gets lower than the dry compression. Combining the information obtained in Figs. 4.17 and 4.19, the result shows that the flow coefficient must significantly increase to accommodate more mass flow rate contributed by overspray especially when the density reduces, rather than increases, after overspray is applied. Whereas, in saturated fogging (Case 2S), no additional mass is added after the compressor inlet and density is persistently higher, so the flow coefficient is low. The striking difference between the saturated fogging and overspray is clearly seen in Fig. 4.19.

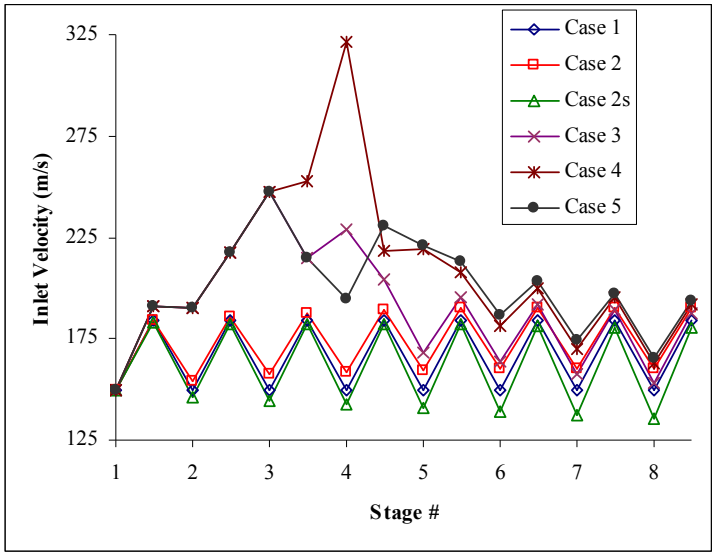

Figure 4.18 Inlet velocity (actual magnitude) variations at each stage

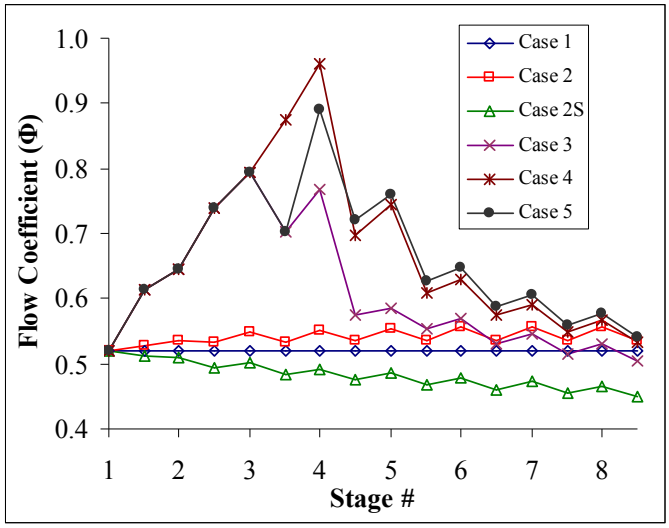

Figure 4.19 Flow coefficient (ϕ) variations. Note the striking difference between saturated fogging (case 2S) and overspray (cases 3, 4 and 5).

4.2.5 Effect on Compressor Power

Changes in compressor power consumption and compressor blade loading are important issues related to fogging. Specific work (kJ/kg) will be discussed separately first via work coefficient (Ψ), followed by stage and integrated power (kW) including the effect of increased mass flow. Figure 4.20 shows the rotor work coefficient (Ψ), which reflects the specific work normalized by the rotational kinetic energy without including the effect of mass flow rate. This value increases 5-10% when ambient temperature increases 12°C (21.6°F) in Case 2 and decreases as expected when overspray is applied (Cases 3, 4 and 5). Since the rotor work coefficient is deemed as the specific work of each stage normalized by the rotating kinetic energy, the effect of additional water (vapor) mass is therefore not included. Although the inlet velocity does not change for different cases due to the constant-volume flow rate nature of the compressor, the mass flow rate changes, and therefore, the rotor work co-efficient changes from the very first stage for different cases. It is puzzling to see that overspray reduces the stage work in the early stages, but it significantly increases the work in the later stage. This is in contrast to conventional wisdom that says fogging/overspray can reduce temperature and reduce the compressor's work. This issue will be further investigated and discussed later after the issue of mass flow rate is examined.

When mass flow rate is considered, the required compressor power is shown in Figs. 4.21 and 4.22. The curve patterns in Fig. 4.21 are similar to those in Fig. 4.20, but there are some minor differences. For example, the rotor work coefficient of Case 2 in Fig. 4.20 is higher than Case 1 because more specific work is required to compress hotter air based on an equal amount of mass flow rate. Whereas, in Figs. 4.21 and 4.22 the power for Case 2 is almost the same as Case 1 downstream of stage 2 because the hotter air in Case 2 carries less mass flow rate (25.77kg/s for Case 2 vs. 26.91kg/s for Case 1) and requires less compressor power. The reduced mass flow rate self-compensates the reduced compressor efficiency resulting in an almost identical compressor power. Therefore, the effect of mass flow rate is not obvious for Cases 1 and 2 due to this self-compensation effect. Saturated fogging of Case 2S actually brings Case 2 from hot environment to an almost identical condition to ISO case with a mass flow rate of 26.25 kg/s and a power consumption of 7.905 MW, which is the second least among all cases. Similar to its effect on the stage variation of rotor work coefficient (or specific work), overspray reduces the stage power in the earlier stages (1 and 2) but significantly increases the stage power in the later stages. The conventional belief that fogging can reduce the compressor power is violated in the cases of overspray and comes as a surprise. A more thorough investigation is therefore launched and described in detail below.

Figure 4.23 shows a traditionally textbook-like p-v diagram for an ideal Brayton cycle. If the inlet temperature is cooled from state 1" to 1, the compressor specific work can be qualitatively shown as the area enclosed by the curve and the ordinate axis and is reduced from area 1'-2'-b'-a' to area 1-2-b-a. Indeed many papers have shown fogging/overspray reduces compressor specific work such as the recent papers shown by Li and Zheng (2004), Payne and White (2008), Bagnoli et. al. (2008 a, b) and Bianchi et. al. (2007) including the earlier study presented by the author. After further investigation, the discrepancy is explained by the following reason: the theoretical GT cycle diagram shown in Fig. 4.23 is plotted by assuming the pressure ratio maintains at a constant value. In this study, the pressure ratios increase as fogging is applied as shown in Fig. 4.16. Case 2S gives the highest pressure ratio of 8.6.

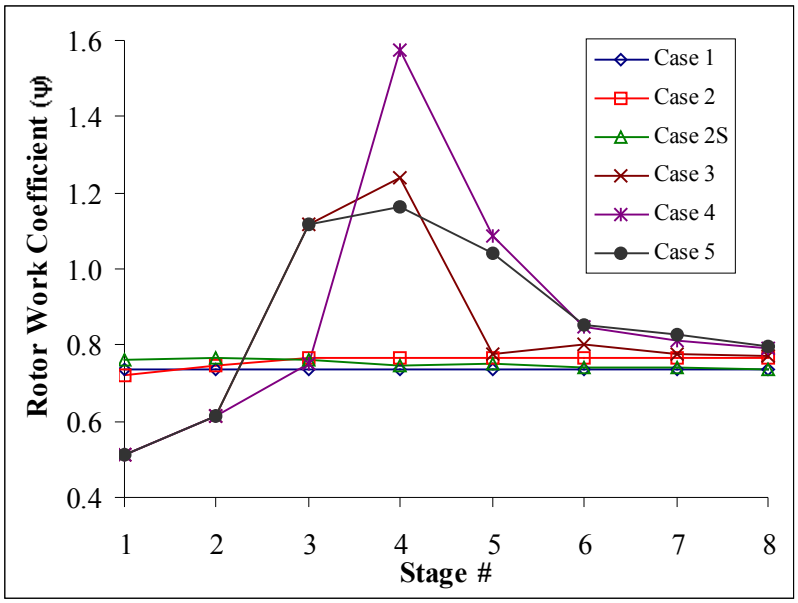

Figure 4.20 Variation of rotor work coefficient (Ψ)

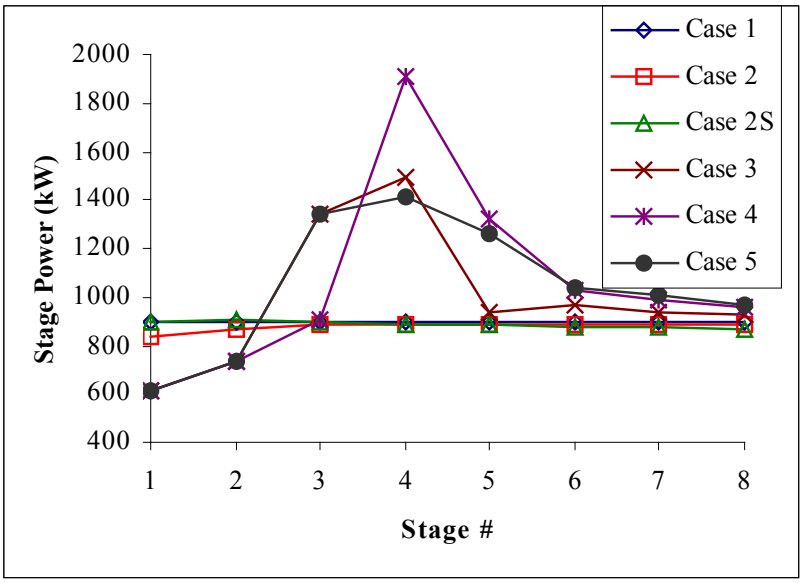

Figure 4.21 Variation of compressor stage power

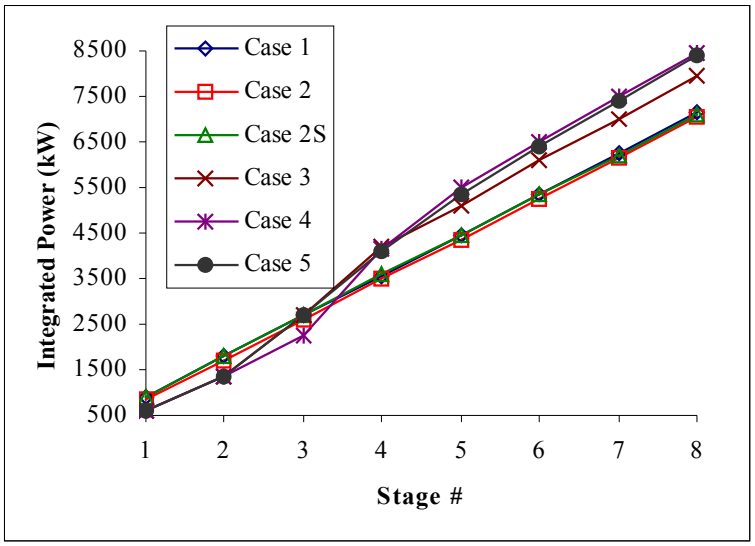

Figure 4.22 Variation of compressor integrated power

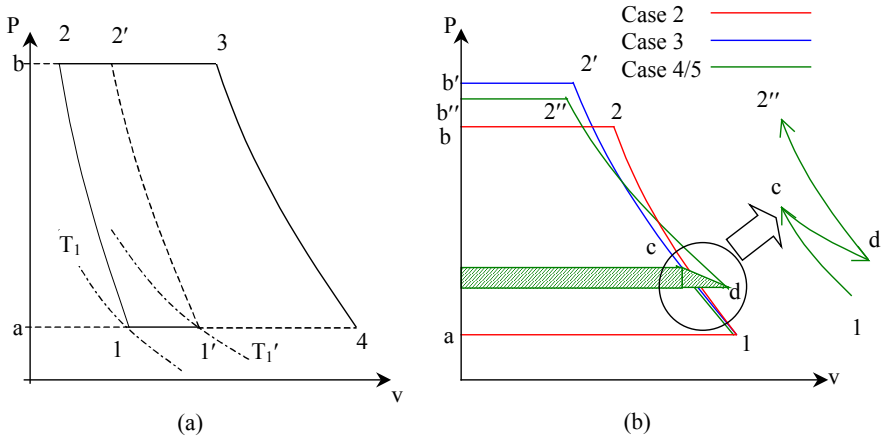

Fig 4.23: P-v diagrams for the Brayton cycle. (a) Inlet saturated cooling with a constant pressure ratio. (b) Theoretical representation of cases 2, 3, 4 and 5. The shaded area represents the double compression work due to the interstage spray.

For a clear illustration, Fig. 4.24 is plotted to show a theoretical representation of the process of Case 3 (1-2" for inlet overspray) and Case 4 (1-c-d-2"' for inlet overspray + interstage spray) on a p-v diagram. It shows that compressor specific work actually increases due to the extra area enclosed by the additional compressor discharge pressure for Cases 2S, 3, 4, and 5. In addition, especially for interstage cooling in Cases 4 and 5, extra work takes place due to the area

enclosed by 1-c and d-2". The process c-d shows that the pressure drop is due to additional evaporation. A portion of the shaded area represents the extra power needed for "recompressing" the gas with reduced pressure due to local spray and should be counted twice. If this additional power for pressure increase is more than the savings due to overspray, the total compressor power will increase. This happens for Cases 3, 4, and 5 in this study, but not for Case 2S. The actual process is shown in Figs. 4.24 and 4.25. Note that the p-v diagram shows the specific work, which is independent of the mass flow rate, so the added mass due to fogging does not enter into discussion here. The added mass due to water overspray will further exert a negative impact on the compressor's work as shown in Fig. 4.25. The difference of specific work and power is revealed clearly in Case 2S, where the specific work (249 kJ/kg) is less than that of Case 2 (251 kJ/kg), whereas the power for Case 2S (7.095 MW) is more than that of Case 2 (7.078) due to increased mass flow rate in Case2S.

This additional workload due to overspray also exerts an increased loading requirement to the later stage of the compressor blades as previously shown in Fig. 4.20. In terms of the velocity diagram, Fig. 4.18 shows and explains that axial velocity increases, as does the inlet velocity at each stage, which increases the difference between the tangential components of the inlet velocity. The increase of the tangential component of velocity can increase the workload of local stage by 100% (e.g. see Stage 4 in Fig. 4.18). This significant increase of local blade loading could possibly induce rotating stall and push the overall compressor operation toward the surge limit.

Since both pressure ratio and compressor power increase after overspray fogging is applied, it would be interesting to find out under which conditions, with or without fogging, produce pressure more effectively by comparing the ratio of compressor power/ pressure ratio: P_c/r_p .

The data in Table 4.6 show the ratio of the compressor power to pressure ratios are 882, 894, 759, 868, 972, and 979 (kW) for Cases 1-5, respectively. Case 2S with the saturated fogging at the GT inlet is most effective among the six cases. Interstage fogging is the least effective.

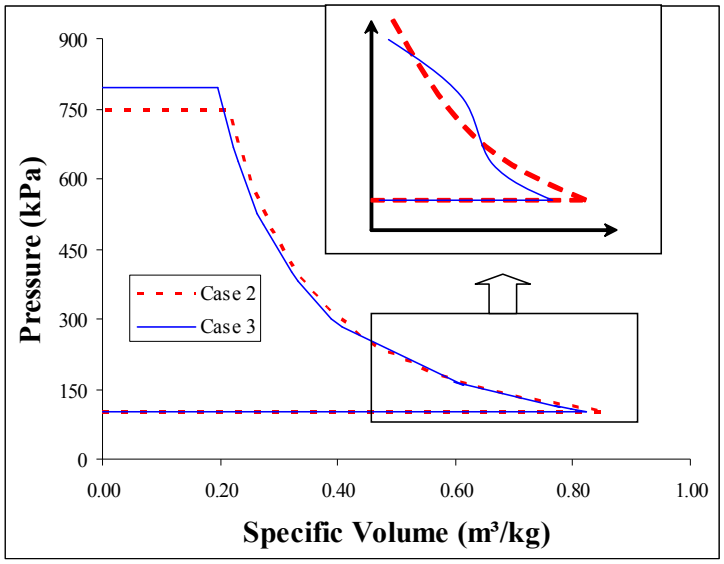

Figure 4.24 P-v diagram illustration of actual wet compression processes of cases 2 and 3

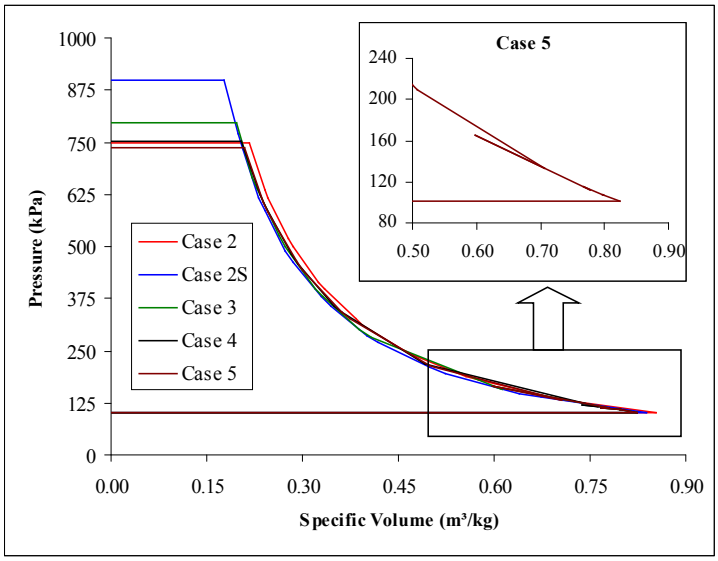

Figure 4.25 P-v diagram illustration of actual compression processes of cases 2, 3 and 4. (A portion of the double compression work is qualitatively shown in Fig. 4.23)

4.2.6 Assessment of using a Constant Shape Factor and the Generalized Compressor Performance Curve

As stated in Chapters 1 and 2 about the performance charts used by previous researchers especially Bagnoli et. al. (2008), in this part of the study an assessment of the use of Shape

Factors (SF) by calculating SF from the current results obtained from known compressor geometry and settings was made. Recall that implementation of the SF approach is a non-voluntary option because the compressor performance maps are deemed proprietary by the manufacturers and generally not available to the public. The concept of SF was introduced by Cerri et. al. (1993). The value of SF typically varies between -0.5 and 1. The negative SF values are usually associated with transonic or supersonic stages. Since a detailed stage design for the compressor is not available, an average SF value is usually assigned to all the stages of a compressor. However, SF values are closely dependent on the characteristics of each compressor and vary significantly. Guessing a SF value for a specific engine could incur a large uncertainty and requires guidance from field test data such as the values shown by Muir et. al. (1989). An ill assigned (or guessed) SF value will lead to misleading or even completely false results. Therefore, continuously examining the approach to using SF and providing means to improve it, if possible, are indispensable.

It should be noted that the SF parameter serves as a "tuning" unknown parameter which is determined to minimize the mean square error between measured (or available) data on a gas turbine and the corresponding data computed by the Cycle Program. Only one SF value is determined for each compressor performance map. When calculate the potential changes of pressure ratio, flow coefficient, and work function during wet compression, the same shape factor of dry compression is assumed and is used for each stage such as by Eq. (4.6) below. This practice implicitly assumes the compressor performance map does not change, and the operating point of each stage during the wet compressor goes on an excursion within the same compressor performance map of the dry compression. This assumption may introduce some errors because Klepper et. al. (2004) showed the compressor performance maps changed with wet compression. Since the change of local stage during wet compression has been calculated by using a constant SP in several published papers, we can mathematically back calculate the SP if the operating condition of the local stage is known. To this end, seeing what the SF values are at each stage of this study is interesting. Although back calculating the SF for each stage is not the appropriate way to interpret the function of SF, it is hoped the results of this study will shed some light into the mysterious SF values and provide opportunities for improving the method of utilizing the generalized compressor performance curve.

The procedure for calculating SF value is shown below:

(a) Shape Factor is formulated in equation (4.6),

$$\psi^* = \psi^*_{max} - \frac{\left(\psi^*_{max} - 1\right)\left[\phi^*_{\psi_{max}} + SF\left(\phi^*_{\psi_{max}} - 1\right) - \phi^*\right]^2}{\left[\phi^*_{\psi_{max}} + SF\left(\phi^*_{\psi_{max}} - 1\right) - 1\right]^2} \tag{4.6}$$

This is manipulated as a quadratic equation of SF as:

$$a.\,SF^2 + b.\,SF + c = 0 \tag{4.7}$$

Where, $a = \frac{1-\psi^*}{\psi^*_{max} - 1}\left(\phi^*_{\psi_{max}} - 1\right)^2$,

$$b = 2\frac{\psi^*_{max} - \psi^*}{\psi^*_{max} - 1}\left(\phi^*_{\psi_{max}} - 1\right)^2 - 2\left(\phi^*_{\psi_{max}} - 1\right)\left(\phi^*_{\psi_{max}} - \phi^*\right),$$

$$c = \frac{\psi^*_{max} - \psi^*}{\psi^*_{max} - 1}\left(\phi^*_{\psi_{max}} - 1\right)^2 - \left(\phi^*_{\psi_{max}} - \phi^*\right)^2,$$

Here, $\psi^* = \frac{\psi}{\psi_D}$ and $\phi^* = \frac{\phi}{\phi_D}$ [Where D denotes for Design Value]

ψ^*_{max} is the maximum value of all stages

$\phi^*_{\psi_{max}}$ is the ϕ^* value for maximum ψ^*_{max}

According to Muir et. al. (1989) the SF values are between 0 and 1. The positive root, which is less than unity found from Eq. (4.6), is acceptable for this study because the stages are subsonic. Equation (4.6) is an empirical equation, so the SF value calculated from this equation serves only as a reference value and is subject to further verification. In Eq.(4.6) the normalized rotor work coefficient has to be greater than unity to find a solution for SF, otherwise Eq. (4.6) no longer holds true. This is based on the design practice that the design point is optimized and the off-design condition will require more compressor work. The condition of normalized rotor work coefficient being greater than unity has made Eq. (4.6) not applicable when inlet or interstage fogging is used, especially when the rotor work coefficient increases.

The result shows the stage SF value varies between 0.55 and zero for Case 2S, between 0.95 and zero for Case 2 and between 0.6 and -0.05 for fogging Case 3 (See Table 4.6). The negative SF value at stage 4 in Case 3 implies the air velocity is very high. The large variation of

SF values from stage to stage and from case to case implies the conventional practice of selecting a single SF value to represent one specific compressor, especially fogging/overspray, may not be appropriate and requires improvement. Some of the values of SF are out of range in Table 4.6. The approach of assigning a single SF value in employing the generalized compressor performance curve will be a subject for future study.

4.2.7 Overall GT System Analysis

The unexpected result of both increased compressor specific power and total power due to fogging raised our anxiety concerning finding out its impact on the overall gas turbine output and efficiency. To this end, the pressure ratio obtained from the stage-stacking result is used as input to the FogGT program Khan and Wang (2005 & 2006). In addition, the overall compressor efficiency is calculated from Eq. (4.8) and used by Wang and Khan (2008a) and provided as an input to FogGT.

$$\eta_c = \frac{r_P^{(k-1)/k} - 1}{r_P^{(k-1)/k\eta} - 1} \tag{4.8}$$

In the meantime, the overall compressor efficiency obtained by Eq. (4.8) is also compared with the isentropic compressor efficiency defined in Eq. (4.9) as the ratio of isentropic compressor power (Pc_s) and actual compressor power (P_c) from stage-stacking result.

$$\eta_{cs} = \frac{Pc_s}{P_c} \tag{4.9}$$

Since FogGT treats the compressor as a black box, the interstage fogging of Cases 4 and 5 cannot be adequately simulated before the stage-stacking scheme is fully incorporated into FogGT. Hence, only Case 3 is submitted for GT system simulation. The overall GT system performance and comparison between stage-stacking and non-stacking schemes are shown in Table 4.4.

First, let us examine the difference between the stage-stacking and FogGT (non-stacking) results of the overall compressor power. For Cases 1 and 2, the differences are small, at about

2.2% and 0.74%, respectively. For overspray Case 3, FogGT underpredicts the compressor power by about 6%. These differences are caused by minor differences of moist air specific heat, which is kept as a constant value of 1.38 during stage-stacking calculation as well as in Eq. (4.8) Nonetheless, FogGT, similar to the stage-stacking scheme, also calculates higher compressor power (P_c) and specific work (W_c) for Case 3 than non-fogging cases (1 and 2). Although ovespray requires more compressor power, it also produces higher pressure ratio. Therefore, to fairly evaluate the compressor performance, comparison of the power consumed by raising per unit pressure ratio is made. In Table 4.4, Case 3 shows improved compressor effectiveness by about 3% from Case 2 (0.97MW vs. 0.94MW per unit pressure ratio).

Table 4.4 Comparison of stage-stacking and non-stacking results for compressor and the GT system.

Cases		**Case 1**	**Case 2**	**Case 2S**	**Case 3**
CET (K)	Non-stacking	540.2	562.8	581.4	520.4
	Stacking	**541.9**	**557.9**	**551.1**	**533.4**
Specific Works	Wc (kJ/kg) [Non-stacking]	259.4	274.7	301.9	286.3
	Wc (kJ/kg) [Stacking]	**265.3**	**272.6**	**270.2**	**297.6**
	W_f (kJ/kg) [Non-stacking]	11.39	11.52	12.57	13.72
	W_t (kJ/kg) [Non-stacking]	592.2	592.1	633.7	648.5
	W_{net} (kJ/kg) [Non-stacking]	321.4	305.9	319.3	348.4
P_c (kW)	Non-stacking	6981	7078	7905	7497
	Stacking	**7139**	**7026**	**7093**	**7948**
	% of difference	**2.26%**	**-0.74%**	**-10.3%**	**6.01%**
P_f (kJ/kg) [non-stacking]		306.5	296.9	329.2	359.4
P_t (kJ/kg) [non-stacking]		15935	15259	16594	16981
P_{net} (kW)	Non-Stacking	8648	7883	8360	9124
	Stacking	**8490**	**7936**	**9172**	**8674**
	% of difference	**-1.83%**	**0.67%**	**9.71%**	**-4.94%**
Air flow rate (kg/s)		26.91	25.77	26.19	26.19
Inlet Air Density (kg/m^3)		1.222	1.170	1.193	1.213
Fuel flow rate (kg/s)		0.5787	0.5484	0.5484	0.6059
Thermal Efficiency [Non-stacking]		29.86%	28.73%	30.46%	30.09%
Overall Compressor Efficiency (%)	**From Pc_s/Pc**	**87.53**	**90.22**	**99.78**	**84.48**
	From Eq. 3	**89.51**	**89.55**	**89.53**	**89.56**
	% of difference	**2.26%**	**-0.74%**	**-10.3%**	**6.01%**
Pressure Ratio [Stacking]		**7.45**	**7.23**	**8.59**	**8.42**
Power/Pressure Ratio (kW) [Stacking]		958.4	971.9	825.4	943.8

(Net output power = Turbine power -fuel pump power -compressor power)

In Table 4.4, the compressor efficiency defined by Eq. (4.8) shows the compressor efficiency is not affected by overspray (89.55% vs. 89.56%). However, the isentropic efficiency defined by Eq. (4.9) shows a significant decrease from 90.22% to 84.54% due to fogging. It

seems puzzling why fogging results in such a big reduction of isentropic efficiency. A further investigation discovered that the referenced isentropic power for each case is different because the inlet temperature is different. The overspray case (Case 3) is based on a lower isentropic power than nonfogging case (Case 2). Hence, the isentropic efficiency reduces. Therefore, the most fair way for comparing the compressor effectiveness still goes back to the last row in Table 4.4, as Pc/p_r.

Regarding the turbine output, both the specific turbine output work (W_t) and the total turbine power (P_t) increase, resulting in a significant net GT output power increase of 15.7% for Case 3. Most people attribute the increased net GT output power to the increased mass flow rate for overspray cases. Actually, most of the credit should be given to the specific network output increase, which already contributes up to 14.1%. If the specific net output work were not increased much, we then could conclude that the increased net output is attributed to increased mass flow rate. Increased mass flow rate is not the major cause of increased GT output power because increased mass flow rate also contributes to increased consumption of compressor power. Despite the significant increase of GT net output power, the efficiency only increases 1.2 percentage points (or 4.7%). If the compressor power calculated by stage-stacking scheme is used for output power and efficiency calculation, the output enhancement will be 9.35%, and the thermal efficiency will be almost the same.

4.2.8 Comparison with Previous Studies in Compressor Power Consumption and Compressor Efficiency for Wet Compression

The present result of reduced isentropic compressor efficiency due to wet compression is consistent with Sanaye et. al. (2006) Abdelwahab (2006), and Roumeliotis and Mathioudakis (2007), but inconsistent with Bagnoli et. al. (2008 a, b). The present result of increased compressor power consumption due to wet compression is consistent with Bagnoli et. al. (2008 a) and Roumeliotis and Mathioudakis (2007), but inconsistent with Sanaye et. al. (2006) Abdelwahab (2006). The present result of increased specific compressor power due to wet compression, to the authors' knowledge, has not been presented by other researchers in the open literature. A recap of previous studies are summarized below:

Bagnoli et. al. (2008 b) used the Shape Factor for the calculation, but they did not mention the criteria for its selection. The shape factor determined the stage efficiency and

constant shape factor were used for all stages. Their results showed that compressor power increased with an increase of injected water and efficiency also increased with an increase of injected water. Sanaye et. al. (2006) also used constant shape factor value to calculate each stage performance and showed that the pressure ratio increases with an increase of injected water amount. Their results showed that both the compressor efficiency and compressor power decrease with an increase of injected water amount. Abdelwahab (2006) showed a shift in peak efficiency to higher flow rates as well as deterioration in the peak efficiency as the water injection rates increase. His results showed that stage speed increased due to water injection to achieve higher design pressure ratio. Both the power reduction capability and the polytropic efficiency decrease with the increase of the stage pressure ratio.

It is encouraging to know that the present results are supported by the recent experimental results from Roumeliotis and Mathioudakis (2007). They showed that the compressor power increased by water injection and the increased compressor power was linear with the quantity of water entering the stage. As a result, the compressor isentropic efficiency decreases linearly with the amount of water injected.

4.2.9 Summary on Equilibrium Method

Investigation on six fogging and non-fogging cases with equilibrium stage-stacking scheme gives the following result:

(a) The compressor performance of saturated fogging (dry compression) is strikingly differently from overspray (wet compression). The stage pressure ratio enhances during all fogging cases as does the overall pressure ratio. With saturated fogging (no overspray), the compressor achieves the highest pressure ratio and requires less specific compressor work than without fogging. However, the results of overspray and interstage spray unexpectedly show that both the specific and overall compressor power do not reduce but actually increase. Analysis shows this increased power is contributed by increased pressure ratio, and for interstage overspray, "recompression" contributes to more power consumption.

(b) Saturated fogging (Case 2S) brings down the specific compressor work from a hot ambient condition (Case 2); however, due to increased mass flow, the overall compressor power increases.

(c) It is unexpected to see that air density actually decreases, instead of increases inside the compressor with overspray. Analysis shows that overspray induces an excessive reduction of temperature which leads to an excessive reduction of pressure, so the increment of density due to reduced temperature is less than decrement of air density affected by reduced pressure as air follows the polytropic relationship. In contrast, saturated fogging results in increased density as expected.

(d) The compressor power/ pressure ratio values show that saturated fogging is most effective in producing pressure ratio, whereas interstage fogging is least effective.

(e) The local blade loading significantly increases immediately after the interstage spray. In this study, a 2% interstage fogging can increase the local blade loading up to 100%. This significant increase of local blade loading could induce rotating stall locally near the spray location.

(f) Overspray increases axial velocity, flow coefficient, the blade inlet velocity, the incidence angle, and the tangential component of velocity. Saturated fogging results in opposite phenomena.

(g) Shape factor used in the generalized compressor performance curve varies throughout the compressor stages in the present study. Therefore, using one single shape factor value throughout the compressor may not be adequate, nor is it appropriate to use the same shape factor value for both dry and wet compression.

(h) Using the pressure ratio obtained from stage-stacking scheme to calculate the overall GT performance shown non-stage-stacking system simulation could underpredict the compressor power by about 6% and net GT output by about 2% in 1% oversprayed case.

Table 4.5 Detailed stage-stacking data (pressures, temperature, velocity, flow coefficient, Mach numbers and density) for all cases. (Shaded areas represent the stator in corresponding stage and the non-shaded rows represent rotor stages.)

Stage	Stagnation Pressure (kpa)					
	Case 1	Case 2	Case 2S	Case 3	Case 4	Case 5
1	115.6	115.1	116.1	106.1	106.1	106.1
1.5	161.6	157.4	167.0	114.3	114.3	114.3
2	161.6	157.4	167.0	114.3	114.3	114.3
2.5	219.0	211.7	232.5	127.1	127.1	127.1
3	219.0	211.7	232.5	127.1	127.1	127.1
3.5	288.6	279.4	313.8	210.3	141.4	210.3
4	288.6	279.4	313.8	210.3	141.4	210.3
4.5	371.8	359.6	410.7	341.0	275.7	270.6
5	371.8	359.6	410.7	341.0	275.7	270.6
5.5	469.5	454.0	526.4	445.9	407.9	395.0
6	469.5	454.0	526.4	445.9	407.9	395.0
6.5	583.0	563.8	662.0	575.7	535.9	521.6
7	583.0	563.8	662.0	575.7	535.9	521.6
7.5	713.0	689.5	819.0	723.9	683.2	669.0
8	713.0	689.5	819.0	723.9	683.2	669.0
8.5	861.2	831.7	997.8	893.7	850.2	835.1

Stage	Static Pressure (kpa)					
	Case 1	Case 2	Case 2S	Case 3	Case 4	Case 5
1	101.3	101.3	101.3	101.3	101.3	101.3
1.5	134.9	132.2	138.2	107.2	107.2	107.2
2	144.9	139.3	148.1	107.3	107.3	107.3
2.5	185.9	180.1	196.4	114.4	114.4	114.4
3	202.3	188.6	209.2	112.0	112.0	112.0
3.5	248.5	240.4	268.9	165.2	121.3	165.2
4	271.9	251.2	285.8	159.7	115.0	132.7
4.5	324.1	312.8	356.8	282.8	219.2	209.2
5	355.0	325.7	377.8	300.7	218.8	213.5
5.5	413.6	398.7	462.4	381.2	340.7	326.0
6	452.8	414.2	488.6	399.8	356.0	341.3
6.5	518.2	499.5	587.0	500.8	459.9	445.0
7	566.2	517.8	618.4	524.4	480.2	464.3
7.5	639.0	615.4	732.4	638.2	597.0	582.4
8	696.2	636.4	769.2	667.2	622.3	606.8
8.5	777.3	748.2	899.8	796.9	752.8	737.6

Stage	Static Temperature (K)					
	Case 1	Case 2	Case 2S	Case 3	Case 4	Case 5
1	288.0	300.0	294.2	294.2	294.2	294.2
1.5	315.2	326.3	322.1	299.1	299.1	299.1
2	321.7	331.2	328.0	299.2	299.2	299.2
2.5	348.0	359.0	356.2	305.1	305.1	305.1
3	356.5	363.8	362.2	303.3	303.3	303.3
3.5	380.7	392.6	389.7	340.1	310.6	340.1
4	390.6	397.5	396.1	337.1	306.2	321.0
4.5	413.3	425.9	422.7	396.5	368.9	364.2
5	424.2	430.9	429.1	403.0	368.7	366.1
5.5	445.7	459.1	455.3	431.8	418.3	413.1
6	457.4	464.2	462.0	437.3	423.2	418.2
6.5	478.0	492.3	487.5	466.9	455.7	451.5
7	490.2	497.4	494.3	472.6	461.0	456.6
7.5	510.0	525.2	519.5	500.5	491.1	487.6
8	522.6	530.3	526.3	506.4	496.5	493.0
8.5	541.9	557.9	551.1	533.4	524.8	521.7

Stage	Density (kg/m³)					
	Case 1	Case 2	Case 2S	Case 3	Case 4	Case 5
1	1.2225	1.1705	1.1926	1.2131	1.2131	1.2131
1.5	1.4879	1.4049	1.4861	1.2550	1.2550	1.2550
2	1.5656	1.4583	1.5636	1.2556	1.2556	1.2556
2.5	1.8561	1.7391	1.9095	1.3017	1.3017	1.3017
3	1.9717	1.7973	2.0005	1.2845	1.2845	1.2845
3.5	2.2688	2.1226	2.3891	1.6709	1.3537	1.6709
4	2.4190	2.1901	2.4989	1.6302	1.3127	1.4177
4.5	2.7213	2.5386	2.9116	2.4538	2.0376	1.9699
5	2.9038	2.6123	3.0362	2.5674	2.0349	1.9991
5.5	3.2194	2.9983	3.5041	3.0111	2.7650	2.6811
6	3.4347	3.0814	3.6514	3.1179	2.8541	2.7705
6.5	3.7637	3.5076	4.1576	3.6698	3.4260	3.3437
7	4.0091	3.5985	4.3191	3.7953	3.5408	3.4531
7.5	4.3488	4.0499	4.8658	4.3585	4.1370	4.0636
8	4.6231	4.1479	5.0458	4.5021	4.2626	4.1882
8.5	4.9789	4.6346	5.6368	5.1114	4.8766	4.8047

Stage	Inlet Velocity (m/s)					
	Case 1	Case 2	Case 2S	Case 3	Case 4	Case 5
1	150.00	150.00	150.00	150.00	150.00	150.00
1.5	183.68	183.96	183.40	191.34	191.34	191.34
2	150.00	154.23	146.57	190.27	190.27	190.27
2.5	183.68	185.67	182.16	217.59	217.59	217.59
3	150.00	157.61	144.48	247.47	247.47	247.47
3.5	183.68	187.67	182.35	215.12	252.75	215.12
4	150.00	158.63	142.27	229.00	321.80	194.93
4.5	183.68	188.98	182.14	204.15	218.45	230.30
5	150.00	159.65	140.79	168.40	219.29	221.44
5.5	183.68	189.86	181.93	195.90	207.63	213.01
6	150.00	160.10	138.75	164.02	181.08	186.62
6.5	183.68	190.30	181.34	192.28	200.17	203.25
7	150.00	160.03	137.14	157.38	170.22	174.57
7.5	183.68	190.47	180.83	189.59	195.19	197.21
8	150.00	160.09	135.57	153.10	163.06	165.94
8.5	183.68	190.53	180.27	187.66	192.08	193.45

Stage	Absolute Mach Number					
	Case 1	Case 2	Case 2S	Case 3	Case 4	Case 5
1	0.440	0.431	0.435	0.439	0.439	0.439
1.5	0.515	0.507	0.508	0.553	0.553	0.553
2	0.417	0.422	0.402	0.550	0.550	0.550
2.5	0.491	0.488	0.480	0.620	0.620	0.620
3	0.396	0.411	0.378	0.708	0.708	0.708
3.5	0.469	0.471	0.459	0.578	0.714	0.578
4	0.378	0.396	0.356	0.618	0.919	0.538
4.5	0.450	0.455	0.440	0.508	0.563	0.597
5	0.363	0.382	0.337	0.416	0.565	0.573
5.5	0.433	0.440	0.423	0.465	0.500	0.516
6	0.349	0.369	0.321	0.387	0.433	0.449
6.5	0.418	0.426	0.408	0.440	0.462	0.471
7	0.337	0.357	0.306	0.358	0.391	0.402
7.5	0.405	0.413	0.394	0.419	0.434	0.440
8	0.327	0.345	0.293	0.336	0.361	0.368
8.5	0.393	0.401	0.381	0.402	0.413	0.417

Stage	Relative Mach Number					
	Case 1	Case 2	Case 2S	Case 3	Case 4	Case 5
1	0.953	0.932	0.932	0.949	0.949	0.949
1.5	0.661	0.659	0.659	0.802	0.802	0.802
2	0.902	0.900	0.900	1.090	1.090	1.090
2.5	0.629	0.627	0.627	0.913	0.913	0.913
3	0.856	0.862	0.862	1.258	1.258	1.258
3.5	0.602	0.594	0.594	0.792	1.036	0.792
4	0.818	0.821	0.821	1.109	1.457	1.211
4.5	0.577	0.567	0.567	0.586	0.733	0.727
5	0.784	0.787	0.787	0.819	1.020	1.011
5.5	0.556	0.544	0.544	0.559	0.598	0.609
6	0.755	0.757	0.757	0.779	0.831	0.846
6.5	0.537	0.524	0.524	0.525	0.555	0.564
7	0.730	0.730	0.730	0.734	0.772	0.785
7.5	0.520	0.508	0.508	0.499	0.522	0.528
8	0.707	0.707	0.707	0.699	0.728	0.737
8.5	0.504	0.492	0.492	0.476	0.496	0.502

Stage	Flow Coefficient (Φ)					
	Case 1	Case 2	Case 2S	Case 3	Case 4	Case 5
1	0.521	0.521	0.521	0.521	0.521	0.521
1.5	0.521	0.529	0.511	0.613	0.613	0.613
2	0.521	0.536	0.509	0.645	0.645	0.645
2.5	0.521	0.533	0.495	0.738	0.738	0.738
3	0.521	0.548	0.501	0.794	0.794	0.794
3.5	0.521	0.534	0.483	0.703	0.875	0.703
4	0.521	0.551	0.492	0.768	0.962	0.891
4.5	0.521	0.535	0.475	0.574	0.698	0.722
5	0.521	0.555	0.486	0.585	0.745	0.759
5.5	0.521	0.536	0.467	0.553	0.608	0.627
6	0.521	0.556	0.478	0.570	0.629	0.647
6.5	0.521	0.536	0.460	0.531	0.574	0.588
7	0.521	0.556	0.472	0.546	0.591	0.606
7.5	0.521	0.536	0.455	0.516	0.549	0.559
8	0.521	0.556	0.466	0.531	0.566	0.577
8.5	0.521	0.536	0.449	0.504	0.533	0.541

Table 4.6 Detailed stage-stacking data (work, flow, shape factor) for all cases

Stage	Stage Pressure Ratio					
	Case 1	Case 2	Case 2S	Case 3	Case 4	Case 5
1	1.398	1.368	1.438	1.077	1.077	1.077
2	1.355	1.345	1.392	1.112	1.112	1.112
3	1.318	1.320	1.350	1.655	1.112	1.655
4	1.288	1.287	1.309	1.622	1.951	1.287
5	1.263	1.263	1.282	1.308	1.479	1.460
6	1.242	1.242	1.258	1.291	1.314	1.321
7	1.223	1.223	1.237	1.257	1.275	1.283
8	1.208	1.206	1.218	1.235	1.244	1.248

Stage	Rotor Work Coefficient					
	Case 1	Case 2	Case 2S	Case 3	Case 4	Case 5
1	0.737	0.718	0.761	0.514	0.514	0.514
2	0.737	0.747	0.766	0.612	0.612	0.612
3	0.737	0.768	0.761	1.119	0.753	1.119
4	0.737	0.764	0.748	1.239	1.577	1.162
5	0.737	0.766	0.749	0.778	1.086	1.041
6	0.737	0.767	0.743	0.803	0.846	0.854
7	0.737	0.764	0.740	0.778	0.814	0.827
8	0.737	0.764	0.737	0.769	0.789	0.795

Stage	Stage Isentropic Power (KW)					
	Case 1	Case 2	Case 2S	Case 3	Case 4	Case 5
1	-821.0	-766.4	-826.8	-567.9	-567.9	-567.9
2	-821.0	-797.3	-832.3	-677.3	-677.3	-677.3
3	-821.0	-818.9	-827.6	-1237.4	-832.5	-1237.4
4	-821.0	-815.4	-813.3	-1370.2	-1760.7	-1297.2
5	-821.0	-817.2	-813.9	-860.7	-1213.0	-1161.8
6	-821.0	-818.7	-807.1	-888.5	-944.1	-953.8
7	-821.0	-815.1	-804.1	-860.1	-908.6	-923.1
8	-821.0	-814.8	-800.9	-850.0	-880.8	-887.6

Stage	Degree of Reaction					
	Case 1	Case 2	Case 2S	Case 3	Case 4	Case 5
1	0.816	0.820	0.810	0.872	0.872	0.872
2	0.816	0.823	0.796	0.999	0.999	0.999
3	0.816	0.817	0.781	1.018	1.146	1.018
4	0.816	0.810	0.770	0.870	1.056	0.926
5	0.816	0.807	0.762	0.798	0.871	0.857
6	0.816	0.804	0.756	0.795	0.817	0.821
7	0.816	0.803	0.752	0.786	0.805	0.810
8	0.816	0.803	0.748	0.779	0.796	0.800

Stage	de Haller Number					
	Case 1	Case 2	Case 2S	Case 3	Case 4	Case 5
1	0.726	0.737	0.712	0.854	0.854	0.854
2	0.726	0.726	0.703	0.850	0.850	0.850
3	0.726	0.716	0.698	0.671	0.835	0.671
4	0.726	0.716	0.699	0.573	0.558	0.640
5	0.726	0.715	0.695	0.710	0.628	0.642
6	0.726	0.713	0.694	0.694	0.692	0.693
7	0.726	0.714	0.693	0.699	0.697	0.695
8	0.726	0.714	0.692	0.699	0.701	0.702

Stage	Shape Factor					
	Case 1	Case 2	Case 2S	Case 3	Case 4	Case 5
1	N.A.	N.A.	N.A.	N.A.	N.A.	N.A.
2	N.A.	*	*	-0.463	*	*
3	N.A.	0.000	0.078	0.019	-0.490	0.488
4	N.A.	0.717	0.104	0.000	0.000	0.000
5	N.A.	0.642	0.326	*	*	0.079
6	N.A.	0.524	0.448	*	*	0.752
7	N.A.	0.951	0.554	0.598	*	0.414
8	N.A.	0.951	*	*	*	0.304

* Out of range

Table 4.7 Rotor-stator camber line geometries and stage information. Incidence angle i is for the i-th rotor stage and deviation angle δ is for the flow leaving i+0.5th stator.

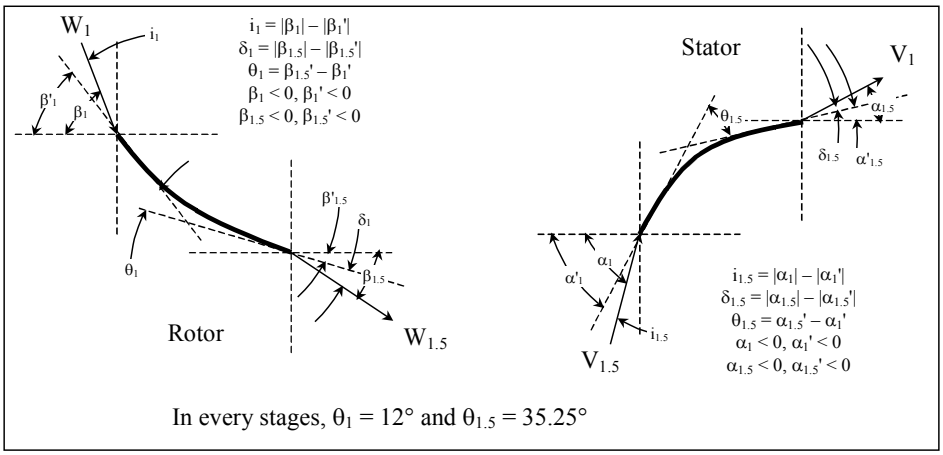

Stage	Hub to Tip Ratio	Tip Diameter (m)	Hub Diameter (m)	β1' / β1.5'	α1' / α1.5'	Case 1		Case 2		Case 2S		Case 3		Case 4		Case 5	
						i1 / δ1	i1.5 / δ1.5	i1 / δ1	i1.5 / δ1.5	i1 / δ1	i1.5 / δ1.5	i1 / δ1	i1.5 / δ1.5	i1 / δ1	i1.5 / δ1.5	i1 / δ1	i1.5 / δ1.5
1	0.6357	0.5600	0.3560	-62.47	0.00	0.00	0.00	0.00	0.00	0.00	0.00	0.00	0.00	0.00	0.00	0.00	0.00
1.5	0.6906	0.5418	0.3742	-50.47	35.25	0.00	0.00	0.00	-1.07	0.00	1.41	0.00	-12.53	0.00	-12.53	0.00	-12.53
2	0.7037	0.5376	0.3784	-62.47	0.00	0.00	0.00	0.42	-1.07	-0.27	1.41	1.97	-12.53	1.97	-12.53	1.97	-12.53
2.5	0.7442	0.5252	0.3908	-50.47	35.25	0.00	0.00	0.42	-0.94	-0.27	3.39	1.97	-22.55	1.97	-22.55	1.97	-22.55
3	0.7573	0.5212	0.3948	-62.47	0.00	0.00	0.00	0.96	-0.94	-0.22	3.39	3.80	-22.55	3.80	-22.55	3.80	-22.55
3.5	0.7857	0.5130	0.4030	-50.47	35.25	0.00	0.00	0.96	-0.17	-0.22	5.10	3.80	-15.30	3.80	-30.55	3.80	-15.30
4	0.7977	0.5095	0.4065	-62.47	0.00	0.00	0.00	1.30	-0.17	-0.30	5.10	5.02	-15.30	5.34	-30.55	8.28	-15.30
4.5	0.8181	0.5038	0.4122	-50.47	35.25	0.00	0.00	1.30	0.16	-0.30	6.06	5.02	0.75	5.34	-12.03	8.28	-9.65
5	0.8286	0.5009	0.4151	-62.47	0.00	0.00	0.00	1.53	0.16	-0.39	6.06	2.99	0.75	5.30	-12.03	6.41	-9.65
5.5	0.8441	0.4967	0.4193	-50.47	35.25	0.00	0.00	1.53	0.40	-0.39	7.08	2.99	0.41	5.30	-2.72	6.41	-3.17
6	0.8531	0.4943	0.4217	-62.47	0.00	0.00	0.00	1.65	0.40	-0.59	7.08	2.25	0.41	3.87	-2.72	4.48	-3.17
6.5	0.8651	0.4911	0.4249	-50.47	35.25	0.00	0.00	1.65	0.63	-0.59	7.81	2.25	2.15	3.87	-0.86	4.48	-1.60
7	0.8728	0.4891	0.4269	-62.47	0.00	0.00	0.00	1.70	0.64	-0.77	7.81	1.62	2.15	2.85	-0.86	3.28	-1.60
7.5	0.8822	0.4867	0.4293	-50.47	35.25	0.00	0.00	1.70	0.66	-0.77	8.43	1.62	3.17	2.85	0.69	3.28	0.10
8	0.8888	0.4850	0.4310	-62.47	0.00	0.00	0.00	1.71	0.66	-0.97	8.43	1.16	3.17	2.17	0.69	2.46	0.10
8.5	0.8963	0.4830	0.4330	-50.47	35.25	0.00	0.00	1.71	0.65	-0.97	8.94	1.16	4.12	2.17	1.70	2.46	1.10

4.3 Analysis of Compressor Performance by Stacking Method by Non-equilibrium Stacking Droplet Evaporation Method

The Non-equilibrium study uses the same compressor that was used for equilibrium method. The ISO condition (60°F and 60% Relative Humidity) is used as the design case, and the diameters (hub and tip diameters) are determined at the design condition. The axial velocity (150 m/s) is designed as a constant value throughout the compressor with the following parameters: rotor speed (12,000 RPM), rotor turning angle (12°), inlet pressure (1atm), 0.5% stagnation pressure loss occurred in each stator (which is different from equilibrium method) and polytorpic small stage efficiency (92%). A 2D compressor airfoil geometry and stage setting at the mean radii are employed. The detailed stator and rotor information are given in Table 4.13. Eight cases are studied with the ISO condition being the baseline (design case); one was studied on a hot day, one was studied on the same hot day with 2% overspray cooling and another was studied with saturation cooling (Case 2S), and the other four cases were studied with same 2% overspray cooling using non-equilibrium heat transfer model for droplet evaporation having four different droplet diameters (10μm, 15μm, 20μm and 30μm for cases 4, 5, 6 and 7 respectively):

Case 1: Designed baseline case at ISO condition (288K and 60% RH).

Case 2: Under hot weather at 300K and 60% RH

Case 2S: Saturation spray at the 1st rotor inlet at 300K and 60% RH (Equilibrium).

Case 3: 2% (wt) spray at the 1st rotor inlet at 300K and 60% RH (Equilibrium).

Case 4: Case 3 with droplet diameter of 10 μm (Non-equilibrium)

Case 5: Case 3 with droplet diameter of 15 μm (Non-equilibrium)

Case 6: Case 3 with droplet diameter of 20 μm (Non-equilibrium)

Case 7: Case 3 with droplet diameter of 30 μm (Non-equilibrium)

In Case 1 (design case), the axial velocity is kept as a constant in each stage by adjusting the flow area (i.e. hub and tip diameters). The variation of hub and tip diameters in different stages is shown in Fig. 4.26. For the cases of inlet fogging, the designed geometry is unchanged; the local flow velocity vector, thermal properties, rotor loading condition of each stage are calculated by the stage-stacking scheme. An example showing the effect of fogging on the velocity diagram is illustrated in Fig. 4.27 by juxtaposing the velocity diagrams of Stage 2 in

Cases 1, 3 and 4 for comparison between equilibrium and non-equilibrium cases. The following differences are observed:

a. All the velocity directions and magnitudes are changed. For example, the absolute rotor inlet velocity changes from purely axial direction to deviating 0.39° for Case 2, 1.89° for Case 3, and 1.94° for Case 4 from the axis.

b. The flow coefficient ($\phi = V_a/U$) increases 2.7% for Case 2, 22.3% for Case 3 and 23.6% for Case 3.

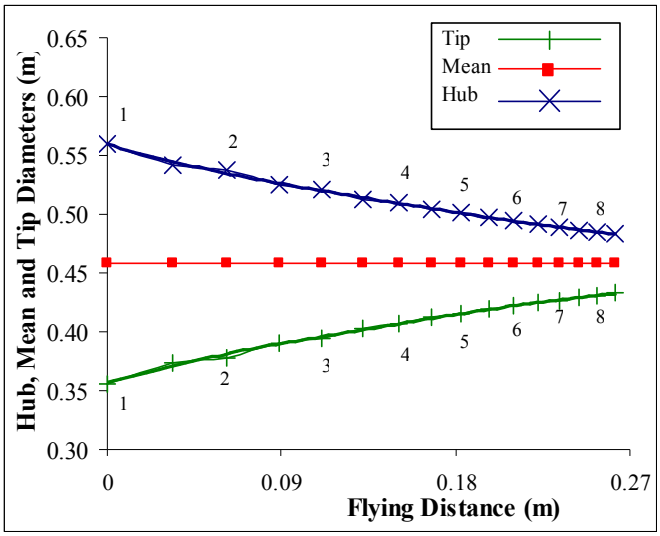

Figure 4.26 Designed compressor tip and hub diameters (the numbers on the top of the curves represent the stage numbers)

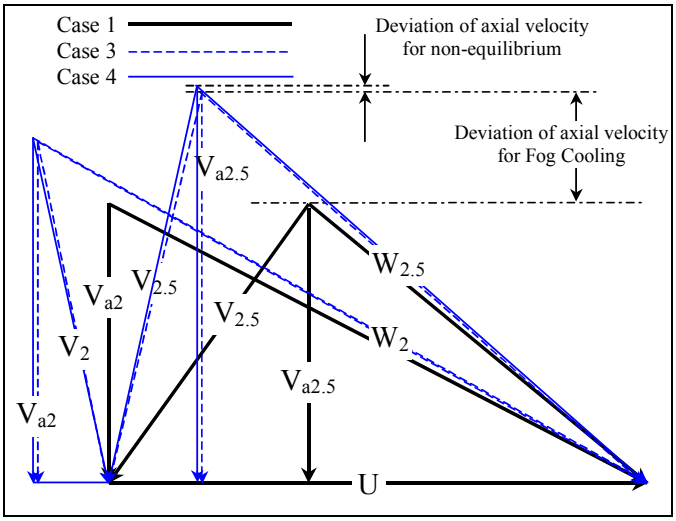

Figure 4.27 Comparison of velocity diagrams for cases 1, 3 and 4 in second stage (V_2 and W_2 for cases 3 and 4 almost coincide)

4.3.1 Effect on Droplet Size

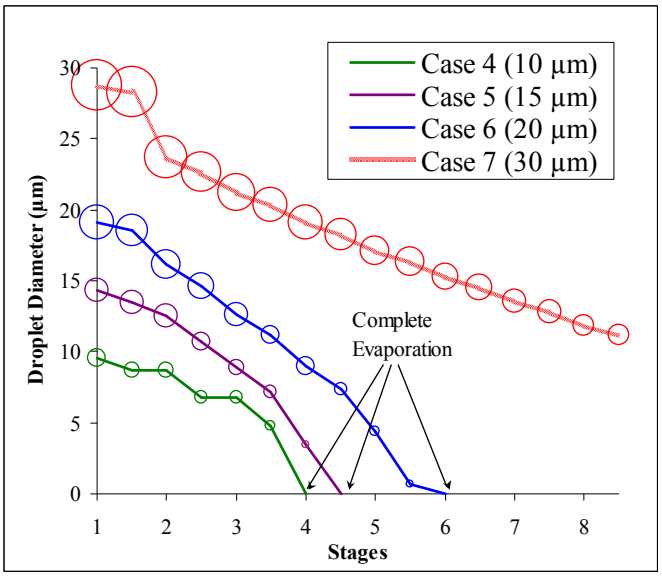

Figure 4.28 Reduction of diameter for non-equilibrium cases (The approximate diameter of the droplet is shown)

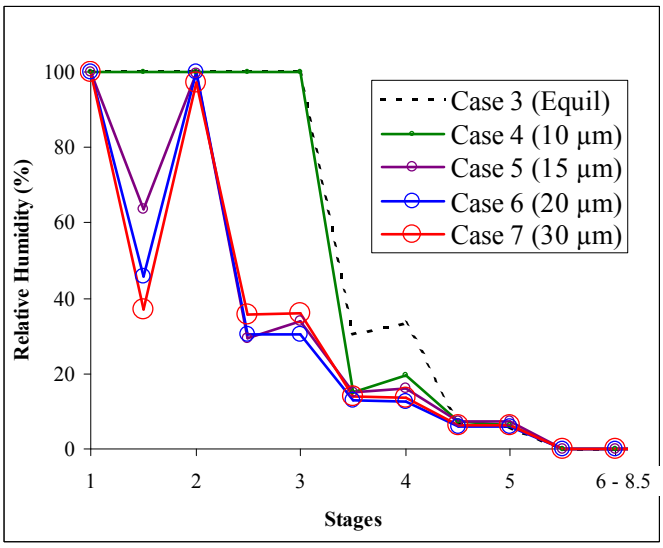

Figure 4.29 Variation of relative humidity for overspray cases

Figure 4.28 shows the droplet diameter variation in different stages. Droplets of all the cases evaporate completely before the compressor exit except Case 7. In general, evaporation is faster in the later stages due to an increase of droplet surface area over volume ratio with smaller droplets and increase of temperature. The water in Case 7 does not complete evaporation because the residence time is short comparing to the required evaporation time. The smallest droplet diameter found for this case is 11.2 µm (Table 4.11).

4.3.2 Effect on Evaporation Rate

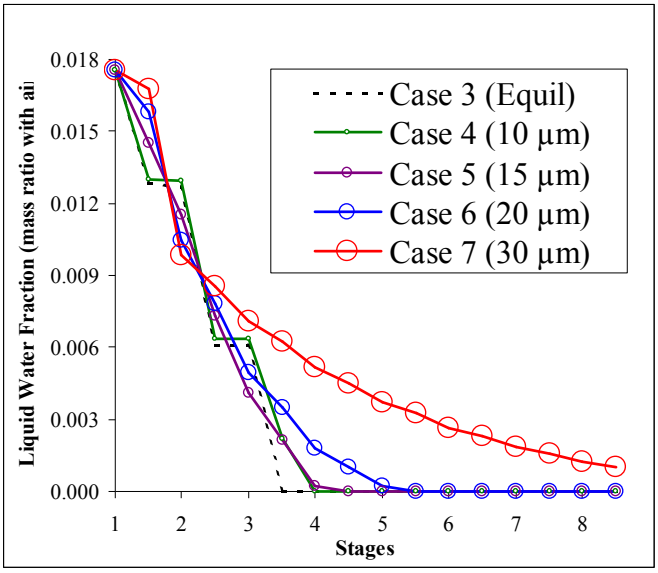

Figure 4.30 Variation of remaining liquid water fraction (mass ratio of water over moist air) in each stage for overspray cases

Evaporation rate depends on relative humidity, droplet size (diameter), water vapor diffusion coefficient, heat transfer to droplet, and surrounding temperature etc. In the equilibrium method, a sufficient amount of water is allowed to evaporate to achieve saturation (100% RH) at the end of each stage until all the water evaporates as shown in Case 3 in Fig 4.29. Figure 4.29 shows the relative humidity variation along the compressor, while Fig. 4.30 shows the remaining liquid water in the air. The status and composition of wet air can be clearly seen from the information provided by these two figures and Table 4.12. For example, in Case 3, there is sufficient water to achieve saturation until stage 3 (the third rotor); the water completely

evaporates at the end of stage 3.5 (the third stator), so the relative humidity is 100% for all stages up to the third rotor. After the third stage, the relative humidity generally reduces due to increased pressure and temperature in the later stages. For example, in the beginning of the fourth stage, the pressure is 164 kPa and temperature is 339K, for which saturation vapor pressure is 25.3 kPa and 0.113 kg of water per kg of air is needed to saturate the air, but only 0.0335 kg of vapor is available which gives a 30% relative humidity.

When non-equilibrium method is employed with the same conditions as Case 3, the result is shown as Case 4 in Fig 4.28. In Case 4, water evaporates completely at the end of stage 4, which is ½ stage later than Case 3. This implies that the result of using equilibrium method is very close to the non-equilibrium method for droplet size of 10 μm. However, when the droplet sizes increase, it takes longer for water to completely evaporate. Cases 5 and 6 show 15 μm and 20 μm droplets completely evaporate at stages 4.5 and 5.5, respectively. Again, droplets at 30μm do not completely evaporate at the exit of the compressor. There is about 6% (0.001kg vs. 0.0175kg) of the initial amount of water remains with the final droplet diameter at around 11.2 μm. This shows that the droplet diameter does not play any role in the equilibrium method, but significantly affect the droplet evaporation rate in the non-equilibrium method.

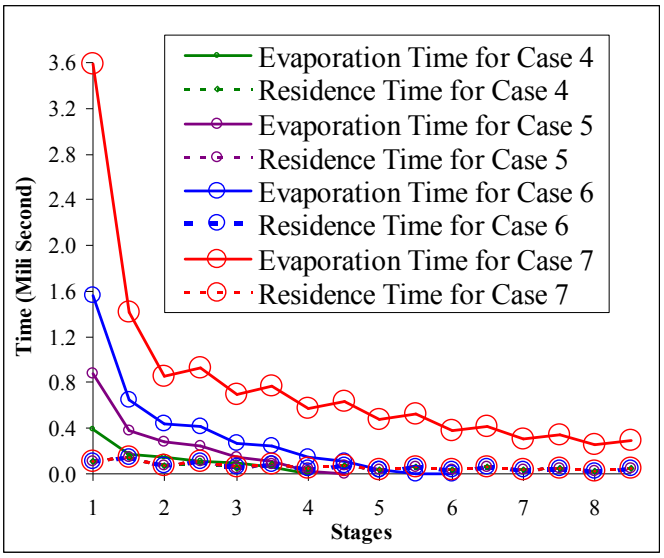

Figure 4.31 Residence time vs. evaporation time for non-equilibrium cases (Residence time for all four cases coincide with one another)

Evaporation of droplet is characterized by particle's aerodynamic residence time and the time required for evaporation as described in the model development. When the droplets reside inside a stage longer than the required evaporation time, all the droplets evaporate; on the other hand, if the aerodynamic residence time is shorter than the evaporation time, droplets become smaller and fly into next stage. Figure 4.31 shows the aerodynamic residence time are close (between 0.1-0.2 ms) for all droplet sizes at all stages; whereas the evaporation time varies significantly with the droplet sizes, roughly in proportional to diameter square (d^2). For example, at the first stage 30 μm droplets require 3.6 ms to evaporate versus 0.4 ms for 10 μm droplets, which is almost 9-fold shorter.

4.3.3 Effect on Air and Droplet Temperature

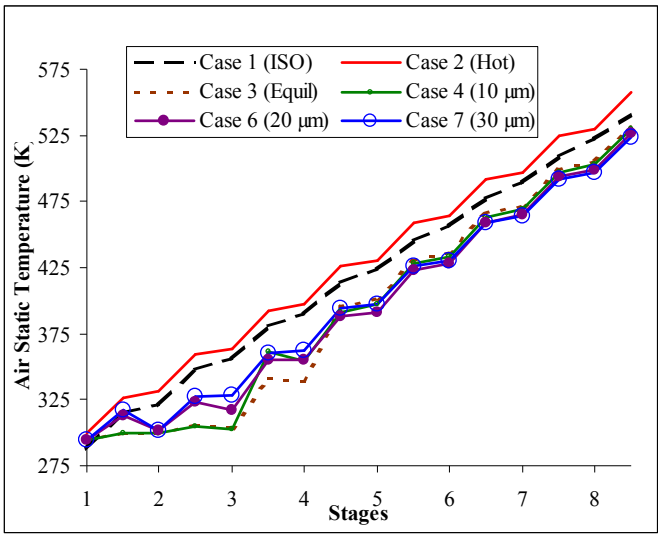

Figure 4.32 Air static temperature variations for all cases

Figure 4.32 shows the static temperature variation in different stages for all cases. The temperature for Case 2 is higher than Case 1 in every stage. In Case 3, the temperature drops 6°C, 31°C, and 60°C in the first three stages respectively from Case 2 and maintains a relatively constant value for the first three stages before the completion of evaporating all the water droplets. Non-equilibrium method (Case 4) results in a very similar evaporation and temperature reduction as equilibrium method (Case 3) except between stages 3 and 4 where the liquid completely evaporates in Case 3 but not in Case 4. Cases 6 and 7 have slower evaporation, which makes air temperature reduction less in the earlier four stages, but once all water evaporates and

the vapor is superheated downstream of stage 4.5, the curves for equilibrium and all non-equilibrium cases are almost coincided to one another, except Case 7 has a bit lower temperature due to its unfinished evaporation.

Figure 4.33 shows the droplet temperature variation and the difference between droplet and air temperatures. It is interesting to notice that the droplet temperature never catches up with the air temperature.

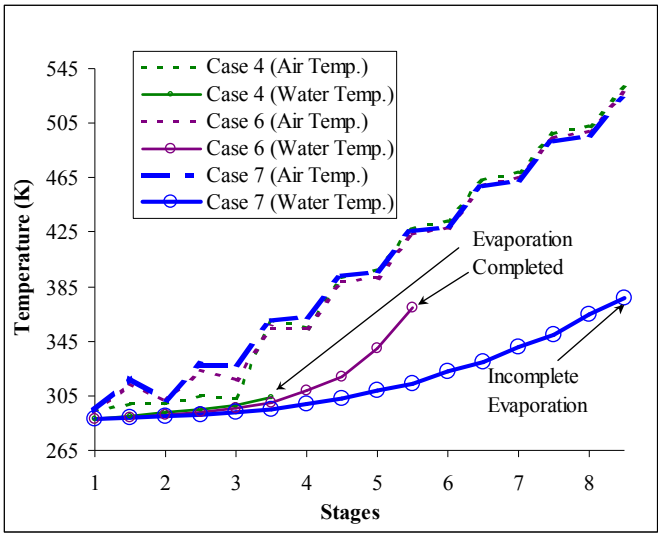

Figure 4.33 Air and droplet temperature variation for non-equilibrium cases

4.3.4 Effect on Velocity

In the design case (Case 1), the axial velocity, flow coefficient ($\Phi=V_{ax}/U$) and the inlet velocity at each rotor inlet is designed as the same value throughout the compressor by changing the air passage cross-sectional area to satisfy mass conservation. However, when fogging is applied, the air velocity increases significantly and then falls off to the values without fogging after water droplets completely evaporate. The variation of inlet velocity at each stage is shown in Fig. 4.34. Cases 1 and 2 only differ at the ambient temperature, so their inlet velocities follow a similar variation trend with Case 2's inlet velocities a bit higher. Significant increase of velocity occurs in stages 2 to 5 when fogging is applied in Cases 3 and 4. Both cases reach a peak velocity of 250 m/s at stage 3 rotor inlet. The only major difference between Cases 3 and 4 is at stage 4 where equilibrium method (Case 3) predicts a complete liquid evaporation showing

a continuous high velocity; whereas, Case 4 predicts only partial liquid evaporation with less temperature reduction and less velocity increase.

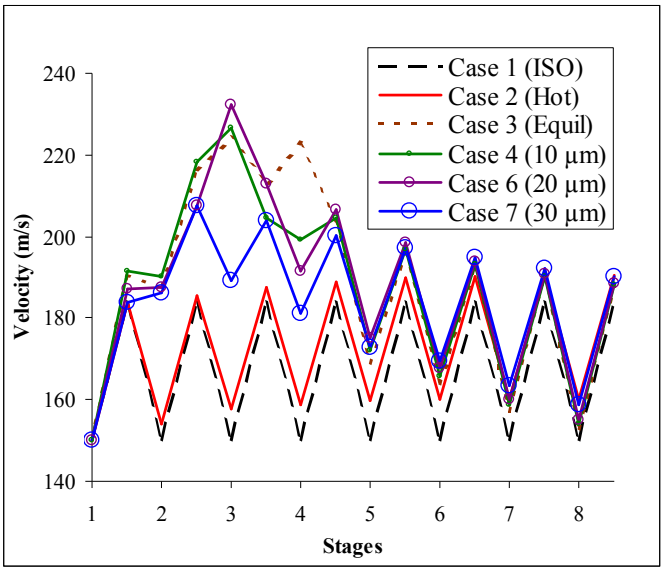

Figure 4.34 Inlet velocity variations for all cases

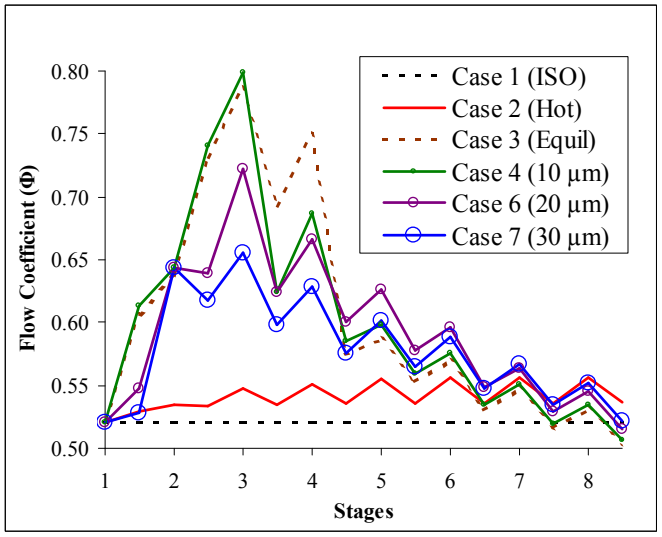

Figure 4.35 Flow coefficient variations for all cases

As the temperature drops due to fogging in Cases 3 and 4 (Fig. 4.32) the static pressure also drops from Stages 2 to 5 (Fig. 4.36), which results in a reduction of density and an increase in axial velocity to conserve the mass. This is also reflected in the flow coefficient increase in

Fig. 4.35. On the other hand, due to slower evaporation of larger droplets in Cases 6 and 7, temperature does not have any sudden drop, so these two cases have less drastic changes in velocity and flow coefficient. Overall speaking, all the fogging cases (Cases 3-7) have higher flow coefficients until 7th stage; afterwards their flow coefficients drop below Case 2. This behavior is consistent with the results obtained by White and Meacock (2004), where they showed that the flow coefficient (ϕ) increases till third stage and then decreased and eventually got lower than the dry compression values.

Combining the information obtained in Figs. 4.32 and 4.35, the results show that the flow coefficient must significantly increase to accommodate more mass flow rate contributed by overspray especially when the air (not air-liquid mixture) density reduces, as shown in Fig. 4.36, rather than increases after overspray is applied. The trend of decreased air density with overspray fogging seems counter-intuitive initially, but this phenomenon has specifically explained earlier in 4.2.3.

4.3.5 Effect on Pressure

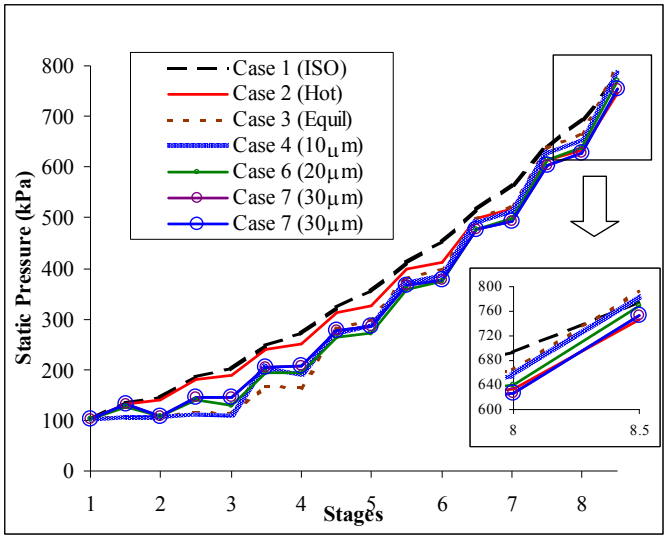

Figure 4.36 Stage static pressure variation for all cases

The static pressure distributions are shown in Fig. 4.36. Saturated fogging (Case 2S) increases static pressure as expected, while overspray reduces the local static pressure due to continuous water evaporation inside the compressor. Equilibrium method (Case 3) results in

lower static pressure between stages 3 and 4, but ends up with a little higher pressure than non-equilibrium cases.

Figures 4.39 and 4.40 show the local and accumulative stagnation pressure ratios. Again, Case 2S (saturated fogging) is shown to achieve the highest overall stagnation pressure ratio (8.54), which is noticeably above the stagnation pressure ratio from non-equilibrium Cases 4, 5, 6 and 7 with the values of 7.63, 7.58, 7.48 and 7.33, respectively (see Fig. 4.40 or Table 4.10).

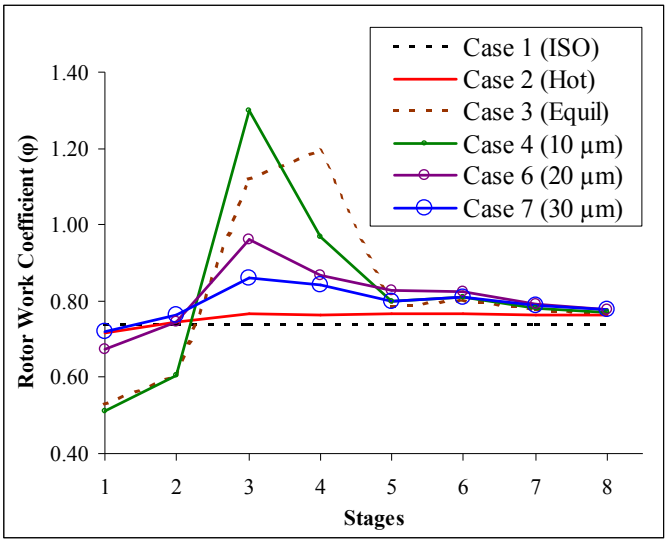

Figure 4.37 Rotor work coefficient (ψ) variation for all cases

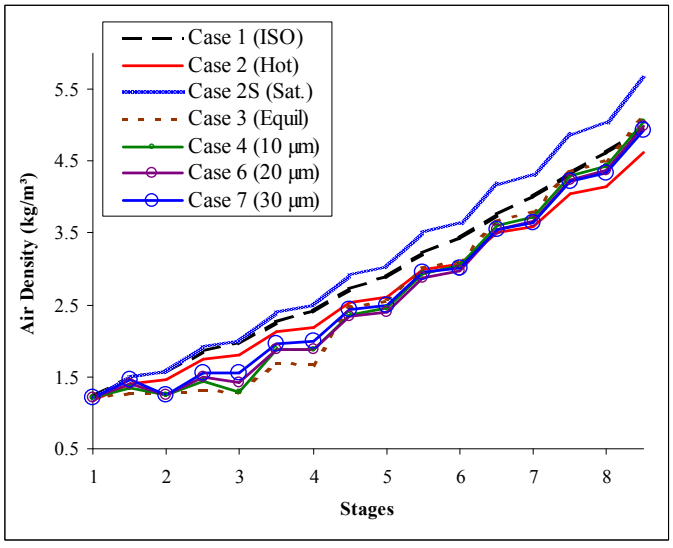

Figure 4.38 Moist air density variation for all cases

For Case 2, when ambient is hot, the local stagnation pressure ratio at the first stage drops from 1.396 of the ISO condition (Case 1) to 1.366. At the last stage, the local stagnation pressure ratio of Case 2 is 1.206 versus 1.208 of Case 1. When fogging is applied in Case 3, the local stagnation pressure ratio experiences a significant drop from 1.4 to 1.0 at the first stage due to reduced temperature, but the local stagnation pressure ratios of Stags 2-4 immediately rise above 1.6, indicating the rotors of these two stages work very hard as evidenced in their high work coefficients (ψ) shown in Fig. 4.37. Not until the fifth stage, does the local stagnation pressure ratio of Case 3 reduce to a level around 1.32, which is about 5% higher than Case 1.

When non-equilibrium method is applied in Case 4, the local stagnation pressure ratio is higher than those calculated by equilibrium method in Case 3 at stages 1-3. An obvious difference between Case 3 and 4 (or equilibrium versus non-equilibrium approaches) is between Stage 3 and 4 where all liquid is predicted completely evaporated in Cases 3 but not yet in Case 4. This difference results in more cooling, lower static temperature (Fig. 4.32), lower static pressure (Fig. 4.36), and lower density (Fig. 4.38) in Case 3, but higher local stagnation pressure ratio between stages 3.5 and 5 than in Case 4. More liquid evaporated accompanied with low overall density leads to more volume flow rate and hence higher inlet velocity (Fig. 4.34) and flow coefficient (Fig. 4.35) for Case 3 between stages 3.5 and 4.

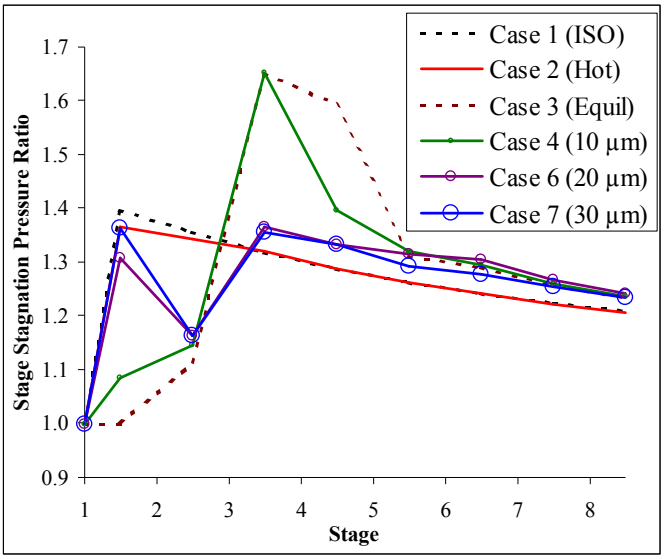

Figure 4.39 Stage overall stagnation pressure ratio variation for all cases

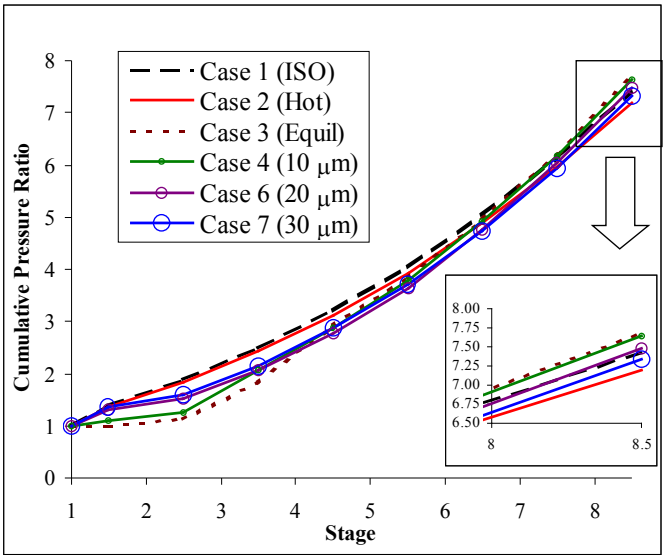

Figure 4.40 Cumulative overall stagnation pressure ratio variation for all cases

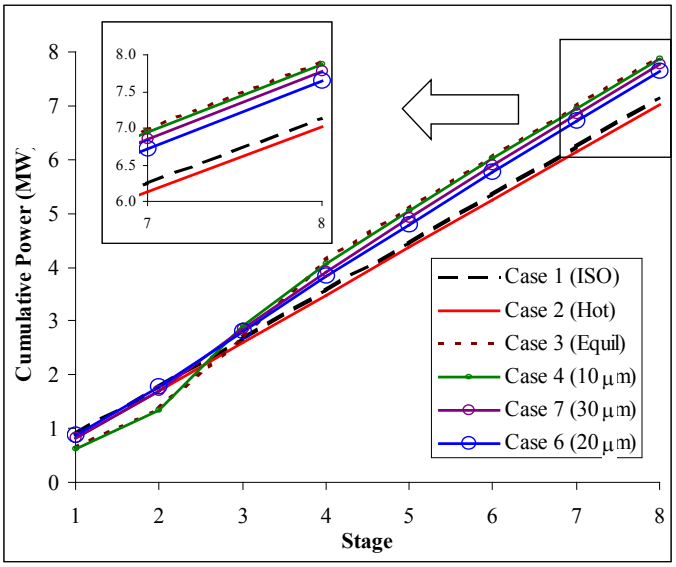

Figure 4.41 Cumulative stagnation compressor power variation for all cases

4.3.6 Effect on Compressor Power

The required compressor power (MW) is shown in Fig. 4.41 and the specific work (kW/(kg/s) = kJ/kg) in P-v diagram is shown in Fig. 4.42. In contrast to saturated fogging which actually reduces compressor power, overspray (Cases 3 versus Case 2) increases both specific

compressor work by 8.65% due to increased pressure ratio and the total compressor power by 12.6% due to increased mass flow rate. This seemingly counter-intuition phenomenon was explained in detail previously in 4.2.5 and is not repeated here. Basically, overspray increases stagnation pressure ratio and the compressor work increases, which can be represented by the area on the left of the compression curve on the P-v diagram.

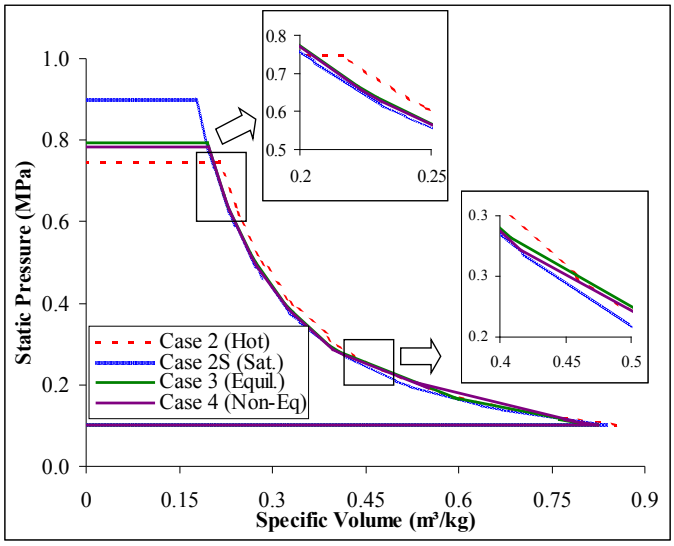

Figure 4.42 P-v diagram to show specific work for four cases

The specific work for Case 3 (272 kJ/kg) is very close to Case 4 (271 kJ/kg). The total powers for both cases are also very close (7.909 MW vs. 7.873 MW) because their mass flow rates are identical (26.71 kg/s) as shown in Table 4.8. As the diameter increases from 10 μm to 30 μm, the specific work decreases from 271 to 263 kJ/kg. Since less power is used to produce less pressure ratio, a fair way to compare the compressor performance is to compare the compressor power per unit increase of pressure ratio (W_c/P_r) in Table 4.8. As it can be seen, equilibrium method (Case 3) predicts more efficient compression with W_c/P_r = 1028 kW than non-equilibrium Case 4 with W_c/P_r = 1031 kW by assuming instantaneous water evaporation. Case 2S, having achieved W_c/P_r = 830 kW, is the most effective in all cases due to its complete evaporation before compression. This fact is revealed in Fig. 4.42, which shows the P-v curve of Case 2s is situated at the leftmost of all the curves and requires the least amount of specific work (248 kJ/kg) among all cases, although it produces the highest stagnation pressure ratio (8.54).

Among the four non-equilibrium cases, Case 4 with 10 μm (smallest droplet) is most effective among the 4 non-equilibrium cases and Case 7 (30 μm droplet) is the least effective.

Table 4.8 Overall compressor performance and net gas turbine output power

Cases	Mass flow rate (kg/s)	Specific Work (kJ/kg)	Comp. Power (MW)	P_r	Comp. Power /P_r (kW)	Net GT Output (MW)
1	26.91	244	7.139	7.42	962	8.609
2	25.77	251	7.024	7.20	975	7.904
2S	26.25	248	7.088	8.54	830	8.357
3	26.71	272	7.909	7.69	1028	9.039
4	26.71	271	7.873	7.63	1031	9.057
5	26.71	270	7.838	7.57	1035	8.971
6	26.71	268	7.780	7.48	1040	8.912
7	26.71	263	7.647	7.34	1042	8.912

The present result of increased compressor power consumption due to wet compression is consistent with Bagnoli et. al. (2006), Roumeliotis and Mathioudakis (2007) and Wang and Khan (2008a, b), but inconsistent with Abdelwahab (2006) and Sanaye et. al. (2006). It is encouraging to know that the present results are supported by the recent experimental results from Roumeliotis and Mathioudakis (2007). They showed that the compressor power increased by water injection and the increased compressor power was linear with the quantity of water entering the stage. As a result, the compressor isentropic efficiency decreases linearly with the amount of water injected.

Although the compressor power consumption increases in the saturated fogging and overspray cases, the total gas turbine net power increases nonetheless.

Table 4.9 Detailed stage-stacking data (pressures, temperature, velocity, flow coefficient, Mach numbers and density) for all cases. (Shaded areas represent the stator in corresponding stage and the non-shaded rows represent rotor stages.)

Stage	Stagnation Pressure (kPa)						
	Case 1	Case 2	Case 3	Case 4	Case 5	Case 6	Case 7
1	115.6	115.1	115.7	115.7	115.7	115.7	115.7
1.5	161.6	157.4	115.7	125.6	142.5	151.6	158.0
2	161.4	157.2	115.7	125.6	142.4	151.4	157.8
2.5	218.9	211.5	128.7	143.9	168.3	176.3	183.9
3	218.6	211.2	128.6	143.8	168.1	176.2	183.7
3.5	288.5	279.0	212.9	250.6	243.1	240.6	249.5
4	288.1	278.6	212.5	250.0	242.8	240.5	249.2
4.5	371.4	358.9	339.1	330.2	325.8	321.1	332.6
5	371.0	358.5	338.5	329.8	325.4	320.7	332.2
5.5	468.9	453.0	444.5	436.1	432.4	422.4	429.7
6	468.4	452.5	443.9	435.5	431.9	421.9	429.2
6.5	582.0	562.5	574.0	565.1	561.3	551.1	549.4
7	581.4	561.9	573.3	564.5	560.7	550.4	548.8
7.5	711.6	687.5	721.8	712.7	709.8	698.1	688.7
8	710.9	686.9	721.1	712.0	708.0	697.3	688.0
8.5	859.2	829.1	891.0	881.3	877.2	866.1	850.1

Stage	Static Pressure (kPa)						
	Case 1	Case 2	Case 3	Case 4	Case 5	Case 6	Case 7
1	101.3	101.3	101.3	101.3	101.3	101.3	101.3
1.5	134.9	132.2	108.5	107.2	117.0	125.6	131.5
2	144.7	139.3	108.7	107.3	107.7	108.4	108.7
2.5	185.8	180.0	115.7	113.9	132.9	139.9	146.2
3	201.9	188.4	113.3	111.3	114.4	129.0	146.7
3.5	248.4	240.1	167.9	205.3	193.9	191.1	203.6
4	271.4	250.7	164.1	191.5	193.9	193.0	207.9
4.5	323.8	312.2	281.4	272.1	267.9	264.1	277.8
5	354.3	325.0	298.5	288.3	283.1	272.2	286.6
5.5	413.1	397.8	379.9	371.2	367.5	357.2	366.3
6	451.7	413.1	398.2	388.9	384.9	373.8	378.2
6.5	517.3	498.2	499.3	490.4	486.6	476.2	475.6
7	564.6	516.2	522.6	513.2	509.2	498.3	493.2
7.5	637.7	613.7	636.2	627.2	623.4	612.8	604.1
8	694.1	634.3	664.9	655.1	650.9	639.5	627.0
8.5	775.4	745.8	794.2	784.4	780.3	769.2	753.8

Stage	Static Temperature (K)						
	Case 1	Case 2	Case 3	Case 4	Case 5	Case 6	Case 7
1	288.0	300.0	294.2	294.2	294.2	294.2	294.2
1.5	315.2	326.3	299.5	299.2	307.1	313.3	317.5
2	321.5	331.2	299.7	299.3	300.4	301.4	301.9
2.5	348.0	358.9	305.4	305.0	318.8	323.5	327.7
3	356.4	363.6	303.8	303.2	306.4	316.7	328.0
3.5	380.7	392.4	341.0	361.0	355.4	354.9	360.2
4	390.4	397.3	339.0	354.4	355.4	354.9	362.2
4.5	413.2	425.7	395.2	391.5	389.7	388.1	393.7
5	424.0	430.6	401.4	397.5	395.5	391.3	397.0
5.5	445.6	458.9	430.6	427.8	426.6	423.1	426.1
6	457.1	463.9	436.0	433.1	431.8	428.2	429.7
6.5	477.8	492.0	465.6	463.3	462.2	459.4	459.2
7	489.9	497.0	471.3	468.8	467.8	465.0	463.7
7.5	509.8	524.8	499.1	497.1	496.2	493.8	491.8
8	522.3	529.8	505.0	502.9	501.9	499.4	496.7
8.5	541.6	557.5	531.9	530.0	529.2	527.1	524.0

Stage	Density (kg/m^3)						
	Case 1	Case 2	Case 3	Case 4	Case 5	Case 6	Case 7
1	1.222	1.170	1.213	1.213	1.213	1.213	1.213
1.5	1.488	1.405	1.268	1.255	1.337	1.409	1.458
2	1.564	1.458	1.269	1.256	1.253	1.255	1.256
2.5	1.856	1.738	1.314	1.296	1.448	1.503	1.553
3	1.969	1.795	1.294	1.275	1.292	1.411	1.554
3.5	2.268	2.120	1.694	1.879	1.883	1.881	1.961
4	2.416	2.187	1.666	1.818	1.879	1.876	1.989
4.5	2.719	2.535	2.450	2.406	2.365	2.344	2.442
5	2.899	2.608	2.559	2.508	2.463	2.395	2.497
5.5	3.216	2.993	3.009	2.974	2.939	2.881	2.948
6	3.428	3.075	3.115	3.077	3.040	2.978	3.014
6.5	3.759	3.501	3.669	3.634	3.599	3.542	3.551
7	4.001	3.591	3.793	3.758	3.724	3.667	3.648
7.5	4.342	4.041	4.357	4.326	4.295	4.244	4.211
8	4.613	4.137	4.500	4.466	4.432	4.377	4.324
8.5	4.970	4.623	5.108	5.074	5.042	4.990	4.924

Stage	Inlet Velocity (m/s)						
	Case 1	Case 2	Case 3	Case 4	Case 5	Case 6	Case 7
1	150.0	150.0	150.0	150.0	150.0	150.0	150.0
1.5	183.7	184.0	190.6	191.4	187.2	184.9	183.9
2	150.0	154.1	187.5	190.1	187.7	185.9	186.1
2.5	183.7	185.6	216.0	218.2	207.4	207.4	207.5
3	150.0	157.6	223.9	226.8	232.3	209.6	189.2
3.5	183.7	187.6	213.3	204.4	213.0	210.8	204.0
4	150.0	158.6	222.7	199.2	191.6	192.1	181.0
4.5	183.7	188.9	203.4	204.5	206.7	206.1	200.2
5	150.0	159.7	168.7	172.1	175.3	180.3	172.9
5.5	183.7	189.8	195.7	196.9	198.4	200.6	197.1
6	150.0	160.1	163.9	165.9	167.9	171.4	169.4
6.5	183.7	190.3	192.2	193.0	194.0	195.5	194.8
7	150.0	160.0	157.2	158.6	160.0	162.5	163.3
7.5	183.7	190.4	189.5	190.1	190.7	191.7	192.3
8	150.0	160.1	152.9	154.0	155.1	157.0	158.9
8.5	183.7	190.5	187.5	188.0	188.5	189.4	190.3

Stage	Absolute Mach Number						
	Case 1	Case 2	Case 3	Case 4	Case 5	Case 6	Case 7
1	0.440	0.431	0.439	0.439	0.439	0.439	0.439
1.5	0.515	0.507	0.551	0.553	0.535	0.523	0.518
2	0.417	0.421	0.541	0.549	0.541	0.535	0.534
2.5	0.491	0.487	0.615	0.622	0.579	0.575	0.572
3	0.396	0.411	0.639	0.713	0.660	0.586	0.520
3.5	0.469	0.471	0.573	0.527	0.561	0.556	0.535
4	0.378	0.396	0.6	0.510	0.504	0.506	0.473
4.5	0.450	0.455	0.507	0.516	0.519	0.519	0.502
5	0.363	0.382	0.417	0.430	0.437	0.452	0.431
5.5	0.433	0.440	0.466	0.472	0.474	0.482	0.473
6	0.349	0.369	0.387	0.395	0.399	0.409	0.404
6.5	0.418	0.426	0.44	0.444	0.446	0.451	0.450
7	0.337	0.357	0.358	0.363	0.366	0.373	0.375
7.5	0.405	0.413	0.419	0.422	0.423	0.426	0.429
8	0.327	0.346	0.336	0.340	0.342	0.347	0.353
8.5	0.393	0.401	0.402	0.404	0.405	0.408	0.411

Stage	Relative Mach Number						
	Case 1	Case 2	Case 3	Case 4	Case 5	Case 6	Case 7
1	0.953	0.932	0.949	0.949	0.949	0.949	0.949
1.5	0.661	0.659	0.793	0.802	0.744	0.700	0.672
2	0.902	0.899	1.078	1.089	1.048	1.012	0.991
2.5	0.629	0.628	0.905	0.918	0.784	0.736	0.699
3	0.857	0.862	1.245	1.264	1.150	1.056	0.979
3.5	0.602	0.595	0.74	0.655	0.655	0.665	0.650
4	0.818	0.822	1.087	0.940	0.928	0.938	0.908
4.5	0.577	0.568	0.59	0.602	0.609	0.620	0.605
5	0.785	0.787	0.823	0.838	0.848	0.866	0.845
5.5	0.556	0.545	0.56	0.567	0.571	0.580	0.574
6	0.756	0.757	0.781	0.790	0.794	0.806	0.801
6.5	0.537	0.525	0.525	0.530	0.533	0.539	0.541
7	0.730	0.731	0.735	0.741	0.744	0.753	0.756
7.5	0.520	0.508	0.499	0.503	0.505	0.510	0.515
8	0.707	0.708	0.7	0.702	0.705	0.713	0.720
8.5	0.504	0.493	0.477	0.480	0.482	0.486	0.492

Stage	Flow Coefficient (Φ)						
	Case 1	Case 2	Case 3	Case 4	Case 5	Case 6	Case 7
1	0.521	0.521	0.521	0.521	0.521	0.521	0.521
1.5	0.521	0.529	0.607	0.613	0.576	0.547	0.528
2	0.521	0.535	0.637	0.644	0.646	0.644	0.644
2.5	0.521	0.533	0.731	0.741	0.663	0.639	0.618
3	0.521	0.547	0.787	0.799	0.789	0.722	0.655
3.5	0.521	0.534	0.692	0.624	0.623	0.624	0.598
4	0.521	0.551	0.750	0.687	0.665	0.666	0.628
4.5	0.521	0.536	0.574	0.585	0.595	0.600	0.576
5	0.521	0.555	0.586	0.598	0.609	0.626	0.601
5.5	0.521	0.536	0.553	0.559	0.566	0.578	0.565
6	0.521	0.556	0.569	0.576	0.583	0.596	0.588
6.5	0.521	0.536	0.530	0.535	0.540	0.549	0.548
7	0.521	0.556	0.546	0.551	0.556	0.564	0.567
7.5	0.521	0.536	0.516	0.519	0.523	0.529	0.534
8	0.521	0.556	0.530	0.534	0.538	0.545	0.552
8.5	0.521	0.537	0.503	0.507	0.510	0.515	0.522

Table 4.10 Detailed stage-stacking data (pressure ratio, power, rotor work coefficient, deHaller number) for all cases

Stage	Stage Pressure Ratio						
	Case 1	Case 2	Case 3	Case 4	Case 5	Case 6	Case 7
1	1.396	1.366	1.000	1.085	1.231	1.308	1.364
2	1.355	1.344	1.112	1.146	1.181	1.164	1.164
3	1.318	1.319	1.651	1.652	1.444	1.365	1.356
4	1.288	1.287	1.593	1.395	1.341	1.333	1.333
5	1.263	1.262	1.311	1.321	1.327	1.316	1.292
6	1.241	1.242	1.291	1.295	1.298	1.305	1.278
7	1.223	1.222	1.258	1.260	1.263	1.267	1.254
8	1.208	1.206	1.234	1.236	1.238	1.241	1.234
Overall	**7.436**	**7.199**	**7.684**	**7.634**	**7.582**	**7.481**	**7.333**

Stage	Stage Power (KW)						
	Case 1	Case 2	Case 3	Case 4	Case 5	Case 6	Case 7
1	892.4	833.0	634.5	617.1	725.8	811.6	865.3
2	892.4	864.6	725.5	725.8	885.1	897.5	918.2
3	892.4	889.8	1346.0	1562.8	1360.1	1155.1	1032.2
4	892.4	886.2	1435.8	1165.3	1038.3	1041.2	1011.4
5	892.4	888.3	942.3	962.5	975.3	995.2	961.6
6	892.4	889.9	966.7	973.7	979.3	991.7	974.3
7	892.4	886.1	934.7	939.9	944.8	953.0	949.2
8	892.4	885.8	923.2	925.9	929.0	934.6	935.1
Overall	**7139**	**7024**	**7909**	**7873**	**7838**	**7780**	**7647**

Stage	Rotor Work Coefficient						
	Case 1	Case 2	Case 3	Case 4	Case 5	Case 6	Case 7
1	0.737	0.718	0.528	0.513	0.604	0.675	0.720
2	0.737	0.746	0.604	0.604	0.736	0.747	0.764
3	0.737	0.767	1.120	1.300	1.132	0.961	0.859
4	0.737	0.764	1.195	0.969	0.864	0.866	0.841
5	0.737	0.766	0.784	0.801	0.811	0.828	0.800
6	0.737	0.767	0.804	0.810	0.815	0.825	0.811
7	0.737	0.764	0.778	0.782	0.786	0.793	0.790
8	0.737	0.764	0.768	0.770	0.773	0.778	0.778

Stage	de Haller Number						
	Case 1	Case 2	Case 3	Case 4	Case 5	Case 6	Case 7
1	0.726	0.737	0.846	0.855	0.803	0.762	0.736
2	0.726	0.727	0.851	0.854	0.773	0.755	0.736
3	0.726	0.716	0.666	0.592	0.615	0.668	0.696
4	0.726	0.716	0.586	0.652	0.688	0.691	0.695
5	0.726	0.715	0.709	0.705	0.702	0.700	0.707
6	0.726	0.713	0.694	0.693	0.693	0.692	0.698
7	0.726	0.715	0.699	0.699	0.699	0.698	0.701
8	0.726	0.715	0.699	0.699	0.699	0.699	0.702

Table 4.11 Non-equilibrium data (Droplet temperature, diameter, evaporation/boiling time, residence time) for all cases

Stage	Droplet Temp. (K)			
	Case 4	Case 5	Case 6	Case 7
1	288.0	288.0	288.0	288.0
1.5	289.9	289.5	289.2	288.7
2	292.7	291.8	291.1	289.8
2.5	294.5	293.8	292.7	290.8
3	297.7	297.3	295.9	292.9
3.5	304.1	302.2	299.6	295.0
4	351.0	319.0	308.6	299.0
4.5	392.4	389.7	318.4	302.6
5	398.3	395.5	339.5	308.8
5.5	428.6	426.5	369.3	314.1
6	433.9	431.8	428.2	322.5
6.5	463.9	462.2	459.4	329.6
7	469.5	467.8	464.9	340.8
7.5	497.7	496.2	493.8	350.2
8	503.5	501.9	499.4	364.7
8.5	530.5	529.2	527.1	376.6

Stage	Droplet Dia.(μm)			
	Case 4	Case 5	Case 6	Case 7
1	9.573	14.359	19.145	28.718
1.5	8.666	13.475	18.491	28.295
2	8.647	12.482	16.105	23.684
2.5	6.828	10.727	14.641	22.598
3	6.828	8.841	12.569	21.243
3.5	4.790	7.139	11.200	20.321
4	0.000	3.415	8.986	19.101
4.5		0.000	7.345	18.264
5			4.349	17.135
5.5			0.678	16.352
6			0.000	15.288
6.5				14.551
7				13.534
7.5				12.828
8				11.854
8.5				11.198

Stage	Evap./ Boil. Time (ms)			
	Case 4	Case 5	Case 6	Case 7
1	0.3900	0.8775	1.5600	3.5852
1.5	0.1753	0.3766	0.6440	1.4101
2	0.1475	0.2798	0.4349	0.8602
2.5	0.1112	0.2423	0.4107	0.9277
3	0.0940	0.1497	0.2712	0.6985
3.5	0.0559	0.1116	0.2441	0.7715
4	0.0000	0.0278	0.1457	0.5778
4.5		0.0000	0.1142	0.6375
5			0.0426	0.4739
5.5			0.0019	0.5207
6			0.0000	0.3837
6.5				0.4208
7				0.3106
7.5				0.3411
8				0.2580
8.5				0.2910

Stage	Residence Time (ms)			
	Case 4	Case 5	Case 6	Case 7
1	0.1048	0.1048	0.1048	0.1048
1.5	0.1460	0.1493	0.1511	0.1519
2	0.0705	0.0731	0.0755	0.0771
2.5	0.1027	0.1080	0.1080	0.1080
3	0.0478	0.0521	0.0559	0.0593
3.5	0.0897	0.0860	0.0870	0.0898
4	0.0467	0.0488	0.0484	0.0495
4.5	0.0747	0.0740	0.0742	0.0764
5	0.0426	0.0422	0.0415	0.0423
5.5	0.0656	0.0652	0.0644	0.0656
6	0.0365	0.0363	0.0359	0.0361
6.5	0.0573	0.0570	0.0566	0.0568
7	0.0321	0.0319	0.0316	0.0316
7.5	0.0504	0.0502	0.0499	0.0498
8	0.0282	0.0281	0.0279	0.0278
8.5	0.0445	0.0444	0.0442	0.0440

Table 4.12 Phase data for comparison among equilibrium, different droplet size in non-equilibrium cases

Stage	Liquid Water Fraction				
	Case 3	Case 4	Case 5	Case 6	Case 7
1	0.01754	0.01754	0.01754	0.01754	0.01754
1.5	0.01282	0.01301	0.01450	0.01581	0.01678
2	0.01264	0.01293	0.01152	0.01044	0.00984
2.5	0.00610	0.00637	0.00731	0.00785	0.00855
3	0.00610	0.00637	0.00410	0.00496	0.00710
3.5	0	0.00220	0.00216	0.00351	0.00622
4	0	0	0.00024	0.00181	0.00516
4.5	0	0	0	0.00099	0.00451
5	0	0	0	0.00021	0.00373
5.5	0	0	0	0	0.00324
6	0	0	0	0	0.00265
6.5	0	0	0	0	0.00228
7	0	0	0	0	0.00184
7.5	0	0	0	0	0.00156
8	0	0	0	0	0.00123
8.5	0	0	0	0	0.00104

Stage	Water Vapor Fraction				
	Case 3	Case 4	Case 5	Case 6	Case 7
1	0.01596	0.01596	0.01596	0.01596	0.01596
1.5	0.02069	0.02049	0.01901	0.01770	0.01673
2	0.02087	0.02058	0.02199	0.02307	0.02367
2.5	0.02741	0.02714	0.02619	0.02566	0.02496
3	0.02741	0.02714	0.02941	0.02854	0.02641
3.5	0.03351	0.03131	0.03135	0.03000	0.02729
4	0.03351	0.03351	0.03327	0.03170	0.02835
4.5	0.03351	0.03351	0.03351	0.03252	0.02900
5	0.03351	0.03351	0.03351	0.03330	0.02978
5.5	0.03351	0.03351	0.03351	0.03351	0.03027
6	0.03351	0.03351	0.03351	0.03351	0.03086
6.5	0.03351	0.03351	0.03351	0.03351	0.03123
7	0.03351	0.03351	0.03351	0.03351	0.03167
7.5	0.03351	0.03351	0.03351	0.03351	0.03195
8	0.03351	0.03351	0.03351	0.03351	0.03227
8.5	0.03351	0.03351	0.03351	0.03351	0.03247

Table 4.13 Rotor-stator camber line geometries and stage information. Incidence angle i is for the i-th rotor stage and deviation angle δ is for the flow leaving i+0.5th stator.

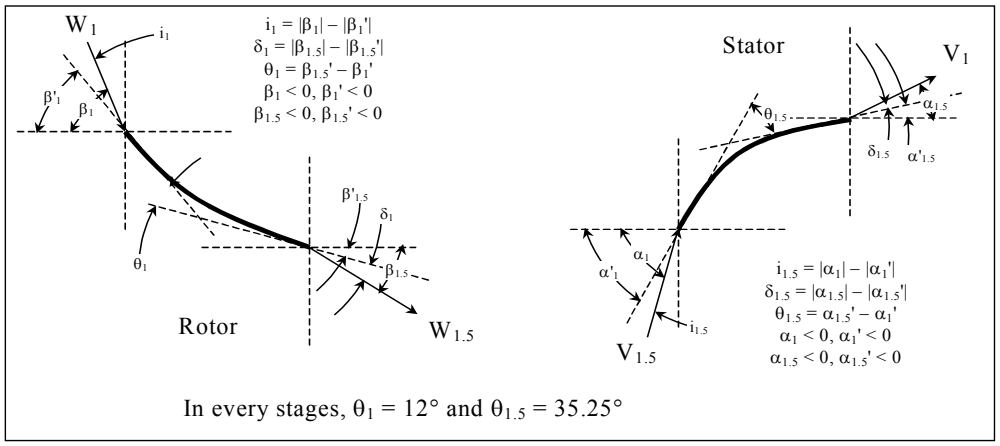

Stage	Hub to Tip Ratio	Tip Dia. (m)	Hub Dia. (m)	Chord Length (cm)	β_1' / $\beta_{1.5}'$	α_1' / $\alpha_{1.5}'$	Case 1		Case 2		Case 3		Case 4		Case 5		Case 6		Case 7	
							i_1/δ_1	$i_{1.5}/\delta_{1.5}$	i_1/δ_1	$i_{1.5}/\delta_{1.5}$	i_1/δ_1	$i_{1.5}/\delta_{1.5}$	i_1/δ_1	$i_{1.5}/\delta_{1.5}$	i_1/δ_1	$i_{1.5}/\delta_{1.5}$	i_1/δ_1	$i_{1.5}/\delta_{1.5}$	i_1/δ_1	$i_{1.5}/\delta_{1.5}$
1	0.636	0.560	0.356	3.400	-62.47	0.00	0.00	0.00	0.00	0.00	0.00	0.00	0.00	0.00	0.00	0.00	0.00	0.00	0.00	0.00
1.5	0.691	0.542	0.374	2.794	-50.47	35.25	0.00	0.00	0.00	-1.07	0.00	-11.76	0.00	-12.54	0.00	-7.59	0.00	-3.55	0.00	-0.97
2	0.703	0.538	0.378	2.658	-62.47	0.00	0.00	0.00	0.39	-1.07	1.89	-11.76	1.94	-12.54	3.22	-7.59	4.26	-3.55	4.98	-0.97
2.5	0.744	0.525	0.391	2.240	-50.47	35.25	0.00	0.00	0.39	-1.01	1.89	-22.01	1.94	-22.91	3.22	-12.14	4.26	-7.68	4.98	-4.28
3	0.757	0.521	0.395	2.111	-62.47	0.00	0.00	0.00	0.93	-1.01	3.76	-22.01	3.83	-22.91	6.54	-12.14	5.82	-7.68	4.47	-4.28
3.5	0.786	0.513	0.403	1.833	-50.47	35.25	0.00	0.00	0.93	-0.24	3.76	-14.31	3.83	-6.74	6.54	-2.55	5.82	-3.63	4.47	-2.80
4	0.797	0.510	0.406	1.721	-62.47	0.00	0.00	0.00	1.28	-0.24	4.79	-14.31	4.92	-6.74	5.34	-2.54	5.05	-3.63	3.84	-2.80
4.5	0.818	0.504	0.412	1.529	-50.47	35.25	0.00	0.00	1.28	0.10	4.79	0.40	4.92	-0.60	5.34	-1.17	5.05	-2.17	3.84	-1.15
5	0.828	0.501	0.415	1.434	-62.47	0.00	0.00	0.00	1.51	0.10	2.94	0.40	3.19	-0.60	3.49	-1.17	3.92	-2.17	3.16	-1.15
5.5	0.844	0.497	0.419	1.292	-50.47	35.25	0.00	0.00	1.51	0.34	2.94	0.37	3.19	-0.08	3.49	-0.47	3.92	-1.20	3.16	-0.75
6	0.853	0.494	0.422	1.212	-62.47	0.00	0.00	0.00	1.64	0.34	2.22	0.37	2.41	-0.08	2.61	-0.46	2.94	-1.20	2.75	-0.75
6.5	0.865	0.491	0.425	1.106	-50.47	35.25	0.00	0.00	1.64	0.58	2.22	2.18	2.41	1.81	2.61	1.44	2.94	0.83	2.75	0.73
7	0.873	0.489	0.427	1.039	-62.47	0.00	0.00	0.00	1.69	0.58	1.60	2.18	1.74	1.81	1.88	1.44	2.11	0.83	2.21	0.73
7.5	0.882	0.487	0.429	0.957	-50.47	35.25	0.00	0.00	1.69	0.61	1.60	3.21	1.74	2.94	1.88	2.64	2.11	2.14	2.21	1.75
8	0.889	0.485	0.431	0.901	-62.47	0.00	0.00	0.00	1.70	0.61	1.13	3.22	1.25	2.94	1.37	2.64	1.56	2.14	1.77	1.76
8.5	0.896	0.483	0.433	0.836	-50.47	35.25	0.00	0.00	1.70	0.60	1.13	4.16	1.25	3.90	1.37	3.63	1.56	3.20	1.77	2.61

4.4 Comparison between Equilibrium and Non-equilibrium Method

This paper compares the results of thermal equilibrium and non-equilibrium methods for overspray fogging through stag-stacking scheme with given mean-line blade and 8-stage compressor configurations. The results are summarized below:

1. Saturated fogging achieves highest pressure ratio augmentation and reduces compressor power consumption; whereas overspray actually increases both the specific and overall compressor power for both equilibrium and non-equilibrium cases. Nevertheless, the net GT power output increases with saturated or overspray fogging.
2. Non-equilibrium method differs from the equilibrium method due to the change of evaporation rate. Droplet size doesn't play a role in equilibrium approach, but plays a major role in affecting the result in the non-equilibrium case. For small droplet size of 10 μm, the droplet evaporation rate is fast, so the non-equilibrium method predicts close results as the equilibrium method. Larger droplets lead to slower evaporation, reduction of pressure ratio, and less effective compressor performance than the smaller droplets.
3. Equilibrium method predicts that wet compression increases axial velocity, blade inlet velocity, incidence angle, and tangential component of velocity. Non-equilibrium methods predict a similar trend except with lesser increments as the droplet size increases.
4. In the present study, the equilibrium method predicts that all the water droplets evaporate completely at the end of stage 3, while the non-equilibrium approach predicts that the completion of evaporation delays; but all droplets completely evaporate in the compressor except approximately 10% of the biggest droplets (30μm) escape from the compressor.
5. Saturated fogging increases air density; however, both equilibrium and non-equilibrium methods predict that wet compression actually reduces air density in the earlier 70% of the compressor.
6. Non-equilibrium predicts small droplets relax the load in the earlier stages, but increases the load in the later stages. Larger droplets show less load changes.

CHAPTER FIVE

NUMERICAL MODEL AND RESULTS OF CFD SIMULATION

The 3-D, time-averaged, transient Navier-Stokes equations as well as equations for mass conservation, energy conservation, and species transport are numerically solved. The governing equations for conservation of mass, momentum, and energy are given as:

$$\frac{\partial \rho}{\partial t} + \frac{\partial}{\partial x_i}(\rho u_i) = S_m \tag{5.1}$$

$$\frac{\partial}{\partial t}(\rho u_j) + \frac{\partial}{\partial x_i}(\rho u_i u_j) = \rho \bar{g}_j - \frac{\partial P}{\partial x_j} + \frac{\partial}{\partial x_i}\left(\tau_{ij} - \rho\overline{u'_i u'_j}\right) + F_j \tag{5.2}$$

$$\frac{\partial}{\partial t}(\rho c_p T) + \frac{\partial}{\partial x_i}(\rho c_p u_i T) = \frac{\partial}{\partial x_i}\left(\lambda \frac{\partial T}{\partial x_i} - \rho c_p \overline{u'_i T'}\right) + \mu\Phi + S_h \tag{5.3}$$

where τ_{ij} is the symmetric stress tensor defined as

$$\tau_{ij} = \mu\left(\frac{\partial u_j}{\partial x_i} + \frac{\partial u_i}{\partial x_j} - \frac{2}{3}\delta_{ij}\frac{\partial u_k}{\partial x_k}\right) \tag{5.4}$$

The source terms (S_m, F_j and S_h) were used to include the contributions from the dispersed phase (water droplets in this study). $\mu\Phi$ is the viscous dissipation and λ is the heat conductivity.

In wet compression with fog cooling, water droplets evaporate as water vapor, which is then transported to its surrounding flow through mass diffusion and convection. The flow mixture consists of three main components: water vapor (H_2O), oxygen (O_2) and nitrogen (N_2). The equation for species transport is

$$\frac{\partial}{\partial t}(\rho C_j) + \frac{\partial}{\partial x_i}(\rho u_i C_j) = \frac{\partial}{\partial x_i}\left(\rho D_j \frac{\partial C_j}{\partial x_i} - \rho\overline{u'_i C'_j}\right) + S_j \tag{5.5}$$

where C_j is the mass fraction of the species (j) in the mixture, and S_j is the source term for this species. D_j is the diffusion coefficient.

Notice the terms of $\rho\overline{u'_i u'_j}$, $\rho c_p \overline{u'_i T'}$, and $\rho\overline{u'_i C'_j}$ represent the Reynolds stresses, turbulent heat fluxes and turbulent concentration (or mass) fluxes, which need be modeled properly for a turbulent flow. The Reynolds number of the main flow (based on the duct height

and the inlet condition specified later) is about 400,000 in this study. Therefore, turbulence model needed to be included.

5.1 Turbulence Models

Selection of an appropriate turbulence model is important because the current state-of-the-art turbulence modeling has been formulated based on different flow structures. None of any turbulence models can predict all the flow well. In two similar studies related to tiny water droplet transport in mist film cooling by Wang and Li (2007) and mist impinging jet cooling by Wang and Dhanasekaran (2008), they both concluded that, among six different turbulence models investigated, the Reynolds Stress Model (RSM) delivered the best performance, followed by RNG and standard k-ε model. Other models included k-ω and the shear-stress transport (SST) k-ω model. Without going details of each model, in short, RNG k-ε model was derived using renormalization group theory (Choudhury, 1993). It has an additional term in the ε-equation to improve the accuracy for rapidly strained flows. It uses the effective viscosity to account for low-Reynolds-number effects. Theoretically, this model is more accurate and reliable than the standard k-ε model. The standard k-ω model is an empirical model based on transport equations for the turbulence kinetic energy (k) and the specific dissipation rate (ω), which can also be considered as the ratio of ε to k (Wilcox, 1998). The low-Reynolds-number effect is accounted for in the k-ω model. The SST model is mixture of the k-ω model and the k-ε model: close to the wall it becomes the k-ω model while in the far field the k-ε model is applied (Menter, 1993). The RSM model provides a second-moment closure of Reynolds stress tensor to account for anisotropic and nonequilibrium turblent flow with multiscaled integral and dissipation length scales. Based on the above two studies, although RSM delivered the best prediction, this study select the k-ε model based on the following reason: the results of k-ε were within 10% difference from RSM but only required approximately one tenth of the computational time. Therefore, only the formulating of k-ε model is described below.

The standard k-ε model, based on the Boussinesq hypothesis, relates the Reynolds stresses to the mean velocity as

$$-\rho\overline{u'_i\,u'_j} = \mu_t\left(\frac{\partial u_i}{\partial x_j}+\frac{\partial u_j}{\partial x_i}\right)-\frac{2}{3}\rho k\delta_{ij} \tag{5.6}$$

where k is the turbulent kinetic energy, and μ_t is the turbulent viscosity given by

$$\mu_t = \rho\, C_\mu\, k^2 / \varepsilon \tag{5.7}$$

where C_μ is a constant and ε is the dissipation rate. The equations for the turbulent kinetic energy (k) and the dissipation rate (ε) are:

$$\frac{\partial}{\partial t}(\rho k)+\frac{\partial}{\partial x_i}(\rho u_i k)=\frac{\partial}{\partial x_i}\left[\left(\mu+\frac{\mu_t}{\sigma_k}\right)\frac{\partial k}{\partial x_i}\right]+G_k-\rho\varepsilon \tag{5.8}$$

$$\frac{\partial}{\partial t}(\rho\varepsilon)+\frac{\partial}{\partial x_i}(\rho u_i \varepsilon)=\frac{\partial}{\partial x_i}\left[\left(\mu+\frac{\mu_t}{\sigma_\varepsilon}\right)\frac{\partial \varepsilon}{\partial x_i}\right]+C_{1\varepsilon}G_k\frac{\varepsilon}{k}-C_{2\varepsilon}\rho\frac{\varepsilon^2}{k} \tag{5.9}$$

The term G_k is the generation of turbulence kinetic energy due to the mean velocity gradients.

The turbulent heat flux and mass flux can be modeled with the turbulent heat conductivity (λ_t) and the turbulent diffusion coefficient (D_t), respectively.

$$\rho c_p\overline{u'_i\,T'} = -\lambda_t\frac{\partial T}{\partial x_i} = -c_p\frac{\mu_t}{Pr_t}\frac{\partial T}{\partial x_i} \tag{5.10}$$

$$\rho\overline{u'_i\,C'} = -\rho D_t\frac{\partial C}{\partial x_i} = -\frac{\mu_t}{Sc_t}\frac{\partial C}{\partial x_i} \tag{5.11}$$

The constants $C_{1\varepsilon}$, $C_{2\varepsilon}$, C_μ, σ_k, and σ_ε used are: $C_{1\varepsilon}$ = 1.44, $C_{2\varepsilon}$ = 1.92, C_μ = 0.09, σ_k = 1.0, σ_ε =1.3 as shown by Launder et. al. (1972). The turbulence Prandtl number, Pr_t, is set to 0.85, and the turbulence Schmidt number, Sc_t, is set to 0.7.

5.1.1 Enhanced Wall Function

The above k-ε model is mainly valid for high Reynolds number fully turbulent flow. Special treatment is needed in the region close to the wall. The enhanced wall function is one of several methods that model the near-wall flow. In the enhanced wall treatment, the two-layer model is combined with the wall functions. The whole domain is separated into a viscosity-affected region and a fully turbulent region by defining a turbulent Reynolds number, Re_y,

$$Re_y = y\, k^{1/2} / \nu \tag{5.12}$$

where k is the turbulence kinetic energy and y is the distance from the wall. The standard k-ε model is used in the fully turbulent region where $Re_y > 200$, and the one-equation model of Wolfstein (1969) was used in the viscosity-affected region with $Re_y < 200$. The turbulent viscosities calculated from these two regions are blended with a blending function (θ) to smoothen the transition.

$$\mu_{t,enhanced} = \theta\ \mu_t + (1 - \theta)\ \mu_{t,l} \tag{5.13}$$

where μ_t is the viscosity from the k-ε model of high Reynolds number, and $\mu_{t,l}$ is the viscosity from the near-wall one-equation model. The blending function is defined so it is equal to 0 at the wall and 1 in the fully turbulent region. The linear (laminar) and logarithmic (turbulent) laws of the wall are also blended to make the wall functions applicable throughout the entire near-wall region.

5.2 Dispersed-Phase Model (Water Droplets)

5.2.1 Droplet Flow and Heat Transfer

Based on the Newton's 2nd Law, droplets motion in the airflow can be formulated by

$$m_p\ d\mathbf{v_p} / dt = \Sigma\mathbf{F} = F_D + F_g + F_P + F_P + F_O \tag{5.14}$$

where m_p is the droplet mass, and $\mathbf{v_p}$ is the droplet velocity (vector). The right-hand side is the combined force acted on the droplets, which are F_D (drag force), F_g (gravity and buoyancy force), F_P (pressure force), F_S (Saffman lift force), F_O (Other forces). The following are the parameters for magnitude order of various forces for the present study. The density ρ_p and size d_p of particle are 998.2 kg/m^3 and 10μm, respectively. The air density ρ_a is 1.23 kg/m^3, and its dynamic viscosity coefficient μ are 1.85×10^{-5} kg/(m·s). The average value of pressure gradient $\partial p/\partial x$ is about 3.2×10^4 Pa/m. The value of (u_a-u_p) is near 60 m/s, where u_p and u_a the velocity of particle and air, respectively; the average value $d(u_a-u_p)/dt$ is about 60,000 m/s². $f(Re_p) \sim 3.2$. Taking the above conditions into account, the magnitude order of various forces can be acquired following Wang et. al.'s (2007) study.

$$F_D = -3\pi d_p \mu (u_p - u_a) f(Re_p) \approx 3.4\times10^{-7}$$

$$F_g = \tfrac{1}{6}\pi d_p^3 (\rho_p - \rho_a) g \approx 5.1\times10^{-12}$$

$$F_P = \tfrac{1}{6}\pi d_p^3 \frac{\partial P}{\partial x} \approx 1.7\times10^{-11}$$

$$F_s = 1.61(\mu\rho_a)^{\frac{1}{2}} d_p^2 (u_a - u_p)\left|\frac{\partial u_a}{\partial y}\right|^{\frac{1}{2}} \approx 2.3\times10^{-8}$$

where, g is the gravitational acceleration, Re_p is the droplet Reynolds number and $f(Re_p)$ is the correction factor for Stokes-drag force, which are expressed as,

$$Re_p = \frac{\rho_a |u_a - u_p| d_p}{\mu} \quad \text{and} \quad f(Re_p) = C_D \frac{Re_p}{24}$$

According to the Stokes law for Re < 1, $C_D\ Re_p/24 = 1$. There are many models to formulate the term $C_D\ Re_p/24$ for higher particle Reynolds number, which are already discussed in Chapter 2.3.3.

Without considering the radiation heat transfer, droplet's heat transfer depends on convection and evaporation as given in the following equation.

$$m_p c_p \frac{dT}{dt} = \pi d^2 h(T_\infty - T) + \frac{dm_p}{dt} h_{fg} \tag{5.15}$$

where h_{fg} is the latent heat. The convective heat transfer coefficient (h) can be obtained with an empirical correlation from Ranz et. al. (1952):

$$Nu_d = \frac{hd}{\lambda} = 2.0 + 0.6\, Re_d^{0.5}\, Pr^{0.33} \tag{5.16}$$

where Nu is the Nusselt number, and Pr is the Prandtl number.

The mass change rate or vaporization rate in Eq. (5.15) is governed by concentration difference between droplet surface and the air stream,

$$-\frac{dm_p}{dt} = \pi d^2 k_c (C_s - C_\infty) \tag{5.17}$$

where k_c is the mass transfer coefficient, and C_s is the vapor concentration at the droplet surface, which is evaluated by assuming the flow over the surface is saturated. C_∞ is the vapor concentration of the bulk flow, obtained by solving the transport equations. The values of k_c can be given from a correlation similar to Eq. (5.16) by Ranz et. al. (1952).

$$Sh_d = \frac{k_c d}{D} = 2.0 + 0.6 Re_d^{0.5} Sc^{0.33} \tag{5.18}$$

where Sh is the Sherwood number, Sc is the Schmidt number (defined as ν/D), and D is the diffusion coefficient of vapor in the bulk flow.

When the droplet temperature reaches the boiling point, the following equation can be used to evaluate its evaporation rate given by Schiller et. al. (1933):

$$-\frac{dm_p}{dt} = \pi d^2 \left(\frac{\lambda}{d}\right)(2.0 + 0.46 Re_d^{0.5}) \ln\left[1 + c_p (T_\infty - T)/h_{fg}\right]/c_p \tag{5.19}$$

where λ is the gas/air heat conductivity, and c_p is the specific heat of the bulk flow.

Theoretically, evaporation can occur at two stages: (a) when the temperature is higher than the saturation temperature (based on local water vapor concentration), water evaporates, and the evaporation is controlled by the water vapor partial pressure (Eq. 5-17) until 100% relative humidity is achieved; (b) when the boiling temperature (determined by the air-water mixture pressure) is reached, water continues to evaporate (Eq. 5.19). After the droplet evaporates due to either high temperature or low moisture partial pressure, the vapor diffuses into the main flow and is transported away by convection.

5.2.2 Mixture's Properties

The current study deals with a mixture including O_2, N_2, H_2O vapor and liquid H_2O. The mixture's properties are calculated by mass-weighted average. As the gas mixture is compressible, the density of the mixture is formulated based on the idea gas law as,

$$\rho = \frac{P + P_{op}}{RT \sum_i \frac{Y_i}{M_i}} \tag{5.20}$$

where, P = Local static pressure

P_{op} = Operating pressure

R = Universal Gas Constant (8.314 kJ/kmole.K)

T = Static temperature

Y_i = Mass fraction of species i

M_i = Molecular weight of species i

However, the existence of incompressible liquid water makes the mixture a non-ideal gas mixture of O_2, N_2, H_2O vapor as a gas with liquid H_2O. The gas-liquid density is calculated as,

$$\rho = \frac{1}{\sum_i \frac{Y_i}{\rho_i}} = \frac{1}{\frac{Y_{\text{liq } H_2 0}}{\rho_{\text{liq } H_2 0}} + \frac{Y_{\text{gas mixture}}}{\rho_{\text{gas mixture}}}} \tag{5.21}$$

Specific heat of the mixture is calculated as a mass fraction average of the pure species heat capacities as,

$$Cp = \sum_i Y_i Cp_i \tag{5.22}$$

Constant dilute approximation is used to find mixture's diffusion coefficient as,

$$D = \frac{1 - X_i}{\sum_{j, j \neq i} \frac{X_i}{D_{ij}}} \tag{5.23}$$

X_i = Molar fraction of species i

Property values for water saturation used in FLUENT are not precise enough to cover the temperature region for this study. By default, the water vapor pressure is limited from 284K to 425K and there were no data points between 284K and 273 K. For any condition with a temperature below 284K, the calculation has given an unrealistic result with temperature distribution lower than the web-bulb temperature during evaporation.

For example, in the original database, if the vapor pressure at 5°C (278K) is required, the program extrapolates from the closest two temperature points by default and gives 604 pascal, which is,

$$\frac{284 - 278}{295 - 284} = \frac{1329 - P_{sat}}{2658 - 1329} \quad \Rightarrow P_{sat} = 604\,\text{Pa} \qquad [P_{sat} = \text{Saturation pressure}]$$

But according to the steam property table, this value is 872.1 pascal, which is 31% off. The deviation becomes worse when temperature is lower than 278K. According to the extrapolation in the original database, the saturated vapor pressure at 273.01K is 1.2 pascal, whereas the actual value is 611.3 pascal. The added data points significantly improve the accuracy of the predicted results. Piecewise linear manner is selected to interpolate all property values.

Table 5.1 Additional water property added to the FLUENT database

Data No.	Temperature (K)	Vapor Pressure (Pa)
1.	273.01	611.3
2.	278	872.1
3.	284	1329
4.	295	2658
5.	307	5316
6.	315	7974
7.	325	13289
8.	340	26579
9.	356	53158
10.	373	101000
11.	393	202000
12.	425	505000

5.2.3 Stochastic Particle Tracking

The turbulence models discussed above can only obtain time-averaged velocity. Using this velocity to trace the droplet will result in an averaged trajectory. In a real flow, the instantaneous velocity fluctuation would make the droplet move around this averaged track. However, the instantaneous velocity is not simulated in the current computation because the turbulence is modeled in time-averaged terms. One way to simulate the instantaneous turbulent effect on droplet dispersion is to "improvise" the random turbulent fluctuation by using the stochastic tracking scheme. Basically, the droplet trajectories are calculated by imposing the instantaneous flow velocity ($\bar{u} + u'$) rather than the average velocity ($\bar{u}$). The velocity fluctuation is then given as:

$$u' = \zeta\left(\overline{u'^2}\right)^{0.5} = \zeta(2k/3)^{0.5} \tag{5.24}$$

where ζ is a normally distributed random number shown by Kuo et. al. (1986). This velocity will apply during the characteristic lifetime of the eddy (t_e), which is a time scale calculated from the turbulent kinetic energy and dissipation rate ($t_e = 0.3\ k/\varepsilon$). The time scale varies from case to case and it is essential that an adequate time scale be provided in the calculation. A typical value in this study calculated from empirical formula ($0.3\ k/\varepsilon$) is about 0.05 seconds. After this time period, instantaneous velocity will be updated with a new ζ value until a full trajectory is obtained. When the stochastic tracking is applied, the basic interaction between droplets and continuous phase stays the same, which is accounted by the source terms in the conservation equations. The source terms are not directly but rather indirectly affected by the stochastic method; so formulation of the source terms is not affected by implementing the stochastic tracking method. For example, the drag force between a water droplet and the steam flow depends on the slip velocity calculated by the averaged Navier-Stokes equations. When the stochastic tracking method is used, a random velocity fluctuation is imposed at an instant of time, and the drag force will be calculated based on this instantaneous slip velocity. The source term associated with this instantaneous drag force enters into the momentum equation without any additional formulation. For a steady-state calculation, the "instant of time" means "each iteration step."

5.3 Droplet Dynamics

5.3.1 Droplet Breakup

A literature review on droplet breakup has been conducted in Chapter 1 Section 1.1.3.1. In this study, the Taylor Analogy Breakup (TAB) model is used which was developed by O'Rourke and Amsden (1987). This method was based upon Taylor's analogy between an oscillating and distorting droplet and a spring mass system, where the spring surface tension forces, droplet drag force and droplet viscosity forces were made analogous to restoring, external, and damping forces as shown in Eqs (5.25) and (5.26). The equation governing a damped, forced oscillator is,

$$F_{sp} - k_{sp}x - d_{sp}\frac{dx}{dt} = m\frac{d^2x}{dt^2} \tag{5.25}$$

$$\frac{F_{sp}}{m} \sim \frac{\rho_a u^2}{\rho_w d}$$
$$\frac{k_{sp}}{m} \sim \frac{\sigma}{\rho_w d^3} \qquad (5.26)$$
$$\frac{d_{sp}}{m} \sim \frac{\mu_w}{\rho_w d^2}$$

where x is the displacement of the droplet from its spherical undisturbed position. The coefficients of this equation are taken from Taylor's analogy:

When the droplet oscillations grow to a critical value of Weber number, droplets break up into a number of child droplets. In the work of O'Rourke and Amsden (1987), the critical value for Weber number is 6.

5.3.2 Droplet Coalescence

A literature review on droplet breakup has been conducted in Chapter 1 Section 1.1.3.2. O'Rourke's model is used in this study and described here. The probability of two droplets colliding is derived from the point of view of the larger droplet, called the collector droplet and identified below as the number 1. The smaller droplet is identified in the following derivation as the number 2. The calculation is in the frame of reference of the larger droplet, so the velocity of the collector droplet is zero. Only the relative distance between the collector and the smaller droplet is important in this derivation. If the smaller droplet is on a collision course with the collector, the centers will pass within a distance of $\frac{1}{2}(d_1+d_2)$. More precisely, if the smaller droplet center passes within a circle centered around the collector of area $\frac{1}{4}\pi(r_1+r_2)^2$ perpendicular to the trajectory of the smaller droplet, a collision will take place. This disk can be used to define the collision volume, which is the area of the aforementioned disk multiplied by the distance traveled by the smaller droplet in one time step, namely $\frac{1}{4}\pi(r_1+r_2)^2 V_{rel}\,\Delta t$, where V_{rel} is the relative velocity between the two droplets. The algorithm of O'Rourke uses the concept of a collision volume to calculate the probability of collision. Rather than calculate whether or not the position of the smaller droplet center is within the collision volume, the algorithm calculates the probability of the smaller droplet being within the collision volume. It is known that the smaller droplet is somewhere within the continuous-phase cell of volume ~~V~~. If there is a uniform probability of the droplet being anywhere within the cell, then the chance of the droplet being

within the collision volume is the ratio of the two volumes. Thus, the probability of the collector colliding with the smaller droplet is,

$$P_1 = \frac{\pi(d_1 + d_2)^2 V_{rel} \Delta t}{4\forall} \tag{5.27}$$

Eq. (5.27) can be generalized for parcels, where there are n_1 and n_2 droplets in the collector and smaller droplet parcels, respectively. The collector undergoes a mean expected number of collisions given by

$$\bar{n} = \frac{n_2 \pi(d_1 + d_2)^2 V_{rel} \Delta t}{4\forall} \tag{5.28}$$

The actual number of collisions that the collector experiences is not generally the mean expected number of collisions. The probability distribution of the number of collisions follows a Poisson distribution, according to O'Rourke, which is given by,

$$P(n) = e^{-\bar{n}} \frac{\bar{n}^n}{n!} \tag{5.29}$$

where n is the number of collisions between a collector and other droplets.

5.3.1 Droplet Erosion

A literature review of particle erosion on surface was conducted in Chapter 1 Section 1.1.3.3. In this study, the rate of erosion (kg/m^2s) is formulated considering all the factors described in the chapter 1 as,

$$R = \begin{cases} \dfrac{\dot{m}_p K f(\alpha)(V\sin\alpha - V_{cr})^n}{A_{face}} & (V\sin\alpha \geq V_{cr}) \\ 0 & (V\sin\alpha < V_{cr}) \end{cases} \tag{5.30}$$

Where, K is a Material constant, α is the impact angle of the particle path with the wall face, $f(\alpha)$ is a function of impact angle, V is the relative particle velocity, V_{cr} is the critical velocity below which erosion does not take place, n is a constant, and A_{face} is the area of the cell face at the wall. $V\sin\alpha$ is the normal component of the droplet velocity, which is responsible for erosion and was shown by Nesic (1991). Nokleberg and Sontvedt (1998) used this model and found the erosion tests gave peak erosion rates 2-3 times larger than calculated. They reasoned that this large

difference was contributed by the variations of surface geometry, particle sharpness and reflection velocities after several impacts in the chokes. They suggested the value of $f(\alpha)$ in a piecewise linear manner between three data points for ductile materials as: $f(0°) = 0$, $f(20°) = 1.0$, and $f(90°) = 0.3$ and two points linear relationship for brittle materials between $f(0°) = 0$ and $f(90°) = 1.0$.

Haugen et. al. tested a total of 28 materials at impact angles of 7.5°, 22.5° and 90° with test velocities at 22, 55, and 320 m/s. Impact angles 22.5° and 90° are selected in this study since maximum erosion is achieved at those angles for ductile and brittle materials, respectively. Their study provided the value of $K = 2\times10^{-9}$ and $n = 2.6$ for steel. The value of $f(\alpha)$ and n are completely dependent on the eroding material; it does not bear any relationship with the type of particles. Bowden and Field (1964) showed that the stress pulse produced by high-speed liquid impact is intense and of a duration of only 1 or 2μs. On the other hand, a solid-to-solid impact has, by comparison, a much longer impact time of the order of hundreds of microseconds. Based on this discovery, it is assumed in the present study that the K value for the liquid droplets is about two orders of magnitude less than solid's K value. Therefore, K is selected as 2×10^{-11}, which is $1/100^{th}$ of the steel's K value. n is selected as 2.6 and $f(\alpha)$ is modeled by the piecewise linear approach between three data points: $f(0°) = 0$, $f(20°) = 1.0$, and $f(90°) = 0.3$ as stated in the previous paragraph. The critical velocities for erosion initiation for different materials were reported by Bitter (1963a, b) and the critical velocity for steel was 0.668m/s. Erosion model built in the FLUENT is a solid particle erosion model, which is not fit for the current application with liquid erosion, so an user defined function (UDF) is written and is incorporated into the FLUENT program.

5.4 Numerical Method

The commercial software package FLUENT (version 6.2.16) from Ansys, Inc. is adopted for this study. The simulation uses the segregated solver, which employs an implicit pressure-correction scheme and decouple the momentum and energy equations according to FLENT manual (2005). The SIMPLE algorithm is used to couple the pressure and velocity (Patankar, 1980). Second order upwind scheme is selected for spatial discretization of the convective terms and species. Lagrangian trajectory calculations are employed to model the dispersed phase of droplets. The impact of droplets on the continuous phase is considered as source terms to the

governing equations. After obtaining an approximate flow field of the continuous phase (airflow in this study), droplets are injected and their trajectories are calculated. At the same time, drag, heat and mass transfer between the droplets and the airflow are calculated.

Iteration proceeded alternatively between the continuous and discrete phases. Twenty iterations in the continuous phase are conducted between two consecutive iterations in the discrete phase. Converged results were obtained after the specified residuals are met. A converged result renders mass residual of 10^{-3}, energy residual of 10^{-6}, and momentum and turbulence kinetic energy residuals of 10^{-3}. These residuals are the summation of the imbalance for each cell and scaled by a representative of the flow rate. Typically, 200-300 iterations are needed in initial time steps, and after 20 time steps (i.e. 6,000 iterations), 20-30 iterations are needed to obtain a converged result in each time step, which took about 2~3 hours on a 2.2 GHz Pentium 4 personal computer. To allow accurate transfer of information across the sliding mesh interface, the iteration time step must be at least less than 50% of the time required to pass one mesh.

For 3-D analysis, typically, 400 to 500 iterations are needed to obtain a converged result in each time steps, which takes about 90 hours in a cluster of 9 parallel computers of each 2.8 GHz Pentium 4 personal computer. The transient time step is set for 0.1 millisecond for a total of 100 steps. For 3600 RPM rotating speed, this gives a total period of 0.01 second with a progress of 30 pitch passing. The time step is set in such a way that it becomes shorter than the time requires for the rotor to rotate a single pitch, which is 33.33 ms. Otherwise the discrete phase data won't be continuous in two consecutive pitch passings.

5.5 Two-Dimensional Analysis

5.5.1 Geometrical Configuration

The geometries of the compressor rotor and stator airfoils are taken from Hsu and Wo (1998) with a chord length of 0.06m, a gap distance of 6 mm, and a blade pitch of 42 mm, as shown in Fig.1. The whole computational domain (area A-B-C-D-E-J-I-H-G-F) is divided into four sub-domains including the inlet sub-domain (area A-B-G-F), the rotor sub-domain (area B-C-H-G), the stator sub-domain (area C-D-I-H) and the exit sub-domain (area D-E-J-I). The width

of all the sub-domains are the same as a blade pitch of 42mm. Length of inlet and exit sub-domain are 60 mm each. The inlet and exit sub-domains are rectangular, and the other two sub-domains consist of two vertical straight lines and two repeated curves (e.g. BC and GF in the rotor sub-domain and CD and HI in the stator sub-domain). Here BC and CD are formed following the centerline of the rotor-stator flow passage. GH and HI are the repetitions of BC and CD, respectively. The inlet fogging is simulated at 4 spray locations uniformly spaced at ⅛, ⅜, ⅝, ⅞ inlet between A and F.

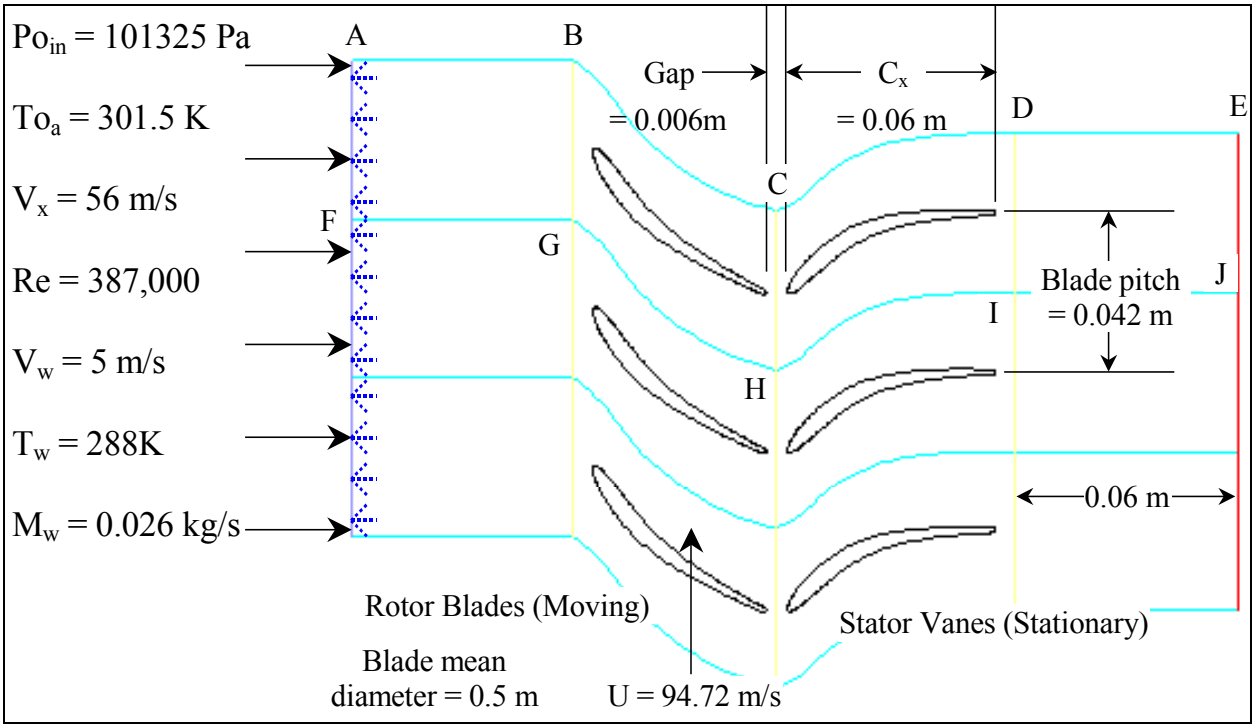

Figure 5.1 Computational domain

5.5.2 Boundary Conditions

5.5.2.1 Continuous Phase

The stagnation condition of the inlet main flow is assigned as 1 atm air at 301.5K (static temperature is 300K), and 60% RH (or with the absolute humidity at 0.01369 kg/kg dry air) moving at a uniform velocity of 56 m/s. The inlet condition is assigned by fixing the total pressure as 101,325 Pa and total temperature at 301.5K, as shown in Fig. 5.1 and the exit

condition is assigned by fixing the static pressure as a value that will give the inlet velocity of 56 m/s. Since the exit static pressure is not known, iteration will take place to try different exit pressures until the inlet velocity reaches an average value of 56 m/s. Under these assigned conditions, the inlet static pressure, static temperature, and velocity will be calculated cell by cell and will not be uniform. There was an attempt to assign a uniform velocity at the inlet. However, if a constant velocity were assigned as the inlet condition, the total pressure would be calculated cell-by-cell and would not be uniform, which is not consistent with reality. Rotor rotates at 3600 RPM with the translational velocity of 94.72 m/s. The turbulent intensity is assigned as 1% for both 2-D and 3-D analyses.

The computed mass flow rate is 2.645 kg/s per unit width. This amount (2.645 kg/s) is then used to calculate the amount of water, which is 1% and becomes 0.02645 kg/s. However, the air mass for fogging case is not just 1% more, because the inlet density increases due to the change of inlet temperature and pressure, which makes the mass flow rate of air as 2.658 kg/s without water.

The backflow (reverse flow) temperature, if any, is set to 310 K. All the walls in the computational domain are adiabatic and have non-slip velocity boundary condition. BG, CH and DI are the interfaces between the consecutive sub-domains. The surface A-B-C-D-E is repeated upon the surface of F-G-H-I-J and is used here as periodic boundary, i.e. the data is calculated at A-B-C-D-E are used at F-G-H-I-J as the input.

5.5.2.2 Sliding Mesh Data Transfer

BG, CH and DI are the stationary-sliding interfaces between the stationary and moving sub-domains. The calculated data at the exit of the inlet stationary domain (CH) is transferred via the sliding mesh algorithm to the inlet of moving rotor subdomain, and the similar transfer of data is passed between moving rotor subdomain to the stator subdomain. The meshes are shown in Fig. 5.2.

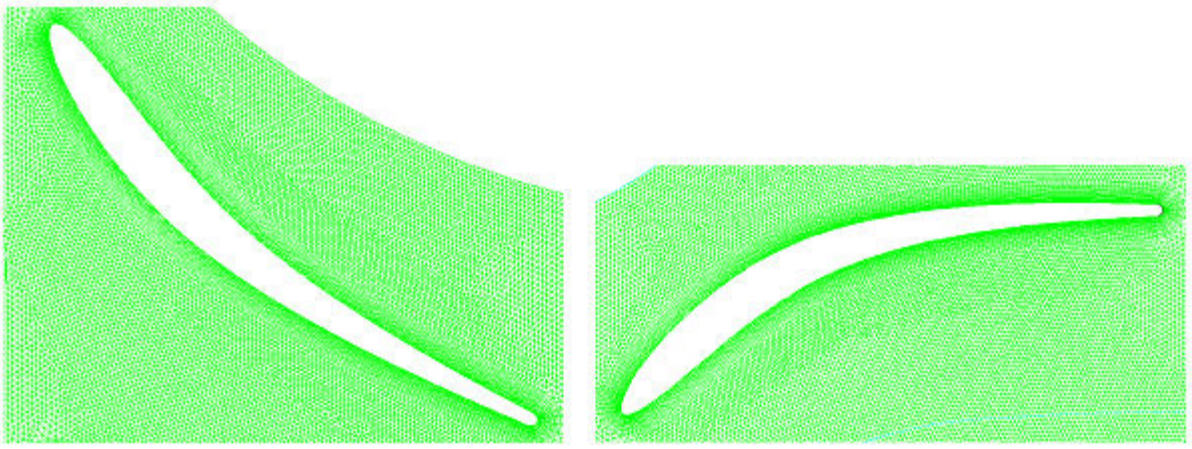

(a) Rotor (b) Stator

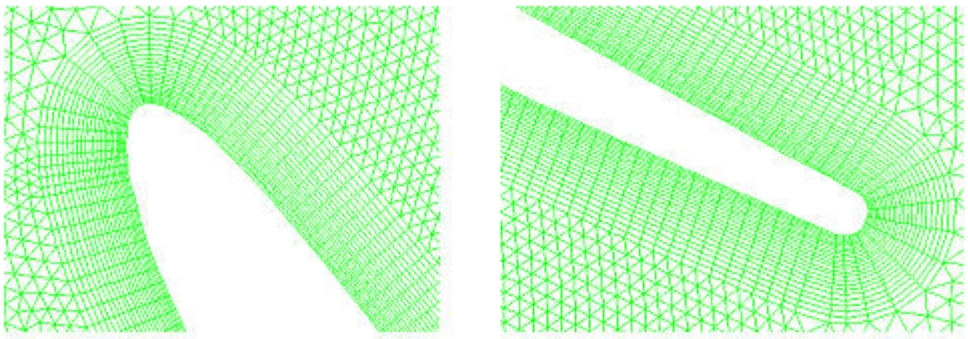

(c) Leading and Trailing edges of Rotor

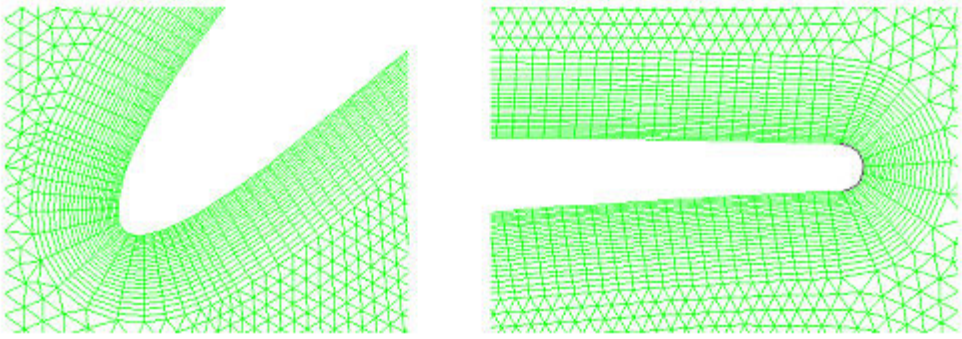

(d) Leading and Trailing edges of Stator

Figure 5.2 Meshes for (a) rotor (overall), (b) stator (overall), (c) leading and trailing edges of rotor and (d) leading and trailing edges of stator

5.5.2.3 Dispersed Phase

The droplet size is uniformly given as 10 μm. Although in the real spray applications the water droplet sizes posses a nonuniform distribution, for the purpose of an easy tracking of droplet size variations during the course of evaporation, using uniform droplet size provides a convenient controlling tool. The effect of droplet sizes can be compared between the 5μm and 10μm cases. The mass ratio of water droplet over airflow is 1%, which is 0.02645 kg/s at 288K. The effect of turbulent dispersion on droplet trajectories is calculated by tracking a number of trajectories with the stochastic method.

The boundary condition for droplets at the walls is assigned as either reflected, trapped, or maintaining as a liquid film. Usually, when the wall temperature is 28°C (=50°F) above the water saturation temperature (i.e. at 28^{o}C superheat), the water droplets do not stick to the wall surface; it reflects from the surface. This situation occurs in the later stages of the compressor, but not in the first stage as simulated in the present study. However, since the blade surfaces moved very fast, the impact force may bounce off the droplets when the droplets collided with the surface. In the meantime, the water droplets can also stick to the surface and form a liquid film. Since all three conditions could occur in the real application, this study employed both reflected and filmed boundary conditions at separated cases and the results are compared. The results of the trapped condition should be between the results of reflected and filmed conditions because it assumes water droplets to evaporate when they hit the surfaces. At the outlet, the droplets just simply escape from the computational domain. The model is associated with break-up and coalescence model to see the effect of these models on droplet.

Structured O-mesh is applied to the boundary layer region of rotor and stator and unstructured triangular meshes are constructed outside the boundary layer region, as shown in Fig 5.2(a), (b), (c) and (d). The cells near the leading edge and trailing edges of rotor and stator are the densest.

In the inlet and exit sub-domains, cells are the coarsest. Inlet and exit sub-domains have 12,000 cells each and rotor and stator sub-domains have 30,000 cells each. The total number of cells for 2D cases is 88,000.

5.5.3 Results and Discussions of 2D cases

5.5.3.1 Studied Cases

1. Baseline case: No fogging. Moist air compression (conventionally called dry compression) with the stagnation condition of the ambient air at 301.5K, 60% RH, and 1 atm pressure.
2. Fog cooling case: Ambient condition is the same as the baseline case with 1% overspray of water.

In this study, the term "fogging" indicates the action of generating the fog. Depending on the amount of injected water, "saturation fogging" implies the process of saturating the air to 100% relative humidity and "overspray" implies the process of injecting more than the water amount required to achieve saturated air. Strictly speaking, a 1% overspray implies the amount of water that weighs 1% of the dry air flow is injected, in addition to the amount required to saturate the air. However, for simplicity, overspray fogging also includes saturation fogging in this study. For example, 1% water overspray with an ambient condition of 300K and 60% RH implies that 0.245% water is needed to saturate the air, and (1 – 0.245) = 0.755% is actually used for overspray.

The term "moist air compression" indicates that no liquid is in the air and the air humidity is not zero. "Wet compression" means liquid droplets present in the air during compression.

5.5.3.2 Static Temperature

The result of static temperature distribution is shown in Fig. 5.3. The baseline case has an mass-weighted average exit temperature of 305.6K. Wet compression reduces that to 305.1K with 10μm water droplets. The baseline case shows locally higher temperature at the stagnation points near the blade's leading edge, over the pressure side of the rotor, and at the trailing edge of the stator. In the non-fogging baseline case, the temperature becomes low on the suction side of the rotor due to local acceleration. Overspray cools the entire domain, specially the outlet sub-domain. Due to the thermal response time needed for water droplets to evaporate, the cooling effectiveness is more pronounced in the later part of the domain, which is more obvious in the entropy distribution (Fig. 5.4).

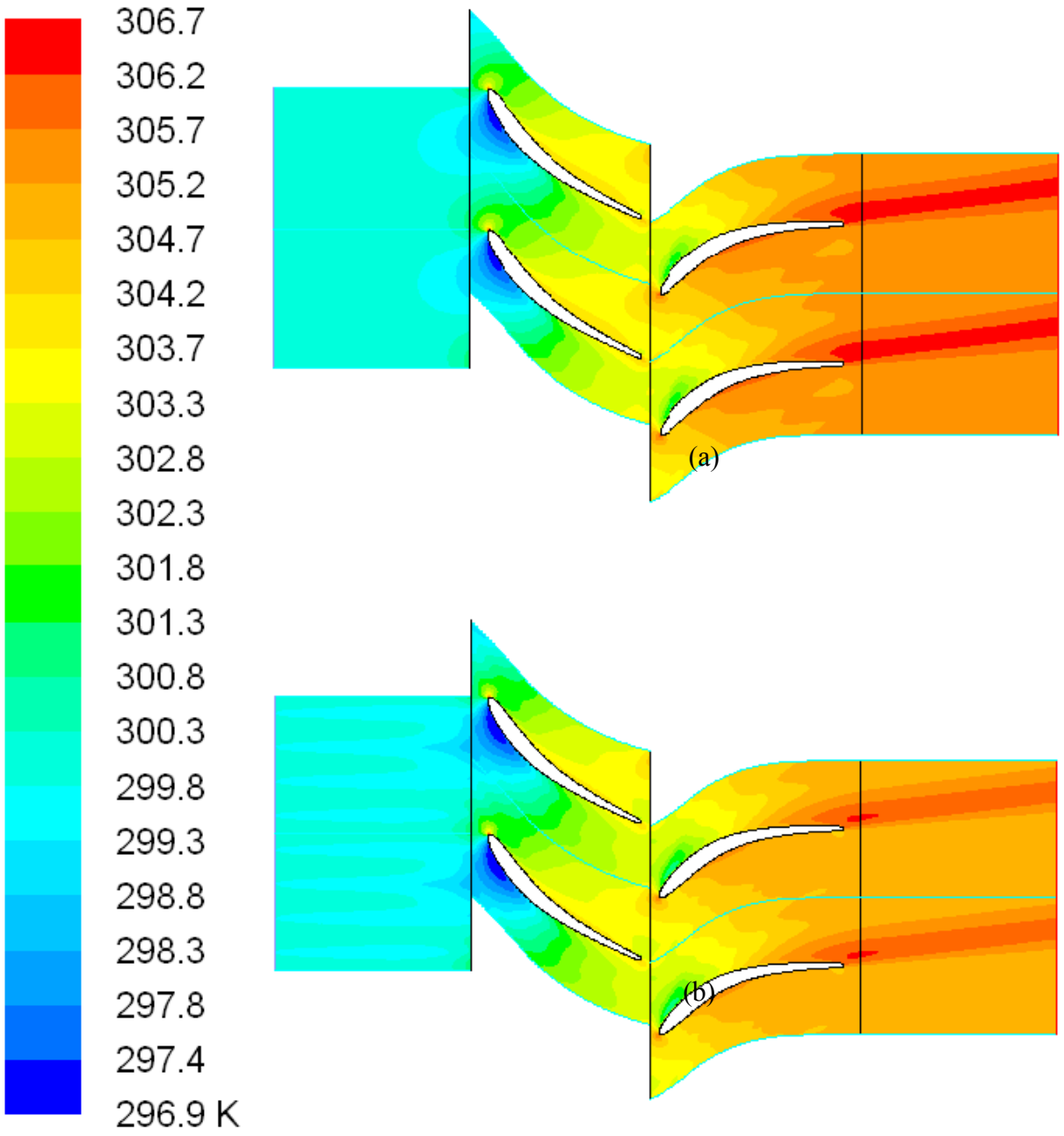

Figure 5.3 Static temperature distribution (a) non-fogging baseline (b) overspray fogging

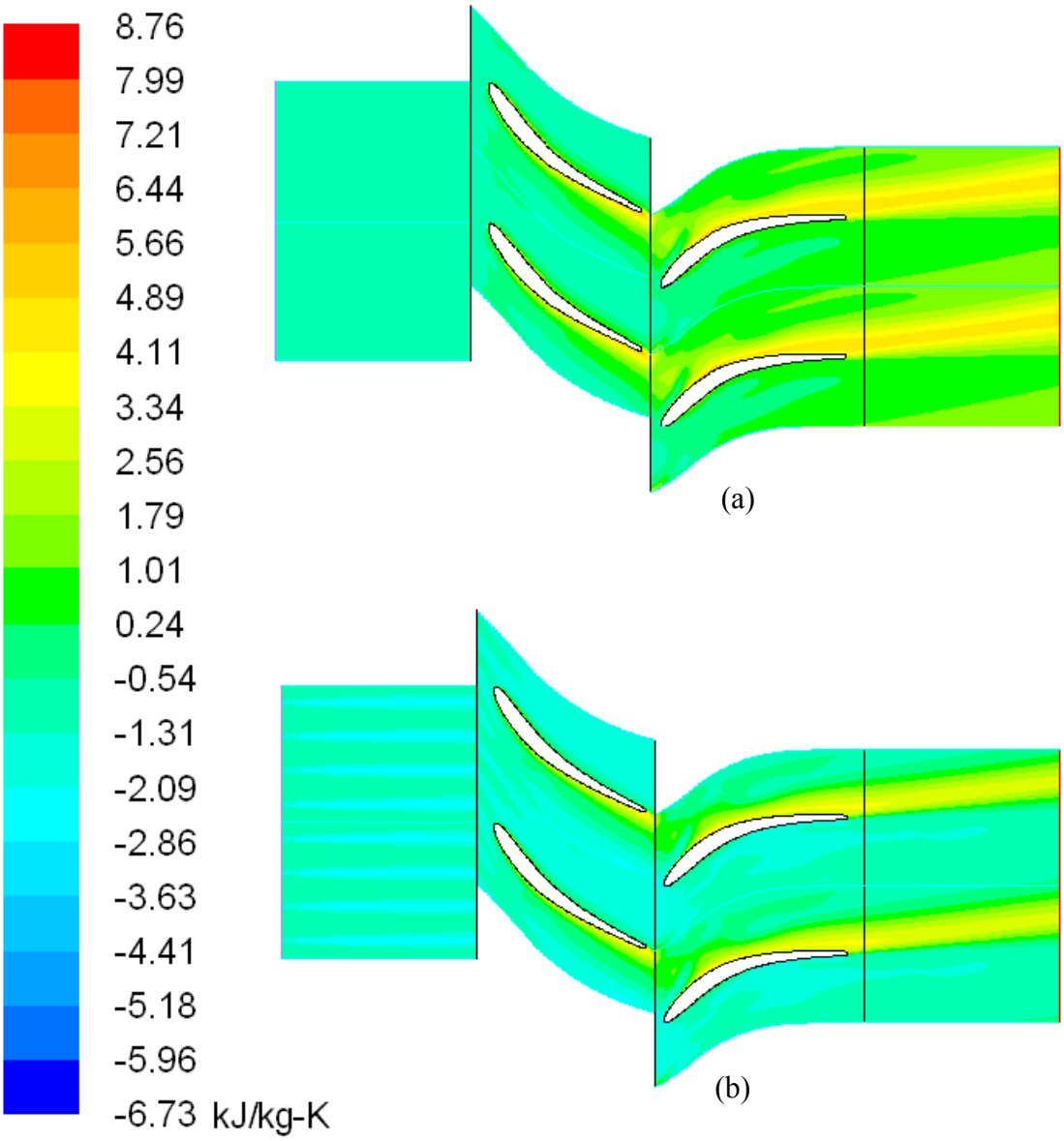

Figure 5.4 Entropy distribution (a) non-fogging baseline (b) overspray fogging

5.5.3.3 Static Pressure

The static pressure distribution over the rotor is shown in Fig. 5.5. Overall, the wet compression produces lower static pressure on the rotor. Overspray produces a bit higher pressure ratio (1.059) than the baseline case (1.057). Droplet evaporation reduces the static temperature, which reduces the static pressure also, that is why the pressure enhancement is not appreciable here in this stage, which is also revealed in Fig. 5.6, where the pressure distribution

over the rotor is shown. More enhancement of pressure is expected in later stages, which is not simulated here.

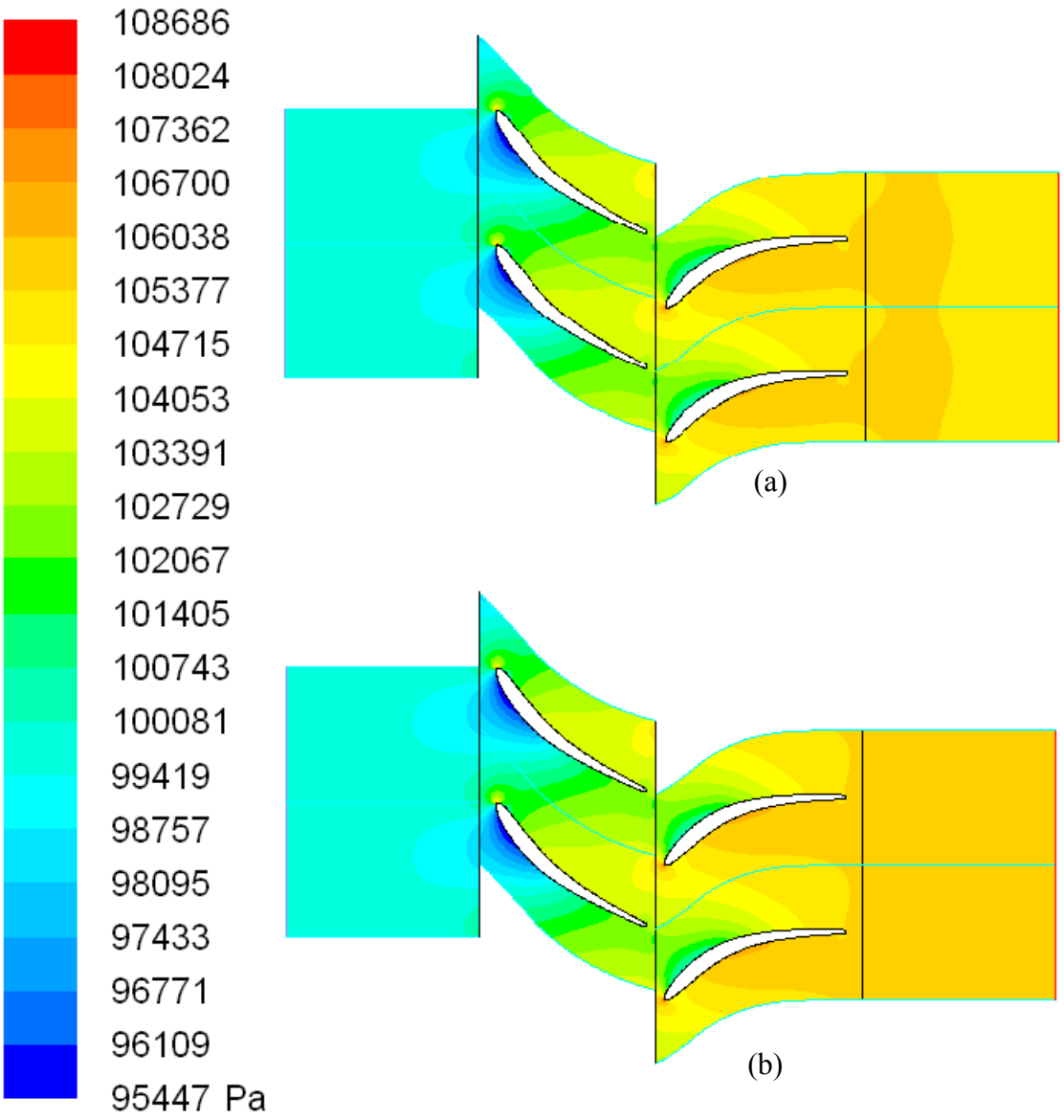

Figure 5.5 Static pressure distribution (a) non-fogging baseline (b) overspray fogging.

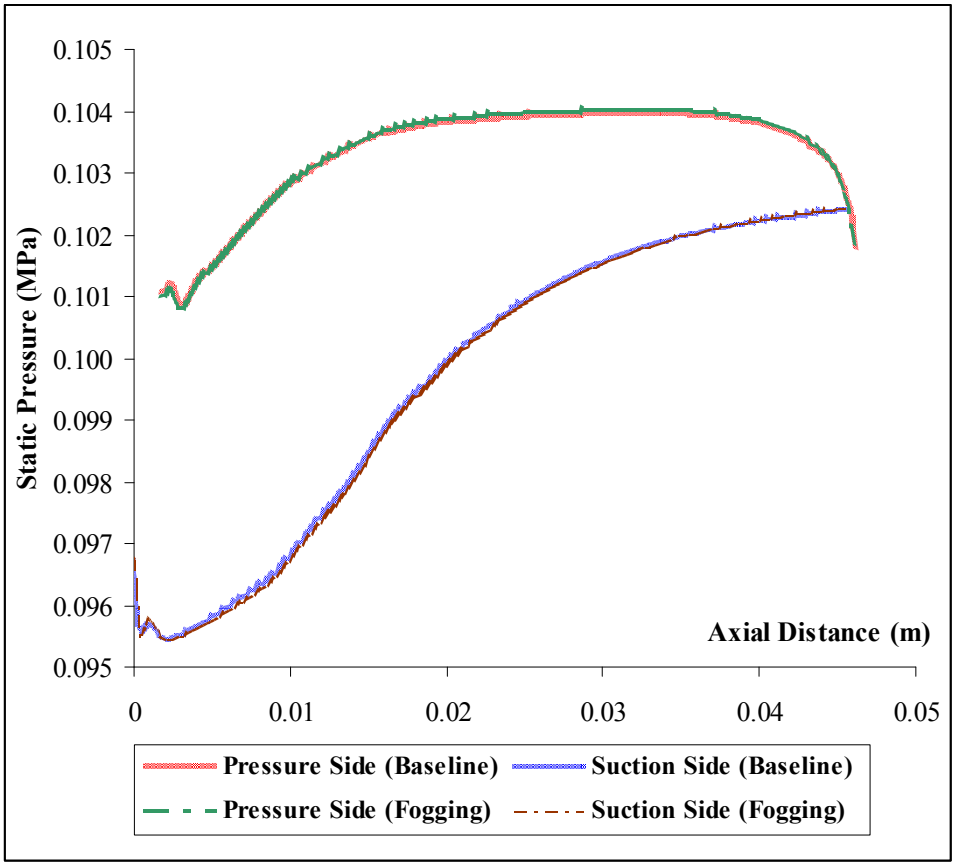

Figure 5.6 Static pressure distribution over the rotor (baseline and fogging pressures almost coincide each other)

5.5.3.4 Velocity

The axial velocity is set to 56 m/s at the rotor inlet. The velocity distribution is shown in Fig. 5.7. The exit axial velocity at the rotor is approximately 53.4 m/s without fogging and 53.5 m/s with fogging. Due to increased volume flow rate from evaporated water, the exit velocity increases from 56.2 m/s without fogging to approximately 57.9 m/s. Figure 5.8 shows the velocity distribution over the stator in a magnified view. It is clear from the figure that a boundary layer is forming over the stator suction and pressure sides. The velocity on the pressure seems slow, but no separation is found.

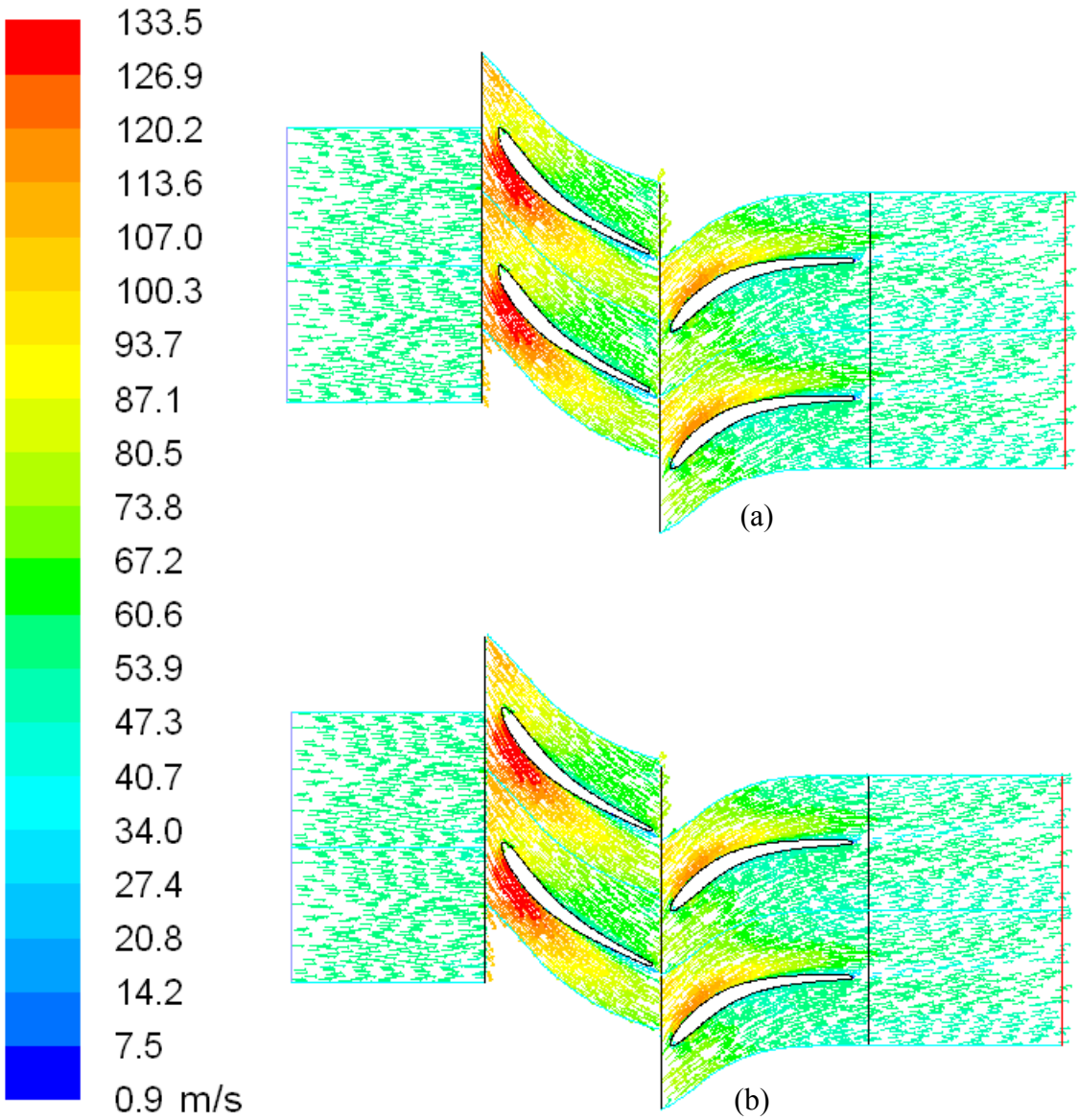

Figure 5.7 Velocity vector (Relative velocity is plotted in the rotor-subdomain area) (a) non-fogging baseline (b) overspray fogging.

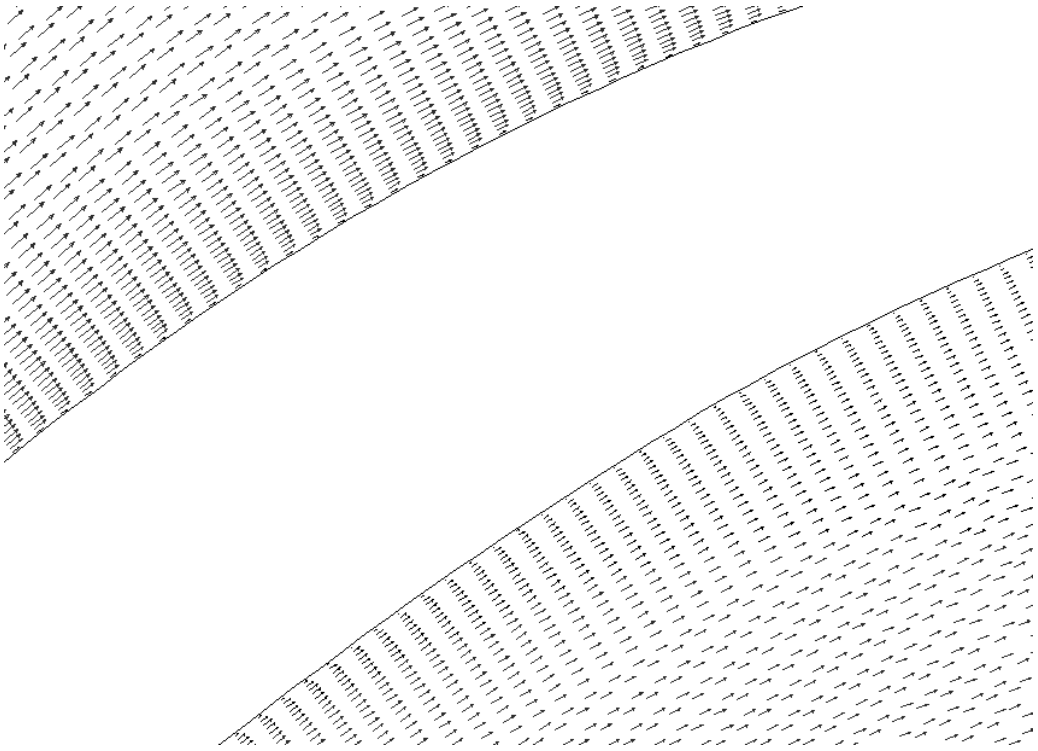

Figure 5.8 Velocity profile over the stator for baseline case.

5.5.3.5 Hydrodynamic Response Time, Slip Velocity and Thermal Response Time

The interaction between the discrete phase and the continuous phase involves heat transfer, mass transfer, and body forces. All these models are built around the relative velocity (i.e. slip velocity) between the droplet and the main flow. According to the drag law and particle response time (Eq. 2.44), the piecewise calculation (dashed line in Fig. 5.9) conducted by hand verifies the CFD result, which provides more detailed variations of slip velocity along the flow path. It is seen that the slip velocity almost becomes zero before reach the rotor inlet at x = 0. The droplets reach approximately 98% of the air velocity within a millisecond, which is right before they reach the rotor inlet. Once the droplets enter the rotor sub-domain, they are subjected to local acceleration and deceleration (or pressure gradients) as seen from increased relative droplet Reynolds number in Fig. 5.10. The slip between droplets and mainstream continuously involves and varies in the stator sub-domain due to local pressure gradients in its curved passage. Eventually, the slip velocity again is reduced once the flow exits the stator sub-domain and enters the straight passage of the exit sub-domain. Most of the droplet relative Reynolds numbers are less than 15.

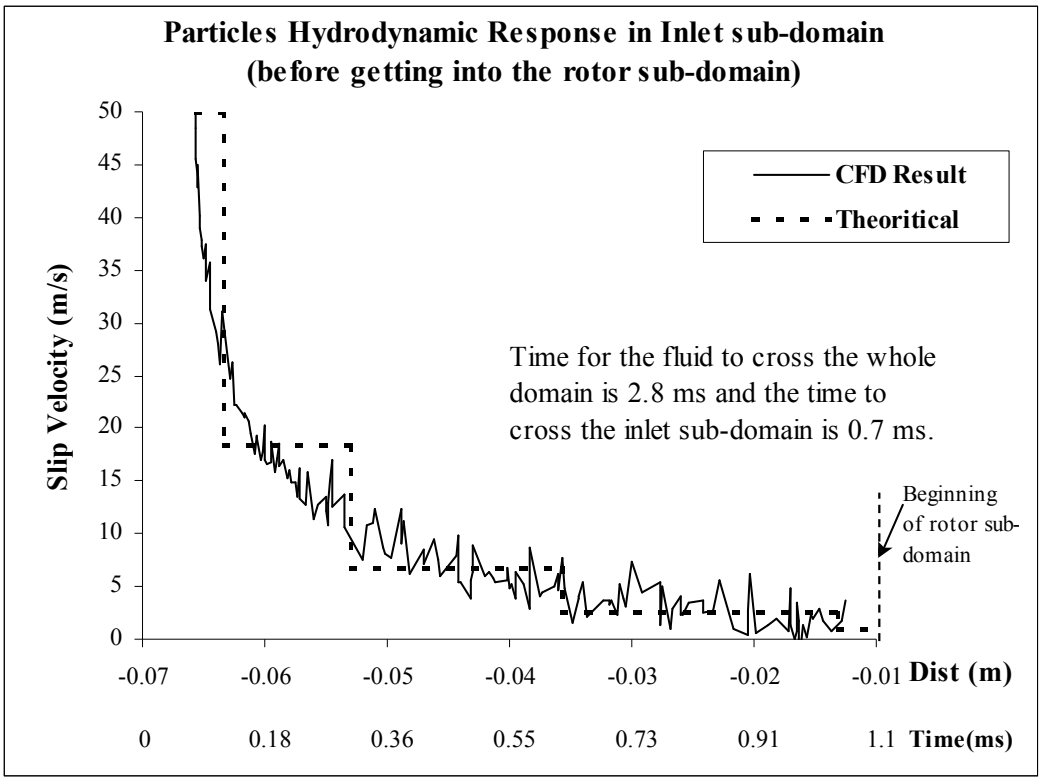

Figure 5.9 Droplet hydrodynamic response showing as slip velocity.

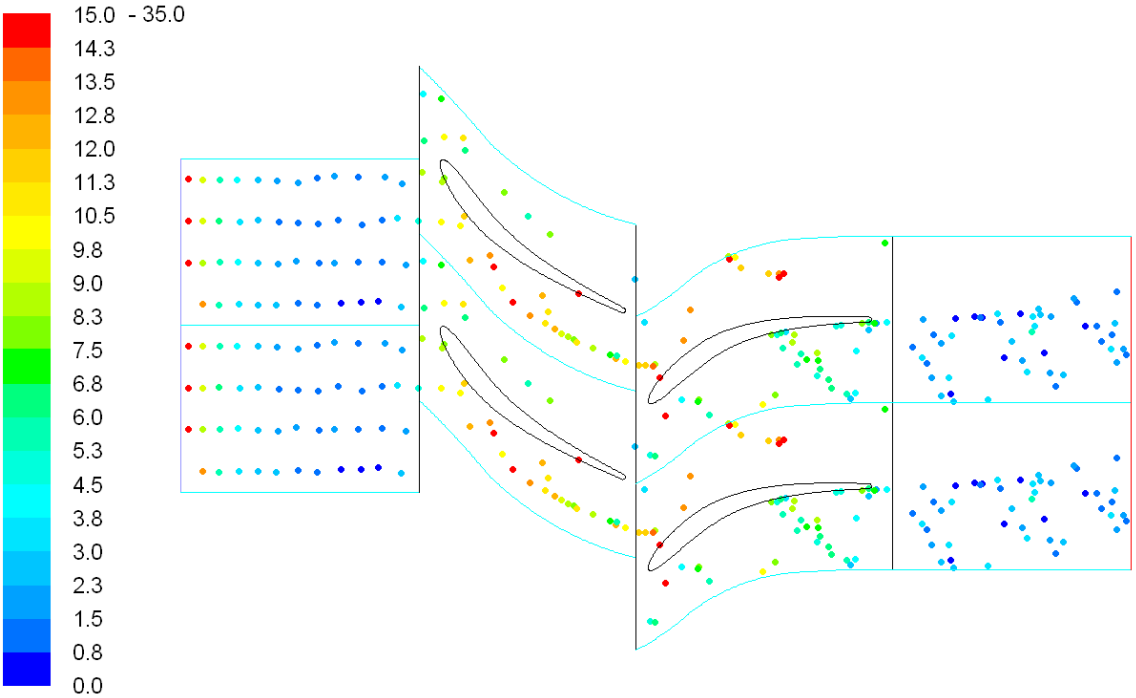

Figure 5.10 Droplet relative Reynolds number distribution.

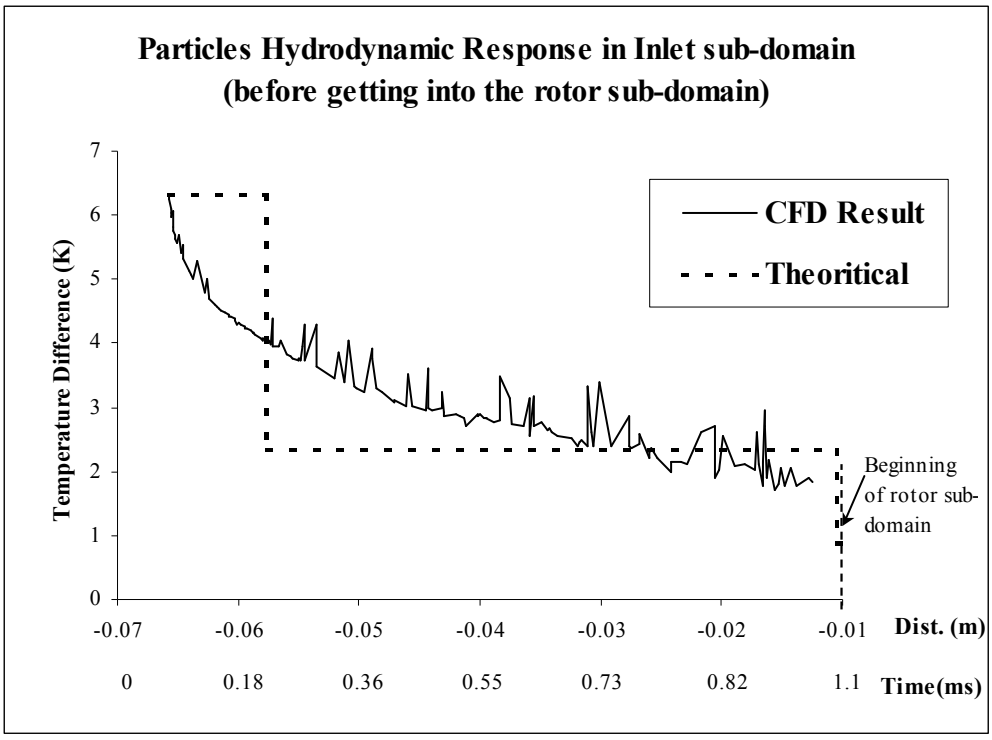

Figure 5.11 Droplet thermal response

Theoretical calculation of thermal response time is more complicated than the calculation of hydrodynamic response time because the temperature and velocity is coupled in Eq. (2.47). Equation (2.47) has been used for piecewise hand calculation to verify the CFD result as shown in Fig. 5.11. The hand calculation shows the droplet temperature is approximately $1^{o}C$ off from the mainstream flow bulk temperature before entering the rotor sub-domain; while the CFD result provides a more detailed variation of droplet temperature along the path and predicts the droplet temperature is approximately $2^{o}C$ below the air temperature before reaches rotor. The hand calculation and CFD result are consistent.

5.5.3.6 Liquid Concentration

The effect of liquid evaporation is seen from the distributions liquid concentration shown in Fig. 5.12. Saturation is not reached at the exit. This means that the droplet thermal response time was longer than the duration of time for most of droplets flying through the entire domain.

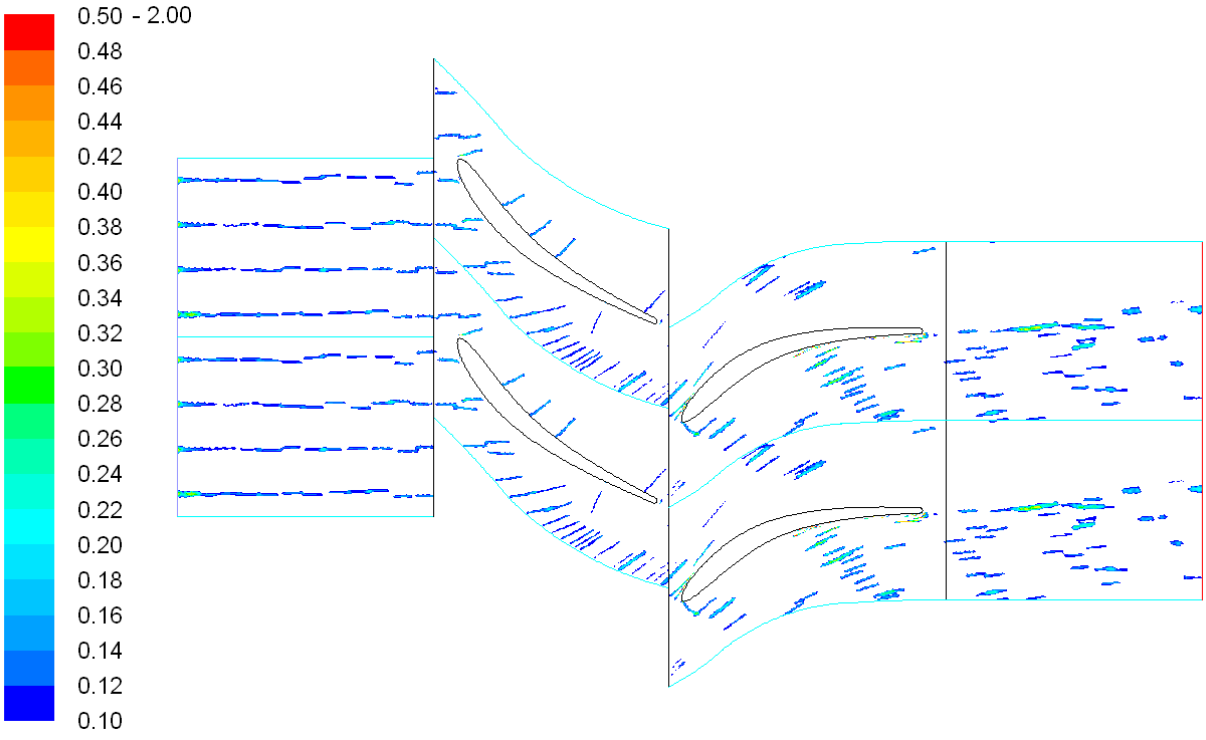

Figure 5.12 Distribution of concentration (kg/m³) of liquid water

5.5.3.7 Droplet Breakup and Coalescence

In the present compressor stage study, the difference with and without considering breakup and coalescence is noticeable, but not remarkable. Figure 5.13(a) shows droplets size distribution without considering breakup and coalescence in a range of 10 to 25μm. To clearly show the effect of breakup and coalescence, the overspray is increased to 4%, as shown in Fig 5.13(b). It is clear from the figure that the droplets experience coalescence before they reach the rotor due to collisions induced by turbulent dispersion downstream of sprays. The droplets reduce sizes due to evaporation before reaching the rotor, but once they enter the rotor domain, coalescence takes place and droplets size increases due to local acceleration and deceleration of the flow field.

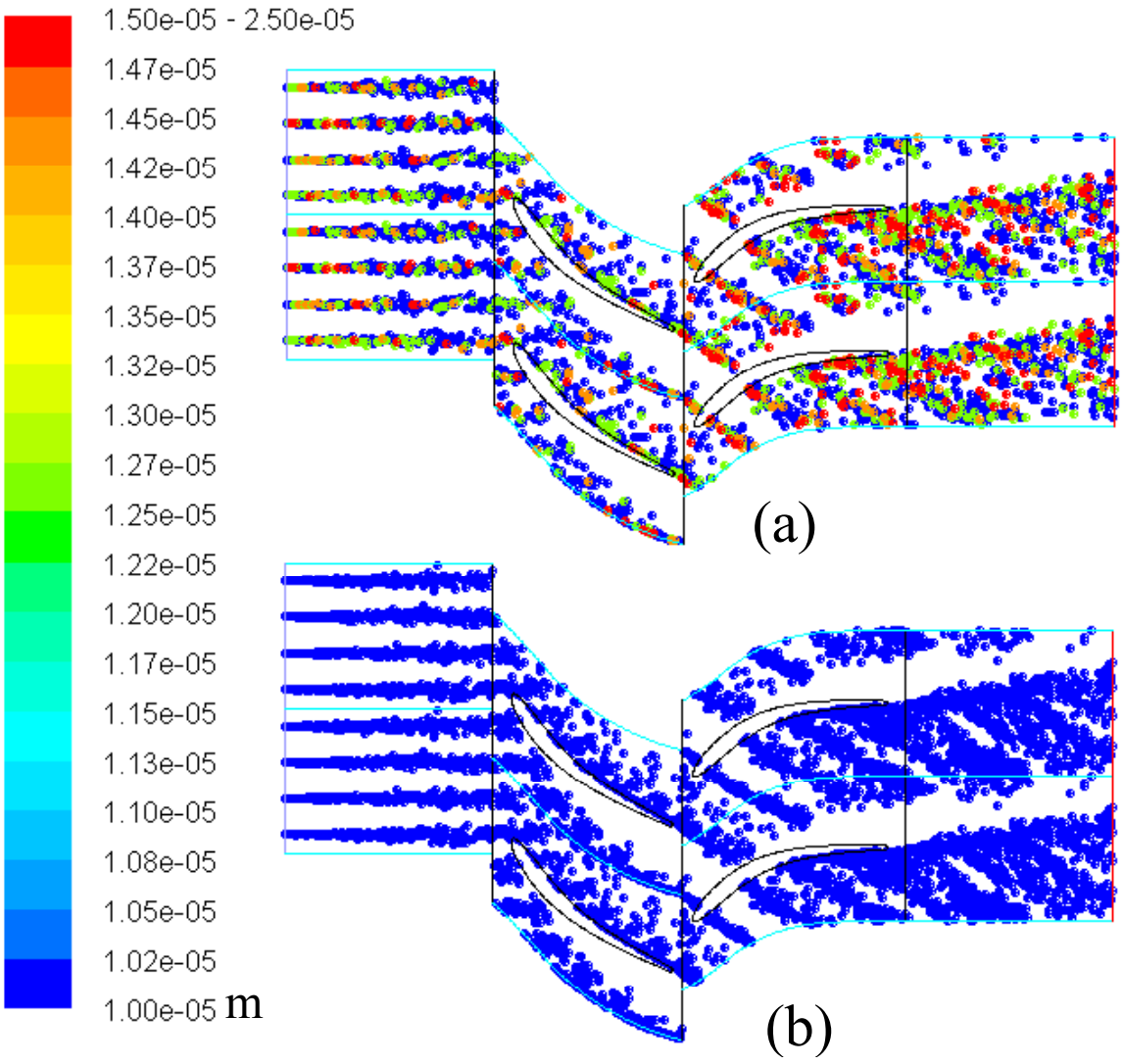

Figure 5.13 Droplet diameter (m) distribution (a) with break-up and coalescence (b) without break-up and coalescence.

5.5.3.8 Droplet Erosion

The blade material used in the current CFD simulation is ductile metal (steel). The largest erosion rate is predicted as 4.23×10^{-9} (kg/m^2-s) or 0.2873 (kg/m^2-yr), which is approximately equivalent to a loss of 17 μm thickness of metal layer per year if the compressor runs for the whole year without any pause. The largest erosion takes place near the rotor trailing edge and stator leading edge.

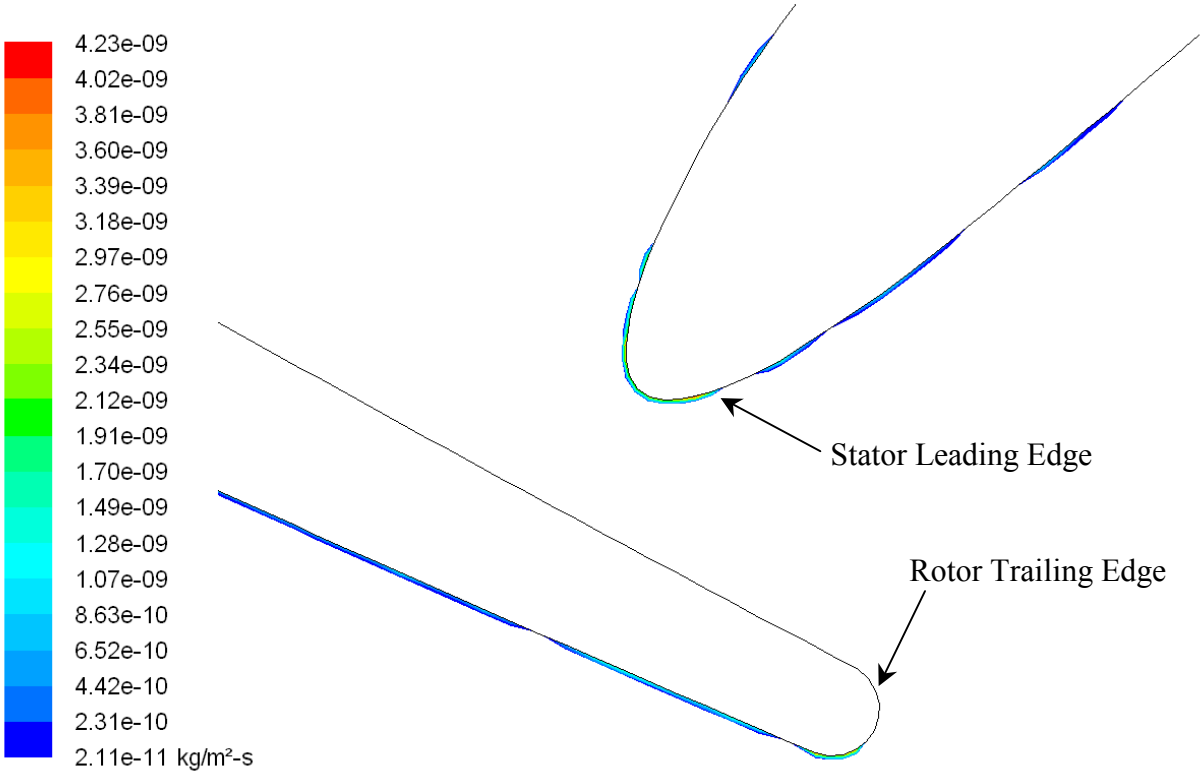

Figure 5.14 Erosion (kg/m^{2}s) distribution on the rotor trailing edge and stator leading edge (The relative position of rotor and stator is not ture)

5.5.3.9 Comparison of Different Rotor-Stator Relative Positions

Static pressure distribution (for overspray cases) for different rotor-stator relative positions (rotating part of the compressor) is shown in Fig. 5.15 for 4% overspray. In each sub-figure, the percentage shown is the percentage of one pitch distance (0.042m) traveled by the rotor. It is found that the static pressure achieved the maximum rise at the 0% position in Fig. 5.16(d) because this position produces the least blockage to the airflow. On the other hand, the 75% position produces the least amount of pressure rise due to the maximum blockage. The pressure ratios at 0%, 25%, 50% and 75% position are 1.067, 1.05, 1.038 and 1.032, respectively. Temperature distribution (Fig. 5.16) is consistent with pressure due to air compression. Less flow blockage results in more effective compression and higher temperature.

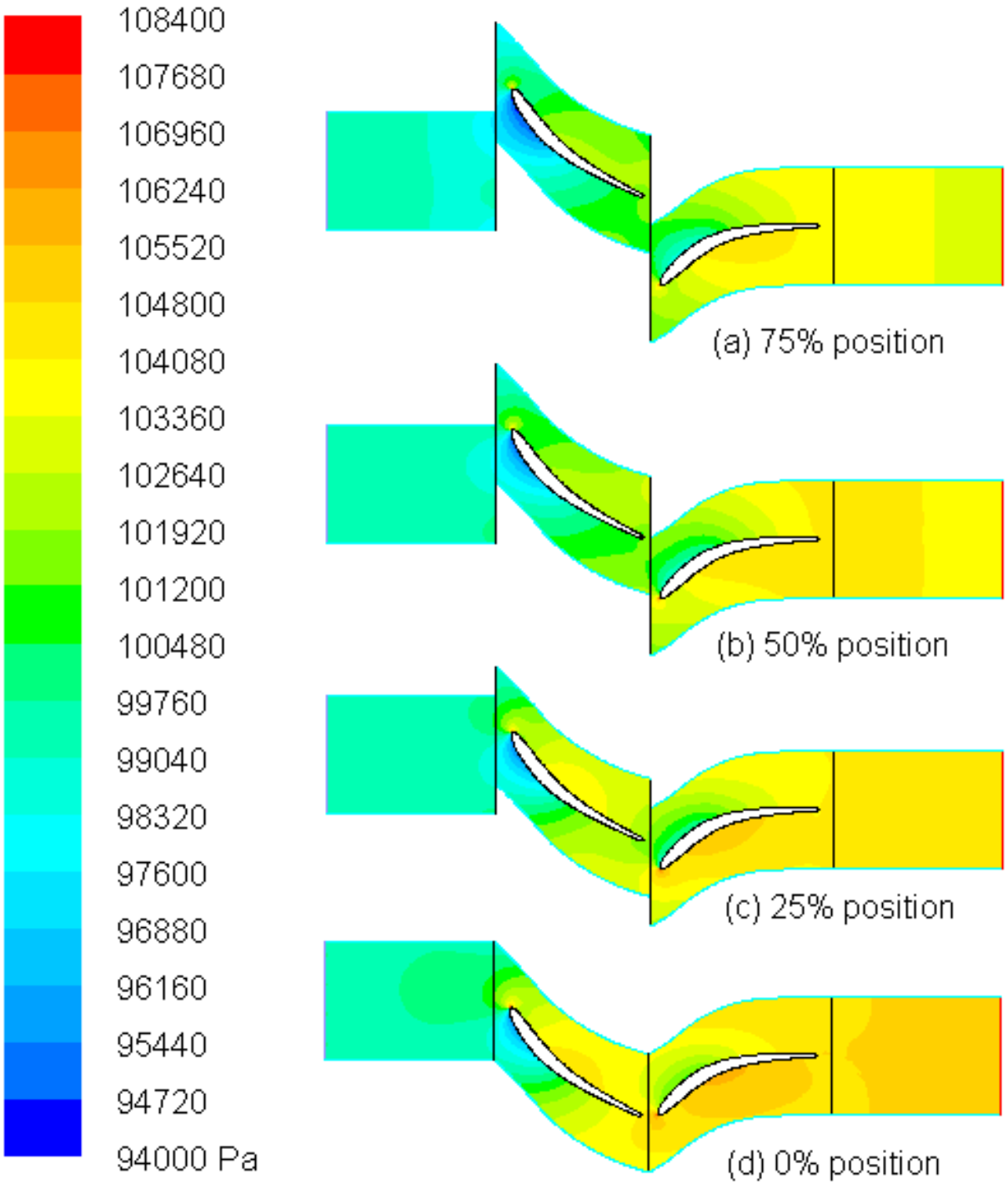

Figure 5.15 Pressure distribution at different rotor-stator relative positions.

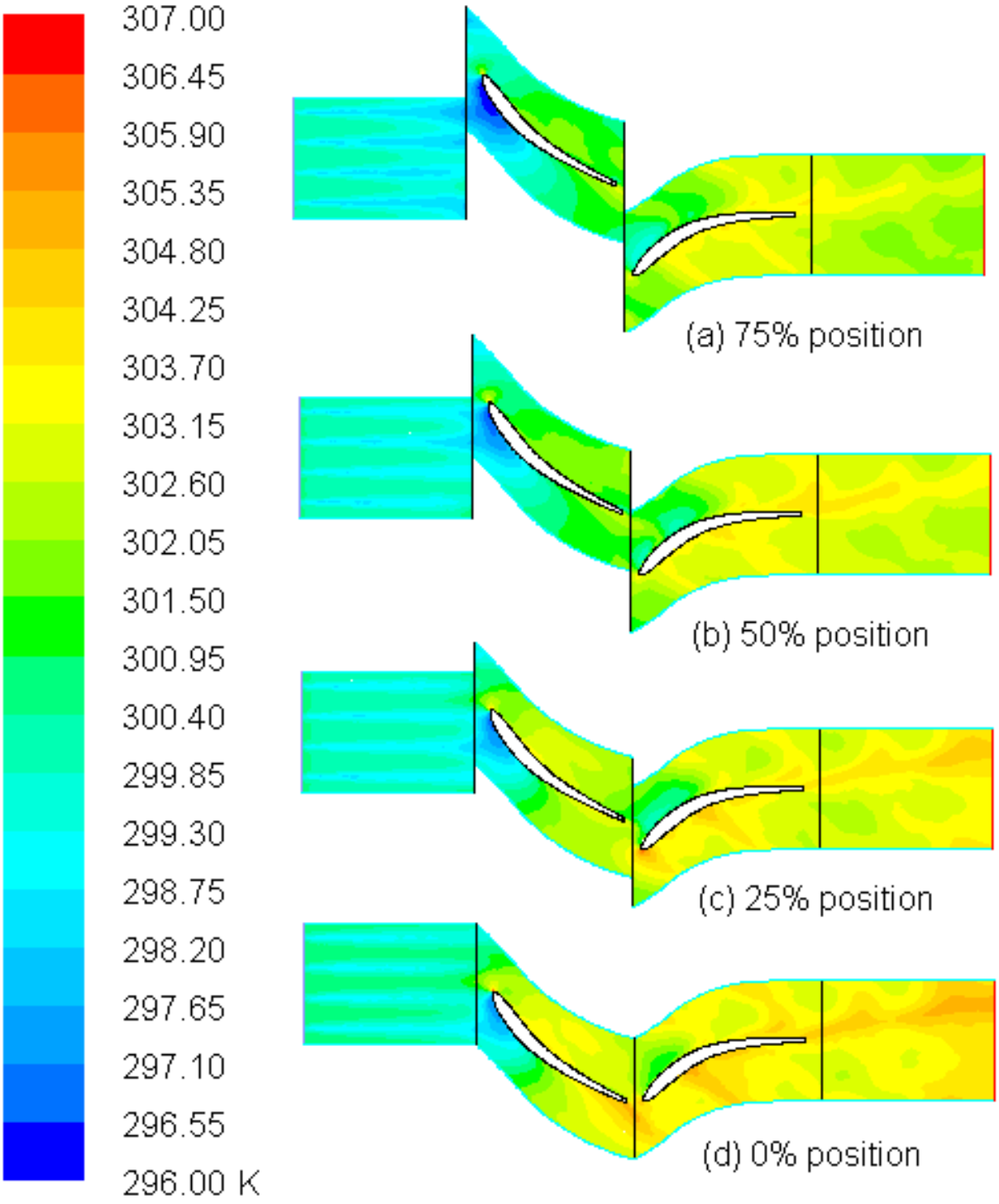

Figure 5.16 Temperature distribution at different rotor-stator relative positions.

5.5.3.10 Comparison of Different Wall Boundary Conditions for Droplets

As explained before, there are three representative types of wall boundary conditions for water droplets including reflect (the droplet bounces back when it touches the wall), film (the droplet accumulates on the wall), and trap (the droplet evaporates as soon as it touches the wall). Since the trap condition fall between the reflect and the film models, the current study conducts a comparison between using the reflect and the film boundary conditions. The comparison shows the difference at the exit of the domain is negligible (Table 5.2) although the wall temperature distribution in Fig. 5.17 shows film boundary condition made the pressure side a bit cooler near the fore body of the airfoil. .

Table 5.2 Comparison of different droplet wall conditions

Wall Boundary Conditions	**Reflect**	**Film**
Inlet Static Pressure (Pa)	99656	99659
Exit Static Pressure (Pa)	105426	105466
Inlet Static Temperature (K)	300.39	300.39
Exit Static Temperature (K)	304.36	304.43
Inlet Relative Humidity (%)	100.3	100.3
Exit Relative Humidity (%)	86.5	86.2
Water Concentration at inlet (kg/m^3)	0.2216	0.2314
Water Concentration at exit (kg/m^3)	0.0341	0.0364

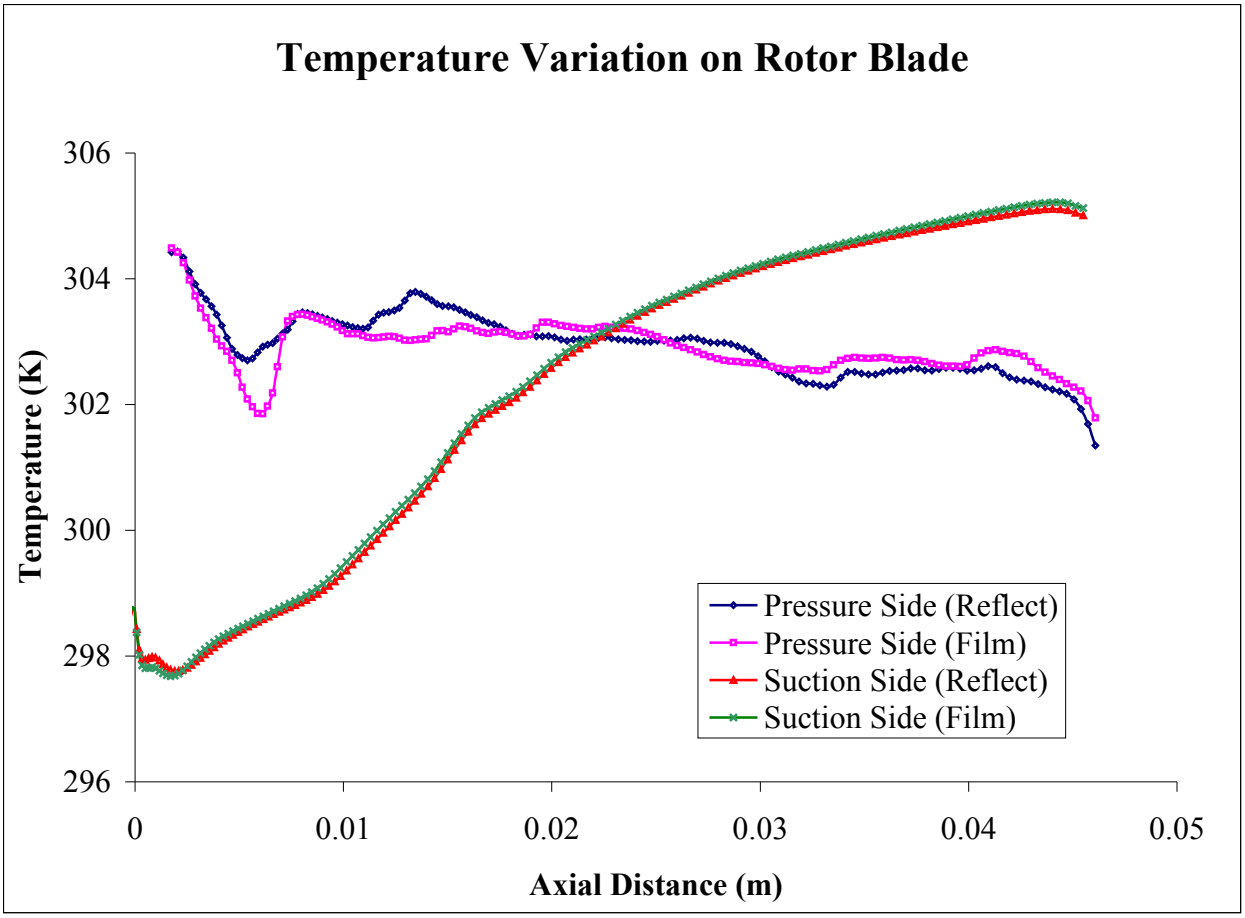

Figure 5.17 Comparison of temperature distributions on the rotor wall for two different types of droplet wall boundary conditions: "Reflect" verses "Film."

It should be noted that the 2-D analysis studied in this study does not include important factors of secondary flow and centrifugal force, which could exert additional effects on the droplet dynamics. But 2-D analysis is a good starting point, especially for validation of some important droplet dynamics, like response time, variation of different boundary condition, variation of different rotor-stator position.

5.6 Three Dimensional Analysis

5.6.1 Geometrical Configuration

Figure 5.18 shows the meshes of inlet, rotor and stator of the 3D computational domain. The mesh number is reduced for clarity. The geometries of rotor and stator are adopted from Hsu and Wo (1998) and 2% of the tip clearance for rotor is imposed here according to Chima (1998) and Gerolymos and Vallet (1999). Figure 5.19(a) shows the periodic meshes of inlet, rotor and stator, and Fig. 5.19(b) shows the close-up view of one pitch of inlet, rotor and stator. Structured mesh is used in the inlet sub-domain and on the blade surfaces; hexahedral meshes are used in rotor and stator sub-domains. Nine hundred thousand meshes are used as the coarse grid for both the baseline and fogging cases, and 1.7 million meshes are used as the finer grid only for baseline. Finer grid is not used for fogging due to limitation of existing computer capacity.

Figure 5.18 Meshes for rotor and stator. (The mesh number is reduced for clarity.)

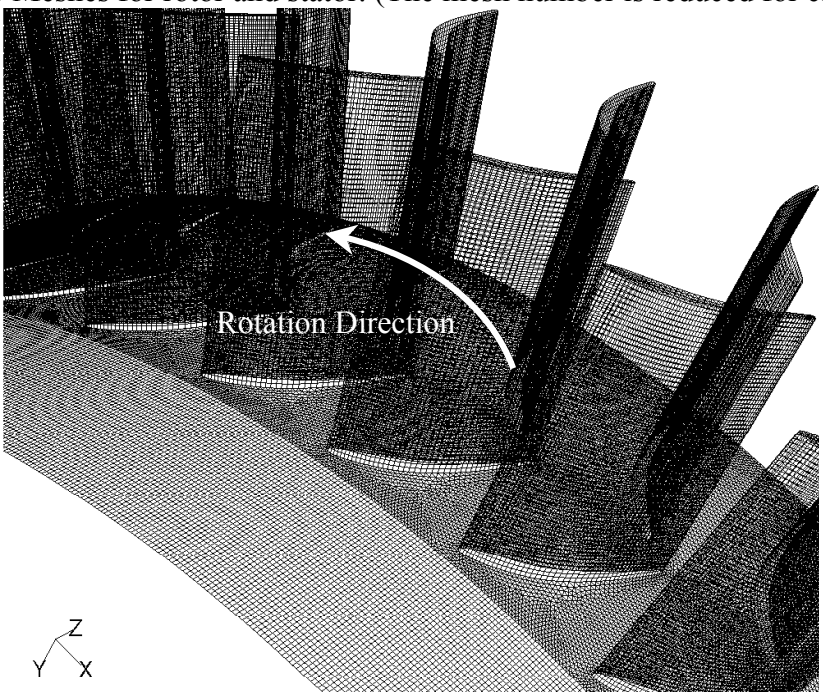

(a) Periodic Meshes

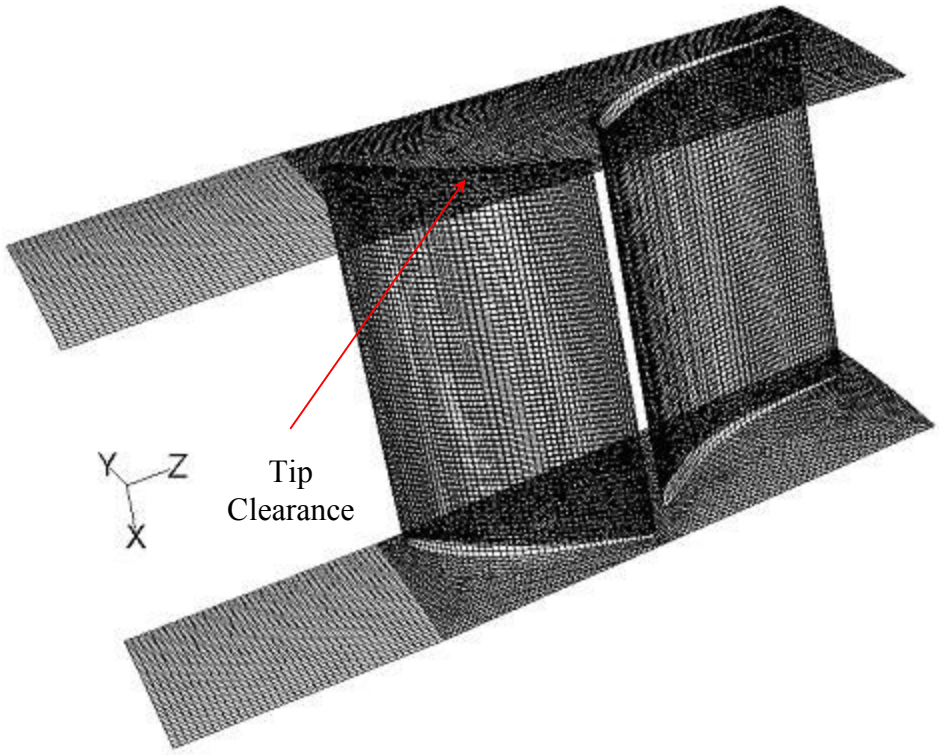

(b) Close-up view of one pitch of inlet, rotor and stator

Figure 5.19 Overall and close-up 3D meshes

Figure 5.20(a) shows how the computational domain has been divided into three sub-domains, namely inner sub-domain, rotor sub-domain and stator sub-domain. This figure also shows the selected surfaces for analysis and discussion including three radial surfaces (y-z planes at 25%, 50% and 75% of blade height respectively), three axial surfaces (x-y planes in the middle of each sub-domains) and one vertical circumferential surface (x-z plane) slicing through the middle of the pitch. The radial surfaces are named as radial-25, radial-50 and radial-75; axial surfaces are named as the developing-plane, rotor-plane and stator-plane, and the x-z vertical slicer is named as the pitch-plane. Twelve cross marks at the inlet of the domain show the locations of water injection. The domain extends axially from z = 0 to z = 0.18m, radially from x = –0.45m to x = –0.36m and circumferentially from –3.6° to +3.6° (or an angular span of 7.2°) for one pitch. A total of 50 pairs of rotors and stators is modeled by applying the periodic boundary on one pitch.

The equations for three radial surfaces are shown in Eq. (5.31).

$$x^2 + y^2 = [-0.45 + 0.25 \times (0.45 - 0.36)]^2 \qquad (5.31a)$$

$$x^2 + y^2 = [-0.45 + 0.50 \times (0.45 - 0.36)]^2 \quad (5.31b)$$

$$x^2 + y^2 = [-0.45 + 0.75 \times (0.45 - 0.36)]^2 \quad (5.31c)$$

Water is sprayed at12 points (4 radial × 3 circumferential), which are equally distant in radial and longitudinal directions at the inlet as shown in Fig. 5.20(a). 4 radial locations are ⅛, ⅜, ⅝ and ⅞ distance from hub to tip. One of the 3 circumferential location is at the y = 0 plane and the other two planes are at –2.4° and +2.4° from the y = 0 plane. Some more radial planes (which are not shown in Fig. 5.20.b) aligned to the spraying points are adapted to analyze the water concentration distribution. These planes are represented by the equations and named as radial-12.5 (eq. 5.31d), radial-37.5 (eq. 5.31e), radial-62.5 (eq. 5.31f) and radial-87.5 (eq. 5.31g):

$$x^2 + y^2 = [-0.45 + \tfrac{1}{8} \times (0.45 - 0.36)]^2 \quad (5.31d)$$

$$x^2 + y^2 = [-0.45 + \tfrac{3}{8} \times (0.45 - 0.36)]^2 \quad (5.31e)$$

$$x^2 + y^2 = [-0.45 + \tfrac{5}{8} \times (0.45 - 0.36)]^2 \quad (5.31f)$$

$$x^2 + y^2 = [-0.45 + \tfrac{7}{8} \times (0.45 - 0.36)]^2 \quad (5.31g)$$

The planes for three axial surfaces (maroon, orange and brown) are at z = 0.03, z = 0.09, and z = 0.15 respectively. These axial surfaces are axisymmetric to y = 0 plane and shown in Fig. 5.20(a).

The equation for the pitch –plane (broken pink line) is y = 0.

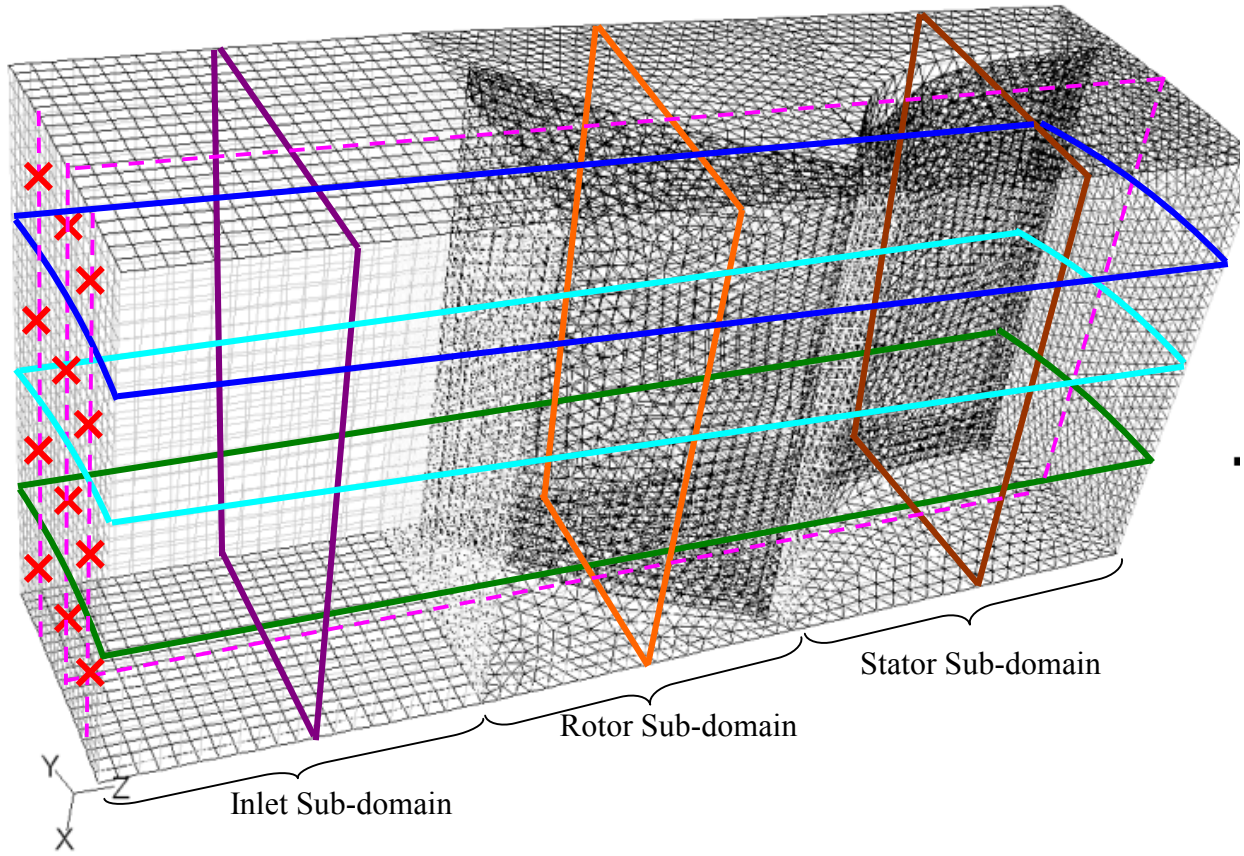

Figure 5.20(a) Selected surfaces for analysis and discussion (3 radial, 3 axial and one circumferential plane). The cross marks show the water injection locations.

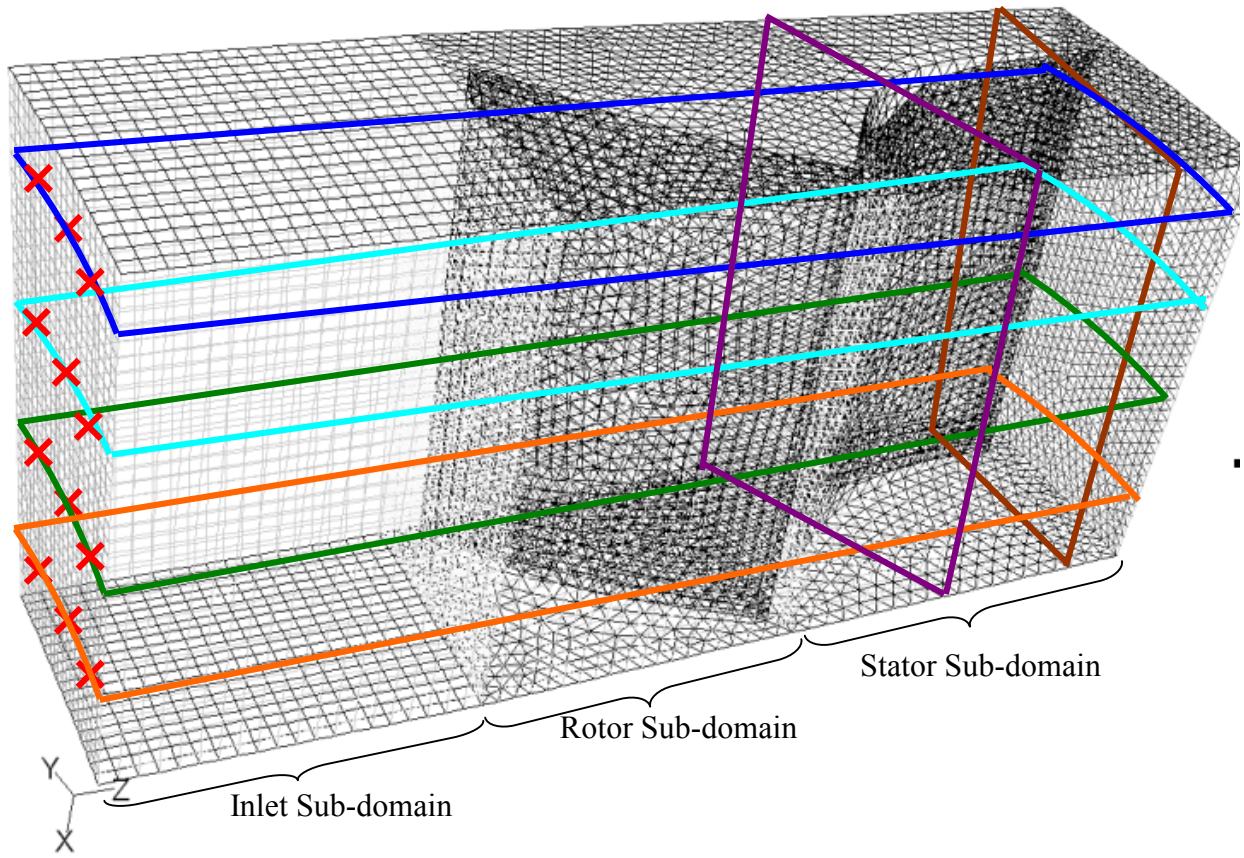

Figure 5.20(b) Specially Selected surfaces for analysis of concentration and secondary flow (The cross marks show the water injection locations)

Figure 5.20(b) shows four new radial planes, which are radial-12.5, radial-37.5, radial-62.5 and radial-87.5, colored as orange, green, cyan and royal blue respectively. Two more planes are adopted for the analysis of secondary flow, which are colored as purple and brown in Fig. 5.20(b). Purple plane is perpendicular to the stator at 20% of its chord length from the leading edge and named as the stator-perpendicular plane, which can be represented by the equation $y + \sqrt{3}\, x = 0.236$. The brown plane is an axial plane ($z = 0.165$), which lies very close to the exit and named as the close-to-exit plane.

5.6.2 Boundary Conditions

5.6.2.1 Continuous Phase

The stagnation condition of the inlet main flow is assigned as 1 atm air at 304.2K (static temperature is 300K), and 60% RH (or with the absolute humidity at 0.01369 kg/kg dry air) moving at a uniform velocity of 91 m/s. The inlet condition is assigned by fixing the total pressure as 101,325 Pa and total temperature at 304.2 K, and the exit condition is assigned by fixing the static pressure as a value that will give the inlet velocity of 91 m/s. Since the exit static pressure is not known, iteration will take place to try different exit pressures until the inlet velocity reaches an average value of 91 m/s. Under these assigned conditions, the inlet static pressure, static temperature, and velocity will be calculated cell by cell and will not be uniform. There was an attempt to assign a uniform velocity at the inlet. However, if a constant velocity were assigned as the inlet condition, the total pressure would be calculated cell-by-cell and would not be uniform, which is not consistent with reality.

The chilled water at 288K (58^{o}F) is atomized and injected at a velocity of 25 m/s. The calculated mass flow rate is 0.4639 kg/s per pitch, which is used to find the amount of water, 0.004639 kg/s, for 1% overspray fogging case.

The static pressure (96.07 kPa) at the inlet and shown in Table 5.3 is a mass-weighted average static pressure, and the calculated total pressure at the exit is mass-weighted average as well. Since there are 50 rows of blades, the rotational periodic (or cyclic) boundary condition is set to simulate 50 rows of rotors and stators. The total mass flow rate for the entire compressor inlet is (0.4639 × 50) = 23.195 kg/s for fogging. The mass flow rate ($\dot{m} = \rho AV$) is calculated, as shown below:

Inlet pressure = 96.07 kPa,

Inlet temperature = 299.89K,

Gas constant for air = 0.287 kJ/kg.K

The air density at inlet is, $\rho_a = \frac{P}{RT} = \frac{96.07}{0.287 \times 299.89} = 1.1038 kg/m^3$

At the inlet, the inlet diameter is, d_i = 0.72m and the outer diameter is, d_o = 0.9m.

The inlet area therefore is $A = \frac{\pi}{4}\left(d_o^2 - d_i^2\right) = \frac{\pi}{4}\left(0.9^2 - 0.72^2\right) = 0.229 m^2$

Inlet velocity is, V = 90.85 m/s and the mass flow rate is,

$\dot{m} = \rho AV = 1.1038 \times 0.229 \times 90.85 = 23.2 kg/s$

The backflow (reverse flow) temperature (if any) is set to 310 K. All the walls (rotor and stator) in the computational domain are assigned as adiabatic with the non-slip velocity boundary condition, i.e zero velocity at all walls. As the compressor has 50 rows of blades, the included angle between two consecutive blade rows is 7.2°. Again, all the parameters are set with rotational periodic boundary conditions, which carry the information from the downward edge to the forward edge along the rotating direction.

5.6.2.2 Disperse Phase (Water Droplets)

The water droplet size is uniformly given as 10 μm. Although uniform distribution of the droplet size is not consistent with a real atomized nonuniform droplet distribution, it is easy to visualize and track the variation of droplet size due to evaporation, break-up and coalescence. The mass ratio of mist over airflow is 1%, which is 4.639 mg/s at the inlet. Mist is injected at 4 radial locations in three longitudinal locations and uniformly distributed between the hub and tip at the inlet plane, as shown by 12 cross marks in Fig. 5.20(a). The boundary condition of droplets at walls is assigned as "reflect", which means the droplets elastically rebound off once reaching the wall. Typically this occurs when the wall temperature is typically 50°F superheated above the saturation temperature. However "film" boundary condition is also tested for comparison. The wall film boundary condition allows liquid droplets to deposit on the wall surface and form a liquid film based on certain criteria (surface tension, surface superheat, Weber number etc., see details below). If the wetting criteria are not satisfied, the droplets will be reflected back from the wall. The true boundary condition lies in between these two models.

At the outlet, the droplets just simply flee/escape from the computational domain. The simulation also incorporates droplets breakup, coalescence and erosion. The erosion model built in the FLUENT is a solid particle erosion model, which is not fit for liquid erosion, so an UDF (User Defined Function) was incorporated with Fluent model, which has already been described earlier in Section 5.3.1.

5.6.3 Results and Discussions

5.6.3.1 Pressure

Compressor's static pressure increases from 96 kPa to 110 kPa with a static pressure ratio 1.146 for the baseline case as shown in Fig. 5.21(a). The lowest static pressure (suction peak) at 86 kPa is found on the suction side of the rotor near the leading edge. The stagnation pressure in the range of 110 and 120 kPa is found at the stagnation region of rotor shown in Fig. 5.21(b).

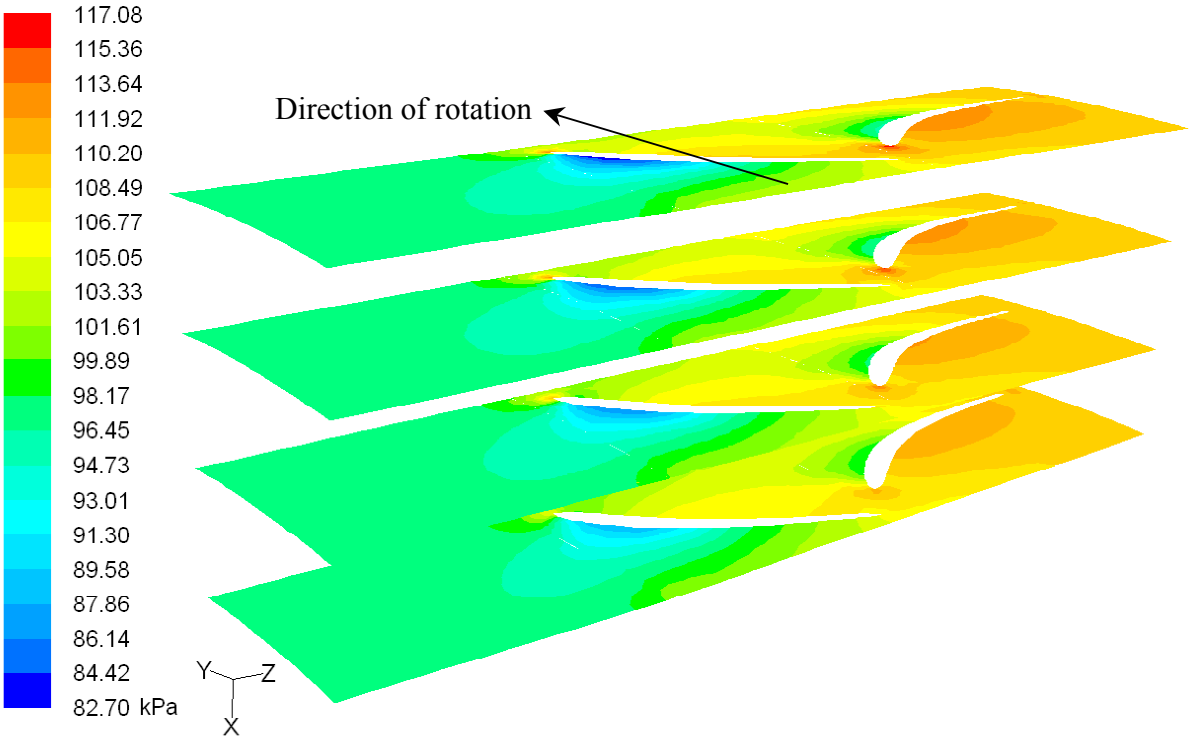

Figure 5.21 (a) Static pressure distribution for baseline case in different radial planes

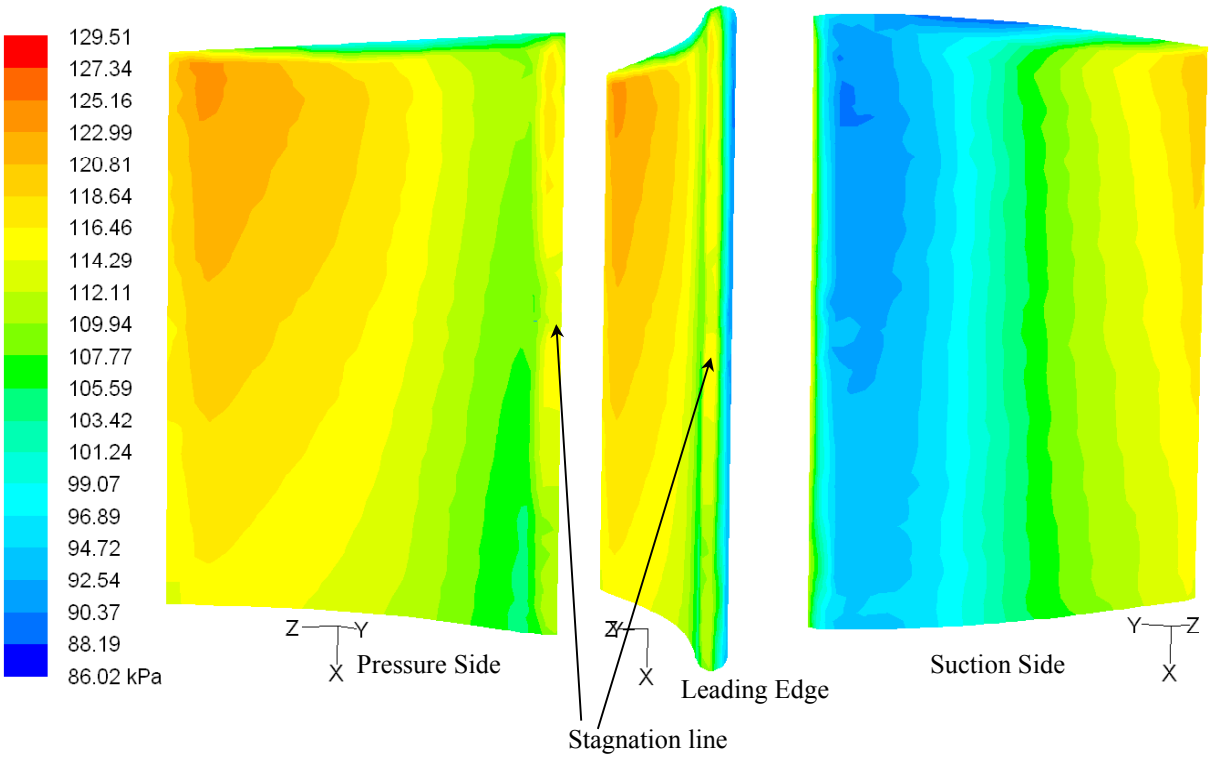

Figure 5.21 (b) Stagnation pressure distribution on the rotor surface for baseline on suction surface, leading edge, and pressure surface.

As fogging is applied, compressor's static pressure increases from 96 kPa at inlet to 110.5 kPa with a static pressure ratio of 1.151, a bit higher than baseline case. When fogging is applied, the stagnation line has not been shifted significantly. The stagnation pressure ranges from 110 to 120 kPa at the stagnation line. The isobar contours for the fogging case and baseline case do not any significant difference.

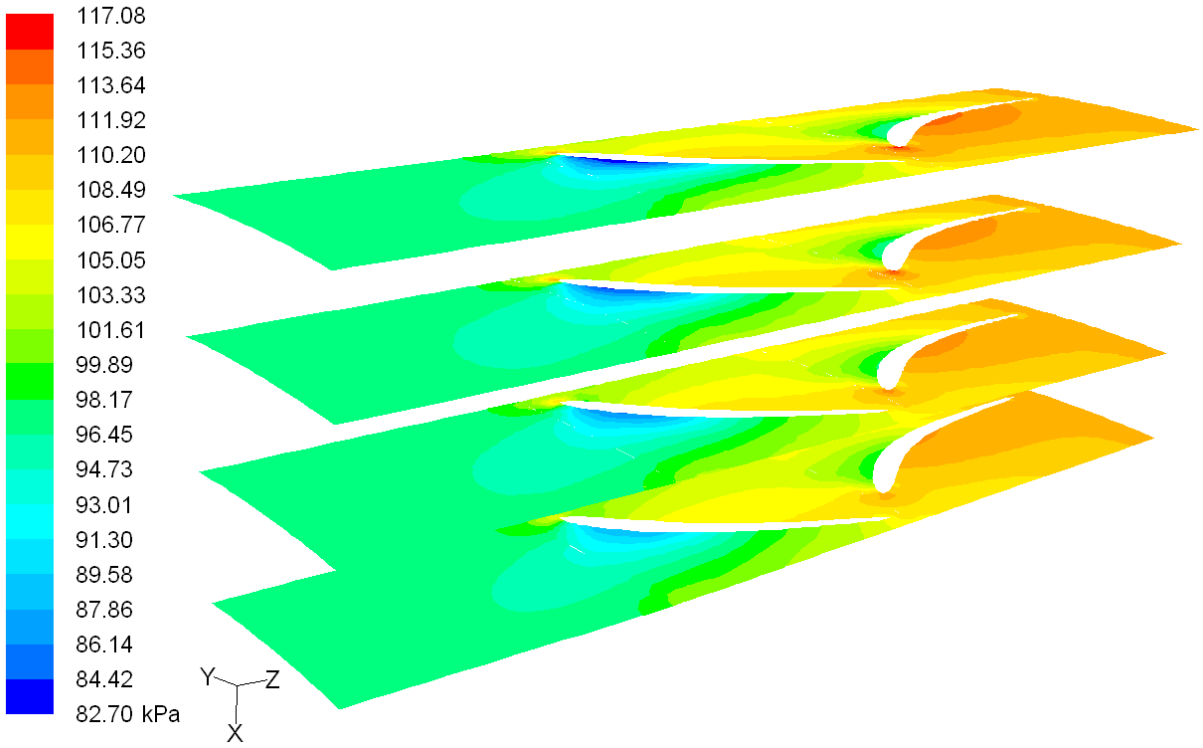

Figure 5.21 (c) Static pressure distribution for fogging case on different radial planes and over the hub.

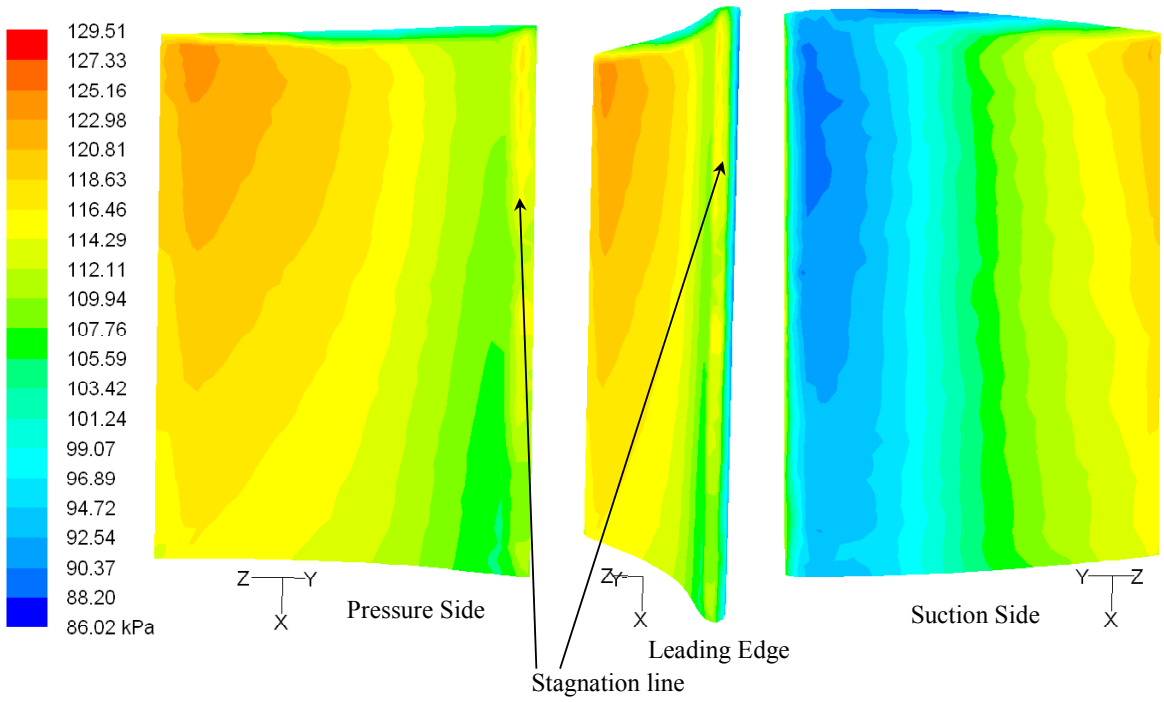

Figure 5.21 (d) Stagnation pressure distribution for fogging case across the rotor surface

5.6.3.2 Static Temperature

The temperature distribution without and with water spray is shown in Figs. 5.22(a) and (b). For baseline case (dry air with 60% relative humidity without fogging), a wide range of temperature distribution is noticed. Inlet portion is almost constant (300K – 301K) everywhere. Temperature significantly drops to 290^{o}C at the leading edge of suction side of rotor due to strong acceleration and pressure drop downstream of the stagnation region (see Fig. 5.21a). Temperature increases from 290K to 311K along the suction side and from 305K to 311K along the pressure side. As expected, the static pressure is higher on the pressure (convex) side and lower on the suction (concave) side as shown in Fig. 5.21(a), and due to the nature of compression, air temperature is higher on the pressure side and lower on the suction side (Fig. 5.22). The average temperature is 313.5K at the exit (as shown in Table 5.3).

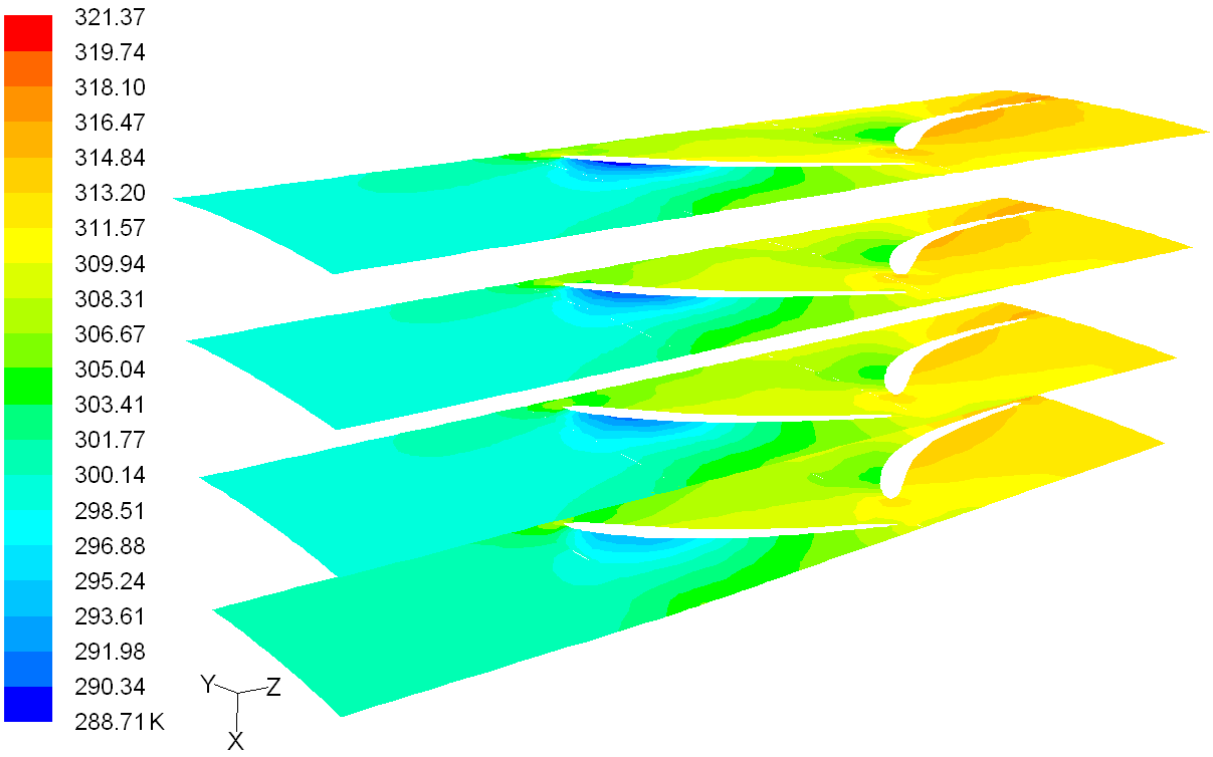

Figure 5.22 (a) Static temperature distribution for baseline case (no fogging) on three radial planes and the hub surface

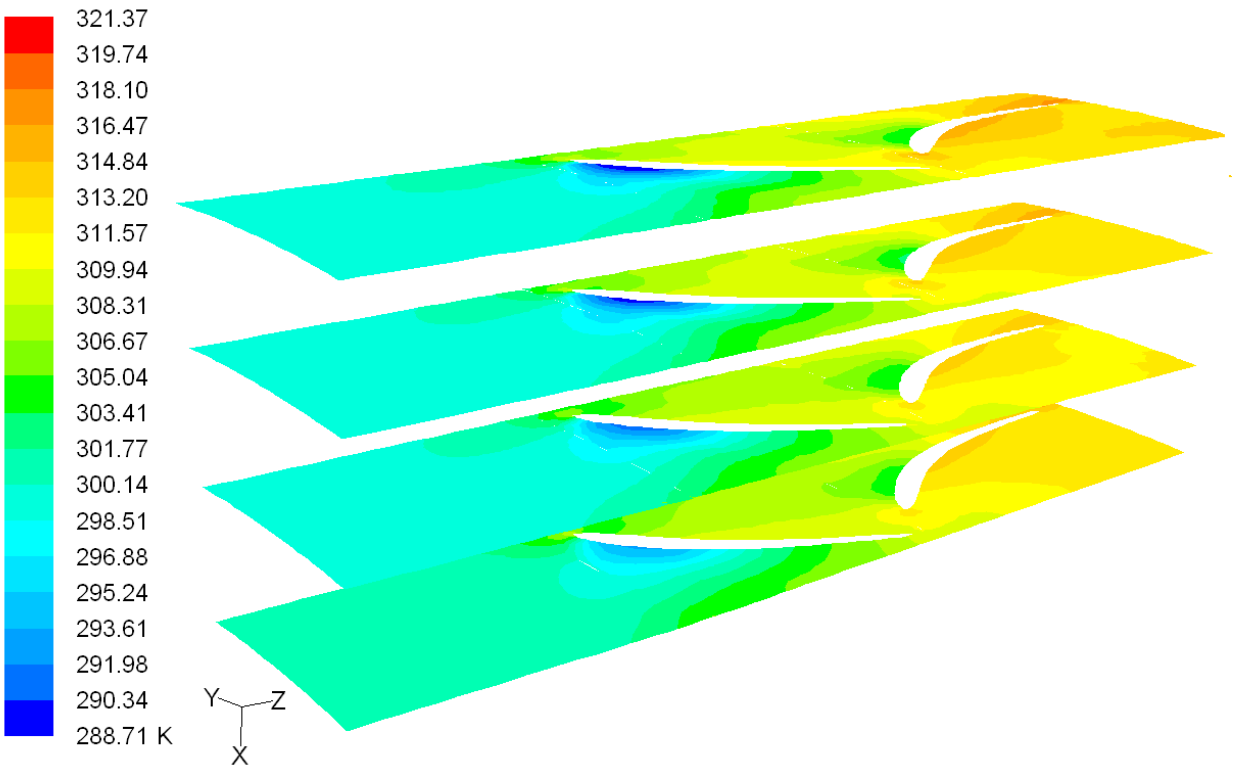

Figure 5.22 (b) Temperature distribution for fogging case on different radial planes and hub surface

For the fogging case (Fig. 5.22b), temperature drops a little from baseline case. Temperature is higher on the pressure side and lower on the suction side for both the rotor and stator for the fogging case. Temperature reduces to 313K at the exit. The minimum temperature of 309K is shown at the radial-25 and hub surfaces near the exit. The general trend in the fogging case shows the temperature decreasing from the hub towards the tip in the rotor passage and in the opposite direction in the stator passage (i.e. lower near the hub).

5.6.3.3 Velocity

The velocity distribution in Fig. 5.23(a) shows that the inlet velocity at rotor is 91 m/s, which does not vary too much with fogging as shown in Fig. 5.23(b). The exit velocity at the rotor is approximately 135 m/s for both the cases like the 2-D case. There is a secondary flow moving from the pressure side towards the suction side.

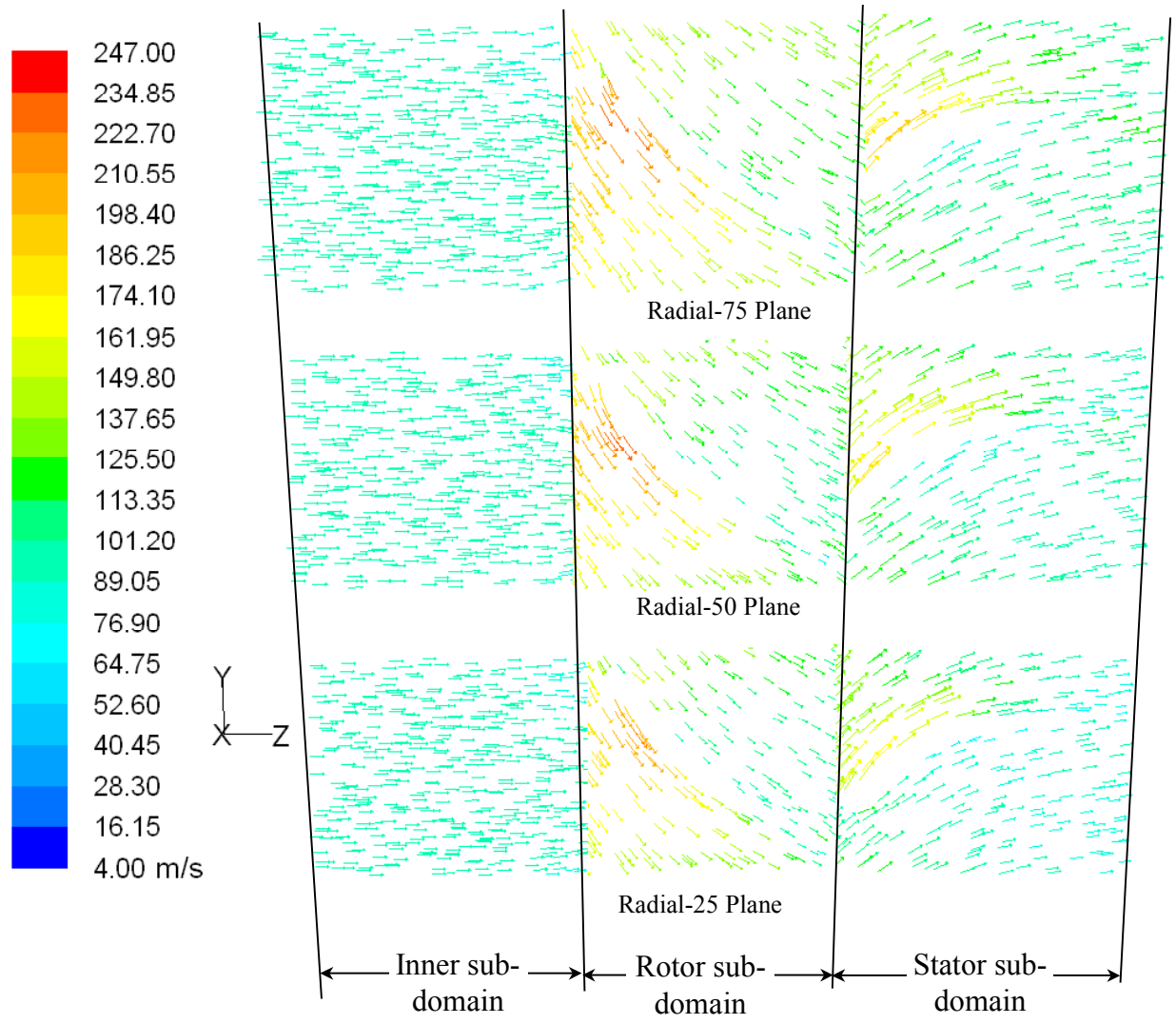

Figure 5.23 (a) Projected horizontal velocity vector for baseline case on different radial planes

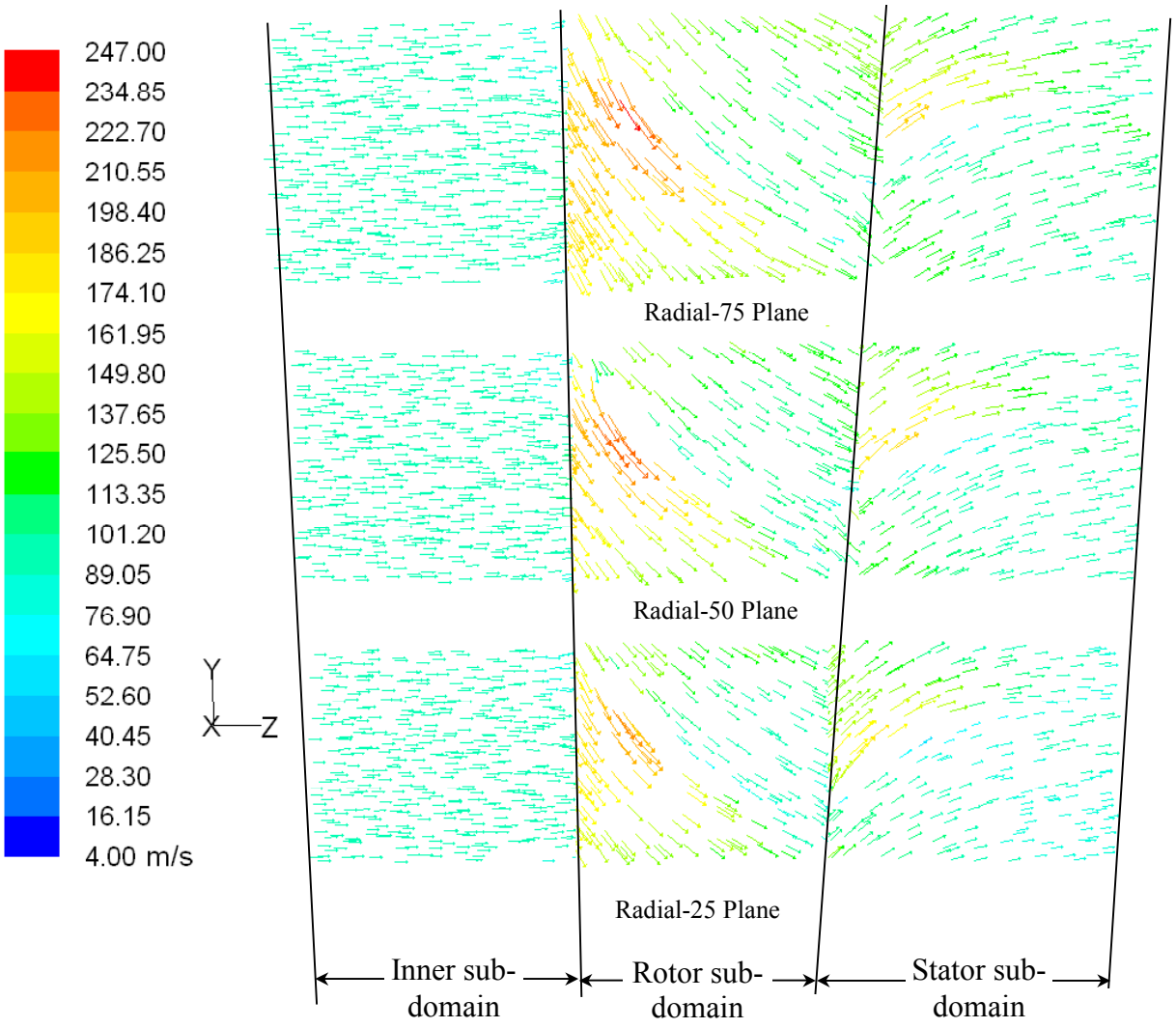

Figure 5.23 (b) Projected horizontal velocity vector for fogging case on different radial planes

5.6.3.4 Slip Velocity and Reynolds Number

Water droplets are injected at the inlet with the velocity of 25m/s along with the continuous phase (air) flowing at a velocity of 91m/s. Initially the droplets have a slip velocity of -66m/s, which keeps decreasing (i.e. tends to zero) along the domain. This slip velocity affects the droplet Reynolds number and the associated drag and droplet evaporation rate. The variation of droplet Reynolds number is shown in Fig. 5.24. The droplet Reynolds number starts at around

15 at the inlet and reduces to almost zero at the end of the inlet sub-domain. As soon as the droplets enter the rotor sub-domain, they accelerate due to additional momentum from the rotational motion of the rotor and the induced centrifugal motion. As a result the droplet slip velocity increases from 0 to 40 m/s (as they move from leading to trailing edge of rotor) and a few particles are found to have a slip velocity more than 100m/s (droplet is faster than the air in rotor subdomain). Therefore, a slip Reynolds number in the range of 0 to 80 is observed. When the droplets enter the stator sub-domain, the slip velocity again decreases (as low as 5 m/s) and results in reduced droplet Reynolds number down to 7.

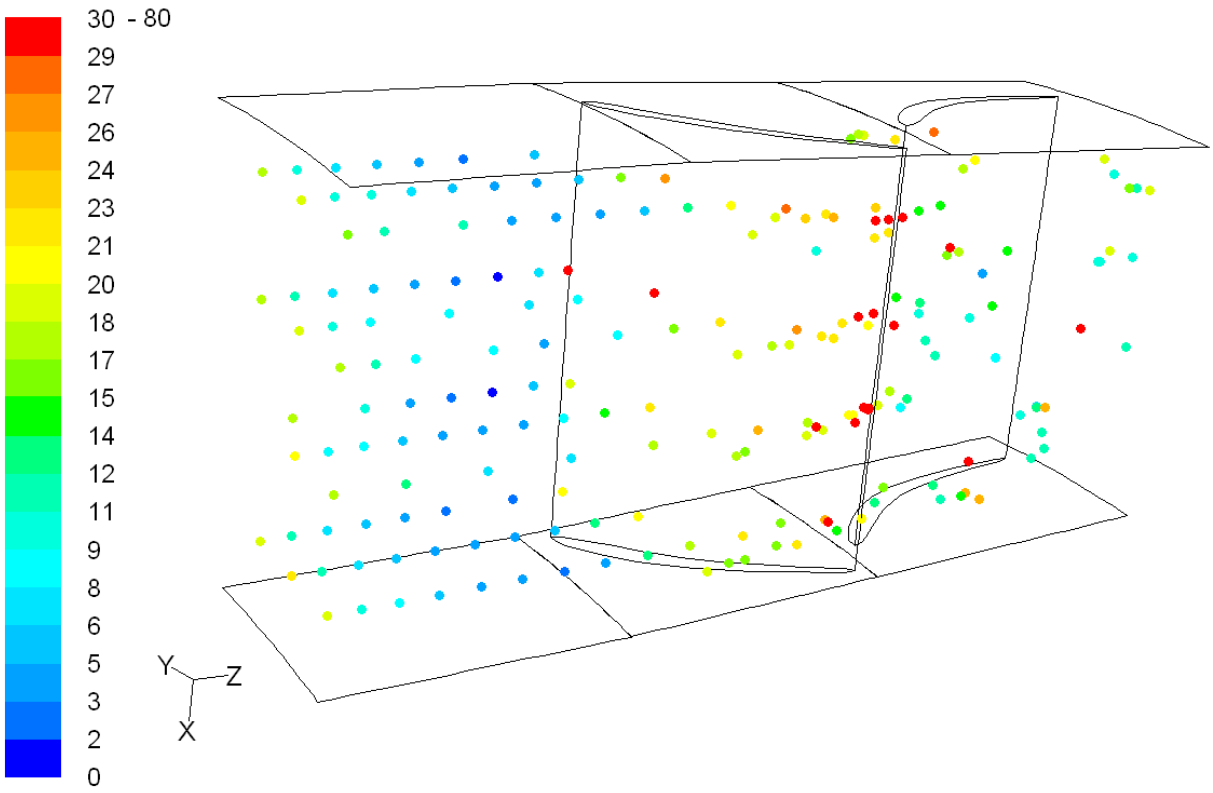

Figure 5.24 Water droplet trrace with droplets' relative Reynolds number

5.6.3.5 Coefficient of Pressure

Figure 5.25(a) shows the contour of pressure coefficient [(P-Po)/(½ρv²)] on three radial planes in the fogging case and fig. 5.25(b) shows the pressure coefficient variation across the rotor and stator. It is obvious that the pressure side has higher pressure and suction side has less pressure. Only one line near the tip region in Fig. 5.25 (b) shows relatively low pressure on the upper plane of the rotor pressure side due to the pressure leakage across the tip clearance.

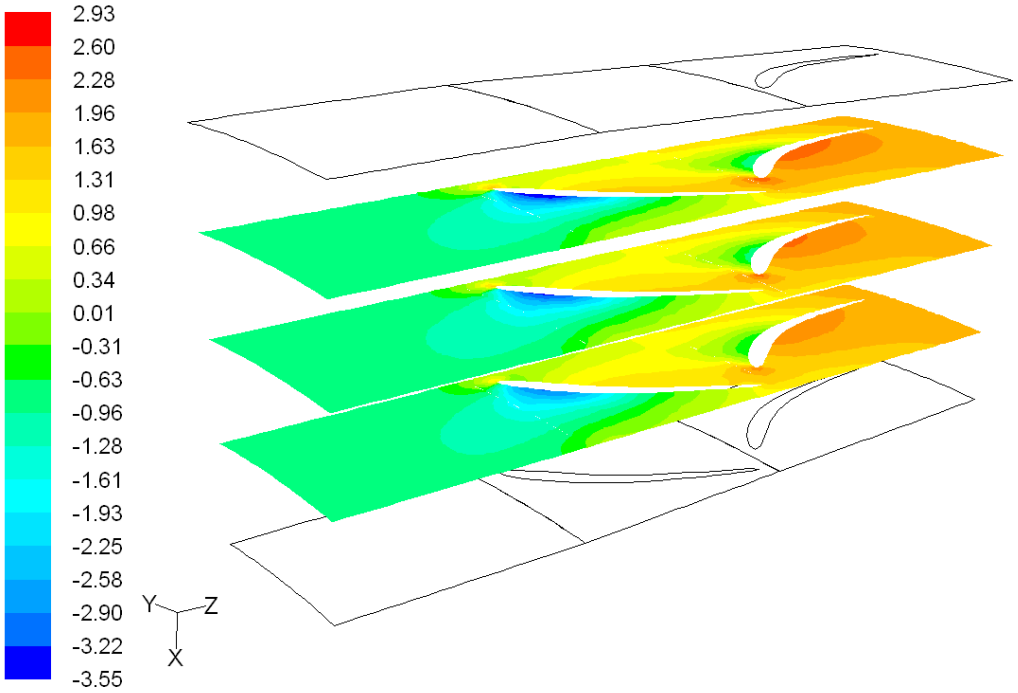

Figure 5.25(a) Contour of pressure coefficient on rotor and stator surfaces on three radial planes for the fogging case

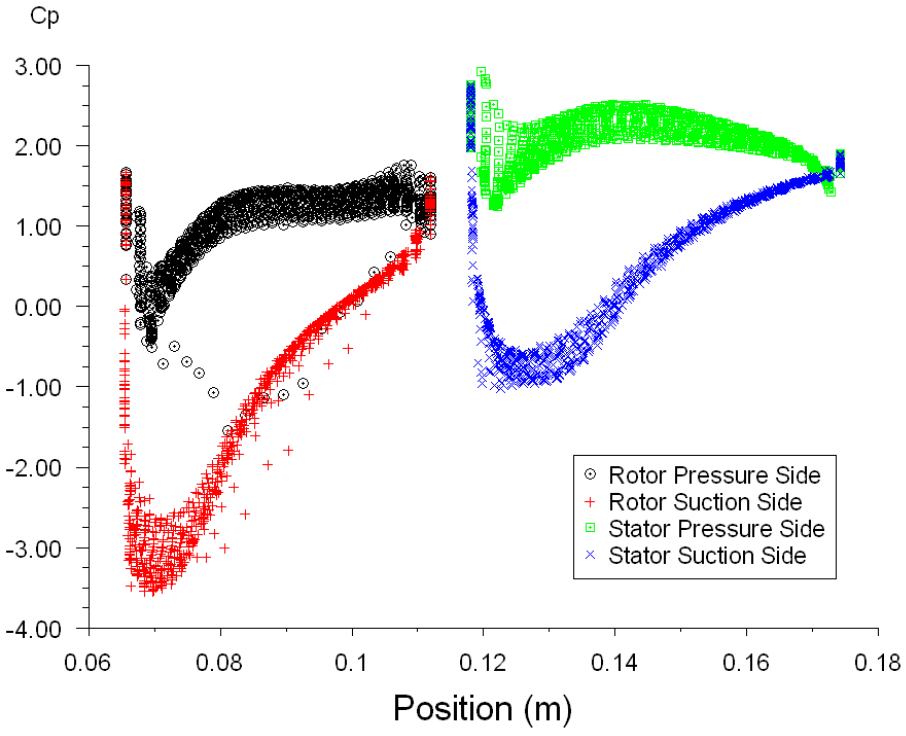

Figure 5.25(b) Variation of pressure coefficient across rotor and stator surfaces

5.6.3.6 Droplet Breakup and Coalescence

Droplet breakup and coalescence are considered in this study. Water droplet evaporation can occur anywhere in the domain. Some droplets can be seen completely evaporated near the trailing edge or the stator Fig. 5.26(a). Droplet coalescence and break-up usually occur as a result of droplet collisions due to flow field changes through, for example, local acceleration/deceleration, centrifugal force, scattered movement of droplets or even turbulent dispersion. Turbulent dispersion is noticed from the very beginning in the inlet domain, so the probability of collisions starts immediately after the water droplets are injected. Figure 5.26(b) shows the droplet diameter distribution without breakup and coalescence. Comparison between 5.26 (a) and (b) clearly shows the effect of including coalescence and breakup models. It is obvious to observe that the droplet diameter does not increase without incorporating the coalescence model.

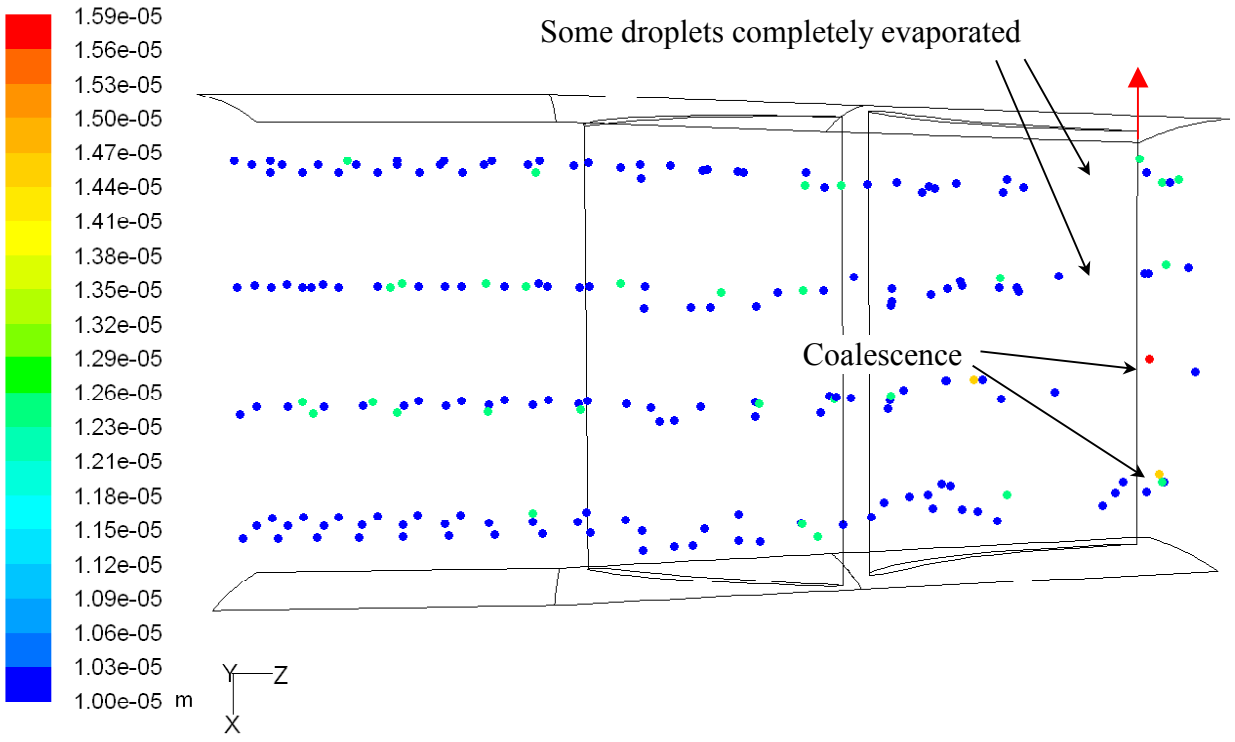

Figure 5.26(a) Water droplet trace with diameter (showing coalescence and evaporation)

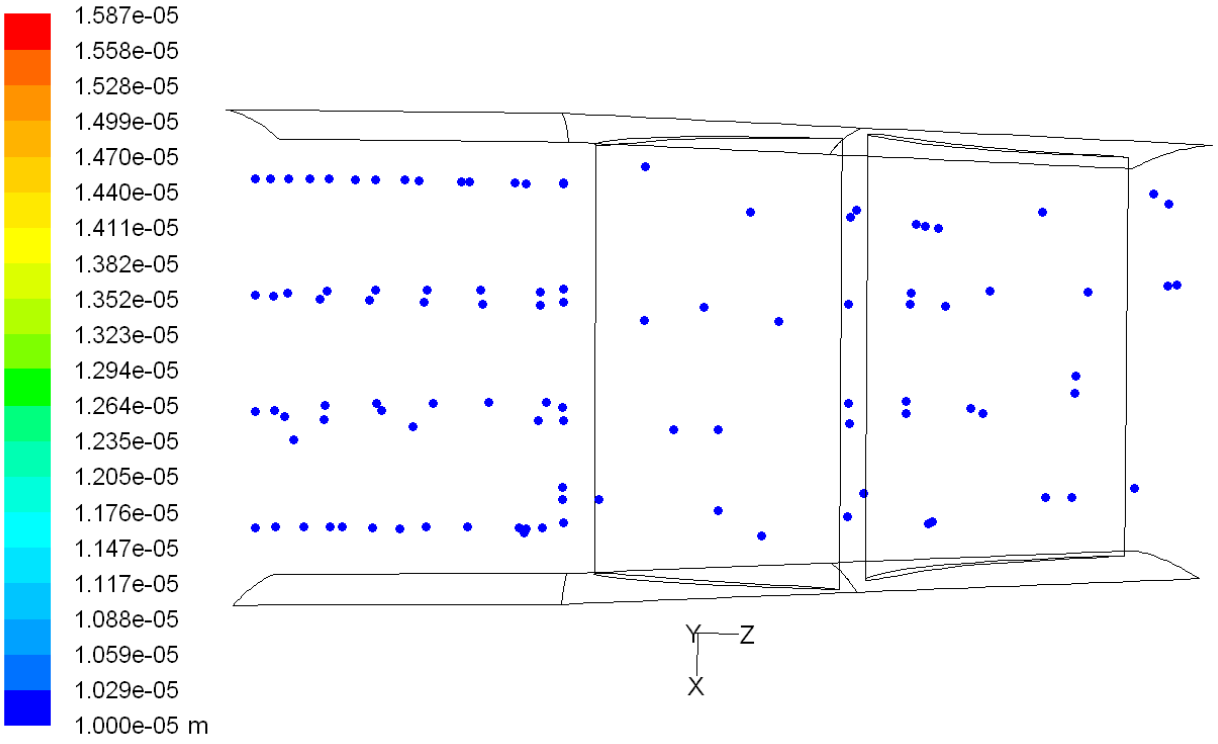

Figure 5.26(b) Water droplet trace with diameter without droplet breakup and coalescence

To help examine the occurrences of droplet breakup and coalescence, four groups of droplet sizes are picked in Fig. 5.26(a) for discussion including 10µm (smallest), 12.6µm (small), 14.4 (big) and 15.9µm (biggest). When two 10µm droplets coalesce, they become a small droplet with a diameter of 12.6µm $\left[=\sqrt[3]{(10)^3+(10)^3}=12.6\right]$, one 12.6µm droplet coalescesing with one 10µm droplet or three 10µm droplet make a big droplet of diameter 14.4µm $\left[=\sqrt[3]{(12.6)^3+(10)^3}=\sqrt[3]{(10)^3+(10)^3+(10)^3}=14.4\right]$and one 14.4µm droplet coalescesing with one 10µm droplet or two 12.6µm droplet coalesce make the biggest droplet (at the exit) $\left[=\sqrt[3]{(14.4)^3+(10)^3}=\sqrt[3]{(12.6)^3+(12.6)^3}=14.4\right]$. Maximum coalescence is noticed in the topmost stream at the inlet-domain. Some big droplets and a few big droplets presents close to the pressure side of the stator.

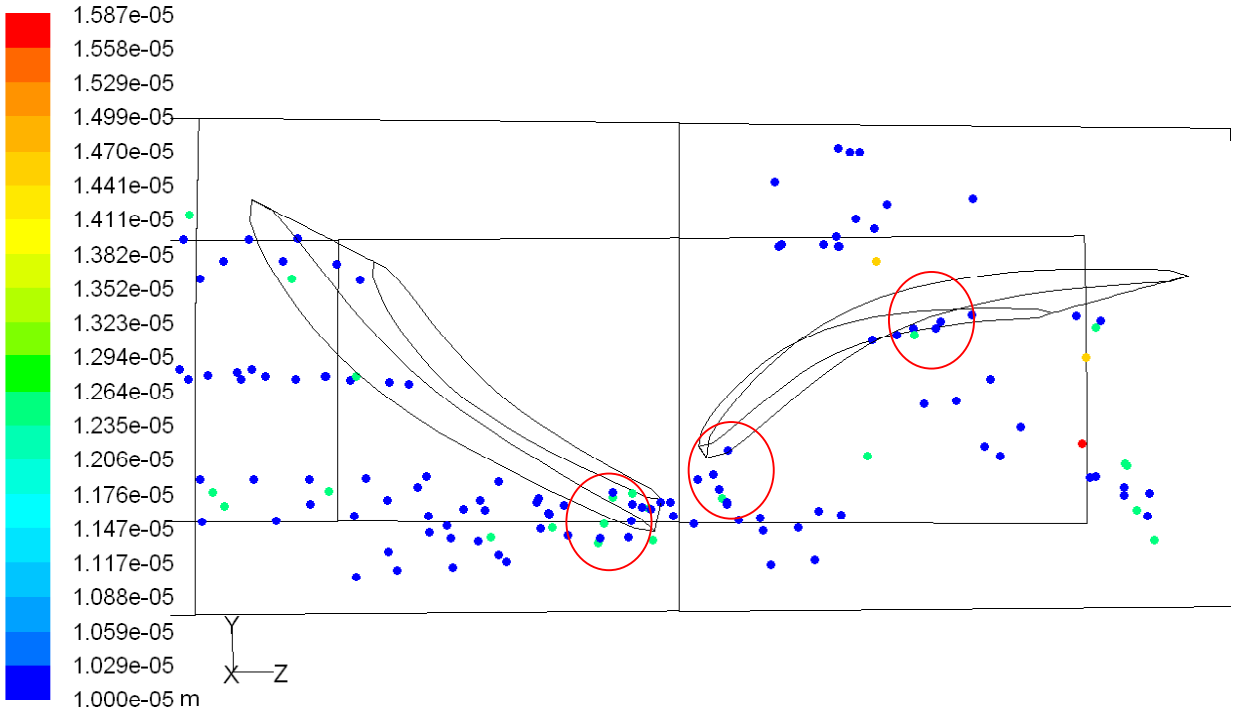

Figure 5.27(a) Accumulation (encircled) of droplets to the blade walls (Top view of Rotor and Stator subdomain)

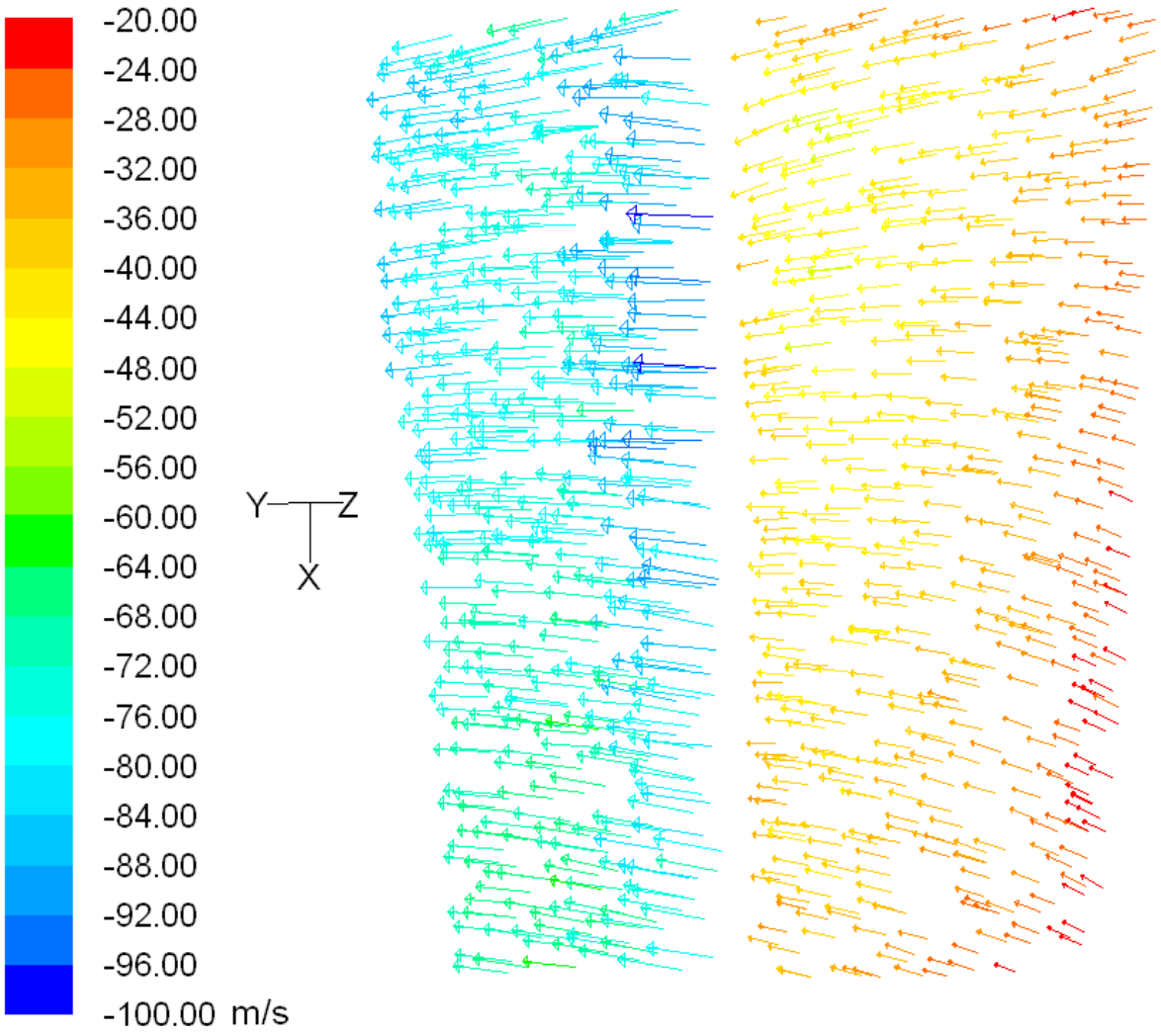

Figure 5.27(b) Secondary flow moving towards the suction surface at 20% chord length from the stator leading edge (The main flow is going away from the viewer perpendicularly; the plane of projection for velocity in this figure is the purple plane shown in Fig. 5.20b).

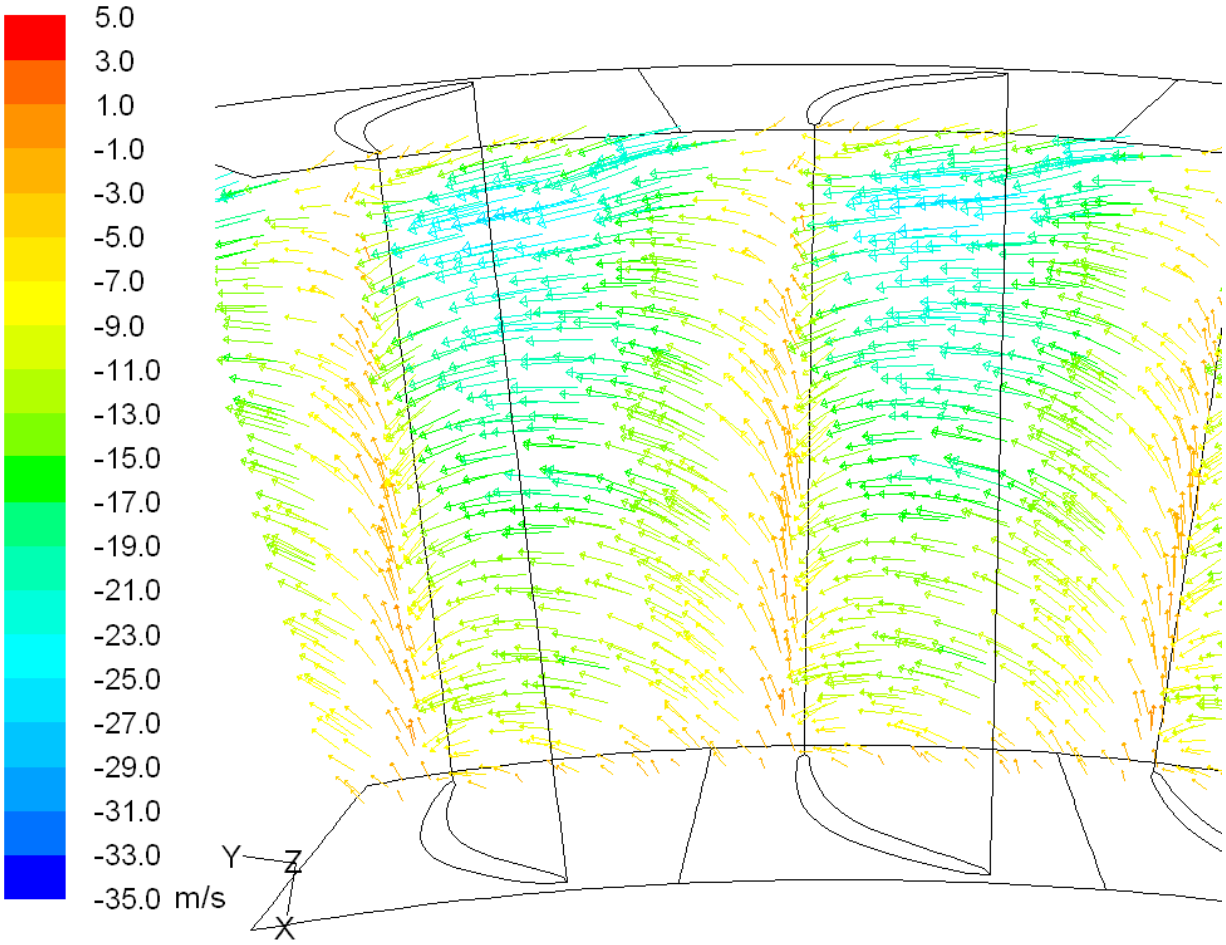

Figure 5.27(c) Secondary flow near the stator exit. (The main flow is going away from the viewer perpendicularly; the plane of projection for velocity in this figure is the brown plane shown in Fig. 5.20b).

Figure 30 shows the liquid droplet concentration. At this periodic position, most of the liquid droplets hit the suction side and leave the pressure side uncooled. A little upward (radial) movement of the droplets (especially in the topmost stream) is seen in the rotor sub-domain (shown by a red arrow in Fig. 5.26a) and at the beginning of the stator sub-domain probably due to the secondary flow motion.

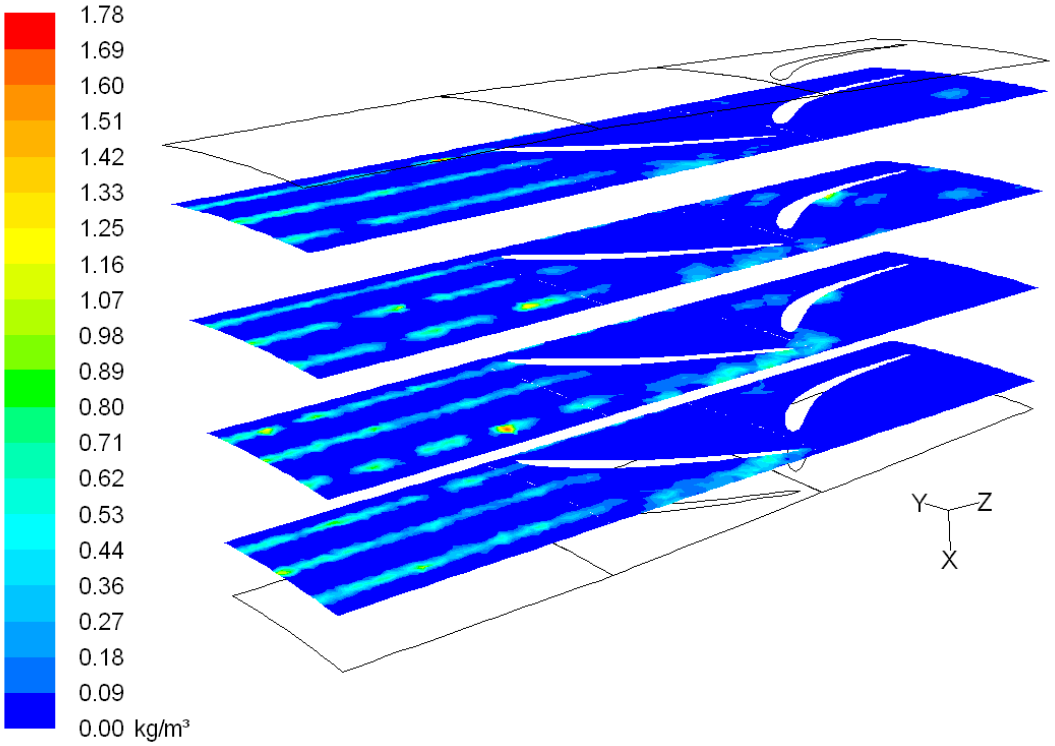

Figure 5.28(a) Liquid concentration on four different radial planes

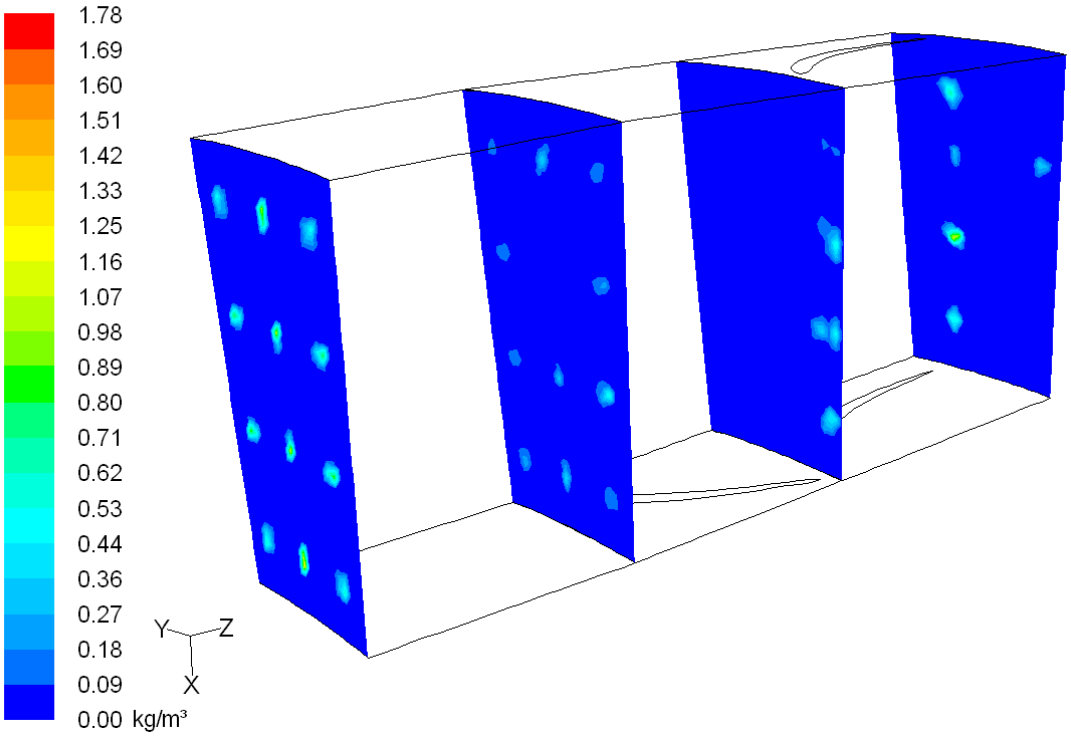

Figure 5.28(b) Liquid concentration on four different axial planes

5.6.3.7 Droplet Erosion

Figure 5.29 (a) shows the erosion on the blade surface and the maximum erosion is quantified as 1.348×10^{-7} kg/m²s, which is equivalent to 0.5mm loss of material in one year given that the compressor runs 24 hours in 365 days in a year. Based on current model, this erosion is pretty serious. According to the boundary conditions, the spray is arranged at four equidistant locations in radial direction. It is noticed that four eroded areas are seen on the suction side in the rotor trailing edge, which are corresponding to the four radial droplet injection locations. CFD animation movie shows that the water droplets hit the rotor blade most at the trailing edge of the suction side. A snap shot can be seen in Fig. 5.27(a). Some droplets also hit on the rotor suction side near the leading edge and cause some erosion as shown in Fig. 5.29 (a). Some droplets hit the stator's pressure side before leaving the domain (as shown by the secondary flow in Fig. 5.27c) and results in some erosion close to the trailing edge of the stator pressure side.

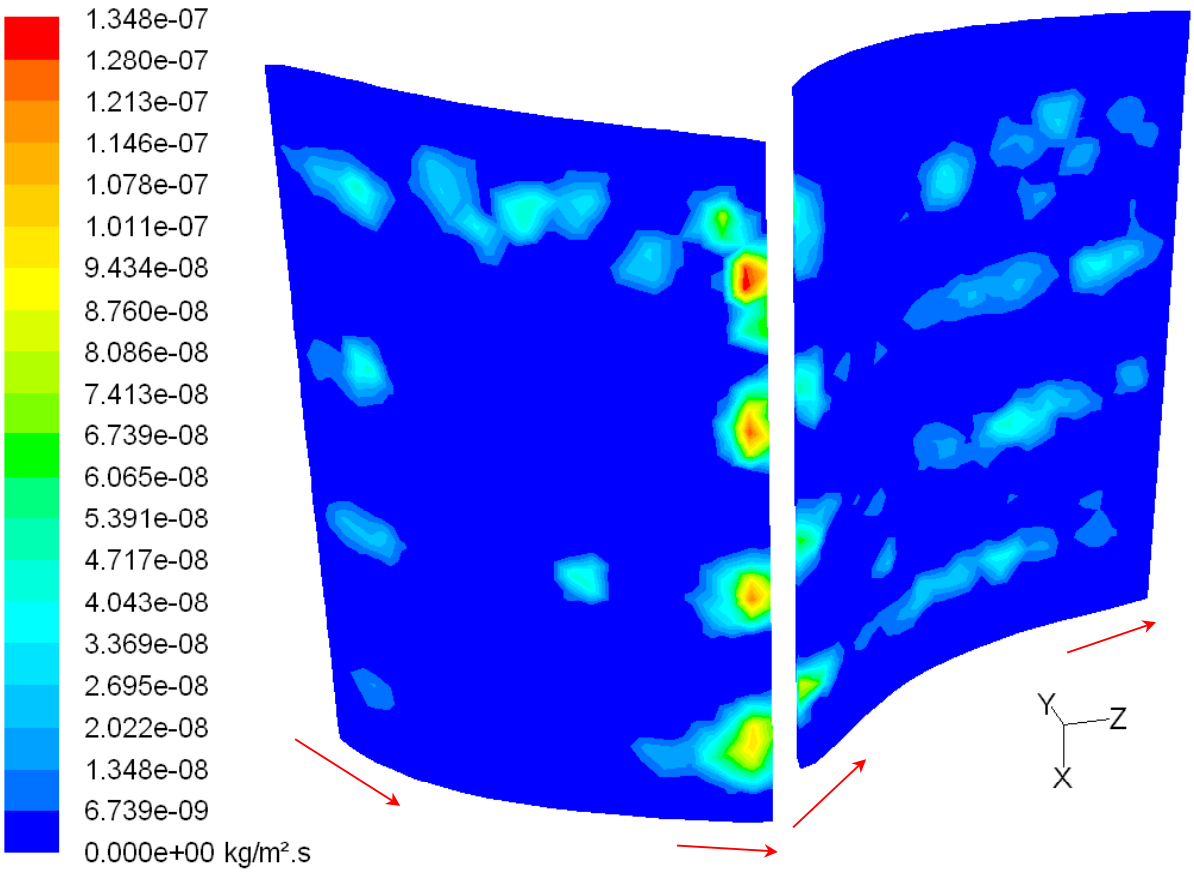

Figure 5.29 (a) Blade erosion on suction side of rotor and pressure side of stator. (The blade at the left is the rotor and the other is the stator. Red arrows show the flow direction.)

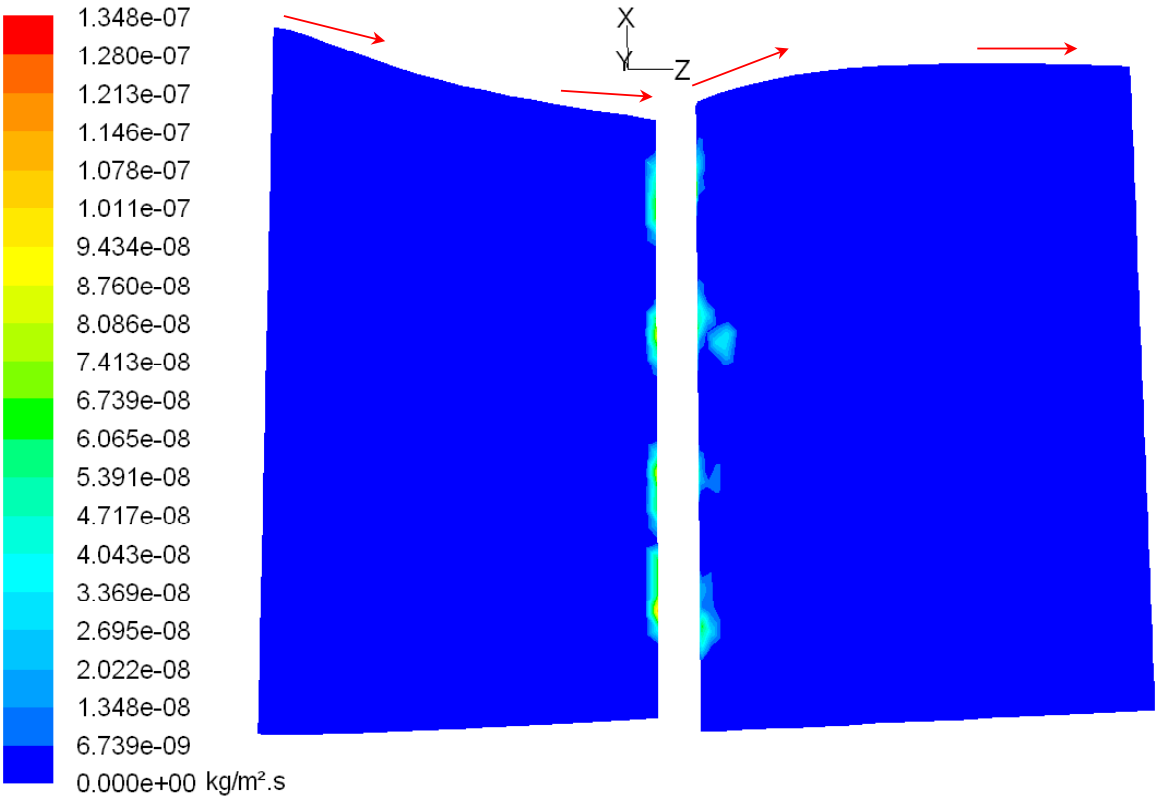

Figure 5.29 (b) Blade erosion on pressure side of rotor and Suction side of stator. (The blade at the left is rotor and the other is stator. Red arrows close to the surfaces show the flow direction)

Erosion on stator occurs mostly on the leading edge of the stator pressure side, as the rotor splashes the droplets towards the pressure side of the stator, which is seen from flow animation movie. The trailing edge of the rotor pressure side has also shown some erosion (Fig. 5.29 b).

5.6.3.8 Comparison of Obtained Results between Stacking Method and CFD Model

Comparison is made between the Stacking method and the CFD model, the results show good agreements in the baseline cases, but noticeable differences in the fogging cases. The major reason is caused by the assigned inlet condition difference. In the stacking method, the air is assumed fully saturated at the compressor inlet after a sufficient duct length to evaporate the droplets downstream of atomizers; whereas, in the CFD model, the water spray is placed in the

CFD domain inlet which is very close to the compressor inlet and give insufficient time for droplets to evaporate to reach saturation state at the compressor inlet. This above difference results in lower temperature and hence lower pressure at the studied flow passage in the stacking method than in the CFD model. For example, the pressure ratios are 1.05 vs. 1.11 for the fogging cases. For 3D cases, the FogGT result shows that the remaining water at the exit is 37%, whereas CFD result gives this value as 94%. This big difference could be caused by more than the effect of inlet condition and requires further study to examine in details of the droplet evaporation models.

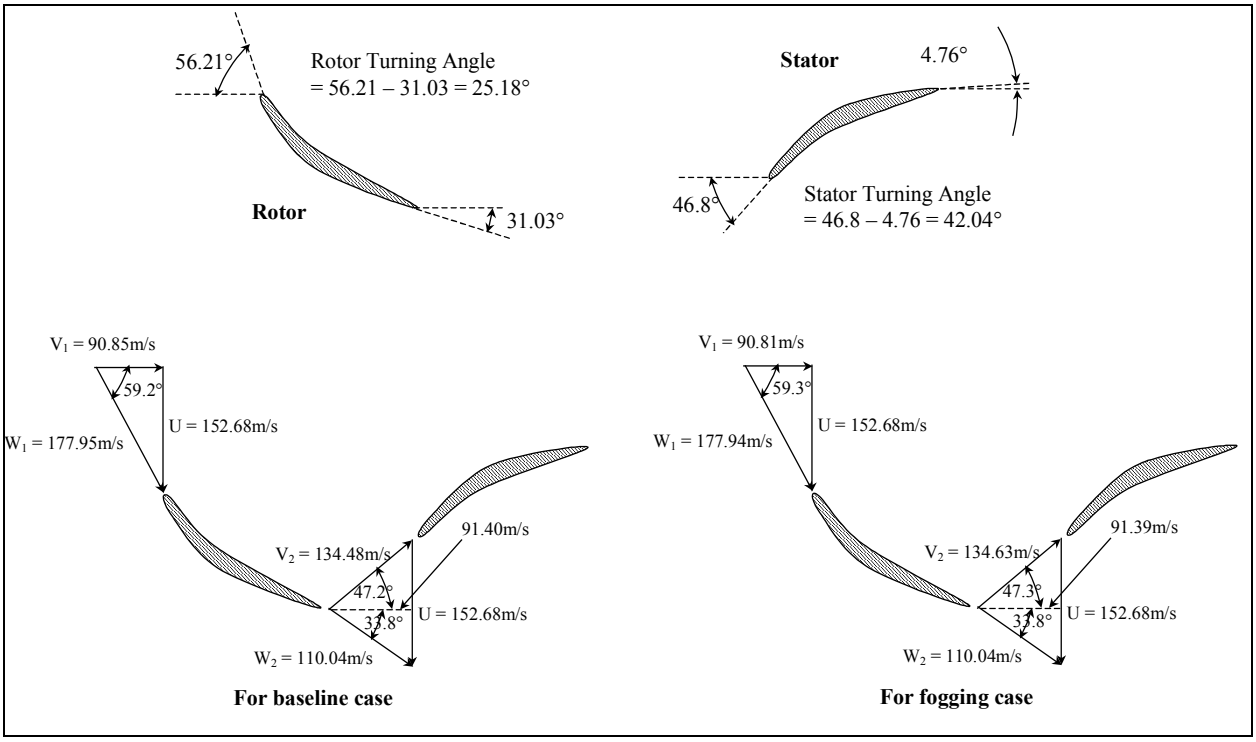

Figure 5.30 Velocity diagrams for rotor and stator for 3D baseline and fogging cases

Table 5.3 Comparison between the stacking method (with FogGT) and the CFD model for 2D and 3D cases

Parameters	Unit	Location	Cases							
			Baseline 2D		Fogging 2D		Baseline 3D		Fogging 3D	
			CFD	FogGT	CFD	FogGT	CFD	FogGT	CFD	FogGT
Static pressure	kPa	Rotor inlet	99.32	99.32	99.29	99.29	96.07	96.07	95.94	95.94
		Stator inlet	103.44	103.77	103.47	101.05	105.55	107.30	105.83	99.91
		Stator exit	105.40	105.76	105.47	101.60	109.98	112.17	110.55	101.29
Static pressure ratio		Rotor inlet to stator exit	1.061	1.065	1.062	1.023	1.145	1.168	1.152	1.056
Total pressure	kPa	Rotor inlet	101.15	101.13	101.15	101.22	101.12	100.72	101.00	100.91
		Stator inlet	107.69	107.55	107.71	102.39	117.02	117.44	117.42	103.05
		Stator exit	107.16	107.52	107.23	102.39	115.61	117.36	116.15	103.04
Total pressure ratio		Rotor inlet to stator exit	1.059	1.063	1.060	1.012	1.143	1.165	1.150	1.021
Static temperature	K	Rotor inlet	299.83	299.83	299.61	293.81	299.89	299.89	299.56	293.71
		Stator inlet	303.60	304.07	303.31	295.26	309.31	310.69	309.05	297.03
		Stator exit	305.55	305.73	305.13	295.68	313.52	314.66	313.21	298.10
Total temperature	K	Rotor inlet	301.39	301.38	301.19	295.31	304.18	303.97	303.85	297.66
		Stator inlet	307.08	307.20	306.78	296.29	318.31	318.82	318.09	299.46
		Stator exit	306.98	307.17	306.57	296.29	317.98	318.75	317.62	299.45
Axial velocity	m/s	Rotor inlet	55.98	55.98	56.21	56.21	90.85	90.85	90.81	90.81
		Stator inlet	55.39	55.24	55.49	55.91	91.40	91.13	91.39	95.74
		Stator exit	53.80	53.60	53.93	55.40	93.26	91.49	92.76	98.34
Tangential velocity	m/s	Rotor inlet	-0.01	0.00	-0.01	0.00	0.88	0.00	0.04	0.00
		Stator inlet	62.63	57.13	62.48	56.82	98.65	91.06	98.87	87.92
		Stator exit	4.44	3.67	4.52	3.31	11.65	4.69	11.15	0.90
Density	kg/m^3	Rotor inlet	1.1402	1.1482	1.1408	1.1791	1.1038	1.1102	1.1036	1.1395
		Stator inlet	1.1727	1.1829	1.1742	1.1922	1.1767	1.1968	1.1811	1.1691
		Stator exit	1.1874	1.1991	1.1897	1.1964	1.2075	1.2354	1.2150	1.1791
Mass flow rate	kg/s	Rotor inlet	2.6450	2.6995	2.6612	2.7836	0.4639	0.4620	0.4628	0.4740
		Stator inlet	2.6450	2.6995	2.6614	2.7836	0.4639	0.4620	0.4644	0.4740
		Stator exit	2.6450	2.6995	2.6636	2.7836	0.4639	0.4620	0.4654	0.4740
Remained liquid water	%	At the end	NA	NA	78.97	60.53	NA	NA	93.79	36.74

* Domain is not extened through here
+ The radial velocity is not considered in FogGT
---- These are 2-d cases

CHAPTER SIX
CONCLUSIONS

6.1 Summary

A thermodynamic model was developed first to analyze the wet compression in the whole gas turbine system, which was followed by the wet compression analysis performed by aero-thermodynamic stage-stacking model with thermally equilibrium and non-equilibrium models, and finally, a CFD model was developed to simulate the wet compression process with water droplets in a single stage axial flow compressor both in 2D and 3D. The CFD model is a viscous, turbulent, and unsteady flow model with a full coupling between the droplets (tracked by Langrangian method) and the airflow (formulated with Eulerian method). An in-house developed code, FogGT, and a commercial code FLUENT were used in the stage-stacking method and CFD simulation, respectively.

The stage-stacking method started with designing an eight-stage axial compressor for ISO ambient condition as the design case. Then the same compressor geometry (design case) was used for different off-design cases starting with a hot case, followed by saturation, overspray and inter-stage spray cases. Overspray up to 2% were analyzed in this method for both thermally equilibrium and non-equilibrium cases, which were compared later. However inter-stage spray was not analyzed in non-equilibrium cases. Distributions of temperature, pressure, humidity, density and aerodynamic parameters were studied in the equilibrium method. The same parameters were also studied in non-equilibrium method, and in addition, variations of droplet diameters and droplet temperature were studied, which were not needed and hence were not included in the calculation of equilibrium method.

In the CFD simulations, the airflow field was solved first to study the moist air (or dry compression) with 60% relative humidity. Water droplets, with 1% of the air mass flow rate. were then introduced, and the flow field was recalculated with the aerodynamic and heat transfer interactions with the droplets using species transport equations coupled with energy and momentum equations. In addition, droplet dynamics was simulated, including droplet collision, break-up and coalescence. Specifically, the concerns on the potential compressor blade erosion

were investigated by incorporating a modified liquid erosion model in the CFD simulation. The 2-D CFD results were analyzed and extended to 3-D wet compression.

Application of GT inlet fogging with GT fired with low calorific value alternative fuels derived from biomass or coal were also investigated. The conclusions are summarized below.

6.2 Conclusions

1. Inlet fogging applied to LCV-fueled GTs:

   - LCV fuel fired gas turbine systems introduces more power consumption of fuel compressor (10-15% of turbine power) comparing with natural gas fired one (2%). As heating value for LCV fuel has more incombustible gases, they need more heat (25-45%) in combustion chamber to achieve the desired turbine inlet temperature (TIT).

   - LCV fuels produce more net output power than natural gas, even though LCV fuels significantly increases fuel compressor power consumption. When LCV fuels are burned, saturated fogging achieves an increase of net output power approximately 1-2%, while 2% overspray achieves 20% net output enhancement. As the ambient temperature or relative humidity increase, the net output power decreases.

   - For LCV fuels, the thermal efficiency is approximately 10~16% (3~5 percentage points) lower than using natural gas. Burning LCV fuels lead to small change in thermal efficiency irrespective of a large increase in net power output, due to increased demand of additional heat input to make up the sensible heat required for increased fuel flow rate including incombustible gases.

2. Stage-stacking wet compression analysis

   - Thermodynamic analysis shows that compressor power increases with the increase of ambient temperature and decreases with the increase of water spray due to increase of air density at the inlet given that the pressure ratio remains same. But stage-stacking scheme surprisingly shows that even though the density increases at the inlet, it decreases than the hot ambient condition in later stages because decrease of temperature (due to inlet

evaporation) reduces pressure faster than temperature, which results in the decrease in density according to polytropic relation (Pv^k = Constant). This fact is supported by the results obtained from both equilibrium and non-equilibrium stage-stacking method.

- Stage-stacking analysis for both equilibrium and non-equilibrium methods show that the pressure ratio increases with the increase of water spray, which leads to the increase in compressor power with overspray --- a result that is contradictory to the conventional belief that inlet fogging reduces compressor power. Nonetheless, the net GT output power increases with fogging.

- Saturated fogging achieves the highest pressure ratio augmentation and reduces compressor power consumption; whereas overspray actually increases both the specific and overall compressor power for both equilibrium and non-equilibrium cases. Saturated fogging is found to be the most effective way of wet compression according to the ratio of power to the pressure ratio, followed by overspray at the inlet. Interstage spray achieved the worst performance.

- The stage-stacking equilibrium method predicts that all the water droplets evaporate completely at the end of stage 3, while the non-equilibrium approach predicts that the completion of evaporation delayed; but all droplets completely evaporate in the compressor except approximately 10% of the biggest droplets (30μm) escaped from the compressor.

- The local blade loading significantly increases immediately after the interstage spray. A 2% interstage fogging increases the local blade loading up to 100%. This significant increase of local blade loading induces rotating stall locally near the spray location. Overspray increases axial velocity, flow coefficient, the blade inlet velocity, the incidence angle and the tangential component of velocity, although the changes are very little.

- Shape factor is a value used to approximate the overall compressor performance;it is not adequate to apply it (the same value) to each compressor stage to evaluate the wet compression effect. Nor is it appropriate to use the same shape factor value for both dry and wet compression.

- Non-equilibrium method differs from the equilibrium method due to the change of evaporation rate. Droplet size doesn't play a role in equilibrium approach, but plays a major role in affecting the result in the non-equilibrium cases. For small droplet size of 10 μm, the droplet evaporation rate is fast, so the non-equilibrium method predicts close results as the equilibrium method. Larger droplets lead to slower evaporation, reduction of pressure ratio, and less effective compressor performance than the smaller droplets.

3. CFD analysis

- Wet compression results obtained from CFD model shows a slight increase in the pressure ratio, which is consistent with the stage-stacking method. Considering the increase in the mass flow rate, wet compression results in shifting the operating point of the compressor toward the surge line.

- The droplet slip velocity affects the droplet Reynolds number and the associated drag and droplet evaporation rate. The droplet Reynolds starts decreasing and reduces to almost zero at the end of the inlet sub-domain both in 2D and 3D cases. As soon as the droplets enter the rotor sub-domain, they accelerate due to additional momentum from the rotational motion of the rotor and the induced centrifugal motion. When the droplets enter the stator sub-domain, the slip velocity again decreases down to very small number.

- The transient results of different rotor/stator relative positions in 2D model show low airflow blockage produces more effective compression and higher temperature rise.

- Different types of droplet boundary conditions (e.g. reflect and film) in 2D model show their effect on results is negligible.

- Droplet break-up and coalescence are shown throughout the domain for both 2D and 3D cases.

- Droplets are accumulated near the rotor pressure side and stator suction side due to the secondary flow in those regions found in 3D model.

- The CFD erosion model predicts that the most eroded area occurs in trailing edge of the rotor suction side and a little in the leading edge of the stator pressure side. The largest erosion rate in 3D is predicted as 1.348×10^{-7} (kg/m²-s), which is approximately equivalent to a loss of 0.5mm thickness of metal layer per year as the worst scenario if the compressor runs without any downtime. The maximum predicted erosion rate obtained from 2D model is much smaller than 3D one, which gives almost 17μm removal of metal per year. The 2D model has a lower velocity at the inlet, and that leads to less erosion in the 2D case.

- Comparison is made between the stacking method and the CFD model; the results show good agreements in the baseline cases, but noticeable differences in the fogging cases. The major reason is caused by the assigned inlet condition difference. The stacking method assumes the air reaches saturation at the rotor inlet after a sufficient traveling time from the fogging location; whereas the CFD method starts spray only a short distance upstream of the rotor inlet. This difference results in lower temperature and hence lowers pressure at the studied flow passage in the stacking method than in the CFD model.

6.3 Recommendations for Future Work

Wet compression is a popular and economic power augmentation technique, but it still needs more research in a number of different areas. All the problems ought to be fully investigated and validated by experiments. Some recommended future work is shown below:

1. Experimental work of wet compression on the compressor only (not with turbine) is recommended to be studied first, followed by the entire GT system.
2. Complete CFD performance analysis for the entire compressor
3. A wet-compression performance map needs to be developed and compared with dry compression. Experiments should follow to validate the results.
4. A droplet evaporation model needs to be studied in detail and improved.

REFERENCES

Abdelwahab, A., 2006, "An Investigation of The Use of Wet Compression In Industrial Centrifugal Compressors," Proceedings of ASME Turbo Expo 2006, Barcelona, Spain, May 8-11, 2006, ASME Paper No: GT2006-90695.

Ahmed, G.R., Yovanovich, M.M. and Culham, J.R., 1997, "Experiment and Approximate Analytical Modeling of Forced Convection from Isothermal Spheres," Journal of Theomophysics and Heat Transfer, Vol. 11, No. 2, April-June 1997, pp. 223-231.

Bagnoli, M., Bianchi, M., Melino, F., Peretto, A., Spina, P.R., Bhargava, R. and Ingistov, S., 2004, "A Parametric Study of Interstage Injection on GE Frame 7EA Gas Turbine," Proceedings of ASME Turbo Expo 2004, Vienna, Austria, June 14-17, ASME Paper No: GT2004-53042.

Bagnoli, M., Bianchi, M., Melino, F. and Spina, P.R., 2008, "Development and Validation of a Computational Code for Wet Compression Simulation of Gas Turbines," ASME Journal of Engineering for Gas Turbines and Power, January 2008, Vol. 130, pp.012004/1-8.

Bagnoli, M., Bianchi, M., Melino, F., Peretto, A., Spina, P.R., Ingistov S. and Bhargava, R.K., 2008, "Application of a Computational Code to Simulate Interstage Injection Effects on GE Frame 7EA Gas Turbine," ASME Journal of Engineering for Gas Turbines and Power, January 2008, Vol. 130, pp.012001/1-10.

Bardon, M.F., 1982, "Modified Brayton Cycles Utilizing Alcohol Fuels," Journal of Engineering for Power, vol. 104, Apr. 1982, pp. 341-348.

Bardon, M.F. and Fortin, J.A.C, 1982, "Methanol Dissociative Intercooling in Gas Turbines," The American Society of Mechanical Engineers ASME Paper No. 82-GT-176.

Bathie, W. W., 1998, Fundamentals of Gas Turbines, 2nd Ed., Chapter 4, John Wiley & Sons, Inc., 1998.

Bhargava, R. and Meher-Homji, C.B., 2002, "Parametric Analysis of Existing Gas Turbines with Inlet Evaporative and Overspray Fogging," Proceedings of ASME Turbo Expo 2002, Amsterdam, The Netherlands, June 3-6, 2002, ASME Paper No: GT2002-30560.

Bhargava, R., Bianchi, M., Melino, F. and Peretto, A., 2003, "Parametric Analysis of Combined Cycles Equipped with Inlet Fogging," Proceedings of ASME Turbo Expo 2003, Atlanta, Georgia, USA, June 16-19, ASME Paper No: GT2003-38187.

Bianchi, M., Melino, F., Peretto, A., Spina, P.R. and Ingistov S., 2007, "Influence of Water Droplet Size and Temperature on Wet Compression," Proceedings of ASME Turbo Expo 2007, Montreal, Canada, May 14-17, 2007, ASME Paper No: GT2007-27458.

Bitter, P.P.A., 1963, "A Study of Erosion Phenomena, Part I," Wear, 6.

Bitter, P.P.A., 1963, "A Study of Erosion Phenomena, Part II," Wear, 6.

Bowden, F.P. and Field, J.E., 1964, "The Brittle Fracture of Solids by Liquid Impact, by Solid Impact, and by Shock," Proceedings of the Royal Society (London) A, Vol. 282, 1964, pp. 331-352.

Boyce, M. P., 2001, "Gas Turbine Engineering Handbook," 2nd ed., Gulf Professional Publishing, pp. 124-125.

Brun, K., Kurz, R. and Simmons, H.R., 2005, "Aerodynamic Instability and Life Limiting Effects of Inlet and Interstage Water Injection into Gas Turbines," Proceedings of ASME Turbo Expo 2005, Reno, Nevada, USA, June 6-9, ASME Paper No: GT2005-68007.

Budindki, K. G., 1996, Engineering Materials Properties and Selection, 5th Ed., Chapter 12 & 13, Prestice-Hall, Inc., 1996.

Cataldi, G., Güntner, H., Matz, C., McKay, T., Hoffmann, J., Nemet, A., Lecheler, S. and Braun, J., 2004, "Influence of High Fogging Systems on Gas Turbine Engine Operation and Performance," Proc. of ASME Turbo Expo 2004, Vienna, Austria, June 14-17, ASME Paper No: GT2004-53788.

Cerri, G., Salvini, C., Procacci, R., Rispoli, F., 1993, "Fouling and Air Bleed Extracted Flow Influence on Compressor Performance," ASME Paper 93-GT-366.

Chaker, M., Meher-Homji, C.B., Mee, T.R., 2004, "Inlet Fogging of Gas Turbine Engines—Part I: Fog Droplet Thermodynamics, Heat Transfer and Practical Considerations," ASME Journal of Engineering for Gas Turbine and Power, July, 2004, Vol. 126, pp. 545-558.

Chaker, M., Meher-Homji, C.B., Mee, T.R., 2004, "Inlet Fogging of Gas Turbine Engines—Part II: Fog Droplet Sizing Analysis, Nozzle Types, Measurement and Testing," ASME Journal of Engineering for Gas Turbine and Power, July, 2004, Vol. 126, pp. 559-570.

Chaker, M., Meher-Homji, C.B., Mee, T.R., 2004, "Inlet Fogging of Gas Turbine Engines—Part III: Fog Behavior in Inlet Ducts, Computational Fluid Dynamics Analysis, and Wind Tunnel Experiments," ASME Journal of Engineering for Gas Turbine and Power, July, 2004, Vol. 126, pp. 571-580.

Chattopadhyay, R., 2001, Surface Wear: Analysis, Treatment, and Prevention, 2nd Ed., Chapter 2, ASM International, 2001.

Chima, R. V., 1998, "Calculation of Tip Clearance Effects in a Transonic Compressor Rotor," Journal of Turbomachinery, January 1998, Vol. 120, pp. 131-140.

Clift, R. and Gauvin, W. H., 1970, "The Motion of Particles in Turbulent Gas Stream," Procedure of Chemeca, Vol. 70.1.14, 1970.

Cohen, H., Rogers, GFC, and Saravanamuttoo, HIH, 1996, "Gas Turbine Theory," 4th ed., Longman, pp. 50-53.

Dixon, S.L., 2005, "Fluid Mechanics and Thermodynamics of Turbomachinery," fifth Ed., Elsevier, pp. 35-39.

Duan, R., Koshizuka, S. and Oka, Y., 2003, "Droplet Breakup Under Impulsive Acceleration Using Moving Particle Semi-Implicit Method," 11th International Conference on Nuclear Engineering, Tokyo, Japan, April 20-23, 2003, Paper No: ICONE11-36029.

Fayall, A., 1966, "Particle Aspects of Rain Erosion of Aircraft and Missiles," Philosophical Transaction of Royal Society (London) A, Vol 260, 1966, pp. 290-291.

Finnie, I. and McFadden, D. H., 1978, "On the Velocity Dependence of the Erosion of Ductile Metals by Solid Particles at Low Angles of Impingement," Wear, 48, pp. 181-190.

Finnie, I., Wolak, J. and Cabil, Y., 1967, "Erosion of Metals by Solid Particles," Journal of Materials, 2, pp. 682-700.

Fluent Manual, Version 6.2.12, 2005, Fluent, Inc.

Folio, F. and Lacour, A., 1996, "Heat Transfer by Conduction and Convection between a Spherical Droplet Particle and a Two-Phase Fluid," International Journal of Rapid Solidification, 1996, pp. 75-89.

Gasparovic, I.N. and Hellemans, J.G., 1972, "Gas Turbines with Heat Exchanger and Water Injection in the Compressed Air," Journal of Combustion, n. 6, vol. 44, pp. 32-40, July 1972 – June 1973.

Gerolymos, G. A. and Vallet, I., 1999, "Tip-Clearance and Secondary Flows in a Transonic Compressor Rotor," Journal of Turbomachinery, October 1999, Vol. 121, pp. 751-762.

Hardy, J.K., 1947, "Evaporation of Drops of Liquid," Communication by the Principal Director of Scientific Research (Air), Reports and Memoranda No. 2805, 1947.

Härtel, C., Pfeiffer, P., 2003, "Model Analysis of High-Fogging Effects on the Work of Compression," Proceedings of ASME Turbo Expo 2003, Atlanta, USA, June 16-19, 2003, ASME Paper No: GT2003-38117.

Handbook of Chemistry, CRC Press, 59th Edition, 1979.

Haugen, K., Kvernvold, O., Ronald, A. and Sandberg, R., 1995, "Sand Erosion of Wear resistant Materials: Erosion in Choke Valves," Wear, 186-187: pp. 179-188, 1995.

Hill, P.G., 1963, "Aerodynamic and Thermodynamic Effects of Coolant Injection on Axial Compressors," The Aeronautical Quarterly, pp. 331-348, Nov. 1963.

Horlock, J.H., 2001, "Compressor Performance with Water Injection," Proceedings of ASME Turbo Expo 2001, New Orleans, Louisiana, USA, June 4-7, 2001, ASME Paper No: 2001-GT0343.

Hsu, S. T. and Wo, A. M., 1998, "Reduction of Unsteady Blade Loading by Beneficial use of Vortical and Potential Disturbances in an Axial Compressor with Rotor Clocking," Journal of Turbomachinery, October 1998, Vol. 120, pp. 705-713.

Ingistov, S., 2001, "Interstage Injection System for Heavy Duty Industrial Gas Turbine Model 7EA," ASME Paper 2001-GT407, Turbo Expo2001, New Orleans.

Keating, A. and Nesic, S., 1999, "Prediction of Two-Phase Erosion-Corrosion in Bends," Second International Conference on CFD in the Minerals and Process Industries, CSIRO, Melbourne, Australia, December 6-8, 1999, pp. 229-236.

Khan, J. R. and Wang, T., 2005, "Development of the Computational Program FogGT for Wet Compression via Fog/Overspray Gas Turbine Inlet Cooling," ECCC Report 2005-07, Energy Conversion and Conservation Center, University of New Orleans.

Khan, J.R. and Wang, T., 2006, "Fog and Overspray Cooling for Gas Turbine Systems with Low Calorific Value Fuels," Proceedings of ASME Turbo Expo 2006, Barcelona, Spain, May 8-11, 2006, ASME Paper No: GT2006-90396.

Khan, J. R. and Wang, T., 2008, "Simulation of Inlet Fogging and Wet-compression in a Single Stage Compressor Including Erosion Analysis," Proceedings of ASME Turbo Expo 2008, Berlin, Germany, June 9-13, 2008, ASME Paper No: GT2008-50847.

Kim, K. H. and Perez-Blanco, H., 2006, "An Assessment of High-Fogging Potential for Enhanced Compressor Performance," Proceedings of ASME Turbo Expo 2006, Barcelona, Spain, May 8-11, 2006, ASME Paper No: GT2006-90482.

Klepper J., Hale A., Davis M., Hurwitz W., 2004, "A Numerical Investigation of the Effects of Steam Ingestion on Compression System Performance," ASME paper No. GT2004-54190.

Kleinschmidt, R.V., 1947, "Value of Wet Compression in Gas-Turbine Cycles," Mechanical Engineering, vol. 69, No.2, pp. 115-116, Feb. 1947.

Kuo, K. Y., 1986, Principles of Combustion, John Wiley and Sons, New York.

Lam, T. C-T. and Dewey, R., 2003, "A Study of Droplet Erosion on Two L-0 Turbine Stages," Proc. of IJPGC 2003, Atlanta, Georgia, USA, June 16-19, IJPGC Paper No: IJPGC2003-40082.

Launder, B. E. and Spalding, D. B., 1972, Lectures in Mathematical Models of Turbulence, Academic Press, London, England.

Li, M. and Zheng, Q., 2004, "Wet Compression System Stability Analysis," Proceedings of ASME Turbo Expo 2004, Vienna, Austria, June 14-17, 2004, ASME Paper No: GT2004-54018.

Li, X. and Wang, T., 2006, "Simulation of Film Cooling Enhancement with Mist Injection," ASME Journal of Heat Transfer, Vol.128 , pp. 509-519, 2006.

Li, X, and Wang, T, 2007, "Effects of Various Modellings on Mist Film Cooling," ASME Journal of Heat Transfer, vol. 129, pp. 472-482, 2007.

Madabhushi, R.K., Leong, M.Y. and Hautman, D.J., 2004, "Simulation of The Break-up of a Liquid Jet in Crossflow at Atmospheric Conditions," Proceedings of ASME Turbo Expo 2004, Vienna, Austria, June 14-17, 2004, ASME Paper No: GT2004-54093.

Martula, D.S., Hasegawa, T., Lloyd, D.R. and Bionnecaze, R. T., 2000, "Coalescence-Induced Coalescence of Inviscid Droplets in a Viscous Fluid," Journal of Colloid and Interface Science 232, 241–253.

Meher-Homji, C.B. and Mee, T.R., 1999, "Gas Turbine Power Augmentation by Fogging of Inlet Air," Proceedings of 28th Turbomachinery Symposium, Houston, Texas, USA, September 1999.

Muir, D. E., Saravanamuttoo, H. I. H. and Marshall, D. J., 1989, "Health Monitoring of variable Geometry Gas Turbine for the Canadian Navy," ASME Journal of Engineering for Gas Turbines and Power, Vol. 124, pp. 155-160.

Murthy, S.N.B., Ehresman, C.M. and Haykin, T., 1986, "Direct and System Effects of Water Ingestion into Jet Engine Compressors," Presented at AIAA/ASME 4.sup.th Joint Fluid Mechanics, Plasma Dynamics and Lasers Conference, May 12-14, 1986.

Nesic, S., 1991, "Computation of Localized Erosion-corrosion in Distributed Two-phase Flow," Ph.D. Thesis, University of Saskachewan, Canada.

Nokleberg, L. and Sontvedt, T., 1998, "Erosion of Oil and Gas Industry Choke Valves Using Computational Fluid Dynamics and Experiment," International Journal of Heat and Fluid Flow 19, 1998, pp. 636-643.

Nolan, J.P. and Twombly, V.J., 1990, "Gas Turbine Performance Improvement Direct Mixing Evaporative Cooling System American Atlas Cogeneration Facility Rifle, Colorado," ASME Paper No. 90-GT-368, 1990.

O'Rourke, P. J., 1981, "Collective Drop Effects on Vaporizing Liquid Sprays," PhD dissertation, Princeton University, New Jersey, 1981.

O'Rourke, P. J. and Amsden, A. A., 1987, "The Tab Method for Numerical Calculation of Spray Droplet Breakup," SAE Technical Paper 872089, 1987.

Pan, Y. and Suga, K., 2005, "Numerical Simulation of Binary Liquid Droplet Collision," Physics of Fluids 17, 082105.

Patankar, S.V., 1980, Numerical Heat Transfer and Fluid Flow, Taylor and Francis , 1980.

Payne, R.C. and White, A.J., 2008, "Three-Dimensional Calculations of Evaporative Flow in Compressor Blade Rows," ASME Journal of Engineering for Gas Turbines and Power, May 2008, Vol. 130, pp.032001/1-6.

Poletavkin, P., 1970, "Cycles and Thermal Circuits of Steam-Gas Turbine Installations, with Cooling of the Gas During Compression by the Evaporation of Injected Water," Institute of High Temperature; vol. 8, No. 3; pp. 662-628, May-Jun. 1970.

Qiang, L.I., Ti-min C.A.I, Guo-qiang, H.E. and Chun-bo, H.U., 2006, "Droplet Collision and Coalescence Model," Applied Math and Mechanics, 27(1):67–73.

Ranz, W. E. and Marshall, W. R. Jr., 1952, "Evaporation from Drops, Part I," Chem. Eng. Prog., 48, pp. 141-146.

Ranz, W. E. and Marshall, W. R. Jr., 1952, "Evaporation from Drops, Part II," Chem. Eng. Prog., 48, pp. 173-180.

Roumeliotis, I., Aretakis, N. and Mathioudakis, K., 2003, "Performance Analysis of Twin-Spool Water Injected Gas Turbines Using Adaptive Modeling," Proceedings of ASME Turbo Expo 2003, Atlanta, Georgia, USA, June 16-19, 2003, ASME Paper No: GT2003-38516.

Roumeliotis I., Mathioudakis K., 2006, "Evaluation of Interstage Water Injection Effect on Compressor and Engine Performance," ASME Journal of Engineering for Gas Turbine and Power, Vol. 128/4, pp. 849-856.

Roumeliotis, I and Mathioudakis, K., 2007, "Water Injection Effects on Compressor Stage Operation," ASME Journal of Engineering for Gas Turbines and Power, Vol. 129, pp. 778-784.

Sanaye, S., Rezazadeh, H. and Aghazeynali, M., 2006, "Effects of Inlet Fogging and Wet Compression on Gas Turbine Performance," Proceedings of ASME Turbo Expo 2006, Barcelona, Spain, May 8-11, 2006, ASME Paper No: GT2006-90719.

Schiller, L., and Naumann, A., 1933, "Uber die grundlegenden Berechnungen bei der Schwekraftaubereitung," Zeitschrift des Vereines Deutscher Ingenieure, 77(12), 318-320.

Sexton, M.R., Urbach, H.B., Knauss, D.T., 1998, "Evaporative Cooling for NOx Suppression and Enhanced Engine Performance for Naval Gas Turbine Propulsion Plants," ASME paper 98-GT-332

Sexton, W.R., Sexton, M.R., 2003, "The Effects of Wet Compression on Gas Turbine Engine Operating Performance," Proceedings of ASME Turbo Expo 2003, Atlanta, Georgia, USA, June 16-19, 2003, ASME Paper No: GT2003-38045.

Shepherd, D. W. and Fraser, D., 2006, "Impact of Heat Rate, Emissions and Reliability from the Application of Wet Compression on Combustion Turbines," Power-Gen International, Las Vegas, Nevada, USA, Nov 28-30, 2006.

Slobodyanyuk, L.I., 1973, "Effect of Water Spraying on Operation of the Compressor of a Gas Turbine Engine," Energeticka, No. 1; pp. 92-95, 1973.

Spina, P. R., 2002, "Gas Turbine Performance Prediction by using Generalized Performance Curves of Compressor and Turbine Stages," Proceedings of ASME Turbo Expo 2002, Amsterdam, The Netherlands, June 3-6, 2002, ASME Paper No: GT2002-30275.

Stegeman, Y.W., Chesters, A.K., vd Vosse, F.N. and Meijer, H.E.H., 1999, "Breakup of (non-) Newtonian droplets in a time-dependent elongational flow," Proceedings PPS-15,'s-Hertogenbosch, 1999.

Tabakoff, W., Hamed, A. and Metwally, M., 1990, "Effect of Particle Size Distribution on Particle Dynamics and Blade Erosion in Axial Flow Turbines," Procedure of International Gas Turbine and Aeroengine Congress and Exposition, 1990, New York, New York, USA, June 11-14, ASME Paper No: 90-GT-114.

Tsuji, Y. and Crowe, C.T., 1997, Multiphase Flows with Droplets and Particles, 1st Ed., Chapter 2 & 4, CRC Press, 1997.

Utamura, M., Takaaki, K., Murata, H. and Nobuyuki, H., 1999, "Effects of Intensive Evaporative Cooling on Performance Characteristics of Land-based Gas Turbine," PWR-Vol34, Joint Power Generation Conference, pp. 321-328.

van den Hengel, E. I. V., Deen, N. G. and Kuipers, J. A. M., 2005, "Application of Coalescence and Breakup Models in a Discrete Bubble Model for Bubble Columns," Ind. Eng. Chem. Res. 2005, 44, 5233-5245.

Wang, S., Liu, G., Mao, J., and Feng, Z., 2007, "Experimental Investigation on the Solid Particle Erosion in the Control Stage Nozzles of Steam Turbine," Proceedings of ASME Turbo Expo 2007, Montreal, Canada, May 14-17, 2007, ASME Paper: GT-2007-27700.

Wang, T., and Dhanasekaran, T.S., 2008, "Calibration of CFD Model for Mist/Steam Impinging Jets Cooling," Proceedings of ASME Turbo Expo 2008, Berlin, Germany, June 9-13, 2008, ASME Paper No: GT2008-50737.

Wang, T., Li, X, and Pinninti, V., 2008, "Simulation of Mist Transport for Gas Turbine Inlet Air Cooling," Numerical Heat Transfer, Part A, 53: 1013-1036, 2008.

Wang, T. and Khan, J. R., 2008, "Overspray and Interstage Fog Cooling in Compressor using Stage-Stacking Scheme -- Part 1: Development of Theory and Algorithm," Proceedings of ASME Turbo Expo 2008, Berlin, Germany, June 9-13, 2008, ASME Paper No: GT2008-50322.

Wang, T. and Khan, J. R., 2008, "Overspray and Interstage Fog Cooling in Compressor using Stage-Stacking Scheme -- Part 2: Case Study," Proceedings of ASME Turbo Expo 2008, Berlin, Germany, June 9-13, 2008, ASME Paper No: GT2008-50323.

Wetzel, I.T. and Jennings, B.H., 1949, "Water Spray Injection of an Axial Flow Compressor," Proceedings of the Midwest Power Conference, vol. XI, pp. 376-380, Apr. 18-19-20, 1949.

White A J., Meacock A J., 2004, "An evaluation of the effects of water injection on compressor performance," ASME J. of Engineering for Gas Turbines and Power, Vol. 126, pp.748-754.

Willems, D.E. and Ritland, P.D., 2003, "A Pragmatic Approach to Evaluation of Inlet Fogging System Effectiveness," Proceedings of IJPGC 2003, Atlanta, Georgia, USA, June 16-19, IJPGC Paper No: IJPGC2003-40075.

Wilson, D.G. and Korakianitis, T., 1988, "The Design of High-Efficiency Turbomachinery and Gas Turbines," Prentice Hall, 2nd ed. pp.79 -87.

Wolfstein, M., 1969, "The Velocity and Temperature Distribution of One-Dimensional Flow with Turbulence Augmentation and Pressure Gradient," International Journal Heat Mass Transfer, 12, pp. 301-318.

Yap, M.R. and Wang, T., 2007, "Simulation of Producer Gas Fired Power Plants with Inlet Fog Cooling and Steam Injection," ASME Journal of Engineering for Gas Turbines and Power, July 2007, Vol. 129, pp.637-647.

Young J. B., 1995, "The Fundamental Equations of Gas-Droplet Multiphase Flow," International Journal of Multiphase Flow, Vol. 21, No. 2, pp.175-191, 1995.

Zheng, Q., Li, M., Sun, Y., 2003, "Thermodynamic Analysis of Wet Compression and Regenerative (WCR) Gas Turbine," Proceedings of ASME Turbo Expo 2003, Atlanta, Georgia, USA, June 16-19, ASME Paper No: GT2003-38517.

Zheng, Q., Sun, Y., Li, S. and Wang, Y, 2003, "Thermodynamic Analysis of Wet Compression Process in the Compressor of Gas Turbine," ASME Journal of Engineering for Gas Turbines and Power, July 2003, Vol. 125, pp.489-496.

VITA

Jobaidur Rahman Khan was born on January 15, 1973 in Dhaka, Bangladesh to Nazma Amin and Aminur Rahman Khan. He received his high school education in Govt. Laboratory High School and Notre Dame College, Dhaka, Bangladesh and graduated on August, 1989. In May 1991, he was admitted to Bangladesh University of Engineering and Technology, Dhaka, Bangladesh. In July 1996, he received his Bachelor of Science Degree in Mechanical Engineering. Following his graduation he was employed as Engineer in Padma Textile Mills Limited, a member of BEXIMCO (Bangladesh EXport IMport COmpany) in Savar, Bangladesh and as Project Engineer in Nestle Bangladesh Limited in Gazipur, Bangladesh.

In August 1998, he was admitted to the Graduate School of the University of New Orleans, and was employed as a graduate assistant by the Department of Mechanical Engineering since January 1999 to January 2001 and received his degree of Master of Science in Engineering in May 2001. Following his graduation he was employed as Engineer in Bayou Information Systems, Inc. He started his doctoral study in University of New Orleans on January 2003 and will finish his Ph.D. in Mechanical Engineering on May 2009.